INTERNATIONAL ATOMIC ENERGY AGENCY
UNITED NATIONS EDUCATIONAL, SCIENTIFIC AND CULTURAL ORGANIZATION
INTERNATIONAL CENTRE FOR THEORETICAL PHYSICS
I.C.T.P., P.O. BOX 586, 34100 TRIESTE, ITALY, CABLE: CENTRATOM TRIESTE

SMR.769 -7

WORKSHOP ON "NON-LINEAR ELECTROMAGNETIC INTERACTIONS IN SEMICONDUCTORS"

1 - 10 AUGUST 1994

Background material for lecture on "Raman effect in semiconductors"

B. JUSSERAND
CNET
Laboratoire de Bagneux
196 Avenue Henry Ravera
BP 107, F-92225 Bagneux Cedex
France

These are preliminary lecture notes, intended only for distribution to participants

Brazilian Journal of Physics, vol. 24, no. 1, March, 1994

Electronic Raman Scattering on Modulation Doped GaAs Quantum Wells: Conduction Band Structure and Collective Effects *

Bernard Jusserand
CNET, Laboratoire de Bagneux
196 Avenue Henri Ravera, 92220 Bagneux, France

Received July 12, 1993

We report on a detailed analysis of electronic Raman scattering results in modulation doped single quantum wells. We illustrate thereby the great power of this technique to get a detailed characterization of the electron density distribution and the band structure in doped heterostructures. We report in particular on a recent observaton, for first time directly by spectroscopy, of the spin splitting of the conduction band of GaAs due to the lack of inversion symmetry.

I. Introduction

Modulation doped structures are of great interest for the study of the quasi-two-dimensional electron gas (2DEG), in both transport and optical experiments because of the high mobility achieved by separating the electrons from the ionized donors. Among these studies, a large amount of work has been devoted to one side modulation doped single quantum wells. This system appears very promising for spectroscopic probes of the integer and fractional quantum Hall effects by optical measurements under quantizing magnetic field[1-3]. On the other hand, electronic Raman scattering is a powerful tool to probe electronic excitations, both collective and single-particle, occuring in a 2DEG. This was first suggested by Burstein et al.[4] and has since been extensively demonstrated[5]. Moreover, in the backscattering set-up, we can change the wavevector in the plane of the 2DEG by simply rotating the sample relative to the fixed incident light wave vector. This provides a unique possibility to determine the dispersion of these excitations and to extract the subband structure as well as the electron density in modulation doped structures[6-11]. More recently, the observation, in different polarization configurations, of distinct spin-density and single-particle excitations, in addition to charge-density waves, opened the way to an independent measure of both direct and exchange-correlation Coulomb interactions of the electron gas[12-14].

In this communication, we will illustrate these possibilities through the presentation of a whole set of electronic Raman scattering results on 180 Å thick GaAs single quantum wells claded between GaAlAs barriers. Modulation doping is obtained from a Si localized doping in the upper barrier only. This results in an asymmetric potential profile due to the self-consistent electric field. Moreover, due to the thin spacer (100Å), the typical electron density lies above $1.0 \times 10^{12}\text{cm}^{-2}$ but the Fermi energy remains below the bottom E_2 of the second subband. We will present Raman scattering results on intersubband and intrasubband transitions both with single particle and collective character on the same sample. From their in-plane dispersion and line-shape, we extract determinations of the electron density, the band structure and the lifetime of the involved states[9,11]. We will in particular report on our recent first spectroscopic observation of the spin splitting of the GaAs conduction band because of the lack of inversion symmetry[10]. All Raman scattering experiments are done at liquid Helium temperature (1.8 K) and under close energy resonance with the fundamental energy gap.

Fig. 1 shows electronic intersubband Raman spectra in parallel (polarized spectra) and crossed (depolarized spectra) polarizations respectively, for several different Raman in-plane wave vectors q. Due to the sym-

---

*Invited talk.

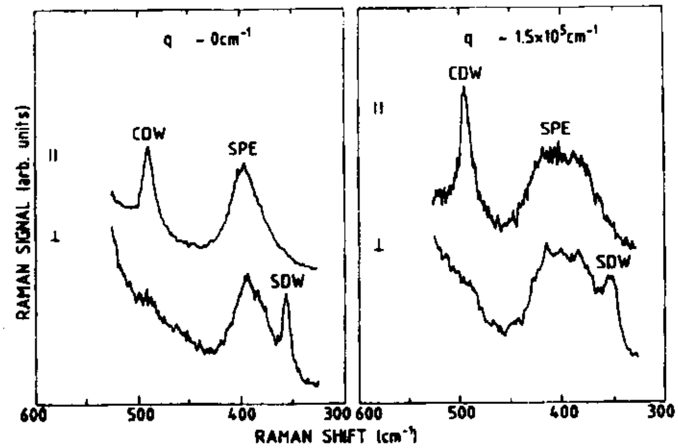

Figure 1: Electronic Raman scattering spectra obtained with a resonance laser energy of 1.64 eV and at pumped liquid He temperature (1.8K). The left side of the figure shows collective (CDW and SDW) and individual (SPE) intersubband excitations of the 2DEG for a very small Raman in-plane wavevector, while the right side exhibits the same excitations at larger q.

metry of the valence band states in GaAs, Raman cross-sections, due to virtual interband processes, in crossed (respectively parallel) polarization have been shown[15] to be related to spin-density (respectively charge density) mechanisms. One thus observes in parallel (respectively crossed) polarization collective charge density waves (CDW) and spin density waves (SDW) occuring in the 2DEG. In strong resonance conditions, one also observes, in both polarizations, a broader band of single particle excitations (SPE), with an intensity comparable to the collective ones, contrary to the theoretical prediction of complete screening. Though the origin of this observation is not yet fully understood, it appears to be very useful: the SPE band indeed peaks at the bare intersubband energy $E_2 - E_1$ of the doped structure (this is only strictly true when assuming the same parabolic dispersion for both subbands). On our sample we can thereby extract an accurate determination of the subband separation (49meV) in good agreement with the estimation deduced from luminescence[11] (48meV). Moreover this band displays a specific behavior as a function of q. Unlike the CDW and SDW, which remain approximatively unchanged, the SPE band is strongly broadened with increasing Raman in-plane wave vector according to the density of intersubband transitions.

This is schematized on Fig. 2 in which we show the

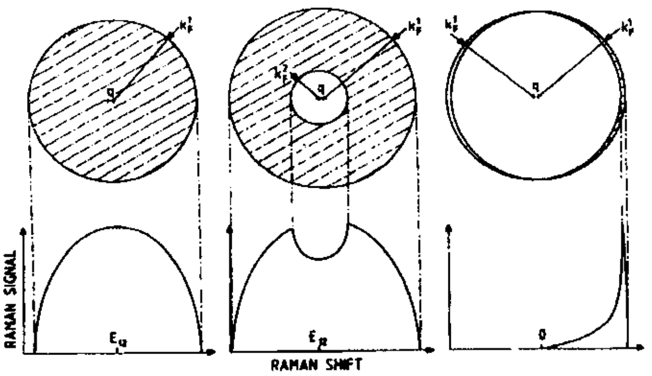

Figure 2: Schematic geometrical determination of the SPE Raman signal for three different band filling situations.

2D Fermi disk associated to the initial and final bands respectively for three different cases: a) the second subband is empty as in the sample discussed in this communication, b) it is partially filled and c) the density is the same in both subbands, a situation which applies to intrasubband transitions. The final state Fermi disk has been shifted by $-\vec{q}$ to account for the Raman wavevector transfer. As the Raman shift amounts to approximately $\hbar^2\vec{q}\cdot\vec{k}/m^*$ when assuming $q << k$, the horizontal scale of the figure can be directly transformed into an energy scale. The Raman signal for each case is then graphically deduced from the length of the equi-energy lines inside the initial and outside the final Fermi disks. In case a, the SPE signal appears as a broad band extending between two cut-off frequencies, shifted by $-\hbar q v_F$ and $+\hbar q v_F$ from the $E_2 - E_1$ energy respectively. The corresponding dispersion curve is shown in Fig.3 and compared to the experimental dispersion. The slope of the SPE dispersion reflects the electron density in E_1. However the accuracy of this determination is limited due to the intrinsic broadening of the transitions (2meV). This quantity reflects the lifetime of both initial and final states. Energy-dependent values are needed to correctly fit the SPE lineshape at every in-plane wavevector[11].

The CDW and SDW lines are not strongly dispersive and, due to the large electron density, they are well separated from the SPE band (see Fig. 1 and 3). Thus one is able to accurately determine their energies, and to deduce the electron density. Using a RPA calculation based on self-consistently determined wavefunctions[6,13], we deduce from the CDW energy an electron density of 1.3×10^{12}cm^{-2}. With this value,

2

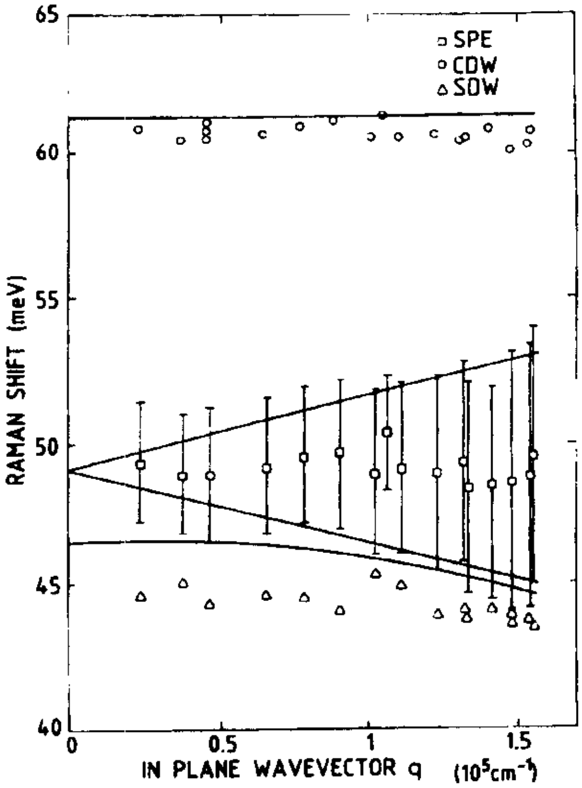

Figure 3: Dispersion curve of the collective (CDW and SDW) and individual (SPE) intersubband excitations of the 2DEG, deduced from Raman scattering experiments as a function of q. The vertical lines are the width at half maximum of the SPE line and the solid lines calculated dispersion curves.

one may extract from self-consistent subbands calculations the potential profile of the structure and the subbands energies. The calculated value of the E_1 to E_2 intersubband energy obtained by this procedure is in very good agreement with experimental values provided by PL and Raman measurements. Moreover, from the experimental SPE, CDW and SDW lines, one may extract an experimental determination of the direct and exchange-correlation Coulomb interaction in quasi-two-dimensional electron gases and compare them to different models of these quantities[12-14].

Let us now turn to the analysis of the intrasubband electronic transitions. The corresponding Raman spectra are shown on Fig. 4 for several in-plane wavevectors in both polarization configurations. As we already explained for the intersubband ones, SPE and collective excitations can be observed simultaneously at strong resonance. The low energy part of the spectra in both polarizations is attributed to SPE band. It extends from zero to a maximum energy $+\hbar q v_F$. However, con-

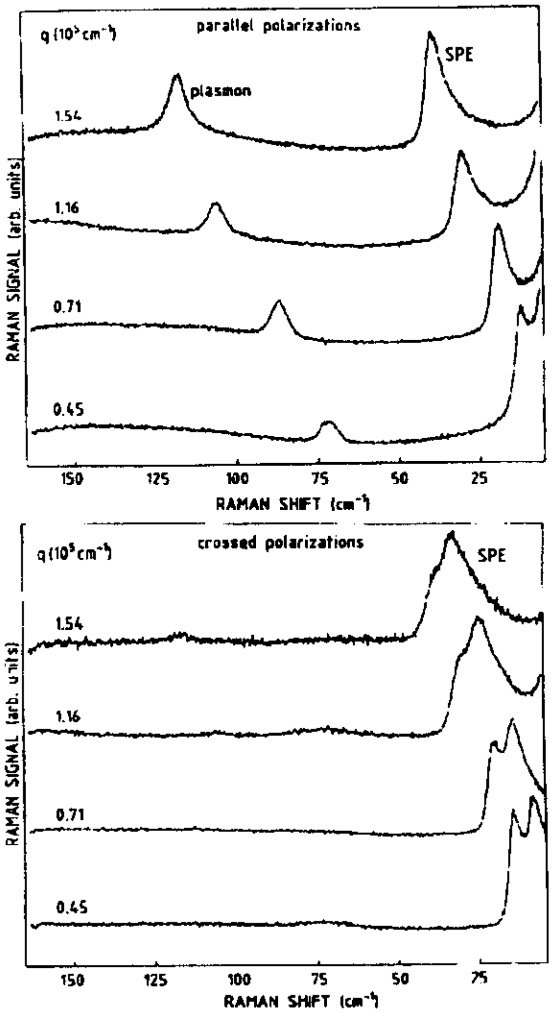

Figure 4: Electronic Raman scattering spectra on intrasubband excitations in parallel (left-side) and crossed (right side) polarizations for several in-plane wavevector.

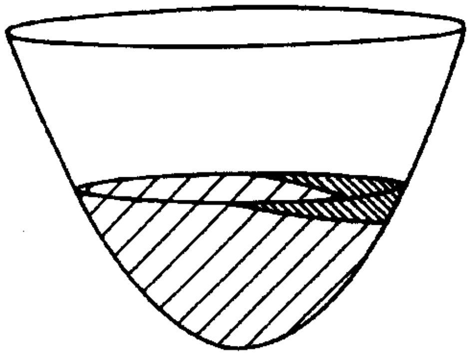

Figure 5: Schematic representation of the states participating to the intrasubband Raman process (thick hatched surface) among the occupied ones in the Fermi sea (thin hatched).

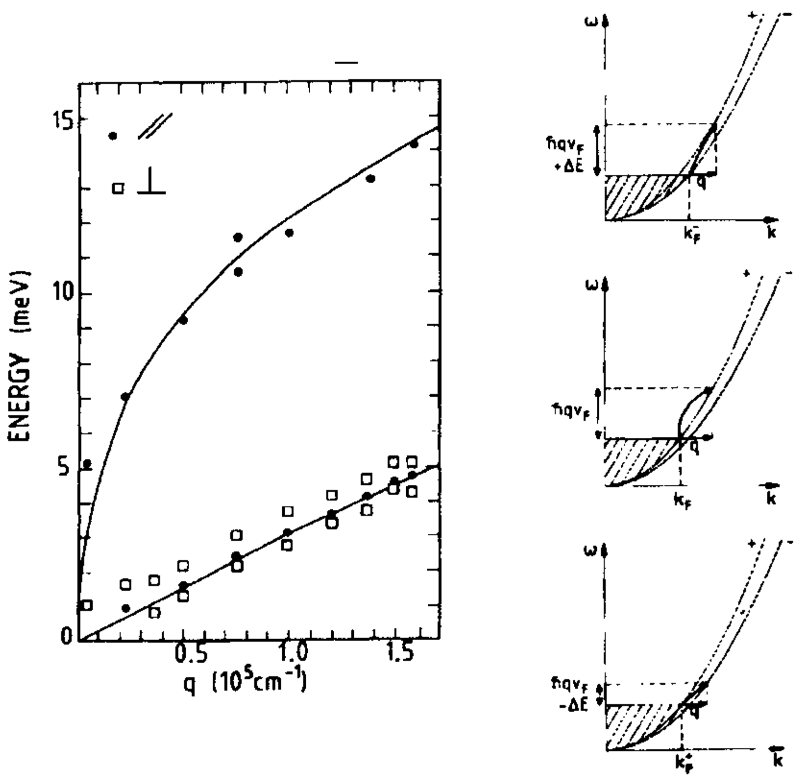

Figure 6: Schematic representation of the different possible intrasubband transitions and the corresponding calculated dispersion curves, also including the plasmon one. A comparison is made with the experimental dispersions.

trary to the intersubband case, it reflects the density of transitions between two occupied subbands: E_1 and E_1. Due to the final state occupation, and because the Raman wavevector is usually much smaller than k_F, the only initial states which can participate in the Raman process (see Fig.2c and 5) are very close to the Fermi level and their in-plane wavevector is oriented along q. Due to this restriction, the Raman line shape is well peaked around $+\hbar q v_F$. Moreover, the lifetime broadening is very small for these transitions ($< 0.2meV$) i.e. ten times less than for intersubband transitions. This is a further indication that this broadening indeed significantly depends on the energy of the involved states. Thanks to these features, the determination of the intrasubband SPE dispersion provides an accurate test of the 2D character of the involved states (linear dispersion) and an accurate determination of the electron density. A value of 1.3×10^{12} cm^2 is deduced from the parallel spectra.

Moreover the Raman line shape is particularly sensitive to the detail of the band structure around $k_F \frac{\vec{q}}{|\vec{q}|}$, which was up to now assumed parabolic and doubly spin-degenerate. This appears in our spectra through a splitting of the SPE band in crossed polarization. This splitting reflects a very small, generally neglected effect in the band structure of GaAs: the additionnal spin splitting due to spin-orbit interaction in crystals without inversion symmetry[10]. Taking into account this splitting and the Raman selection rule, we indeed predict (see Fig. 6) the observation of a single SPE band in parallel polarization, with a cut-off energy $\hbar q v_F$, and two SPE bands in crossed polarization with the same wavevector dependence but shifted from the previous one by respectively $+\Delta E$ and $-\Delta E$, where ΔE is the splitting at the Fermi wavevector in the direction of $\vec{q}$.

These predictions are in perfect qualitative agreement with the experimental dispersion (see Fig. 6) and provide the first direct measure of the spin splitting (0.38 meV). This contrasts with the previous indirect determinations deduced from polarization measurements[16]: in these experiments, the splitting was assumed to be negligible with respect to level broadening and the additional spin orbit effect was estimated from the induced precession of the electron spin in the conduction band. The same mechanism was also involved in the recent spin-splitting determination from

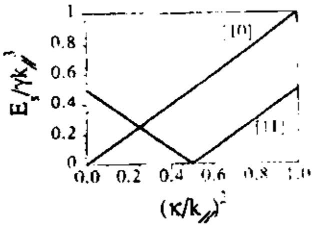

Figure 7: Spin-splitting calculated along [10] and [11] directions as a function of the sample parameter $\kappa/k_\parallel$.

anti-weak-localization studies in magnetoconductance experiments[17]. In our Raman experiment, we are able to measure the splitting because of the specific features of Raman scattering by intra-subband SPE excitations which we previously emphasized and because we are studying modulation doped heterostructures. This indeed allows to obtain large doping concentrations, and thus large splittings ($\Delta E \propto k_F^3$), with high mobilities at low temperature, and thus weak line broadening of the transitions. We compare this accurate determination with models of the spin splitting in heterostructures[18]. Our experimental value is in good agreement with the predicted one averaged over the in-plane directions, thus providing a further support to the description of this splitting in bulk GaAs in terms of an additional spin-orbit coupling of the conduction band with the higher energy anti-bonding p-states[19]. However 2D models predict a large anisotropy of the spin splitting:

$$\Delta E = \gamma(\kappa^4 k_\parallel^2) - (4\kappa^2 - k_\parallel^2)k_x^2 k_y^2)^{1/2}$$

which moreover strongly depends on the confinement wavevector $\kappa^2 =< k_z^2 >$ [20]. This is illustrated on Fig.7 where we show the dependence of the splitting onto the ratio $\kappa/k_\parallel$. The splitting continuously evolves from a 3D situation for vanishing values of the ratio towards a 2D one at large κ. In the former case the splitting moreover is proportionnal to $k_\parallel$ while it varies linearly with $k_\parallel$ in the 2D limit. In between, various situations appear with a splitting along [10] either smaller or larger than along [11]. A systematic study as a function of $\kappa/k_\parallel$ and of the wavevector orientation is therefore of great interest to probe the 2D models of this effect.

The dependence on the wavevector magnitude can be probed by Raman scattering either on different samples with the same parameters except the electron density or, more accurately, by the application of an electric field onto the electron gas using a Schottky contact to deplete the electron channel. The effect of the wavevector orientation can be more easily investigated by turning the sample with respect to the scattering wavevector direction. This allows to select a given direction to be probed in the Fermi sea as shown on Fig. 2 and 5. Some preliminary results on the same sample are shown on Fig.8 [20]. Contrary to the predictions illustrated on Fig.7, we observe a moderate anisotropy which makes us supect some deficiency in the 2D extension. Further experiments on the angular and density dependence of the splitting are in progress and should bring some new light onto this problem.

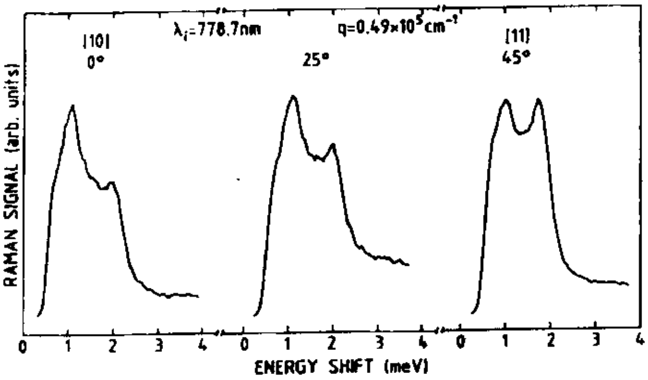

Figure 8: Depolarized intrasubband Raman spectra for the same in-plane wavevector oriented along three different directions in the layer plane.

In conclusion, we illustrated the great power of electronic Raman scattering to probe modulation doped quantum wells and to obtain thereby novel information about the band structure of GaAs and about many body effects at low dimension. The work reported in this communication has greatly benefited from the collaboration for sample preparation and characterization, optical experiments, theoretical analysis and discussions of B. Etienne, V. Thierry-Mieg, A. Izrael, H. Peric, D. Richards, J. Y. Marzin and J. M. Gerard.

References

1. B. B. Goldberg, D. Heiman, A. Pinczuk, L. Pfeiffer and K. West, Phys. Rev. Lett. **65**, 641 (1990).
2. A. J. Turberfield et al, Phys. Rev. Lett. **65**, 637 (1990).
3. W. Chen, M. Fritze, A. V. Nurmikko, C. Colvard, D. Ackley and H. Lee, Phys. Rev. Lett. **64**, 2434 (1990).

4. E. Burstein, A. Pinczuk and S. Buchner: in *Physics of Semiconductors*, edited by B. L. H. Wilson, Inst. Phys. Conf. Ser. No.43, p.1231 (1979).
5. A. Pinczuk and G. Abstreiter, in *Light Scattering in Solids* V, edited by M. Cardona and G. Güntherodt (Springer, Heildeberg, 1988), p.153.
6. G. Fasol, R. D. King-Smith, D. Richards, U. Ekenberg, N. Mestres and K. Ploog, Phys. Rev. B. **39**, 12695 (1989).
7. B. Jusserand, D. R. Richards, G. Fasol, G. Weimann and W. Schlapp, Surf. Sci. **229**, 394 (1990).
8. D. Richards, G. Fasol and K. Ploog, Appl. Phys. Lett. **57**, 1099 (1990).
9. B. Jusserand, D. Richards, B. Etienne, H. Peric and G. Fasol, Surf. Sci **263**, 527 (1992).
10. B. Jusserand, D. Richards, H. Peric and B. Etienne, Phys. Rev. Lett. **69**, 848 (1992).
11. H. Peric, B. Jusserand, D. R. Richards and B. Etienne, Phys. Rev. B**47**, 12722 (1993).
12. A. Pinczuk, S. Schmitt-Rink, G. Danan, J. P. Valladares, L. N. Pfeiffer and K. W. West, Phys. Rev. Lett. **63**, 1633 (1989).
13. D. Gammon, B. V. Shanabrook, J. C. Ryan and D. S. Katzer, Phys. Rev. B. **41**, 12311 (1990).
14. D. Gammon, B. V. Shanabrook, J. C. Ryan, D. S. Katzer and M. J. Yang, Phys. Rev. Lett. **68**, 1884 (1992).
15. D. C. Hamilton and A. L. McWhorther, in *Light Scattering in Solids*, edited by G.B. Wright (Springer, New-York, 1969) p.309.
16. *Optical Orientation*, edited by F. Maier and B. Zakharchenya (North Holland, Amsterdam,1984); H. Riechert, H.J. Drouhin and C. Hermann, Phys. Rev. B**38**, 4136 (1988).
17. P. D.Dresselhaus, C. M. A. Papavassiliou, R. G. Wheeler and R. N. Sacks, Phys. Rev. Lett. **68**, 106 (1992).
18. F. Malcher, G. Lommer and U. Rossler, Superlatt. and Microstruc. **2**, 267 (1986); R. Eppenga and M. F. H. Schuurmans, Phys. Rev. B **37**, 10923 (1988).
19. M. Cardona, N. E. Christensen and G. Fasol, Phys. Rev. B**38**, 1806 (1988).
20. D. Richards. B. Jusserand. H. Peric and B. Etienne, Phys. Rev. B **47**, 16028 (1993).

G

Physica Scripta. Vol. T49, 503–506, 1993

Electronic Raman Scattering on Modulation Doped GaAs Quantum Wells: Conduction Band Structure and Collective Effects

B. Jusserand and H. Peric

France Telecom/CNET/PAB, Laboratoire de Bagneux, 196 Avenue Henri Ravera, 92220 Bagneux, France

D. Richards

Cavendish Laboratory, Madingley Road, Cambridge CB3 0HE, England

and

B. Etienne

CNRS-L2M, Avenue Henri Ravera, 92220 Bagneux, France

Received March 29, 1993; accepted April 2, 1993

Abstract

We report on a detailed analysis of electronic Raman scattering results in modulation doped single quantum wells. We illustrate thereby the great power of this technique to get a detailed characterization of the electron density distribution and the band structure in doped heterostructures. We report in particular on a recent observation, for first time directly by spectroscopy, of the spin splitting of the conduction band of GaAs due to the lack of inversion symmetry.

Modulation doped structures are of great interest for the study of the quasi-two-dimensional electron gas (2DEG), in both transport and optical experiments because of the high mobility achieved by separating the electrons from the ionized donors. Among these studies, a large amount of work has been devoted to one side modulation doped single quantum wells. This system appears very promising for spectroscopic probes of the integer and fractional quantum Hall effects by optical measurements under quantizing magnetic field [1–3]. On the other hand, electronic Raman scattering is a powerful tool to probe electronic excitations, both collective and single-particle, occurring in a 2DEG. This was first suggested by Burstein *et al.* [4] and has since been extensively demonstrated [5]. Moreover, in the backscattering set-up, we can change wavevector in the plane of the 2DEG by simply rotating the sample relative to the fixed incident light wave vector. This provides a unique possibility to determine the dispersion of these excitations and to extract the subband structure as well as the electron density in modulation doped structures [6–11]. More recently, the observation, in different polarization configurations, of distinct spin-density and single-particle excitations, in addition to charge-density waves, opened the way to an independent measure of both direct and exchange-correlation Coulomb interactions of the electron gas [12–24].

In this communication, we will illustrate these possibilities through the presentation of a whole set of electronic Raman scattering results on the same sample: a 180 Å thick GaAs single quantum well claded between GaAlAs barriers. Modulation doping is obtained from a Si localized doping in the upper barrier only. This results in an asymmetric potential profile due to the self-consistent electric field. Moreover, due to the thin spacer (100 Å), the typical electron density lies above $1 \times 10^{12}\,\mathrm{cm}^{-2}$ but the Fermi energy remains below the bottom E_2 of the second subband. We will present Raman scattering results on intersubband and intrasubband transitions both with single particle and collective character on the same sample. From their in-plane dispersion and line-shape, we extract determinations of the electron density, the band structure and the lifetime of the involved states [9, 11]. We will in particular report on our recent first spectroscopic observation of the spin splitting of the GaAs conduction band because of the lack of inversion symmetry [10]. All Raman scattering experiments are done at liquid Helium temperature (1.8 K) and under close energy resonance with the fundamental energy gap.

Figure 1 shows electronic intersubband Raman spectra in parallel (polarized spectra) and crossed (depolarized spectra) polarizations respectively, for several different Raman in-plane wave vectors q. Due to the symmetry of the valence band states in a GaAs, Raman cross-sections, due to virtual interband processes, in crossed (respectively parallel) polarization are related to spin-density (respectively charge density) mechanisms [15]. One thus observes in parallel (respectively crossed) polarization collective charge density waves (CDW) and spin density waves (SDW) occurring in the 2DEG. In strong resonance conditions, one also observes, in both polarizations, a broader band of single particle excitations (SPE), with an intensity comparable to the collective ones, contrary to the theoretical prediction of complete screening. Though the origin of this observation is not yet fully understood, it appears to be very useful: the SPE band indeed peaks at the bare intersubband energy E_2–E_1 of the doped structure (this is only strictly true when assuming the same parabolic dispersion for both subbands). On our sample we can thereby extract an accurate determination of the subband separation (49 meV) in good agreement with the estimation deduced from luminescence [11]

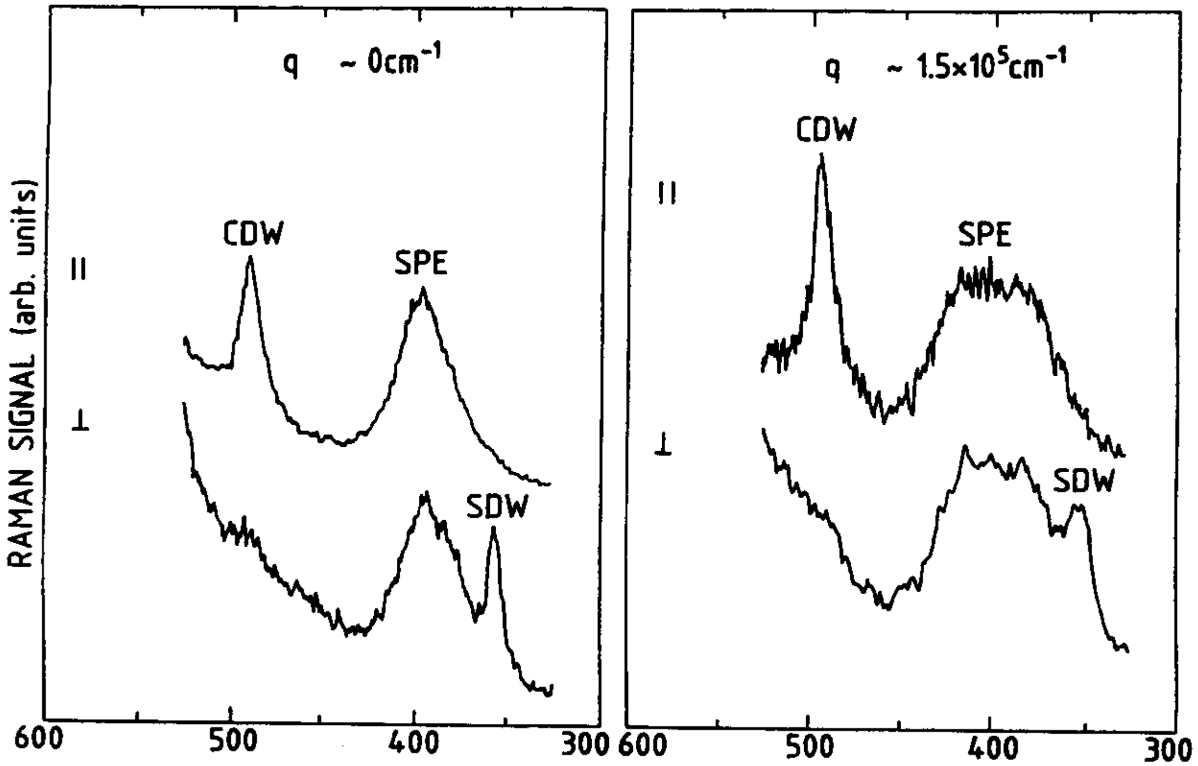

Fig. 1. Electronic Raman scattering spectra obtained with a resonance laser energy of 1.64 eV and at pumped liquid He temperature (1.8 K). The left side of the figure shows collective (CDW and SDW) and individual (SPE) intersubband excitations of the 2DEG for a very small Raman in-plane wavevector, while the right side exhibits the same excitations at larger q.

(48 meV). Moreover this band displays a specific behavior as a function of q. Unlike the CDW and SDW, which remain approximately unchanged, the SPE band is strongly broadened with increasing Raman in-plane wave vector according to the density of intersubband transitions. The cut-off frequencies are shifted by $-\hbar q v_F$ and $+\hbar q v_F$ from the E_2–E_1 energy. This is shown in Fig. 2 and compared to the experimental dispersion. The slope of the SPE dispersion reflects the electron density in E_1. However the accuracy of this determination is limited due to the intrinsic broadening of the transitions (2 meV). This quantity reflects the lifetime of both initial and final states. Energy-dependent values are needed to correctly fit the SPE lineshape at every in-plane wavevector [11].

The CDW and SDW lines are not strongly dispersive and they are well separated from the CDW and SDW lines (see Fig. 2). Thus one is able to accurately determine their energies, and to deduce the electron density. Using a RPA calculation based on self-consistently determined wavefunctons [6, 13], we deduce from the CDW energy an electron density of $1.3 \times 10^{12}\,\mathrm{cm}^{-2}$. With this value, one may extract from self-consistent subbands calculations the potential profile of the structure and the subbands energies. The calculated value of the E_1 to E_2 intersubband energy obtained by this procedure is in very good agreement with experimental values provided by PL and Raman measurements. Moreover, from the experimental SPE, CDW and SDW ines, one may extract an experimental determination of the direct and exchange-correlation Coulomb interaction in quasi-bidimensional electron gases and compare them to different models of these quantities [12–14].

Let us now turn to the analysis of the intrasubband electronic transitions. The corresponding Raman spectra are shown on Fig. 3 for several in-plane wavevectors in both polarization configurations. As we already explained for the intersubband ones, SPE and collective excitations can be observed simultaneously at strong resonance. The low energy part of the spectra in both polarizations is attributed to SPE band. It extends from zero to a maximum energy $+\hbar q v_F$. However, contrary to the intersubband case, it reflects the density of transitions between two occupied subbands: E_1 and E_1. Due to the final state occupation, and because the Raman wavevector is usually much smaller than k_F, the only initial states which can participate to the Raman process are very close to the Fermi level and their in-plane wavevector is oriented along q. Due to this restriction, and to the high quality of the samples with an elastic broadening smaller than 0.2 meV, the Raman line shape is well peaked around $+\hbar q v_F$ and the determination of its dispersion provides an accurate test of the 2D character of the involved states (linear dispersion) and an accurate determination of the electron density. A value of $1.3 \times 10^{12}\,\mathrm{cm}^{-2}$ is deduced from the parallel spectra.

Moreover the Raman line shape is particularly sensitive to the detail of the band structure around $k_F q/|q|$. This appears in our spectra through a splitting of the SPE band in crossed polarization. This splitting reflects a very small, generally neglected effect in the band structure of GaAs: the additional spin splitting due to spin-orbit interaction in crystals without inversion symmetry [10]. Taking into account this splitting and the Raman selection rules, we indeed predict (see Fig. 4) the observation of a single SPE

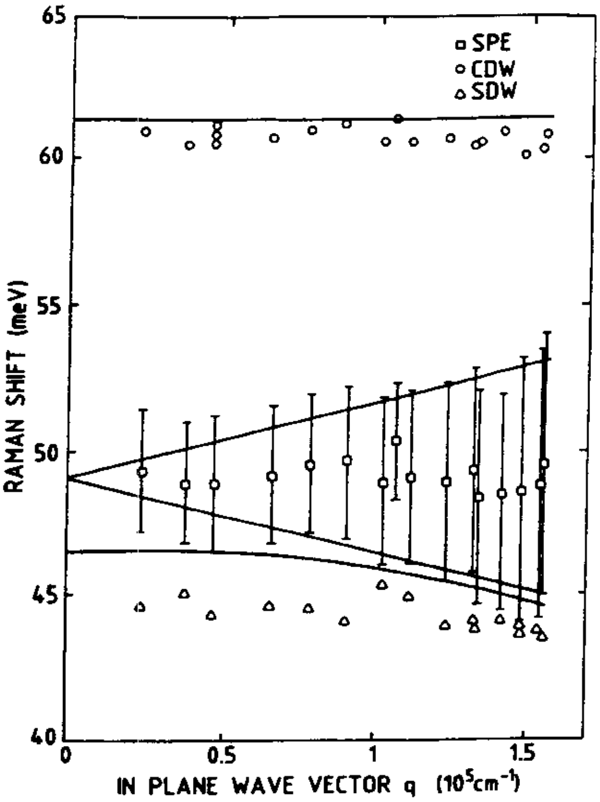

Fig. 2. Dispersion curve of the collective (CDW and SDW) and individual (SPE) intersubband excitations of the 2DEG, deduced from Raman scattering experiments as a function of q. The vertical lines are the width at half maximum of the SPE line and the solid lines the calculated dispersion curves as explained in the text.

band in parallel polarization, with a cut-off energy $\hbar q v_F$, and two SPE bands in crossed polarization with the same wavevector dependence but shifted from the previous one by respectively $+\Delta E$ and $-\Delta E$, where ΔE is the splitting at the Fermi wavevector in the direction of q.

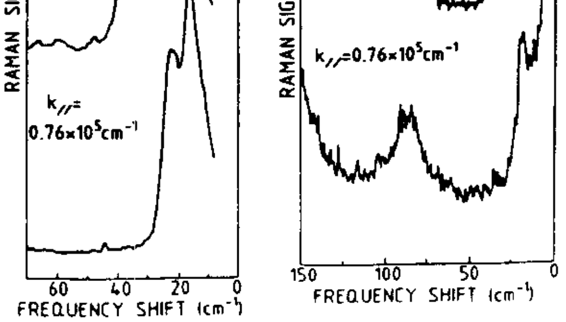

Fig. 3. Electronic Raman scattering spectra on intrasubband excitations in parallel (left side) and crossed (right side) polarizations for several in-plane wavevector.

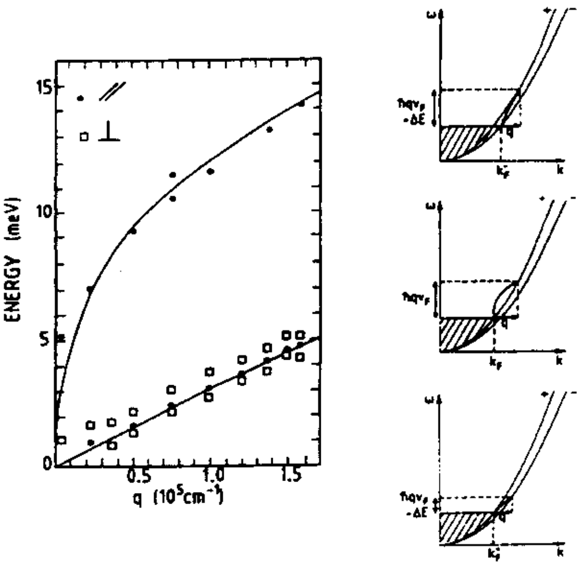

Fig. 4. Schematic representation of the different possible intrasubband transitions and the corresponding calculated dispersion curves, also including the plasmon one. A comparison is made with the experimental dispersions.

These predictions are in perfect qualitative agreement with the experimental dispersion (see Fig. 4) and provide a direct measure of the spin splitting (0.4 meV). We have been able to observe this splitting, contrary to the previous indirect determinations deduced from polarization measurements [16], thanks to modulation doping. This indeed allows to obtain large doping concentrations, and thus large splittings ($\Delta E \propto k_F^3$), with high mobilities, and thus weak line broadening of the transitions. We compare this accurate determination, and its angular variation deduced by rotating the sample with respect to the direction of q [17], with models of the spin splitting in heterostructures [18]. Our average experimental value is in good agreement with the predicted one, thus providing a further support to the description of this splitting in bulk GaAs in terms of an additional spin-orbit coupling of the conduction band with the higher energy anti-bonding p-states [19]. However 2D models predict a large anisotropy of the spin splitting:

$$\Delta E = \gamma(\kappa^4 k_{\parallel}^2 - (4\kappa^2 - k_{\parallel}^2)k_x^2 k_y^2)^{1/2}$$

which moreover strongly depends on the confinement wavevector $\kappa^2 = \langle k_z^2 \rangle$. We observe on the contrary a moderate anisotropy which let us suspect some deficiency in the 2D extension. Further experiments on the density dependence of the splitting are in progress and should bring some new light onto this problem.

References

1. Goldberg, B. B., Heiman, D., Pinczuk, A., Pfeiffer, L. and West, K., Phys. Rev. Lett. 65, 641 (1990).
2. Turberfield, A. J. *et al.*, Phys. Rev. Lett. 65, 637 (1990).
3. Chen, W., Fritze, M., Nurmikko, A. V., Colvard, C., Ackley, D. and Lee, H., Phys. Rev. Lett. 64, 2434 (1990).
4. Burstein, E., Pinczuk, A. and Buchner, S., in: "Physics of Semiconductors" (Edited by B. L. H. Wilson) Inst. Phys. Conf. Ser. No. 43, p. 1231 (1979).
5. Pinczuk, A. and Abstreiter, G., in: "Light Scattering in Solids V" (Edited by M. Cardona and G. Güntherodt) (Springer, Heidelberg 1988), p. 153.

9

6. Fasol, G., King-Smith, R. D., Richards, D., Ekenberg, U., Mestres, N. and Ploog, K., Phys. Rev. **B39**, 12695 (1989).
7. Jusserand, B., Richards, D. R., Fasol, G., Weimann, G. and Schlapp, W., Surface Science **229**, 394 (1990).
8. Richards, D., Fasol, G. and Ploog, K., Appl. Phys. Lett. **57**, 1099 (1990).
9. Jusserand, B., Richards, D., Etienne, B., Peric, H. and Fasol, G., Surf. Sci. **263**, 527 (1992).
10. Jusserand, B., Richards, D., Peric, H. and Etienne, B., Phys. Rev. Lett. **69**, 848 (1992).
11. Peric, H., Jusserand, B., Richards, D. R. and Etienne, B., to appear in Phys. Rev. B.
12. Pinczuk, A., Schmitt-Rink, S., Danan, G., Valladares, J. P., Pfeiffer, L. N. and West, K. W., Phys. Rev. Lett. **63**, 1633 (1989).
13. Gammon, D., Shanabrook, B. V., Ryan, J. C. and Katzer, D. S., Phys. Rev. **B41**, 12311 (1990).
14. Gammon, D., Shanabrook, B. V., Ryan, J. C., Katzer, D. S. and Yang, M. J., Phys. Rev. Lett. **68**, 1884 (1992).
15. Hamilton, D. C. and McWhorter, A. L., in: "Light Scattering in Solids" (Edited by G. B. Wright) (Springer, New York 1969), p. 309.
16. "Optical Orientation" (Edited by F. Maier and B. Zakharchenya) (North-Holland, Amsterdam 1984); Riechert, H., Drouhin, H. J. and Hermann, C., Phys. Rev. **B38**, 4136 (1988).
17. Richards, D., Jusserand, B., Peric, H. and Etienne, B., unpublished
18. Malcher, F., Lommer, G. and Rössler, U., Superlattices and Microstructures **2**, 267 (1986).
19. Cardona, M., Christensen, N. E. and Fasol, G., Phys. Rev. **B38**, 1806 (1988).

INTERFACE ROUGHNESS AND CONFINED VIBRATIONS

Bernard Jusserand

CNET - Laboratoire de Bagneux
196 Avenue Henri Ravera
92220 Bagneux, France

INTRODUCTION

The lattice dynamics of superlattices based on two different pure constituents, like for instance GaAs/AlAs, InAs/GaSb or Si/Ge, is now very well understood and most of the theoretical predictions have been successfully verified by Raman scattering, at least on GaAs/AlAs structures which are available at a very high quality[1].

The optical phonon branches in GaAs and AlAs are well separated in frequency and the optical vibrations of one material cannot propagate into the other one. As a consequence, the optical vibrations in the GaAs/AlAs superlattices are divided into two families whose eigendisplacements are strongly confined either in the GaAs or in the AlAs layers; the penetration depth into the other compound being less than one monolayer. Their frequencies are thus very sensitive to boundary conditions. Assuming perfect interfaces, one can identify the eigenfrequencies of the modes confined in GaAs layers to those of bulk GaAs at a given set of wavevectors k_p :

$$k_p = \frac{p\pi}{(n_1+1)a} \qquad (1)$$

Similar conclusions apply to the optical vibrations confined in the AlAs layers. The LO dispersion in GaAs and AlAs being downwards, the confined phonon energies lie below the bulk GaAs (AlAs) one and decrease with decreasing layer thicknesses. This provides a one-to-one correspondence between the confined frequencies and the layer thicknesses. Equation 1 allows one to define an effective thickness $(n_1 + 1)a$ which is common to all the confined vibrations in perfect layers. These predictions have been checked by different groups[2] with reasonable success. However, a general tendency is observed; the dispersion deduced from Raman scattering on superlattices is flatter than the one obtained by neutron scattering on the bulk constituents. In other words, the effective thickness associated to a confined mode increases when the associated local wavevector (see Equation 1) increases.

The main approximation involved in these models is to consider atomically flat interfaces separating the two pure constituents. In real samples, even of the best quality, the interfaces are never flat due to the growth statistics. Such roughness, which extends over a few monolayers around the nominal interface, can be reasonably neglected for superlattices with moderately small individual layer thickness (> 50 Å). In shorter period structures, however, this roughness leads to quantitative departures from the predictions of the lattice dynamics of perfect samples. This paper will be devoted to a description of Raman scattering experiments focussed on this problem and to a quantitative analysis of the dependence of the phonon frequencies on the spatial characteristics of the roughness, both along the growth axis and in the interface plane. This will lead us to reconsider in detail the lattice dynamics of bulk mixed crystals and of perfect superlattices containing layers of these alloys. The effect of interface roughness will be finally treated before we conclude.

Light Scattering in Semiconductor Structures and Superlattices
Edited by D.J. Lockwood and J.F. Young, Plenum Press, New York, 1991

Experimental Results

The optical vibrations confined in GaAs and AlAs are particularly sensitive to the interfacial imperfections because their frequencies are mainly determined from boundary conditions at each interface. This was first demonstrated[3] through the variation of the confined frequencies as a function of the growth conditions in nominally identical superlattices. We show in Fig. 1 Raman spectra obtained in the $z(x,y)\bar{z}$ configuration on five nominally identical samples grown by Molecular Beam Epitaxy (MBE) at different temperatures T_s ranging from 510°C to 680°C. We know from X-ray diffraction measurements that the macroscopic parameters of the samples are almost identical : d(GaAs)=28Å and d(AlAs)=12Å and independent of temperature. On the other hand, the intensity of the X-ray satellites decreases significantly with increasing T_s. A similar observation is made on the Raman lines associated to the folded acoustic vibrations, which reflect the long range order along the growth axis in a very similar way to the X-ray satellites : the frequencies of the folded acoustic lines remain unchanged but their intensities significantly decrease. Both results suggest, in agreement with some independent knowledge of the growth process, the existence of an increasing interfacial roughness with increasing T_s.

The effect on the optical vibrations is in a way much stronger : we observe a significant down-shift with increasing T_s of all the lines associated with optical phonons confined either in the GaAs or the AlAs layers. In the AlAs energy range, a single line is mainly observed on all the samples associated to the fundamental confined vibration (p=1 in Eq.1). A small line, tentatively assigned to mode 3, is also observed on the sample grown at 510°C but disappears at higher temperature. In the GaAs frequency range, three lines are observed on all samples, corresponding to mode 1,3,5 according to the now well established selection rules. They all shift towards lower frequency and moreover their relative distance strongly varies : they become more or less equidistant at 680°C while the splitting between line 3 and 5 amounts to almost twice the one between line 1 and line 3 at low T_s. Similar shifts in the confined optical vibrations have also been observed on superlattices during a series of successive thermal annealing stages[4].

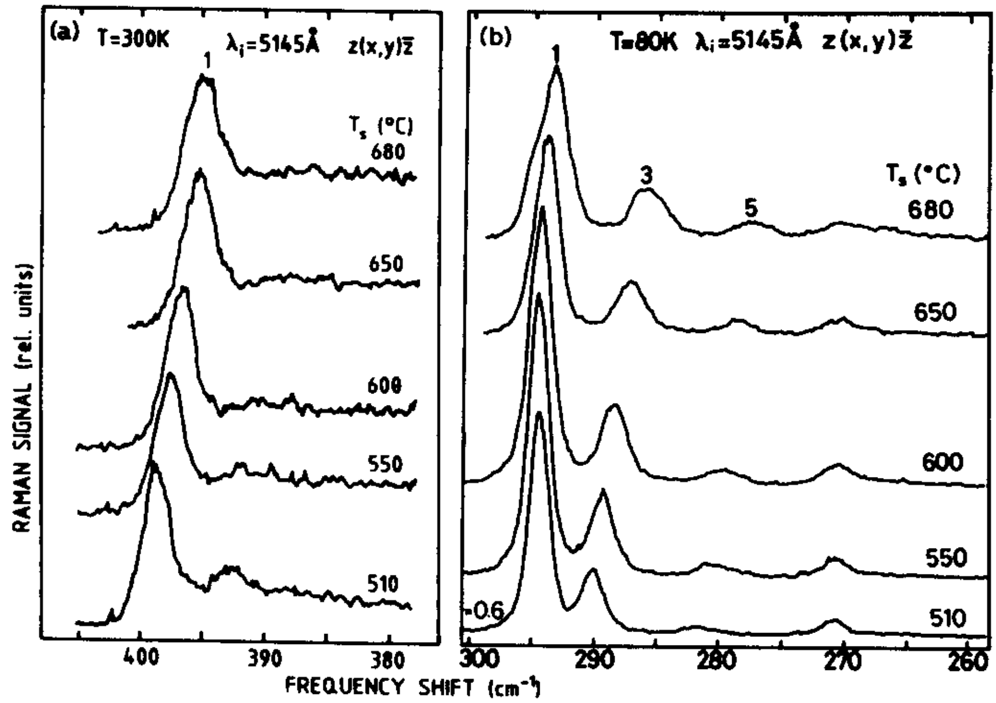

Fig. 1 . Raman spectra in the AlAs-type (a) and GaAs-type (b) frequency range for five GaAs/AlAs superlattices with the same nominal parameters, but grown at different temperature T_s.

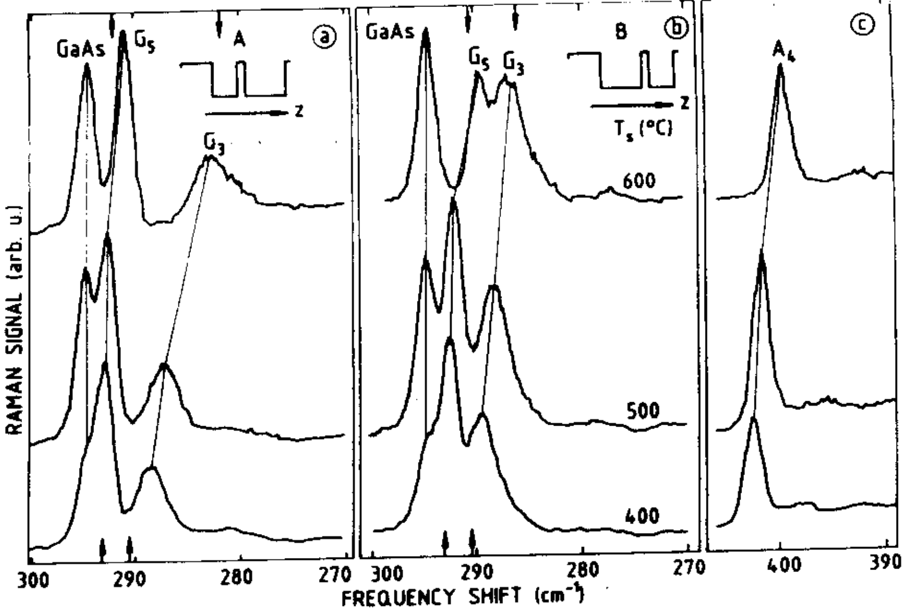

Fig. 2 . a) Raman spectra in the GaAs-type frequency range for three different samples with the same composition sequence A but grown at different temperatures. b) same as a) except that the composition sequence is B. c) same as a) but in the AlAs-type frequency range. In a) and b) the bottom (top) arrows indicate the mode frequencies calculated assuming a perfect (segregation-type) profile.

The dependence of the optical phonon frequency on the growth conditions becomes very strong for very short period superlattices. We show in Fig.2 recent results obtained on samples specially designed to get detailed information on the imperfections of the profile. As shown in the inset, the supercell of each sample contains 4 different layers. Two different sequences have been grown :

$(AlAs)_4(GaAs)_3(AlAs)_1(GaAs)_5$ sequence A
$(AlAs)_4(GaAs)_5(AlAs)_1(GaAs)_3$ sequence B

which are equivalent up to an inversion of the growth direction. The Raman spectra thus must be identical when assuming a perfect realization of the structure and the observed differences are spectroscopic signatures of departures from the nominal composition profile.

Samples are grown by MBE and the superlattice growth temperature ranges from 400 to 600°C. We first characterize the samples using X-ray diffraction and Raman scattering on folded acoustic phonons. We do not observe any systematic change as a function of T_s or of the layer sequence. The measured periods scatter between 3.6 and 3.8 nm, in good agreement with the 3.7 nm nominal value. Moreover, the second X-ray satellite (respectively folded acoustic doublet) is unusually strong with respect to the first one. This demonstrate[5] the presence of an aluminium rich peak inside the GaAs layer which corresponds to the nominal AlAs monolayer. The ratio of satellite intensities only shows small variations from sample to sample.

On the contrary, strong variations are observed in the Raman spectra on confined optical vibrations. We show in Fig.2 the Raman spectra of vibrations confined in GaAs (a and b) or AlAs (c) layers obtained on the samples grown at T_s=400, 500 and 600°C. The spectra in the GaAs energy range contain three main peaks associated respectively with the GaAs buffer layer and the two different GaAs layers in the supercell, labelled G_3 and G_5 according to their nominal thickness. The spectra in the AlAs energy range contain one main peak associated with the thicker AlAs layer labelled A_4. All these layers are very thin, thus preventing the observation of confined modes other than the fundamental one. We are also not able to resolve in these samples the contribution of the AlAs monolayer. Let us first emphasize that the perturbation on the optical vibrations due to a single AlAs monolayer inserted in the GaAs well is much stronger than it is on electronic properties[6]. Each GaAs layer on each side behaves almost independently, which means that the AlAs monolayer acts as an almost infinite barrier.

The Raman spectra qualitatively differ from those which we observed' on $Ga_{1-x}Al_xAs/AlAs$ superlattices, i.e. when the aluminum is homogeneously distributed in the well instead of forming a composition spike. This is strong evidence of our ability to grow an aluminum spike in the monolayer range. This allows us to analyze independently the signals coming from each GaAs layer.

In both series of samples the positions of the peaks G_3, G_5 and A_4 strongly varies as a function of T_s. Morover, the GaAs peaks, but not the AlAs one, display a dramatic dependence on the layer sequence. We indicate in Fig.2a, b the frequencies of the GaAs-type confined modes, calculated assuming a perfect profile. The measured frequencies always lie well below the predicted ones and the difference increases with increasing T_s. The same trend is observed on the single AlAs-type mode. Let us now focus on the difference between sequence A and B. The effective thickness of both GaAs layers is clearly very sensitive to the thickness of the AlAs layer which lies immediately underneath and will be hereafter called the underlying AlAs layer. We plot in Fig.3 the measured line frequencies as a function of these two parameters. One can notice in Fig.3 that this sensitivity is larger in the nominally 3 monolayer than in the nominally 5 monolayer thick GaAs well because the frequency change for a given effective thickness variation is larger. Moroever, a tendency to the saturation in the underlying AlAs thickness dependence is observed at 4 monolayers, the behavior presumably approaching a "bulk-like" limit. On the contrary, the sensitivity to the growth temperature is strongly reduced for small underlying AlAs thicknesses.

On the other hand, the effective thickness of the nominally 4-monolayers-thick AlAs is the same in both sequences, i.e. after either 3 or 5 monolayers of GaAs. We show, however, in Fig.4 some recent Raman spectra in the AlAs energy range obtained on similar samples grown under similar conditions but with thicker GaAs layers and an aluminum spike corresponding to either 1 or 1/2 monolayer of AlAs. In these samples, a clear signal coming from the spike is observed and its frequency depends of the amount of aluminum deposited. This latter result suggests that the AlAs layer properties may also depend on the underlying GaAs thickness.

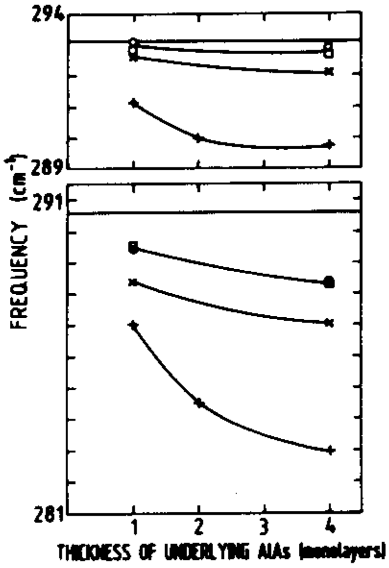

Fig. 3 . Measured frequencies of the GaAs-type fundamental vibrations plotted as a function of the nominal thickness of the underlying AlAs layer. In the upper (lower) part, the results correspond to a nominal GaAs thickness of 5 (3) monolayers. In both parts, the calculated nominal frequency is represented by a horizontal line as it is independent of the underlying AlAs thickness. The experimental results obtained on samples grown at 600, 500, 450 and 400°C are represented by plusses, crosses, open squares and circles respectively. The full lines are a guide to the eye.

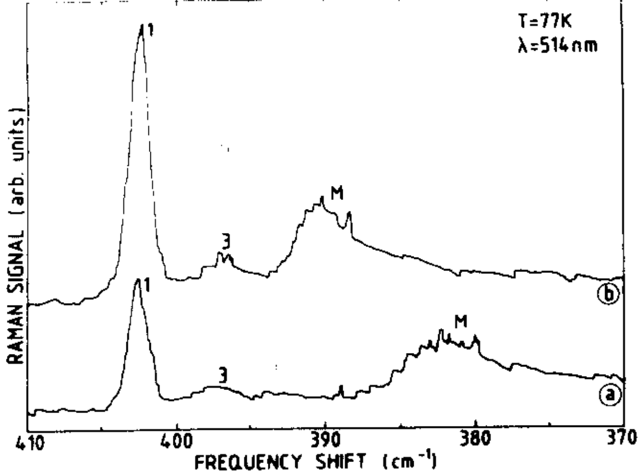

Fig. 4 . Raman spectra in the AlAs-type frequency range for two different samples with the composition sequence $(AlAs)_4(GaAs)_{10}(Ga_{1-x}Al_xAs)_1(GaAs)_8$ and x=0.5 (a) or 1. (b)

The general shape of the spectra is not modified in other respects from sample to sample. Even when the phonon frequencies are very different from the ones calculated using the nominal parameters, we do not observe any significant line broadening. Moreover, line splittings (as recently reported in Ref.2) seem to be absent in our samples. This suggests that the imperfections in these samples are caused by "gradual interfaces" ; the in-plane statistics of the roughness should be such that the optical phonons only see the average in-plane concentration and thus experience an ordered, eventually gradual composition profile along the growth axis, while the translational invariance in the layer planes is preserved. Assuming a gradual profile makes one-dimensional models sufficient to analyze the Raman scattering results. From the data corresponding to the AlAs energy range, the information is too scarce to separate the respective effects onto the confinement of an admixture of gallium and of a change in the composition profile. On the contrary, the observation of three lines in the GaAs energy range makes it possible to determine the composition profile in the gallium-rich parts of the structure with good accuracy. We will present in what follows a detailed 1D calculation of the Raman spectra in superlattices with gradual interfaces and we will introduce, on the basis of a 3D lattice dynamics calculation including the interface roughness, a novel microscopic criterion governing the emergence of this behavior.

The main difficulty in performing both tasks arises from the alloy vibrational behavior. Let us recall some experimental results on this point. The Raman spectra on $Ga_{1-x}Al_xAs$ alloys display the well-known two-mode behavior : two optical phonon Raman lines coexist on the whole concentration range which lie respectively in the range of the pure GaAs and AlAs optical phonons and only slightly shift as a function of the alloy composition. Both this two-mode behavior and the strong confinement in GaAs/AlAs superlattices qualitatively originates from the same feature : the large energy splitting between the optical bands in GaAs and AlAs. A virtual crystal approximation to describe these alloy vibrations is therefore meaningless, contrary to what prevails for the electronic properties.

Raman scattering experiments on bulk alloys provide useful but limited information on the alloy lattice dynamics. Inserting these alloys in superlattices allow us to increase this amount of experimental knowledge. Fig.5 displays some Raman spectra in the GaAs energy range obtained on GaAs/GaAlAs superlattices with similar parameters except for the aluminum concentration in the alloy layers which ranges from 100% to 5%. The frequency of the modes confined in the GaAs layers remain almost unchanged as long as the GaAs-type LO mode of the alloy constituents lies at sufficiently higher frequency. When it is no longer the case, the mode slightly shifts towards higher frequency before to transform into a propagative optical vibration with an energy in the range of overlap of the pure GaAs and GaAlAs alloy optical energy band. This whole behavior is typical of a quantum well and the alloy layers appear to act as very effective barriers for the phonons confined in the GaAs layers with energies above the Raman frequency in the bulk alloy.

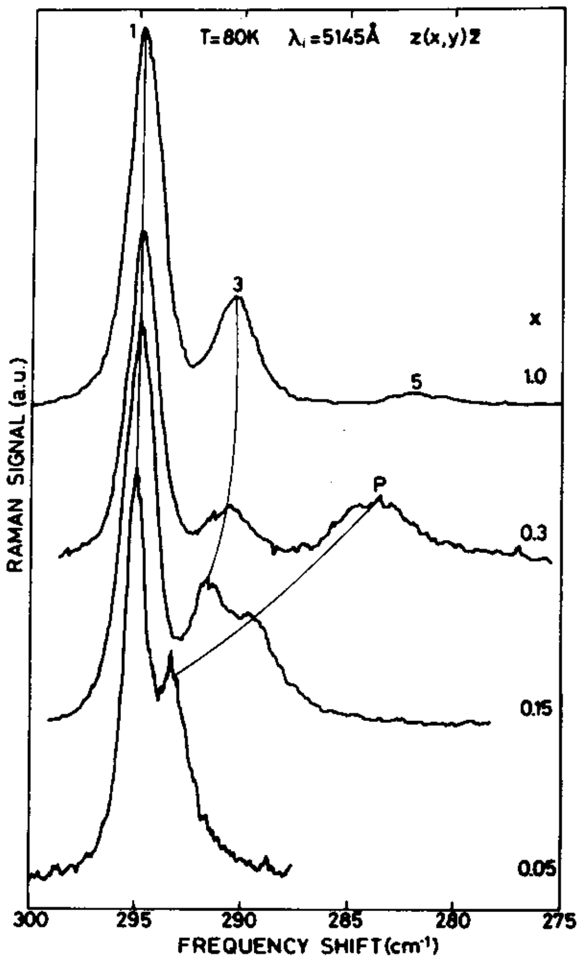

Fig. 5 . Raman spectra in the GaAs-type frequency range for four different GaAs/Ga$_{1-x}$Al$_x$As samples with the same parameters except for the aluminum concentration x in the alloy layers.

Let us now consider the case of GaAlAs/AlAs superlattices and again the GaAs-type optical vibrations in these structures. Fig.6 displays the associated Raman spectra in three samples with an aluminum concentration in the alloy ranging from 0 to 30%. The spectrum at 15% is rather similar to the one at 0%, while for higher aluminum concentration the different lines become poorly resolved. A general shift of the spectra is observed, which maps onto the one in the corresponding bulk alloy. Moreover, three different peaks remain observable. We attribute these optical phonon lines in the thin alloy layer spectra to confined GaAs-type vibrations, comparable to those observed in pure GaAs thin layers; the AlAs layers acting in both cases as very effective barriers. The distance between the peaks appears to decrease with increasing x, while their width increases. This experiment[7] is the first experimental proof of the dispersive character of the GaAs-type vibrations in the GaAlAs alloys. This observation, and the barrier properties which we described in the previous paragraph, strongly suggest that the GaAs-type optical band in the GaAlAs alloys behaves, at least for small Al concentrations, much like the one in a pure compound with effective parameters. We will present in the next section some methods of approximation to define these effective parameters and compare the related predictions to the experimental results on bulk or thin alloy layers. This will justify the use of these parameters in some of the superlattice dynamics calculations presented here.

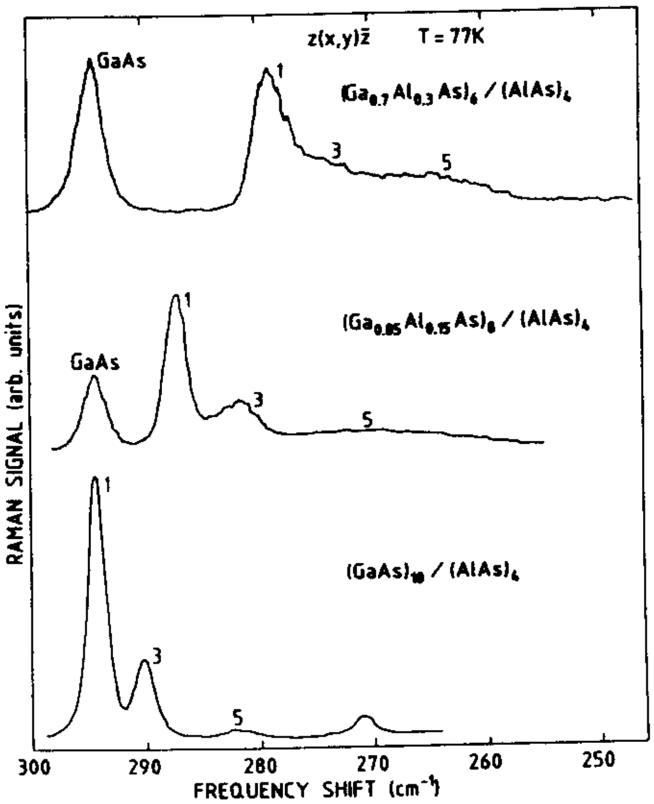

Fig. 6 . Raman spectra in the GaAs-type frequency range for three different $Ga_{1-x}Al_xAs/AlAs$ samples with the same parameters except for the aluminum concentration x in the alloy layers.

Lattice Dynamics of GaAlAs Mixed Crystals

The vibrational properties of the GaAlAs alloy have been analyzed theoretically for a very long time with the aim of qualitatively predict the two-mode behavior and to quantitatively reproduce the Raman scattering results. The favorable feature in this task is the almost identical spring constants of the GaAs and AlAs compounds which essentially differ by the mass of the atom III site. For the remainder of the paper we shall assume that these forces are the same. The first method which was successful in predicting the two-mode behavior is the Random Element Isodisplacement method[8]. It can be reformulated[9] using an effective ordered mass on the disordered site, which is a real quantity but depends on the energy in a rather similar way to the "CPA mass". We will therefore describe directly the Coherent Potential Approximation (CPA), its properties and its predictions.

The CPA description of the alloy[10-13] consists in a fictive ordered crystal which depends only on a frequency dependent isotropic complex mass assigned to the randomly occupied cation sites. This mass is self-consistently determined when one assumes the force constant matrix to be independent of the site occupation and if one demands that a given random occupied site imbedded in the CPA effective medium produces no extra scattering on the average. The CPA crystal being an ordered one, its properties, like phonon densities of states, dispersion curves and Raman activities, can be calculated as for pure compounds. However, some of these notions must be carefully redefined due to the peculiar properties of the CPA mass : it is a complex quantity and varies as a function of the energy, which respectively ensures the CPA crystal to include some disorder effects and to be at each energy the "best" ordered description of the real disordered crystal. Whereas we use a 3D lattice dynamic based on the Overlap Valence Shell Model of GaAs[14] to analyze the experimental results, we prefer to illustrate the CPA predictions on a much simpler system: the GaAlAs linear chain with only nearest neighbor interaction. We thereby retain the main results and in particular the two-mode behavior.

We show in Fig.7 the energy variation of the full density of states, of some partial conditional density of states and of the real and imaginary of the CPA mass at a few different compositions. The two-mode behavior appears in Fig.7 through the existence of two different energy ranges above $200cm^{-1}$ where the density of states is non vanishing. The position and width of these ranges vary only slightly as a function of x. Their respective GaAs-type and AlAs-type character can be further demonstrated using the conditional partial density of states, calculated on the disordered site. It is only large in the lower energy (higher energy) band when the disordered site is occupied by a gallium (aluminum) atom. The associated vibrations thus display a rather confined behavior.

The imaginary part of the CPA mass is also non-vanishing in the range of allowed energies in the alloy, where the alloy fluctuations can easily scatter elastically any given CPA mode. Thus its amplitude qualitatively maps onto the integrated density of states. The variation of the real part is of greater interest for our purpose. It displays strong variation in each energy gap, so to be successively close to the virtual crystal mass, the gallium and the aluminum one in the three allowed energy bands. This behavior is in qualitative agreement with our experimental observations that the GaAlAs well and barriers act **in the GaAs-type energy range** as if the alloy **coincides in this range** with an effective pure compound with an effective mass close to that of gallium. A more precise comparison can be done on the basis of the phonon dispersion curves. Due to disorder, the translational invariance in the crystal is destroyed and dispersion curves should be expected to disappear. The CPA, being an ordered approximation, allows us to reintroduce this notion[15]. However, due to the imaginary part of the CPA mass, the spectral density of states at any value of the wavevector is no longer a set of δ-functions but a continuous function displaying a few peaks which remain rather narrow in GaAlAs. The deduced dispersion curve is thus a thick one, as illustrated in Fig.8 for a few compositions. The zone center properties reproduce well the experimental results on bulk GaAlAs : the frequency decreases with increasing x and an asymmetric line shape develops. Furthermore, using this dispersion curve (in other words using the CPA mass on the disordered sites of the superlattice to perform the superlattices lattice dynamics calculation), we are able[7] to quantitatively explain the Raman scattering results on thin GaAlAs wells presented in Part 1, which provides a new, stringent test of the ability of the CPA to describe the mixed crystal vibrations.

The validity of the CPA for describing the barrier effect of a GaAlAs mixed crystal is not yet well established. The energy range of interest then lies outside the allowed energy bands and, in particular, just above the GaAs-type energy band. In this energy range, the CPA mass

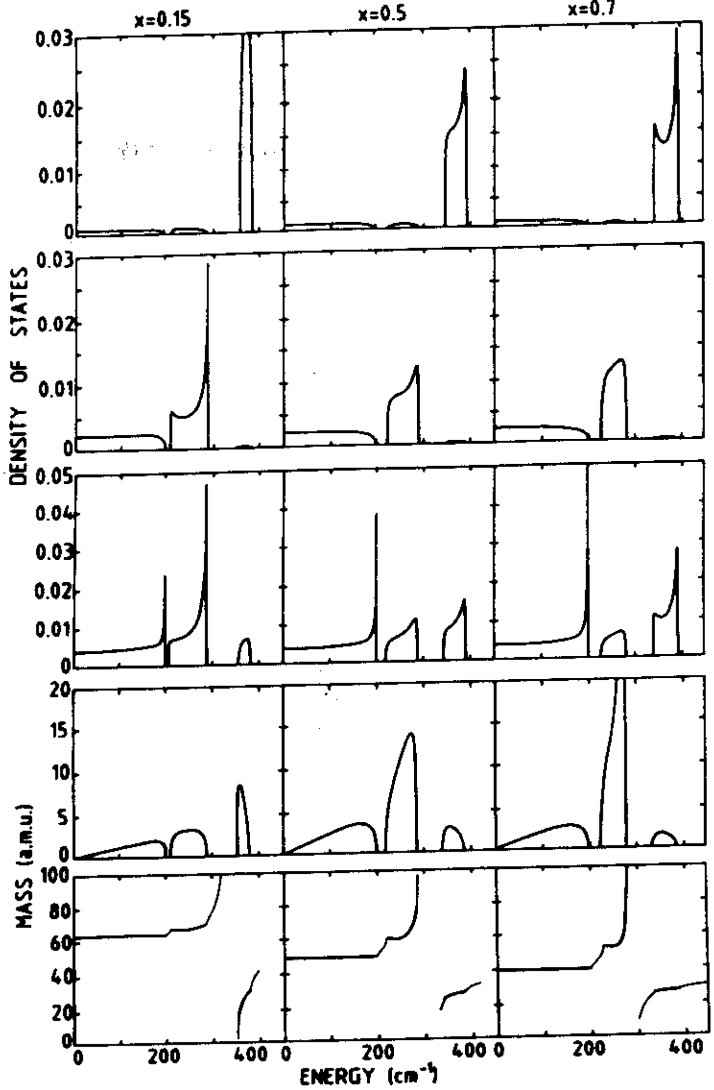

Fig. 7 . From bottom to top, real and imaginary parts of the CPA mass, full density of states, partial conditional densities of states for gallium occupied and aluminum occupied atom III sites, calculated as a function of energy for three different compositions of a $Ga_{1-x}Al_xAs$ mixed linear chain.

is real and usually display a divergence, which reflects the vanishing of the corresponding element of the site Green function. The physical meaning of this divergence has never been investigated, as far as we know, because it does not play any role in the analysis of the bulk alloy properties. Using this mass in the GaAs/GaAlAs superlattice lattice dynamics, as previously done for GaAlAs/AlAs, seems to give reasonable results. We show in Fig.9 the spectral density of states at the zone center and the corresponding Raman activity for a few superlattices comparable to the structure of Fig.5. The agreement is reasonable due to the following qualitative features : i) the CPA mass is real at these energies, which prevents any disorder-induced broadening of the peaks and ii) its real part is quite different from the gallium one which ensures a strong confinement, as long as the aluminum concentration is sufficiently large. For very small values of x, the CPA mass decreases towards the gallium one and the modes become less confined.

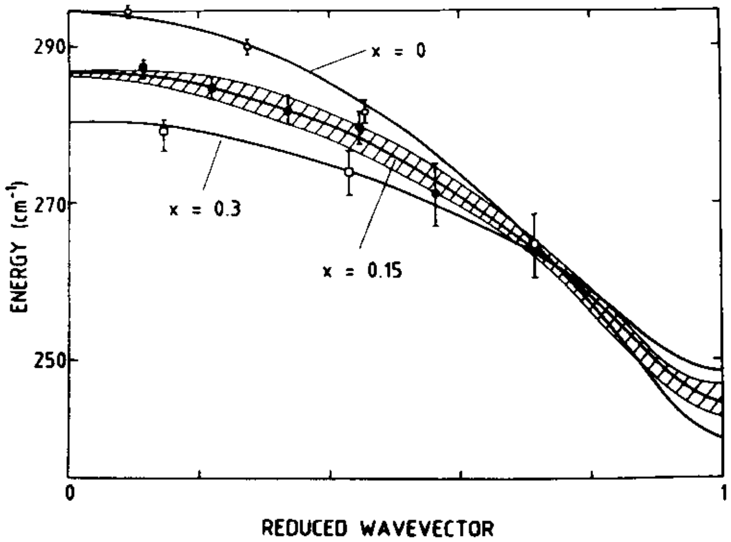

Fig. 8 . Calculated dispersion curves along the superlattice axis of the GaAs-type LO phonon in bulk $Ga_{1-x}As_xAs$ mixed crystals, with x=0, x=0.15 and x=0.30. For x=0.15, the hatched surface reflects the thickness of the dispersion curve, as explained in the text. Open circles, closed circles and open squares correspond to experimental frequencies on the samples of Fig.6, plotted according to Eq.1.

In a more quantitative way, the very steep variation of the effective mass predicted by the CPA at these forbidden energies should be tested by carefully analyzing the confinement energies in GaAs/GaAlAs superlattices. The few experimental results available up to now can be nevertheless well reproduced quantitatively on the basis of a more crude model where the effective mass on the alloy sites is taken constant and real in the small range of interest. In Ref.3, we fitted its value to the alloy GaAs-type Raman frequency. The previous analysis brings some theoretical support to this empirical approach, provided one chooses the zone-center CPA mass as the effective one. We will show in the next section a successful illustration of this method to calculate the confined optical vibrations in superlattices with gradual interfaces.

We are unfortunately far from treating by the CPA the "modulated alloy", i.e. a superlattice with an aluminum concentration continuously varying along the growth axis. Nevertheless, we can extract a lot of new knowlegdge on the alloy lattice dynamics from the CPA, which was up to now successfully verified by experiments on alloy superlattices. An alternative approach to the bulk alloy lattice dynamics was not described in this part : the supercell calculation with a random tossing of the individual site occupations. Some comparison with the effective mass description was already published[11]: significant differences only take place close to the band edges due to the effect of large, unfrequent clusters. One should notice that these energy ranges are of great importance in the superlattice lattice dynamics. Such supercell methods can be easily extended to modulated alloys, except for computational limitations. They should thus show a significant development in the near future. We will present in what follows a first example where mixed interfacial layers are treated.

Confined Vibrations and Interface Roughness

A review of Raman scattering results where the confined optical frequencies depend on the growth conditions was given at the beginning of this paper. We emphasized that the shape of the spectra strongly suggest an interpretation in terms of gradual interfaces. This can be justified if the correlation length of the composition fluctuations in the planes perpendicular to growth axis is much smaller than the "coherence length" of the confined phonons, which

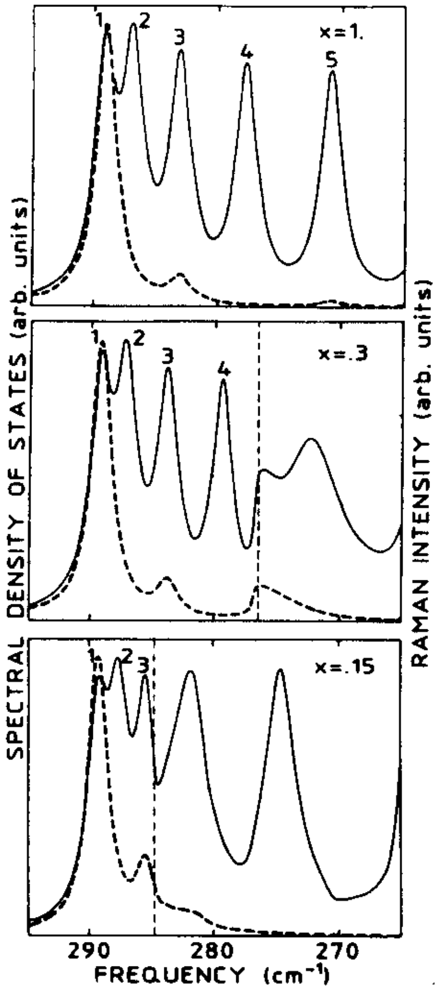

Fig. 9 . Spectral density of states (SDOS) of the GaAs-type LO vibrations (full line) and the associated Raman intensity (dashed line), calculated at a vanishingly small wavevector along the superlattice axis for three different GaAs/Ga$_{1-x}$Al$_x$As structures with the same parameters except for the aluminum concentration x in the barrier. We used the bulk CPA masses in the barrier alloy layer. The vertical dashed line indicates the corresponding LO frequency in the bulk alloy with the same composition.

remains to be defined. Before introducing such a definition and discussing the characteristics of samples where interface terracing should be observed by Raman scattering, we will first quantitatively analyze the presently available experimental results on the basis of lattice dynamics models including a continuously varying mass.

The simplest version of these models was introduced in Ref.3. The parameters of a linear chain with only nearest neighbor interactions is fitted into the dispersion along the (001) direction of the LO phonon in pure GaAs. In a second step, the mass on the atom III site is modified in order the reproduce the GaAs-type LO frequency in the alloy for each value of x. For any given composition profile along the growth axis, we can then diagonalize the dynamical matrix and determine the frequencies of the modes confined in the GaAs-rich parts of the samples (and only these ones). Assuming a gradual profile, for instance an erf-profile, with a varying broadening parameter d_o, we are able to fit this parameter for each spectrum. This fit is only significant when several lines are observed as it is the case of the samples of Fig.1 in the GaAs energy range (but not in the AlAs one). One can then check that the chosen profile is not unreasonable and determine the variation of the parameter d_o as a function of growth conditions. This method is illustrated in Fig.10 where the predicted confined frequencies (modes 1,3 and 5) are shown as a function of d_o for two different choices of the nominal thickness of the well (i.e. when $d_o=0$). Each frequency decreases with increasing d_o. In order words, the effective thickness seen by each vibration decreases. The comparison with the experimental frequencies is satisfactory because the frequencies of modes 1,3 and 5 can be fitted using the same d_o. Moreover, from the effective thickness scale shown on the right part of the figure for each confined vibration, we get the following result : this thickness is no longer constant from mode to mode as it was in the case of the abrupt profile. It increases with increasing confinement shift. This striking result can be simply understood in a perfect confinement picture, where one assumes that a confined vibration of energy Ω can extend in the part of the sample where the aluminum concentration x is lower than x_o such that $\omega_{LO}(x_o)=\Omega$. Fig.11 shows how reasonable this approximation is.

Though some very useful quantitative data onto an independently chosen profile can be extracted from the Raman spectra, it is, however, impossible to draw the profile from this single information. It is, for instance, very difficult to separate the respective contribution of the two interfaces limiting the GaAs well. In order to circumvent this difficulty, we designed samples with the concentration sequences shown in the insets of Fig.2. In these samples with very thin layers of GaAs and AlAs, we only observe the fundamental confined mode, which prevents testing the composition profile as extensively as before. However, on the basis of the observed dependence of the frequencies on the underlying layer thickness, we get a convincing evidence of the dominant role played by the GaAs on AlAs interface roughness. Instead of an erf-profile, we now use a "segregation profile"[16] to model the vibrations. This model was developed to explain chemical surface analysis results of the deposition of GaAs on AlAs and AlAs on GaAs at 600°C. Using these profiles, shown in Fig.12 for both sequences A and B, we get an excellent description of the Raman spectra on samples grown at 600°C. The predicted frequencies are shown at the top of Fig.2. Our observation of a reduction of the roughness of the GaAs on AlAs interface at lower growth temperature should stimulate the understanding of the MBE growth process.

The previous description of the roughness in terms of gradual interfaces remains valid as long as the spatial fluctuations are smaller than the "coherence length" of confined optical phonons. The rest of the paper will be devoted to a definition of this quantity and to a description of the lattice dynamics of superlattices when the gradual interface approximation fails, i.e. in the presence of terraced interfaces.

For this purpose we need to build a supercell which is larger than the basic one, not only along the nominal superlattice axis, but also in the layer plane. As we are interested in the confined modes, which probe a single layer, we can assume without any loss of generality that equivalent interfaces have the same in-plane statistics. We therefore retain the same periodicity along the growth direction as in the perfect structure. Due to limitations in the available computation time and memory, we must use rather crude approximations to account for the in-plane statistics, which result in the model structure shown in the inset of Fig.13. We consider

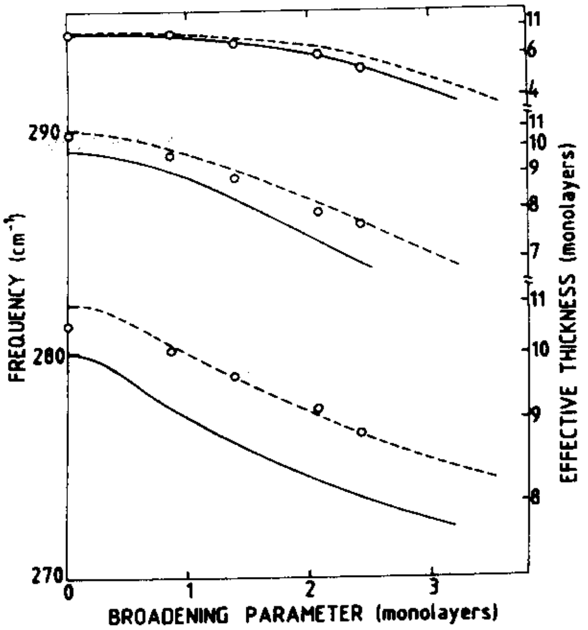

Fig. 10 . Frequency of modes 1,3 and 5 confined in nominally 10 (full lines) or 11 (broken lines) monolayers thick GaAs layers with rough interfaces, calculated as a function of the broadening parameter of the erf-profile. The open circles indicate experimental frequencies deduced from the spectra of Fig.1. The effective thickness corresponding to each confined frequency is shown on the right vertical axis.

one-dimensional fluctuations on a single side of the considered layers while the structure remains perfect along the third direction at this interface (it looks like corrugated cardboard) and along both directions at the other one, which remains atomically flat. Varying the amplitude along z and the distribution along x of the corrugation allows us to handle many different situations.

In Fig.13, we restrict ourselves to a very simple case where the fluctuation is restricted along z to a single interfacial monolayer and looks along x like a lateral superlattice. Two parameters then define the interface : its average aluminum content and its lateral period. This model provides the simplest representation without any empirical parameter of a thin layer with a non-integer thickness. Moreover, it opens the possibility to vary the lateral terraces. When the mass distribution in the supercell is defined, we build up[17] the force constant matrix at a given wavevector in the Brillouin minizone from the bulk matrices at the wavevectors in the full Brillouin zone which are now equivalent due to the modulation.

We show in Fig.13 the predicted frequency of the fundamental vibration confined in a GaAs layer of a thickness $n_1+(1-x)$ monolayers as a function of x for $n_1=2$ and several different in-plane periods a+b between 2 and 40 monolayer thickness, i.e. between 6 and 120Å. a and b are the respective numbers of adjacent Ga and Al atoms in the single interfacial layer (see the inset). The average aluminum content x in the interface layer then takes simple rational values b/(a+b), ranging from 0 to 1. While a single composition x=0.5 can be considered for a+b=2, a series of nine different ones is reproduced for a+b=10. The results display similar trends for other nominal thicknesses, except that the absolute energy variations decrease with increasing n_1.

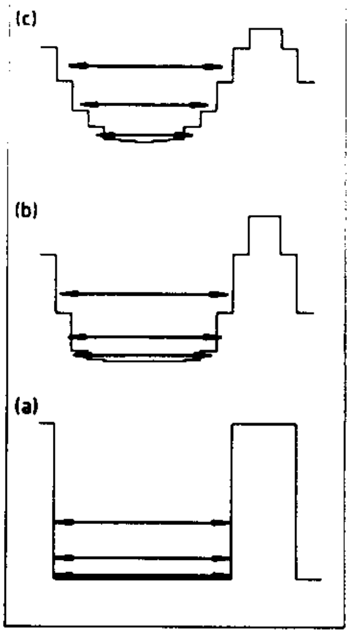

Fig. 11 . Aluminum concentration profiles along the superlattice axis calculated for the structures of Fig. 10 according to an erf-profile with a broadening parameter of 0(a), 1.5(b) and 2.4 (c) monolayers. For each profile, the three arrows correspond to modes 1,3 and 5 confined in the gallium-rich parts of the samples. Their length indicates the effective thickness associated with their frequency. Their vertical position indicates the composition of the bulk alloy whose GaAs-type LO frequency coincides with their frequency.

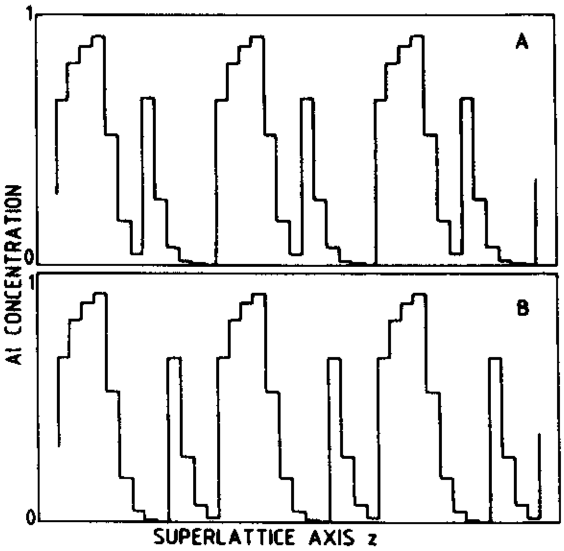

Fig. 12 . Aluminum concentration profiles along the superlattices axis calculated for the sequences A and B of Fig. 2 according to the segregation model of Ref.16.

Let us consider the points on the lowest curve of Fig.13. They correspond to Al concentrations 0.1, 0.25, 0.5, 0.75 and 0.9 and the in-plane atomic distribution in the interface layer is such that isolated Ga or Al atoms are separated by a distance comparable to the one in a 1D random alloy of the same composition. These points give us an estimate of the effect of an intermixed layer with short range (alloy-like) disorder. Between x=0.5 and x=1., the frequency of the confined vibrations remains remarkably close to that obtained with exactly two monolayers. Only one Al atom on each fourth site (x=0.25) almost completely pushes away the vibration from the interfacial layer. This results is in good agreement with the predictions of the 1D model with gradual interfaces.

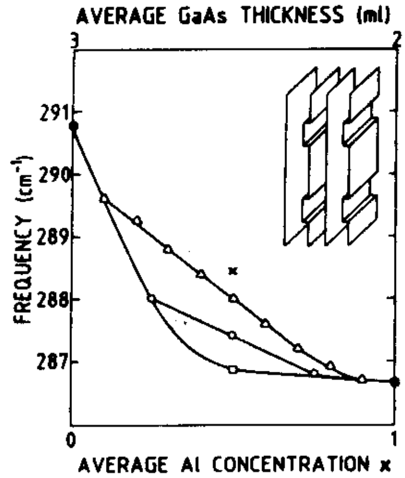

Fig. 13. Frequencies of the fundamental GaAs-type LO vibration calculated for the $(GaAs)_{3-x}(AlAs)_{2+x}$ model superlattice shown in the inset, as a function of the average aluminum concentration x in the in-plane modulated interface atomic layer. Different periods of the in-plane modulation are considered : 2 (open square), 4 (open circles), 10 (open triangles) and 40 (cross) monolayers. The corresponding average thickness (3-x) of the GaAs layers is indicated in the upper scale. The full lines are a guide to the eye.

We can also look in Fig.13 for the variation of the fundamental frequencies as a function of the size of the terraces for a given average concentration. Consider the case where x=0.5 and vary a=b from 1 to 20. The frequency then slightly shifts towards higher values while the eigendisplacement is weakly modified. This result is illustrated in Fig.14 where the amplitude of the eigendisplacement along z on each site in the supercell is shown for a+b=2 and a+b=10. In both cases the eigendisplacement pattern remains very similar to the one in a perfect 5-monolayers-thick GaAs, while the gallium atoms in the interfacial layer are almost at rest. Neither lateral localization nor line splitting is therefore predicted up to this high value of the terrace size. This result is consistent with the absence of any reported observation of such splitting. However it is surprising by comparison with the behavior of electrons confined to a GaAs layer with rough interfaces[18]. Well defined electronic levels, associated to the lowest quantized levels in each thickness, were indeed predicted to appear when the terrace extension exceeds to following dimension :

$$\lambda = \frac{d\sqrt{\frac{m_z}{m_{xy}}}}{p\sqrt{\frac{2\Delta d}{d}}} \qquad (2)$$

where m_z and m_{xy} are the effective mass along z in the bulk constituent (which governs the confinement in quantum wells with infinite barriers) and the one along the layer plane in the superlattice; d and Δd are the nominal thickness and its fluctuation and p is the index of the quantized level. This expression originates in the comparison between the additional confinement energies due to either the reduction of the layer thickness or the lateral localization in the thicker parts. Assuming an isotropic mass, i.e. starting from a cubic crystal and assuming that the confinement does not significantly modify the masses, this length scale does not depend on the actual value of the mass but increases with increasing nominal layer thickness and with decreasing defect amplitude. This model therefore depends on the goemetry of the problem. A naive application of this criterion to the confined vibration which we analyzed previously would let us predict the emergence of lateral localization for very small terraces (respectively 3 and 9 monolayers for $n_l=2$ and 5) in complete disagreement with the predictions of our calculation.

We attribute this disagreement to the long range Coulomb forces which strongly affect the dispersive properties of optical phonons around zone center[19]. We show in Fig.15 the dispersion of the GaAs-type optical phonons with displacement mainly oriented along z, calculated at a fixed finite wavevector along z, k_z=0.01 in reduced units, and an in-plane wavevector k_x varying between 0 and 0.3. The dispersion curve of the fundamental mode is rapidly varying close to zone center due to the increasing associated macroscopic polarization. As a result of this large anisotropy, the lateral localization does not appear even in presence of very large terraces. On the contrary, this macroscopic polarization remains very small for the other odd confined modes and is vanishing for the even ones. As a consequence, their in-plane dispersion curves are smooth close to zone center. We thus predict that the corresponding confined modes should be much more sensitive to interface roughness.

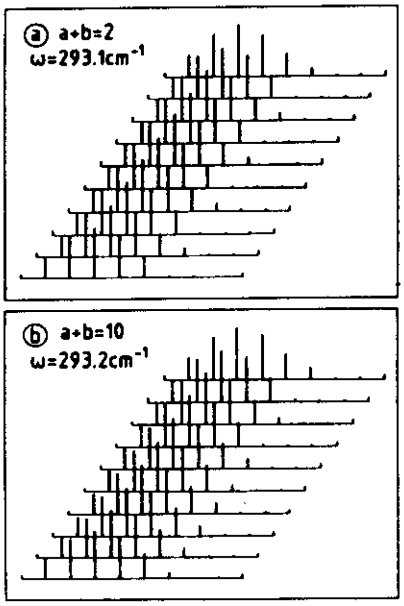

Fig. 14 . Amplitude of the eigendisplacements along z corresponding to the fundamental GaAs-type LO vibrations, shown for the cation sites the supercell of a$(GaAs)_{55}$/$(AlAs)_{25}$ superlattice with two different in-plane modulations : a+b=2 (a) and a+b=10 (b).

2G

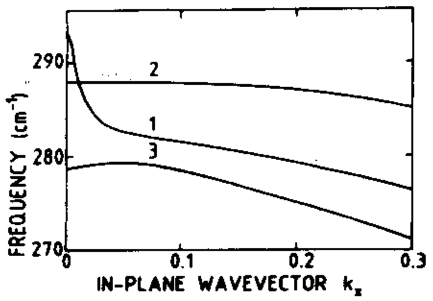

Fig. 15 . Dispersion curves in the layer plane of the higher-frequency GaAs-type optical vibrations calculated for a $(GaAs)_5/(AlAs)_3$ superlattice with perfect interfaces.

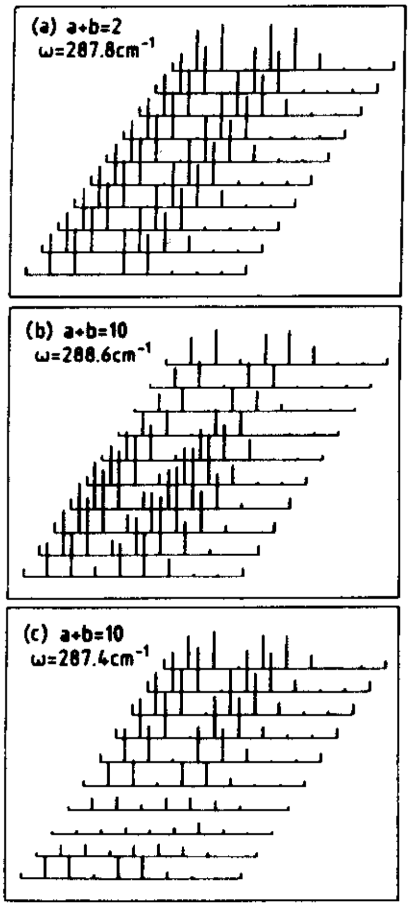

Fig. 16 . Amplitude of the eigendisplacements along z corresponding to the second GaAs-type LO vibrations, shown on the cation sites in the supercell of a $(GaAs)_{5.5}/(AlAs)_{2.5}$ superlattice with two different in plane modulations : a+b=2 (a) and a+b=10 (b and c). In the latter case, two different eigenmodes are displayed, as explained in the text.

We show in Fig.16 some eigendisplacements in the supercell calculated for a corrugated structure with $n_1=5$ and $n_2=3$ and corresponding to the higher even mode (p=2 in Eq.1). We obtain a clear evidence in this case of a mode splitting due to lateral terraces, when they reach a large enough extension. In Fig.16a, we show the eigendisplacement obtained assuming a small in-plane period of 2 monolayers. There is almost no modulation along the x direction, the displacement is hardly distinguishable from the one in the perfect $n_1=5$ GaAs layer. In particular, the displacement of the Ga atom at the center of this perfect well vanishes by symmetry and remains negligible in the locally 6 monolayer thick parts of the rough well. In good agreement with a critical size $\lambda=4$ deduced from Eq. 2, opposite conclusions apply to the sample with larger terraces : two different eigenmodes merge from the p=2 mode of the perfect GaAs layer and exhibit a single node in the vicinity of the center of the layer. The lowest frequency component of the doublet is partially localized in the narrow parts of the GaAs layer and the highest one, more clearly, in the wide parts. A good signature of this difference is again obtained from the displacement of the Ga atom at the center of the narrow parts. Its displacement is vanishingly small for the lowest mode but becomes significant in the wide parts for the highest frequency vibration. The node is now shifted from the gallium side to the neighboring arsenic one.

Similar behavior can be evidenced for the highest index (s>2) confined vibrations, with the qualitative tendency of a decrease in the critical terrace size with an increasing value of s. On the other hand, this critical size for a given value of s increases with increasing nominal thickness n_1. For instance, mode 2 is split in the sample of Fig.16b,c but becomes delocalized when n_1 is increased from 5 ($\lambda=4$) to 10 ($\lambda=12$), the terrace size remaining unchanged. All these variations reflect the change in the perturbative potential and thus in the value of λ.

CONCLUSION

The presence of GaAlAs mixed crystal layers in the GaAs/AlAs superlattices is very difficult and may be impossible to avoid. This makes the lattice dynamics of these structures very difficult to describe. We have attempted to review in this paper the present understanding of this problem. We also emphasized the considerable amount of new information on the lattice dynamics of bulk alloys one can get from their intentional incorporation in superlattices.

ACKNOWLEDGEMENTS

It is a pleasure for us to acknowledge F. Mollot, R. Planel, J.M. Moison, G. Le Roux, J.M. Gérard and J.Y. Marzin for growing or carefully characterizing the samples used in this work and for many helpful discussions.

REFERENCES

1 - for a review on vibrations in superlattices, see B. Jusserand and M. Cardona, in "Light Scattering in Solids V", ed. by M. Cardona and G. Güntherodt (Springer Heidelberg 1989) p.49.

2 - G. Fasol, M. Tanaka, H. Sakaki and Y. Horikoshi, Phys.Rev.B38, 605 (1988) and references therein.

3 - B. Jusserand, F. Alexandre, D. Paquet and G. Le Roux, Appl.Phys.Lett.47, 301 (1986).

4 - D. Levi, S.L. Zhang, M.V. Klein, J. Kem and H. Morkoç, Phys.Rev.B36, 8032 (1987).

5 - R. Cingolani, L. Tapfer, Y.H. Zhang, R. Muralidharan, K. Ploog and C. Tejedor, Phys.Rev.B40, 8319 (1989).

6 - J.Y. Marzin and J.M. Gérard, Phys.Rev.Lett.62, 2172 (1989).

7 - B. Jusserand, D. Paquet and F. Mollot, Phys.Rev.Lett.63, 2397 (1989).

8 - I.F. Chang and S.S. Mitra, Adv.Phys.20, 359 (1971).

9 - D. Paquet, unpublished.

10 - D.W. Taylor, Phys.Rev.156, 1017 (1967).

11 - P.N. Sen and W.M. Hartmann, Phys.Rev.B9, 367 (1974).

12 - R. Bonneville, Phys.Rev.B24, 1987 (1981).

28

13 - B. Jusserand, D. Paquet and K. Kunc, in "Proceedings of the 17th International Conference on the Physics of Semiconductors", ed. by J.D. Chadi and W.A. Harrison, Springer, New York (1985) p.1165.

14 - K. Kunc and H. Bilz, Solid State Commun.19, 1027 (1976).

15 - P. Soven, Phys.Rev.178, 1136 (1969).

16 - J.M. Moison, C. Guille, F. Houzay, F. Barthe and M. Van Rompay, Phys.Rev.B40, 6149 (1989).

17 - G. Kanellis, Phys.Rev.B35, 746 (1987).

18 - D. Paquet, Superlattices and Microstructures 2, 429 (1986).

19 - R. Merlin, C. Colvard, M.V. Klein, H. Morkoç, A.Y. Cho and A.C. Gossard, Appl.Phys.Lett.36, 43 (1980) ; E. Richter and D. Strauch, Solid State Commun.64, 867 (1987) ; S.F. Ren, H. Chu and Y.C. Chang, Phys.Rev.B37, 8899 (1988).

29

CONFINEMENT AND DISORDER EFFECTS ON PHONONS IN SEMICONDUCTOR MICROSTRUCTURES

Bernard JUSSERAND
CNET - Laboratoire de Bagneux
196 Avenue Henri Ravera - 92220 BAGNEUX - FRANCE

INTRODUCTION

The lattice dynamics of superlattices is now very well understood and most of the theoretical predictions have been quantitatively verified by Raman scattering, at least on GaAs/AlAs structures. This system is particularly interesting for several reasons:

- samples are currently available at a very high and controlled quality,
- phonon dispersion curves in the bulk constituents GaAs and AlAs are known,
- almost perfect lattice matching is achieved,
- GaAlAs alloy lattice dynamics is well described by reasonably simple models.

All theses conditions allowed a high degree of sophistication in the comparison between experiments and theory for GaAs/AlAs superlattices[1]. We will review these studies in part 1, and emphasize the relation between the GaAs and AlAs optical mode frequency and the interface roughness. In part 2, we will consider a derived system: $Ga_{1-x}Al_xAs/Ga_{1-y}Al_yAs$ alloy superlattices and we will show how to insert a bulk compound in a superlattice allows to extract much more information on its lattice dynamics than previously available. Finally in part 3, we will quote some experimental results on other systems. We will stress that the addition of strain make the quantitative interpretation much more difficult and review some recent progress in this direction.

I: LATTICE DYNAMICS OF GaAs/AlAs SUPERLATTICES

The optical phonon branches in GaAs and AlAs are well separated in frequency and the optical vibrations of one material cannot propagate into the other one. As a consequence, the optical vibrations in the GaAs/AlAs superlattices are divided into two families whose eigendisplacements are strongly confined either in the GaAs or in the AlAs layers; the penetration depth into the other compound being less than one monolayer. Their frequencies are thus very sensitive to boundary conditions. Assuming perfect interfaces, one can identify the eigenfrequencies of the modes confined in GaAs layers to those of bulk GaAs at a given set of wavevectors k_p :

$$k_p = \frac{p\pi}{(n_1 + 1)a} \qquad (1)$$

J.-P. Leburton et al. (eds.), Phonons in Semiconductor Nanostructures, 61–72.

7c

Similar conclusions apply to the optical vibrations confined in the AlAs layers. The LO dispersion in GaAs and AlAs being downwards, the confined phonon energies lie below the bulk GaAs (AlAs) one and decrease with decreasing layer thicknesses. This provides a one-to-one correspondence between the confined frequencies and the layer thicknesses. Equation 1 allows one to define an effective thickness $(n_l + 1)a$ which is common to all the confined vibrations in perfect layers. These predictions have been checked by different groups[2] with reasonable success.

The main approximation involved in these models is to consider atomically flat interfaces separating the two pure constituents. In real samples, even of the best quality, the interfaces are never flat due to the growth statistics. Such roughness, which extends over a few monolayers around the nominal interface, can be reasonably neglected for superlattices with moderately small individual layer thickness (> 50 Å). In shorter period structures, however, this roughness leads to quantitative departures from the predictions of the lattice dynamics of perfect samples. This part will be devoted to a description of Raman scattering experiments focussed on this problem and to a quantitative analysis of the dependence of the phonon frequencies on the spatial characteristics of the roughness, both along the growth axis and in the interface plane. We will use a simplified description of the lattice dynamics of bulk mixed crystals and of perfect superlattices containing layers of these alloys, which will be justified in part 2.

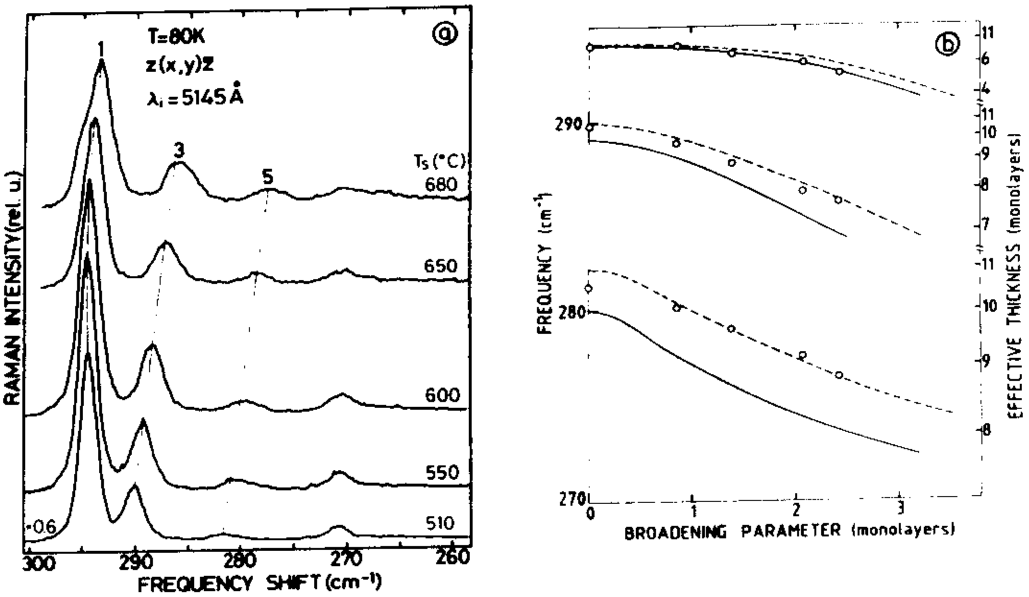

Fig.1: a) Raman spectra in the GaAs-type frequency range for five GaAs/AlAs superlattices with the same nominal parameters, but grown at different temperature T_s. b) Frequency of modes 1,3 and 5 confined in nominally 10 (full lines) or 11 (broken lines) monolayers thick GaAs layers with rough interfaces, calculated as a function of the broadening parameter of the erf-profile. The open circles indicate experimental frequencies deduced from the spectra of a). The effective thickness corresponding to each confined frequency is shown on the right vertical axis.

The optical vibrations confined in GaAs and AlAs are particularly sensitive to the interfacial imperfections because their frequencies are mainly determined from boundary conditions at each interface. This was first demonstrated[3] through the variation of the confined frequencies as a function of the growth conditions in nominally identical superlattices. We show in Fig. 1a Raman spectra obtained in the $z(x,y)\bar{z}$ configuration on five nominally identical samples grown by Molecular Beam Epitaxy (MBE) at different temperatures T_s ranging from 510°C to 680°C. We know from X-ray diffraction measurements that the macroscopic parameters of the samples are almost identical : d(GaAs)=28Å and d(AlAs)=12Å and independent of temperature. Other structural characterizations moreover suggest, in agreement with some independent knowledge of the growth process, the existence of an increasing interfacial roughness with increasing T_s.

The effect on the optical vibrations is strong: we observe a significant down-shift with increasing T_s of all the lines associated with optical phonons confined either in the GaAs or the AlAs layers. For instance, in the GaAs frequency range, three lines are observed on all samples, corresponding to mode 1,3,5 according to the now well established selection rules. They all shift towards lower frequency and moreover their relative distance strongly varies: they become more or less equidistant at 680°C while the splitting between line 3 and 5 amounts to almost twice the one between line 1 and line 3 at low T_s. Similar shifts in the confined optical vibrations have also been observed on superlattices during a series of successive thermal annealing stages[4].

Plotting together a large number of results, using relation 1, a general tendency is observed: the GaAs dispersion deduced from Raman scattering on real superlattices is flatter than the one obtained by neutron scattering on the bulk constituents. In other words, the effective thickness associated to a confined mode increases when the associated local wavevector (see Equation 1) increases. This departure increases when increasing the growth temperature. For AlAs, the situation is even worse. Despite the smaller amount of reliable experimental results, it clearly appears that the confined frequencies usually lie outside the very flat bulk dispersion curve and that no effective thickness can be even defined[5].

The importance of these departures can be also traced on Fig.2. In Fig.2a, we show our experimental determinations of the GaAs-type mode 1 frequencies as a function of the nominal GaAs thickness for different growth temperatures[6]. In Fig.2b, we show the measured AlAs-type mode 1 and mode 3 as a function of the nominal thickness for a given growth temperature[7]. In both cases, we indicate by dashed lines the calculated frequencies in absence of imperfections. We used a input parameters the bulk dispersion curves measured for GaAs and ab initio calculated for AlAs[5]. They always lie significantly above the experimental results. In Fig.2a, the improved agreement with experimental results as T_s decreases is very clear. In Fig.2b, the strong disagreement in the case of AlAs modes is evident: contrary to what applies for GaAs, it is never possible to make coincide experiment and theory by taking a smaller "effective thickness", that is by shifting horizontally the experimental points.

However, apart from these shifts, the general shape of the spectra is not strongly modified from sample to sample. Even when the phonon frequencies are very different from the ones calculated using the nominal parameters, we do not observe any significant line broadening. Moreover, line splittings (as reported in Ref.2) seem to be absent in our samples. This suggests that the imperfections in these samples are caused by "gradual interfaces" ; the in-plane statistics of the roughness should be such that the optical phonons only see the average in-plane concentration and thus experience an ordered, eventually gradual composition profile along the growth axis, while the translational invariance in the layer planes is preserved. Assuming a gradual profile makes one-dimensional models sufficient to analyze the Raman scattering results. From the data corresponding to the GaAs and AlAs energy range, we will determine the composition profile in the gallium-rich and aluminium-rich parts of the structure with good accuracy. We will present in what follows a detailed 1D calculation of the Raman spectra in superlattices with gradual interfaces. We will finally introduce, on the basis of a 3D lattice dynamics calculation including the interface roughness, a microscopic criterion governing the emergence of this behavior.

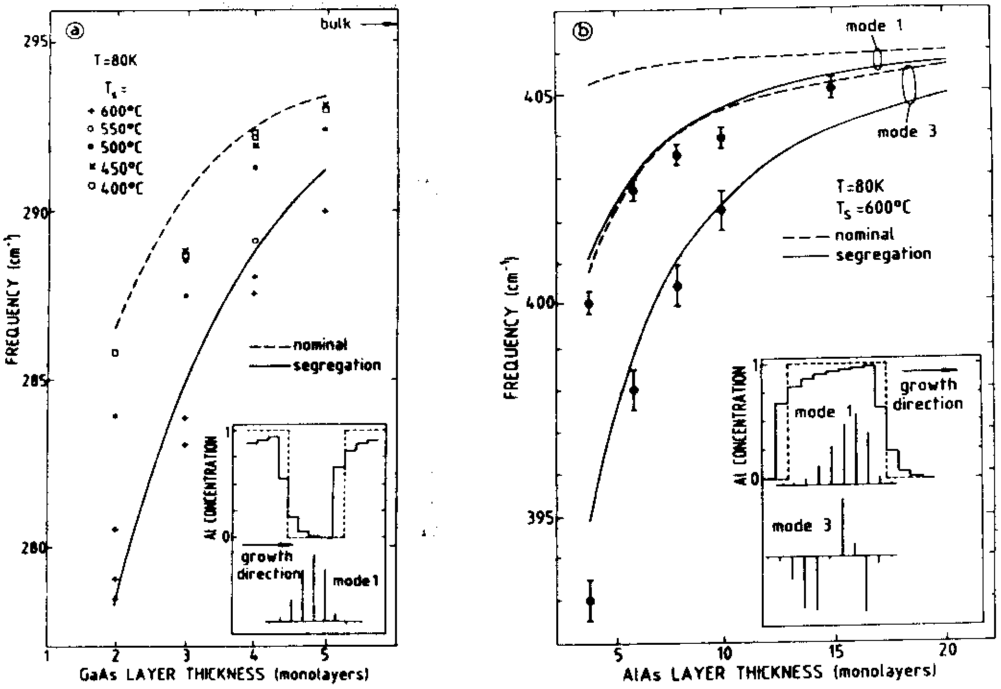

Fig.2: a) Variation of the GaAs-type confined mode 1 measured as a function of the layer thickness in samples grown at different temperatures compared to the predicted variations assuming, respectively, a nominal profile (dashed lines) and a one with segregation at 600°C (full lines). b) same as a) for the AlAs-type confined modes 1 and 3 on samples grown at 600°C.

The main difficulty arises from the alloy vibrational behavior. Let us recall some experimental results on this point. The Raman spectra on Ga$_{1-x}$Al$_x$As alloys display the well-known two-mode behavior : two optical phonon Raman lines coexist on the whole concentration range which lie respectively in the range of the pure GaAs and AlAs optical phonons and only slightly shift as a function of the alloy composition. Both this two-mode behavior and the strong confinement in GaAs/AlAs superlattices qualitatively originates from the same feature : the large energy splitting between the optical bands in GaAs and AlAs. A virtual crystal approximation to describe these alloy vibrations is therefore meaningless, contrary to what prevails for the electronic properties. The vibrational properties of the GaAlAs alloy have been analyzed theoretically for a very long time with the aim of qualitatively predict the two-mode behavior and to quantitatively reproduce the Raman scattering results. The favorable feature in this task is the almost identical spring constants of the GaAs and AlAs compounds which essentially differ by the mass of the atom III site. For the remainder of the paper we shall assume that these forces are the same. The first method which was successful in predicting the two-mode behavior is the Random Element Isodisplacement (REI) method[8]. Coherent Potential Approximation[9-12] was later extensively used to model the lattice dynamics of alloys. Both methods involve an effective ordered mass on the disordered site, which is either real (REI) or complex (CPA) but depends on the energy in a rather similar way. In part II, we will describe the Coherent Potential Approximation (CPA), its properties and its predictions. Let us now focus on the feature of greatest interest for our purpose. The real part of the effective mass displays strong variation in each energy gap, so to be successively close to the virtual crystal mass, the gallium and the aluminum one in the three allowed energy bands. The alloy thus **coincides in the GaAs-type (resp. AlAs-type) optical phonon range** with an effective pure compound with an effective mass close to that of gallium(resp. aluminium).

The simplest version of these models was introduced in Ref.3. The parameters of a linear chain with only nearest neighbor interactions is first fitted into the dispersion along the (001) direction of the LO phonon in pure GaAs. In a second step, the mass on the atom III site is modified in order the reproduce the zone center GaAs-type LO frequency in the alloy for each value of x. For any given composition profile along the growth axis, we can then build up the dynamical matrix using the mass associated to each local composition. By diagonalization, we then determine the frequencies of the modes confined in the GaAs-rich parts of the samples (**and only these ones**). We then follow again the same method for AlAs-type modes. One can thereby check that the chosen profile is not unreasonable. This method is illustrated in Fig.1b where the GaAs-type confined frequencies (modes 1,3 and 5), calculated assuming an erf-profile, are shown as a function of d_0 for two different choices of the nominal thickness of the well (i.e. when $d_0=0$). Each frequency decreases with increasing d_0. In other words, the effective thickness seen by each vibration decreases. The comparison with the experimental frequencies is satisfactory because the frequencies of modes 1,3 and 5 can be fitted using the same d_0. Moreover, from the effective thickness scale shown on the right part of the figure for each confined vibration, we get the following result: this thickness is no longer constant from mode to mode as it was in the case of the abrupt profile. It increases with increasing confinement shift.

Let us now model the experimental results of Fig.2. Instead of an erf-profile, we now use a "segregation profile"[13] to model the vibrations. This model was independently developed to explain chemical surface analysis results of the deposition of GaAs on AlAs and AlAs on GaAs at 600°C. Using these profiles, shown in the inserts of Fig.2 for GaAs and AlAs layers respectively, we get an excellent description of the Raman spectra on samples grown at 600°C. The predicted frequencies are shown by thick lines on the figures. They well reproduce the experimental results. Qualitatively, the dominant effect is the change in the confinement thickness for GaAs-type modes, which do not penetrate in alloy layers even with only 20% of Al. On the contrary alloying effects dominate the AlAs modes because of their very flat dispersion. However, our observation of a strong reduction of the roughness of the GaAs on AlAs interface at lower growth temperature is not reproduced with the segregation model. It is likely to be related to kinetic effects and should stimulate new efforts in understanding of the MBE growth process.

The previous description of the roughness in terms of gradual interfaces remains valid as long as the spatial fluctuations are smaller than the "coherence length" of confined optical phonons. We will now attempt to build up a definition of this quantity and to describe the lattice dynamics of superlattices when the gradual interface approximation fails, i.e. in the presence of terraced interfaces. For this purpose we need to build a supercell which is larger than the basic one, not only along the nominal superlattice axis, but also in the layer plane. As shown in the inset of Fig.3, we consider one-dimensional fluctuations on a single interface while the structure remains perfect along the third direction at this interface (it looks like corrugated cardboard) and along both directions at the other one, which remains atomically flat. Varying the amplitude along z and the distribution along x of the corrugation allows us to handle many different situations. In Fig.3, the rough interface only extends along z over a single monolayer and looks along x like a lateral superlattice. Two parameters then define the interface : its average aluminum content and its lateral period. This model provides the simplest representation without any empirical parameter of a thin layer with a non-integer thickness. Moreover, it opens the possibility to vary the lateral terraces.

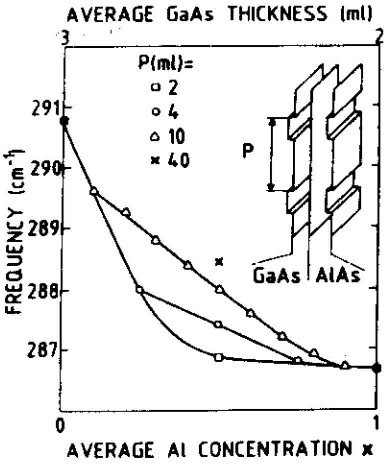

Fig.3: Frequencies of the fundamental GaAs-type LO vibration calculated for the $(GaAs)_{3-x}(AlAs)_{2+x}$ model superlattice shown in the inset, as a function of the average aluminum concentration x in the in-plane modulated interface atomic layer. Different periods of the in-plane modulation are considered : 2 (open square), 4 (open circles), 10 (open triangles) and 40 (cross) monolayers. The corresponding average thickness (3-x) of the GaAs layers is indicated in the upper scale. The full lines are a guide to the eye.

We show in Fig.3 the predicted frequency of the fundamental vibration confined in a GaAs layer of a thickness n_1+(1-x) monolayers as a function of x for n_1=2 and several different in-plane periods a+b between 2 and 40 monolayer thickness, i.e. between 6 and 120Å. a and b are the respective numbers of adjacent Ga and Al atoms in the single interfacial layer (see the inset). The average aluminum content x in the interface layer then takes simple rational values b/(a+b), ranging from 0 to 1. While a single composition x=0.5 can be considered for a+b=2, a series of nine different ones is reproduced for a+b=10. The results display similar trends for other nominal thicknesses, except that the absolute energy variations decrease with increasing n_1. Let us consider the points on the lowest curve of Fig.3. They correspond to Al concentrations 0.1, 0.25, 0.5, 0.75 and 0.9 and the in-plane atomic distribution in the interface layer is such that isolated Ga or Al atoms are separated by a distance comparable to the one in a 1D random alloy of the same composition. These points give us an estimate of the effect of an intermixed layer with short range (alloy-like) disorder. Between x=0.5 and x=1., the frequency of the confined vibrations remains remarkably close to that obtained with exactly two monolayers. Only one Al atom on each fourth site (x=0.25) almost completely pushes away the vibration from the interfacial layer. This results is in good agreement with the predictions of the 1D model with gradual interfaces.

When increasing the size of the terraces a=b from 1 to 20 for a given average concentration x=0.5, the frequency slightly shifts towards higher values while the eigendisplacement is weakly modified. This result is illustrated for n_1=5 in Fig.4 where the amplitude of the eigendisplacement along z on each site in the supercell is shown for a+b=2 (4a) and a+b=10 (4b). In both cases the eigendisplacement pattern remains very similar to the one in a perfect 5-monolayers-thick GaAs, while the gallium atoms in the interfacial layer are almost at rest. Neither lateral localization nor line splitting is therefore predicted up to this high value of the terrace size. This result is consistent with the absence of any reported observation of such splitting. However it is surprising by comparison with the behavior of electrons confined to a GaAs layer with rough interfaces[14]. A naive application of the electronic criterion[14] to the confined vibration which we analyzed previously would let us predict the emergence of lateral localization for very small terraces (respectively 3 and 9 monolayers for n_1=2 and 5) in complete disagreement with the predictions of our calculation. We attribute this disagreement to the long range Coulomb forces which strongly affect the properties of optical phonons around zone center[15]. This results into a large anisotropy of mode 1 dispersion and the lateral localization does not appear even in presence of very large terraces. On the contrary, this macroscopic polarization remains very small for the other odd confined modes and is vanishing for the even ones. As a consequence, their in-plane dispersion curves are smooth close to zone center. We thus predict that the corresponding confined modes should be much more sensitive to interface roughness.

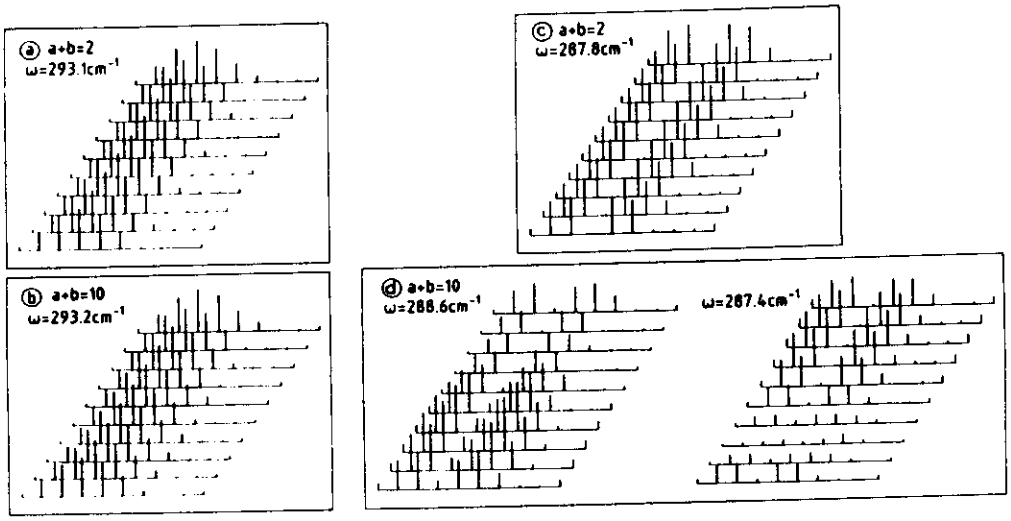

Fig.4: Amplitude of the eigendisplacements on the cation sites in the supercell of a $(GaAs)_{5.5}/(AlAs)_{2.5}$ superlattice with two different in-plane modulations. a) and b) correspond to the fundamental GaAs-type mode when a+b=2 and a+b=10 respectively. c) and d) correspond to the second GaAs-type mode when a+b=2 and a+b=10 respectively. In the latter case, two different eigenmodes are displayed, as explained in the text.

We show in Fig.4 some eigendisplacements in the supercell calculated for the same structure and corresponding to the higher even mode (p=2 in Eq.1). We obtain a clear evidence in this case of a mode splitting due to lateral terraces, when they reach a large enough extension. In Fig.4c, (in-plane period of 2 monolayers), the displacement is hardly distinguishable from the one in the perfect $n_1=5$ GaAs layer. In good agreement with the estimated critical size, opposite conclusions apply to the sample with larger terraces : two different eigenmodes merge from the p=2 mode of the perfect GaAs layer (Fig.4d). The lowest frequency component of the doublet is partially localized in the narrow parts of the GaAs layer and the highest one, more clearly, in the wide parts. Similar behavior can be evidenced for the highest index (s>2) confined vibrations, with the qualitative tendency of a decrease in the critical terrace size with an increasing value of s.

To summarize, Raman scattering spectra on GaAs/AlAs superlattices are quantitatively reproduced assuming gradual interfaces in good agreement with the results of other structural characterizations. They seems to be not sensitive to the, also existing, large terraces. We presented in the previous section some explanations, which partially agree with the experiments. We also develop this point because of its relevance to 1D structures. We would like to emphasize that long range Coulomb forces make difficult the description of phonons in wires or boxes, the longitudinal transverse character being no longer well defined whatever the wavevector direction. This unfortunately prevents the use of the simple models which were so successful in superlattices.

II: LATTICE DYNAMICS OF GaAlAs ALLOYS REVISITED

Raman scattering experiments on bulk alloys provided useful information on the alloy lattice dynamics but limited to zone center properties. The validity of lattice dynamics model, such the CPA, could be also checked at zone center only. Let us recall that the CPA[9-12] consists in a fictive ordered crystal which depends only on a frequency dependent isotropic complex mass assigned to the randomly occupied cation sites. This mass is self-consistently determined when one assumes the force constant matrix to be independent of the site occupation and if one demands that a given random occupied site imbedded in the CPA effective medium produces no extra scattering on the average. The CPA crystal being an ordered one, its properties, like phonon densities of states, dispersion curves and Raman activities, can be calculated as for pure compounds. However, due to the imaginary part of the CPA mass, the spectral density of states at any value of the wavevector is no longer a set of δ-functions but a continuous function displaying a few peaks which remain rather narrow in GaAlAs. The deduced dispersion curve is thus a thick one, as illustrated in Fig.5a for a few compositions. The zone center properties reproduce well the experimental results on bulk GaAlAs : the frequency decreases with increasing x and an asymmetric line shape develops. Furthermore, using this dispersion curve (in other words using the CPA mass on the disordered sites of the superlattice to perform the superlattices lattice dynamics calculation), we are able to calculate the Raman scattering spectra on $Ga_{1-x}Al_xAs/Ga_{1-y}Al_yAs$ superlattices. Inserting alloys in superlattices allowed us to relax this strong constraint in the experimental knowledge and to accurately test the CPA lattice dynamics in bulk GaAlAs.

Fig.5b displays the Raman spectra[16] in the GaAs energy range in three $Ga_{1-x}Al_xAs/AlAs$ superlattices with an aluminum concentration in the alloy ranging from 0 to 30%. The spectrum at 15% is rather similar to the one at 0%, while for higher aluminum concentration the different lines become poorly resolved. A general shift of the spectra is observed, which maps onto the one in the corresponding bulk alloy. Moreover, three different peaks remain observable. We attribute these optical phonon lines in the thin alloy layer spectra to confined GaAs-type vibrations, comparable to those observed in pure GaAs thin layers; the AlAs layers acting in both cases as very effective barriers. The distance between the peaks appears to decrease with increasing x, while their width increases. This experiment is the first experimental proof of the dispersive character of the GaAs-type vibrations in the GaAlAs alloys. Moreover, we plot on Fig.5a the position of the Raman lines according to equation 1. The agreement is quite reasonable and the CPA dispersion curves well supported by these new experimental results.

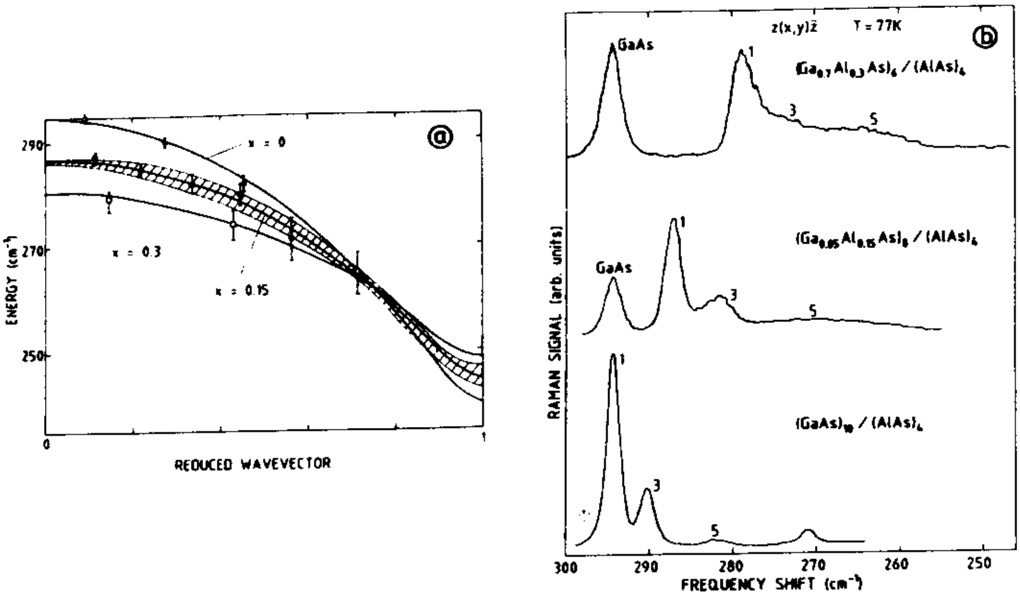

Fig.5: a) Calculated dispersion curves along the superlattice axis of the GaAs-type LO phonon in bulk Ga$_{1-x}$As$_x$As mixed crystals, with x=0, x=0.15 and x=0.30. For x=0.15, the hatched surface reflects the thickness of the dispersion curve, as explained in the text. Open circles, closed circles and open squares correspond to experimental frequencies on the samples of Fig.b, plotted according to Eq.1.
b) Raman spectra in the GaAs-type frequency range for three different Ga$_{1-x}$Al$_x$As/AlAs samples with the same parameters except for the aluminum concentration x in the alloy layers.

Inserting GaAlAs alloys in superlattices moreover allows to probe the dynamical properties in the phonon gaps[17]. Fig.6c displays the Raman spectra in the GaAs energy range on GaAs/AlAs superlattices with a GaAlAs monolayer inserted at the center of the GaAs layer. The parameters are identical except for the Al concentration in the additional barrier. Changing x drives the GaAs confined modes transmission through this barrier (and therefore their frequencies) according to the imaginary dispersion curve in the alloy inside the gap between both optical branches. In Fig.6a, we compare the experimental data with the predictions based on the CPA. The agreement is reasonable in the limited range which we probed. Let us emphasize that the continuous varion of the perturbed frequencies results of a continuous variation of the dynamical response function between a negative value (x=1) and a positive one (x=0). For a critical concentration, the average displacement of the atomic plane vanishes which corresponds to the well known divergence of the CPA mass (see Fig.6b).

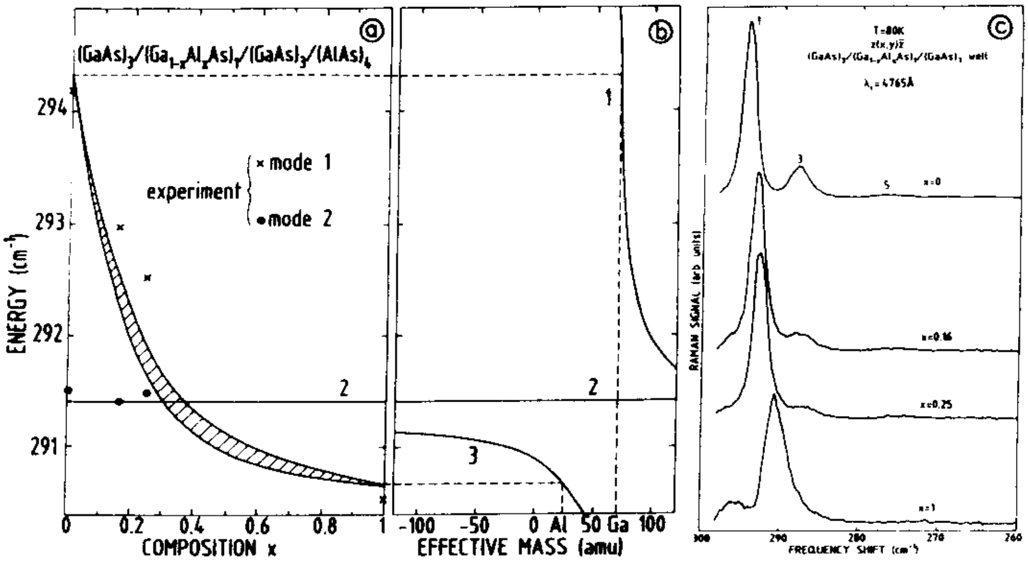

Fig.6: a) Calculated and measured frequencies of the GaAs-type confined modes as a function of the aluminium concentration x in the alloy monolayer b) correspondence with the effective mass in this layer c) Raman spectra in the GaAs-type frequency range for three different superlattices with the same parameters except for the aluminum concentration x in the alloy monolayer.

To summarize, the small amount of experiments which we performed on $Ga_{1-x}Al_xAs/Ga_{1-y}Al_yAs$ superlattices well support the CPA and therefore our description of the imperfect superlattices. This was also demonstrated recently on the basis of different averaging schemes[18] or of supercell calculations[19]. More systematic experiments on alloys should be nevertheless very useful.

III: OTHER SYSTEMS

As compared to the GaAs/AlAs, the understanding of superlattices based on the other couples of compounds is rather limited. This is because the respective effects of interface broadening and strain are difficult to separate: to extract information onto the composition profiles, one needs an accurate knowledge of the dispersion curves of the bulk constituants in the same strain configuration. This is not available, neither experimentally nor theoretically. Moreover, lattice dynamics of alloys with large differences in bonding lengths is usually poorly understood because of topological disorder. Let us illustrate these points on two different systems of technological importance: InAs/GaAs ($\delta a/a=7\%$) and Si/Ge ($\delta a/a=4\%$).

InAs/GaAs superlattices have been extensively studied in the past few years and the large In segregation in this system is now well documented[20]. By Raman scattering, we obtained some evidence of additional peaks in the optical frequency range as compared to the average alloy[21], as illustrated on Fig.7a. Due to the symmetric strain in GaAs and InAs on InP, both zone center LO come closer together. Assuming a rigid shift of the dispersion curves results in a strong overlap configuration, in rough agreement with the experiments. However a quantitative disagreement is obtained as shown on Fig.7b, due maybe to some deformation of the dispersion curves under strain and very likely to the In segregation. We do not attempt to quantify this alloying effect because of the well-known topological disorder in InGaAs. Theoretical efforts to calculate the dispersion curves in real bulk and strained modulated alloys would nevertheless very useful.

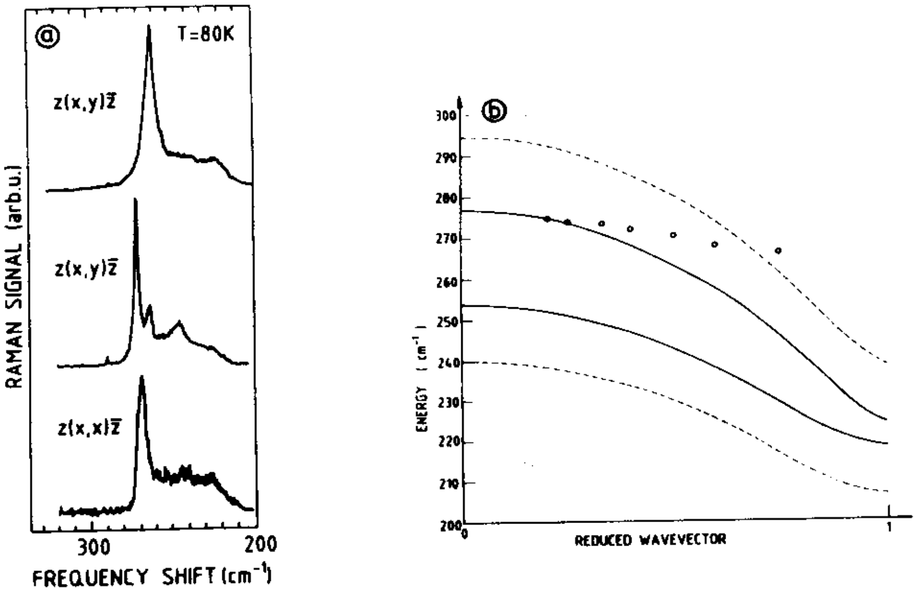

Fig.7: a) Raman spectra in the optical frequency range for a Ga$_{0.47}$In$_{0.53}$As bulk alloy (top spectrum) and for a (InAs)$_4$(GaAs)$_3$ superlattice in two different experimental configurations (center and bottom spectra) b) experimental frequencies plotted according to relation 1 and compared to the LO dispersion curves of the free-standing bulk constituents (dashed lines) and rigidly shifted due to strain (thick lines)

Such efforts are presently under progress for the Si/Ge system, which has been extensively studied experimentally[22]. The situation indeed looks better: strain coexists with interface broadening and superstructures but topological disorder can be reasonably neglected. This makes supercell calculation possible though limited to very small period structures. Semi-quantitative agreement was reported[23] with inclusion of interface roughness but using empirical lattice dynamics without strain. Recent developments[24] in ab initio lattice dynamics of strained Ge and Si should allow a satisfactory description of the experimental results and some quantitative test of the interface roughness models.

ACKNOWLEDGEMENTS

It is a pleasure for us to acknowledge F. Mollot, R. Planel, J.M. Moison, G. Le Roux, J.M. Gerard and J.Y. Marzin for growing or carefully characterizing the samples used in this work and for many helpful discussions.

REFERENCES

1 - for a review on vibrations in superlattices, see B. Jusserand and M. Cardona, in "Light Scattering in Solids V", ed. by M. Cardona and G. Güntherodt (Springer Heidelberg 1989) p.49.

2 - G. Fasol, M. Tanaka, H. Sakaki and Y. Horikoshi, Phys.Rev.B38, 605 (1988) and references therein.

3 - B. Jusserand, F. Alexandre, D. Paquet and G. Le Roux, Appl.Phys.Lett.47, 301 (1986).

4 - D. Levi, S.L. Zhang, M.V. Klein, J. Kem and H. Morkoç, Phys.Rev.B36, 8032 (1987).

5 - S.Baroni, P.Giannozzi and E.Molinari, Phys.Rev.B41, 3870 (1990)

6 - B.Jusserand, F.Mollot, R.Planel, E.Molinari and S.Baroni, Surf.Science267, 171 (1992)

7 - B.Jusserand and F.Mollot, Appl.Phys.Lett.61, 423 (1992)

8 - I.F. Chang and S.S. Mitra, Adv.Phys.20, 359 (1971).

9 - D.W. Taylor, Phys.Rev.156, 1017 (1967).

10 - P.N. Sen and W.M. Hartmann, Phys.Rev.B9, 367 (1974).

11 - R. Bonneville, Phys.Rev.B24, 1987 (1981).

12 - B. Jusserand, D. Paquet and K. Kunc, in "Proceedings of the 17th International Conference on the Physics of Semiconductors", ed. by J.D. Chadi and W.A. Harrison, Springer, New York (1985) p.1165.

13 - J.M. Moison, C. Guille, F. Houzay, F. Barthe and M. Van Rompay, Phys.Rev.B40, 6149 (1989).

14 - D. Paquet, Superlattices and Microstructures 2, 429 (1986).

15 - R. Merlin, C. Colvard, M.V. Klein, H. Morkoç, A.Y. Cho and A.C. Gossard, Appl.Phys.Lett.36, 43 (1980) ; E. Richter and D. Strauch, Solid State Commun.64, 867 (1987) ; S.F. Ren, H. Chu and Y.C. Chang, Phys.Rev.B37, 8899 (1988).

16 - B. Jusserand, D. Paquet and F. Mollot, Phys.Rev.Lett.63, 2397 (1989).

17 - B.Jusserand, F.Mollot, L.Quagliano, G.Le Roux and R.Planel, Phys.Rev.Lett.67, 2803 (1991)

18 - D.Kechrakos, P.R.Briddon and J.C.Inkson, Phys.Rev.B44, 9114 (1991); B.Samson et al., Phys.Rev.B46, 2375 (1992)

19 - E.Molinari, S.Baroni, P.Giannozzi and S. de Gironcoli, Phys.Rev.B45, 4280 (1992)

20 - J.M.Gerard and J.Y.Marzin, Phys.Rev.B45,6313 (1992)

21 - J.M.Gerard, J.Y.Marzin, B.Jusserand, F.Glas and J.Primot, Appl.Phys.Lett.54, 30 (1989)

22 - an exhaustive review is missing to our knowledge; see however J.D.White et al., Phys.Rev.B43, 1685 (1991); K.Eberl et al.,Phys.Rev.B43, 5188 (1991) and ref.23

23 - M.I.Alonso, F.Cerdeira, D.Niles, M.Cardona, E.Kasper and H.Kibbel, J.Appl.Phys.66,5645 (1989)

24 - S.de Gironcoli, Phys.Rev.B46, 2412 (1992)

53

Reprint from

Topics in Applied Physics
Volume 66: **Light Scattering in Solids V**
Superlattices and Other Microstructures
Editors: M. Cardona and G. Güntherodt

Springer-Verlag
Berlin Heidelberg New York
London Paris Tokyo

42

Light Scattering in Solids V

Superlattices and Other Microstructures

Editors: M. Cardona and G. Güntherodt

3. Raman Spectroscopy of Vibrations in Superlattices

Bernard Jusserand and Manuel Cardona

With 58 Figures

> – Jo jamés haguera pogut creure experiència tal si de mos ulls no ho hagués vist. Ara no tinc res per impossible que los hòmens no sàpien fer. En especial tals sabers cauen en gents qui van molt per lo món; e prec-te, pare reverent, me faces gràcia de dir-me totes les coses necessàries per aquest fet del què hi és mester.
>
> *J. Martorell, M. J. de Galba*: Tirant lo Blanch (N. Spindeler, València, 1490)

3.1 Introduction

As already discussed in Vols. I and II of this series [3.1, 2], light scattering spectroscopy of crystals is subject to rather stringent selection rules which arise from the conservation of wavevector $\boldsymbol{k}$: $\boldsymbol{k}$ has to be conserved modulo a vector of the reciprocal lattice or simply conserved if we confine ourselves to the reduced Brillouin zone (BZ). The magnitudes of the wavevectors of the incident and scattered radiation, k_i and k_s $(2\pi n_{i,s}/\lambda_{i,s}$ where the ns are refractive indices and the λs wavelengths) are very small compared to that of a general vector in the BZ ($\sim\pi/a_0$, where a_0 is the lattice constant $\cong 5$ Å). Hence, in order to conserve $\boldsymbol{k}$ the elementary excitation created or annihilated (here a phonon) must have a wavevector of magnitude close to zero, i.e., near the center of the Brillouin zone (Γ-point). Thus, of the many existing excitations, for all $\boldsymbol{k}$s within the reduced BZ (see Fig. 3.1 for phonons in GaAs) we can only investigate by means of (first order) light scattering the excitations for $\boldsymbol{k} \cong 0$. The same restriction applies to most other optical spectroscopies: simple absorption and reflection (or ellipsometry) and non-linear spectroscopies such as hyper-Raman and four-wave mixing (CARS) [3.3] but not to inelastic neutron scattering [3.4]. The wavelength of thermal neutrons is on the order of 5 Å. Therefore, all points in the reduced BZ can be swept by simply changing the angle between the incident and the scattered beam and the crystal orientation. As is well known, the phonon dispersion relations of many crystals have been mapped in this manner [3.5]. Nevertheless, and in spite of the reduced amount of information it yields, light scattering spectroscopy is used frequently as it offers a number of advantages with respect to neutron spectroscopy:

i) The linewidth resolution and the accuracy in the frequency determination are one to two orders of magnitude better than in neutron spectroscopy.

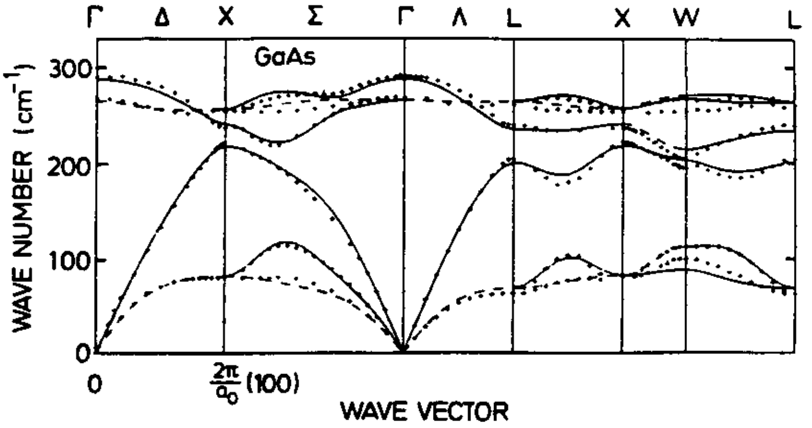

Fig. 3.1. Dispersion relations of phonons in GaAs measured at room temperature with neutron spectroscopy (*points*). The lines represent a theoretical fit. D. Strauch and B. Dorner, private communication

ii) Only microscopic amounts of material are needed for light scattering, as opposed to large crystals (several cm^3) required for neutron spectroscopy. In fact, Raman microprobes using microscope optics have recently become commercially available [3.6]. The laser spot can be focused to ~1 μm and its penetration depth in a semiconducting sample is ~1000 Å. Hence, the technique is most suitable for the investigation of semiconductor microstructures.

iii) Light scattering spectrometers are extremely simple, inexpensive, and ecologically safe when compared with a neutron reactor spectrometer. They are a one-worker instrument and they are fast, especially when used with a multichannel detector [3.7, 8]. Not only spatial resolution but also time resolution (pico- and nanosecond) becomes possible [3.9]. Thus, they can be used for the characterization of semiconducting materials under industrial production conditions.

Several reviews of the applications of Raman spectroscopy to the investigation and characterization of bulk semiconducting materials have appeared [3.10–12]. Optical phonon branches are usually very flat at $k \cong 0$ (quadratic dispersion). Hence, no dispersion is seen in Raman scattering in bulk crystals and the phonon frequency for $k \equiv 0$ is obtained even if k differs somewhat from zero. For acoustic phonons, however, (Brillouin scattering) the dispersion relations are linear (see Fig. 3.1) and this linear dependence of ω on k (i.e., the speed of sound) can be measured in Brillouin spectroscopy [3.10, 13].

The severe restriction imposed upon optical spectroscopies by k-conservation is a direct consequence of the existence of a lattice of translations as symmetry elements. Thus, the thought arises that one may be able to circumvent that restriction by removing, in whole or in part, the translational symmetry operations. Several possibilities of doing so arise:

i) Making the materials amorphous or microcrystalline
ii) Introducing impurities or defects (e.g., mixed crystals such as $Al_xGa_{1-x}As$)
iii) Artificially fabricating a superlattice (e.g. $(AlAs)_7(GaAs)_7$). Such artificial crystals have a much larger lattice constant along the direction of growth than the corresponding single crystals: most of the bulk translation vectors cease to be symmetry operations. These subjects will be considered in detail in the present chapter.
iv) Observing second order (two phonon) spectra: one phonon destroys or lowers the translational invariance while the other scatters in the medium distorted by the first.

Examples of the lifting of selection rules in the cases (i) and (iv) have been given in [3.10, 14]. In these cases, broad bands which correspond to densities of phonon states weighted by a smoothly varying transition probability (matrix element), are observed. We illustrate this in Fig. 3.2 which compares the Raman and infrared spectra of amorphous silicon (a – Si) with spectral densities of phonons obtained both theoretically for a – Si and c – Si, and by neutron scattering for a – Si [3.15]. These spectra show four bands: TA, LA, LO, TO, as

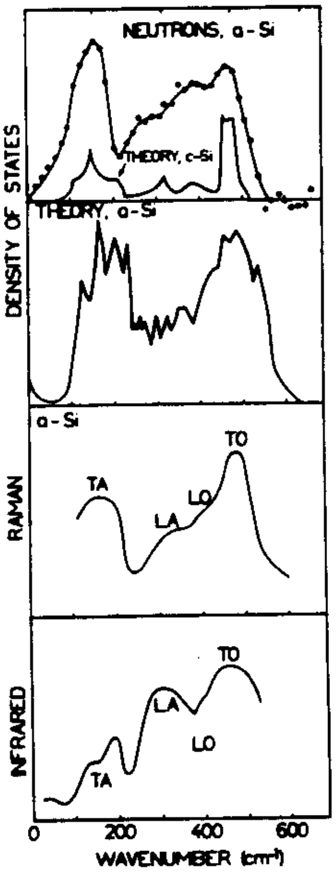

Fig. 3.2. Vibrational spectra of amorphous silicon (a-Si) as observed with infrared, Raman, and neutron scattering spectroscopies. They are compared with calculations of densities of phonons for a-Si and for c (crystalline)-Si [3.15]

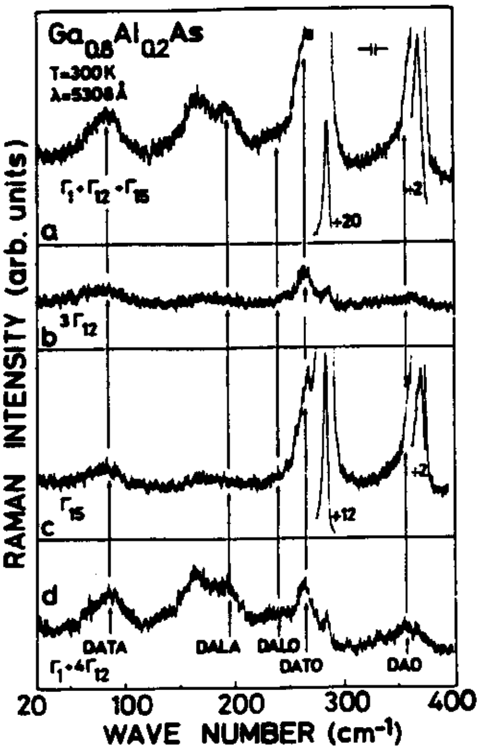

Fig. 3.3. Raman spectra of $Ga_{0.8}Al_{0.2}As$ in several scattering configurations at room temperature showing the disorder activated DATA, DALA, DATO, and DALO bands [3.16]

expected from the dispersion relations of c − Si (roughly similar to Fig. 3.1 but with the vertical scale multiplied by ~1.7).

We show in Fig. 3.3 the Raman spectra of a bulk $Ga_{0.8}Al_{0.2}As$ crystal obtained [3.16] in four scattering configurations which correspond to different combinations of irreducible symmetry components A_1 (also called Γ_1), $E(\Gamma_{12})$, and $T_2(\Gamma_{15})$, see [3.10]. The four bands of phonons mentioned above are also observed in these spectra although they would be forbidden in the perfectly ordered single crystal constituents (GaAs, AlAs). They are thus activated by the chemical disorder of the Ga and Al atoms (disorder activated ≡ DA, DATA, DALA, DALO, and DATO bands). Since $Ga_xAl_{1-x}As$ is a constituent material of many superlattices, similar bands are also expected in the latter (see Fig. 15 of [3.42]).

This chapter is concerned with case (iii) above, i.e., with the reduction of the number of translational invariance operations produced by the formation of a superlattice or multiple quantum well MQW (MQW refers to the large period case in which the electronic states have zero dispersion along the superlattice direction z; see Chap. 4 of this volume). We discuss only superlattices made out of diamond or zincblende-like bulk constituents. Let us assume that the two constituents (e.g. GaAs, AlAs) have the same bulk lattice constants $2a_1 = 2a_2 = 2a$ and layer thicknesses $d_1 = n_1 a_1$, $d_2 = n_2 a_2$, the new translational period along z being $d = d_1 + d_2$ (Fig. 3.4). Because of the enhancement of the

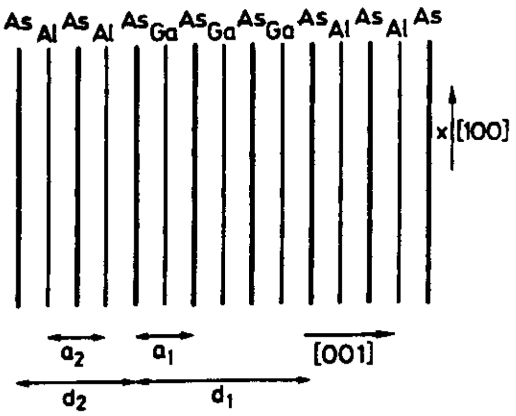

Fig. 3.4. Sketch of a (GaAs)$_{n_1}$/(AlAs)$_{n_2}$ superlattice with $n_1=3$, $n_2=2$. The growth direction is assumed to be $z=[001]$, since this is the most commonly investigated case

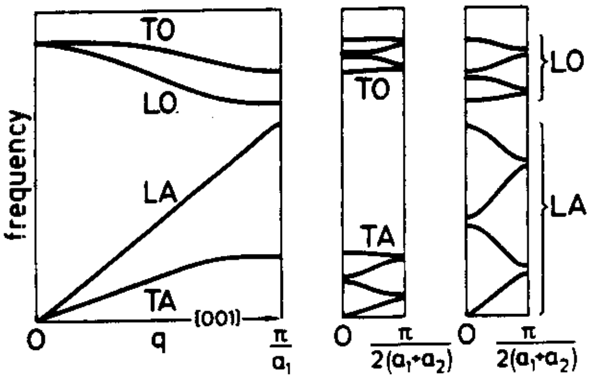

Fig. 3.5. Schematic representation of the folding to the Brillouin zone for $n_1=n_2=2$. Note that the perturbation induced by the superlattice formation is small for the acoustic modes but can be large (e.g. (GaAs)$_2$/(AlAs)$_2$) for the optic ones

period along z the BZ must be folded into a smaller mini-BZ or superlattice BZ (SBZ) in order to stay within the reduced zone scheme. If this is not done we must, equivalently, accept non-conservation of $\boldsymbol{k}$ by reciprocal lattice vectors of the superlattice (umklapp processes). The usual (folded) reduced zone scheme, illustrated in Fig. 3.5, is more comfortable. After folding, new modes appear in the SBZ at $k=0$ (6 longitudinal and 12 transverse in Fig. 3.5). These modes can now be Raman and optically (IR) active. Hence, superlattices are particularly interesting since they can increase the number of vibrational modes accessible to optical spectroscopies. The folding scheme is particularly useful if the phonon dispersion relations of the two materials are similar: one can fold the dispersion relations of one of the constituents (or the average of the two) and treat the difference with the real superlattice by perturbation theory. This scheme works rather well for the acoustic modes: the speeds of sound of most pairs of materials forming superlattices are indeed rather similar and, correspondingly, so are the TA and LA dispersion relations. We shall see that the main effect of the superlattice perturbation is to open "minigaps" in the folded dispersion relations at the center and edges of the SBZ. This treatment is similar to the nearly-free electron model in electronic band structures. Folded acoustic modes are discussed in Sect. 3.4.2.

The situation concerning the optical modes is quite different. The corresponding $\omega(k)$ branches of bulk materials such as GaAs and AlAs are well separated (because of the different cation masses) and rather flat (Fig. 3.1). It thus becomes meaningless to use "average" bands since a state with a given frequency for one material has no counterpart of the *same* frequency in the other, both bands being well separated. The corresponding vibrations in the superlattice are then "*confined*" to either one material or the other, decaying rapidly and exponentially beyond the interfaces. Observations of confined optical modes are discussed in Sect. 3.4.3. We note that folded modes were observed a long time ago by using the system of superlattices provided by the various polytypes of silicon carbide [3.17]. Confined acoustic modes can also be observed for single thin slabs in vacuum (or air) and for a superlattice of slabs using vacuum as a spacer. Such is the case of the *l*ongitudimal *a*coustic *m*odes (LAM) observed in folded polymer chains [3.18].

Under several simplifying assumptions the observation of folded acoustic and confined optic modes in superlattices yields information about the dispersion relations of the constituents. In some cases this information may not be available from other methods because of the lack of sufficiently large single crystals (e.g., AlAs). If independent information is available for the constituents the results for superlattices can be used to characterize their quality, in particular the details of the interfaces (see Sect. 3.4.4).

So far we have assumed that the bulk constituents have the same lattice constant. This is nearly the case for the GaAs-AlAs system (mismatch 0.1%). In many other cases the mismatch can be large (e.g. Ge – Si, 4%). Two possibilities then arise:

i) For thin layers (i.e., small periods) the lattice constants of both constituents remain matched at some average value determined by the substrate (pseudomorphic growth). The constituting layers are then under compressive or extensive strain depending on the details of the structure.
ii) For thicker layers (i.e., large periods) the individual layers relax their relative strain through the creation of misfit dislocations at the interfaces.

Even in the former case, some relaxation is expected to appear when the average superlattice parameter is not matched to that of the substrate. Above a given total thickness, some loss of strain along the axis of the structure then occurs, as recently reported [3.19]. Raman spectroscopy can be advantageously used to determine the strain in the various layers (see Sect. 3.4.4).

We have so far introduced the kinematics of light scattering in superlattices. The mechanisms leading to the scattering are also of interest since they yield detailed information about electron-phonon interaction. The simplest and oldest model is based on assuming bonds whose polarizability is modulated by the phonons [3.20]. Its implications for the case of superlattices are presented in Sect. 3.3.3. The dynamics of scattering by folded acoustic modes can be most simply discussed on the basis of the photo-elastic (elasto-optic) constants, i.e., the effect of strain on the refractive index (see Sect. 3.3.4). A more precise microscopic treatment is, however, required when the laser or scattered frequencies fall near strong electronic resonances such as those between confined valence and conduction levels in MQWs. In this case one introduces explicitly the electron-phonon interaction through deformation potential and Fröhlich mechanisms [3.10]. This is discussed in Sect. 3.5.1. In the bulk materials these mechanisms interfere with each other. In superlattices, however, they apply to phonons of different symmetries and the interference disappears.

We have so far implicitly confined our discussion to superlattice phonons which propagate along the axis of the superlattice. They are those which can lead to scattering in the conventional backscattering configuration. It is also possible, with some additional difficulties, to excite phonons which propagate perpendicular to the superlattice axis ($k_x \neq 0$). This is done by removing the substrate and using the forward scattering configuration (see Sect. 3.4.2 for acoustic phonons). Right angle scattering is also possible provided that one operates with a laser slightly below the lowest absorption edge and uses an appropriately clad superlattice, so as to transform it in an optical waveguide (see Sect. 3.4.3). Of particular interest are modes which decay exponentially (but not necessarily rapidly) around the interfaces and propagate along x or y. These have been labeled interface modes and are discussed in Sects. 3.2.4 and 3.4.3.

Several review articles have already been written on phonons in superlattices. We mention here the recent work of *Klein* [3.21], that of *Jusserand* and *Paquet* [3.22] and of *Cardona* [3.23]. The reader will also find a number of articles of interest in [3.24].

Interest in artificial semiconductor superlattices was kindled by the pioneering work of *Esaki* and *Tsu* [3.25]. The reliable experimental realization of such superlattices had to await the development of commercial molecular beam epitaxy (MBE) equipment. Most of the superlattices used for the work described here were grown by MBE. Some work has, however, been performed on superlattices prepared by the chemical vapor deposition technique involving metal-organic compounds (e.g. trimethyl gallium). A number of books, review articles, and conference proceedings devoted to the growth of superlattices, MQW, and heterojunctions have appeared. The interested reader should look at [3.26–28], other references given in these volumes, and the articles [3.29, 30] about MBE and [3.31a, 31b] about MOCVD. We should conclude by saying that all measurements reported here have been performed with superlattices grown along one of the cubic axes of the bulk constituents. Measurements on superlattices with other orientations (e.g. [111] or [110]) are highly desirable.

3.2 Lattice Dynamics of Superlattices

3.2.1 Survey

A number of models have been developed to describe the phonon dispersion curves of III–V cubic crystals [3.5]. They belong to different families such as shell models, bond charge models, etc. In these models, a large number of unknown parameters are introduced to fit the experimental dispersion curves. More recently, ab initio calculations based on the local density approximation have appeared [3.32]. They provide a good description of the phonon dispersion curves along high symmetry directions. As concerns the superlattices, a great amount of work using approaches of various degrees of complexity has been devoted to the derivation of the dispersion curves using only a knowledge of those of the bulk constituents. Several problems are encountered:

- the choice of the proper lattice dynamical model for the bulk constituents,
- the transferability of the bulk model parameters to the superlattice case, which is reasonable and straightforward for local quantities or very short range interactions but becomes difficult for long range forces,
- numerical difficulties arising from the size of the secular equations in the case of thick layer superlattices.

Lattice dynamical calculations for superlattices fall into two categories. The most general type are simple generalizations of the bulk calculations using force parameters between atoms and dynamic effective charges taken over from the bulk. To this category belongs the work of *Kanellis*[3.33], *Yip* and *Chang* [3.34], and *Richter* and *Strauch* [3.35, 35a]. These calculations yield the dispersion relations of the superlattice for any arbitrary direction of $\boldsymbol{k}$, i.e., for finite k_x, k_y, and k_z.

The philosophy of the other, simpler group of calculations is based on the fact that most experiments (backscattering) measure only the dispersion relations for $k_z \neq 0$, $k_x = k_y = 0$. In the usual case of $k_z \parallel [001]$, one can calculate the dispersion relations by using force constants between $\{001\}$ planes (planar force constants). These planar force constants can be determined for the bulk materials either by fitting experimental dispersion relations or "ab initio" through total energy calculations [3.32, 36]. A schematic diagram of the planar nature of a zincblende-type superlattice grown along [001] is shown in Fig. 3.6. One should note that such a "planar" scheme is equivalent to the calculation of the vibrations of a one-dimensional chain with a basis (primitive cell) containing $2(n_1+n_2)$ atoms. For vanishing in-plane wavevectors ($k_x = k_y = 0$), the longitudinal and transverse vibrations of the chain are not coupled, as they have different symmetry (see Sect. 3.3.2). Their frequencies are thus obtained from separate secular equations, a fact which simplifies the numerical analysis of the problem.

The most elaborate superlattice linear chain model [3.37] is based on ab initio local density calculations of the effective interplanar forces in GaAs [3.32]. In

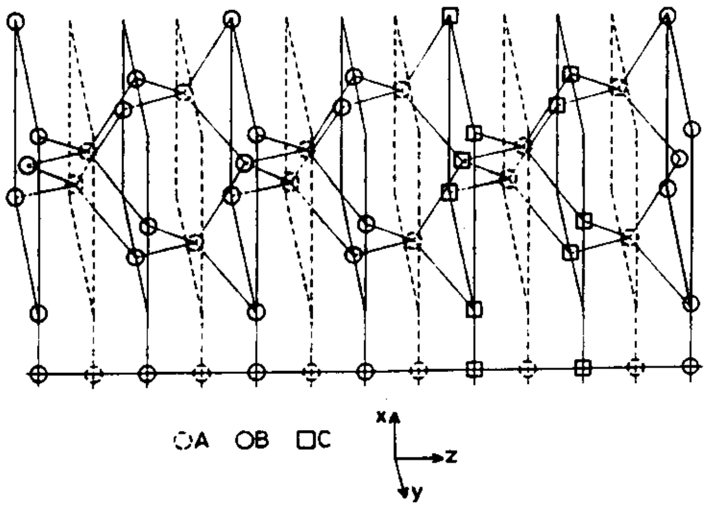

Fig. 3.6. Correspondence between the three-dimensional structure along the superlattice axis and the effective planar linear chain in the case of a $(AB)_4(AC)_2$ structure

this work both longitudinal and transverse dispersion curves are obtained by taking into account all significant interactions, including long range Coulomb forces, through a few short range effective forces. The problem of transferability of the bulk forces is circumvented in this description of GaAs/AlAs superlattices: the difference between the vibrational properties of GaAs and AlAs is mainly attributed to the mass difference between gallium and aluminum. Some corrections in the Coulomb long range interactions are introduced to better describe the longitudinal-transverse splitting of AlAs. These corrections are obtained by introducing an additional term involving a Coulomb interaction between effective charges in a rigid ion model and calculating the extra charge needed to accurately describe the splitting. This somewhat artificial correction preserves the main advantage of the method: the modulated quantities (masses, effective charges) are local and thus directly transferable to the dynamical matrix of the superlattice. The only exception is the effective charge of the As interfacial atom which is different in GaAs and AlAs and must thus be interpolated. This model is particularly well adapted to obtaining realistic dispersion curves with a minimum of arbitrary assumptions. Other fitting procedures which describe the bulk dispersion curves with intermediate range forces, different in both compounds, indeed involve rather questionable interpolation schemes to generate the superlattice interactions.

On the other hand, the spatial extension of the interactions define the sensitivity of any atom in the structure to the existence of a modulation. In the model of [3.37] a large number of atoms is involved in each dynamical matrix and numerical diagonalization is needed to solve the problem, which becomes rather cumbersome for thick layer superlattices. Simpler resolution methods, independent of the thickness of the layers involved, and even providing analytical solutions in some cases, have been developed on the basis of simplified linear chain models. Such models, using a very small number of short range parameters, fitted to bulk dispersion curves, have been introduced in the early works on phonons in superlattices [3.38, 39]. The results, obtained by diagonalization of the corresponding dynamical matrices, appear to be rather good in spite of the rusticity of the models: nearest neighbor interactions often suffice, especially for longitudinal modes. Experimental constraints make the work of theoreticians easier as Raman *backscattering* selection rules for (001) faces only allow the observation of longitudinal modes (see Sect. 3.3.2). By reference to these early calculations, most of the experimental results have been successfully analyzed using the simplest imaginable model: a linear chain with only nearest neighbor short range interactions. We shall refer to it in the following as the "alternating linear chain model". All the parameters are then directly transferable from the bulk constituents to the superlattice, at least in the case where the two constituents AB (e.g. GaAs) and AC (e.g. AlAs) share a common atom A. The more general case (AB/CD) presents several specific aspects such as "wrong bonding" and "interface modes" which have been recently investigated in [3.40]. As pointed out in [3.41] the most interesting feature of alternating linear chain models consists in the reduced range of the interactions: only very few atoms are directly sensitive to the modulation. In the usual example of the GaAs/AlAs structure, only the As atoms located at each interface are affected: they are surrounded by gallium at one side and aluminum at the other. The eigendisplacement of all the atoms, except those at the interfaces, are basically known from bulk properties, and the solution of the dynamical problem thus reduces to the fulfillment of macroscopic boundary conditions at those interfaces. The method is independent of the thickness of the layers and provides, as first shown in [3.41], an analytical dispersion relation. This allows a qualitative analysis of the new vibrational features appearing in the superlattice, in particular the coexistence of:

- propagating modes for the energy ranges where allowed vibrations exist in both bulk constituents, and
- confined modes when the vibrational amplitude is evanescent in one of the constituents, since no propagating bulk modes are available at that frequency.

Since its introduction, this type of calculation has been refined somewhat by various authors to take into account, for instance, unequal nearest neighbor interactions [3.42] and to treat the case of AB/CD structures [3.43]. Some new mathematical methods have been introduced: *Albuquerque* et al. [3.44] have used a transfer matrix technique which allows to treat periodic structures with any given number of different layers per unit cell or even aperiodic structures. Green functions treatments of similar models have also been published [3.45].

The idea of taking advantage of the abrupt shape of the modulation profile and to reduce the problem to some interface boundary conditions, which was later applied in this context, is a usual one in the study of modulated structures with piecewise constant parameters. A classical example is the propagation of electromagnetic waves in layered compounds which gives rise to interference bands [3.46]. In the Kronig-Penney model, which handles the propagation of a free particle in a square wave potential [3.47, 48], some features appear, such as the confinement of the particles, which are formally reproduced in the alternating linear chain model. Moreover, the dispersion relations, obtained in both cases from interface boundary conditions, are very similar. In the context of lattice dynamics, the same ideas were first applied by *Colvard* et al. [3.49] to describe low frequency Raman lines in the elastic approximation. These authors made reference to an old calculation, by *Rytov*,of sound propagation in layered geologic systems [3.50]. Such a propagation is dominated, as in the case of electromagnetic waves, by interferences between sound waves transmitted or reflected at each interface between compounds of different acoustic impedances. Section 3.2.2 will be devoted to the elastic model, as this approximation is relevant to the analysis of numerous experimental results. We will first describe in detail the exact solution of the wave equation and analyze the dispersion relation in terms of band folding and gap opening. We will then compare the results with the more general analysis by Fourier transforms which gives better insight into the details of the eigenwaves. Section 3.2.3 will be devoted to the alternating linear chain model. We shall derive the dispersion relation in the simplest case and analyze the different vibrational behaviors of both dispersion curves and eigendisplacements. In the low frequency range the predictions of the elastic model are recovered, whereas the optical phonon range displays confinement effects which are best analyzed in terms of optical phonon quantum wells. In the case of strong confinement, the results are compared with various calculations relevant to isolated thin slabs. Some original features, such as interface modes appearing in *AB*/*CD* superlattices or surface modes in semi-infinite structures will also be briefly considered.

In Sect. 3.2.4 we shall consider the lattice dynamics for wavevectors off the superlattice axis and the connected problem of the superlattice effect on the long range Coulomb forces and the dielectric constant, which have been neglected up to this point. This subtle problem should be treated using three-dimensional lattice dynamical models in a manner similar to that used for isolated layers [3.51–53]. In spite of the scarcity of experimental results, this field has attracted much theoretical interest in the past few years in connection with two original observations of "slab modes" [3.54] and "interface modes" [3.55]. The former are confined optical phonons propagating in the layer planes whose transverse or longitudinal character is strongly affected by the dielectric modulation. The latter are optical modes, weakly localized at interfaces by the same dielectric modulation, in contrast to the "mechanical" interface modes previously considered which are strongly localized at interfaces by the short range modulation of some lattice dynamical parameter. From these two examples, the dominant role played by the long range forces in the understanding of the in-plane lattice dynamics clearly appears, a fact which gives rise to macroscopic analyses which neglect the microscopic nature of the problem. We will present these analyses and attempt to discuss their validity to describe the real three-dimensional lattice dynamics. Results of full three-dimensional calculations will be presented in Sect. 3.2.5.

3.2.2 Elastic Properties of Superlattices

We shall first consider the modulated structure corresponding to most of the experiments: the alternating stacking of two layers of different compounds A and B defined by their respective mass density ϱ_A and ϱ_B, elastic stiffness constant C_A and C_B (C_{11} is the stiffness constant relevant to the longitudinal acoustic modes propagating along the [001] direction in cubic crystals) and sound velocity v_A and v_B. There is no reference in this model to any crystalline order in the bulk constituents (i.e. it also applies to amorphous constituents) and a similar description is valid for longitudinal as well as transverse modes. The analysis we present in the following has been progressively refined in several papers [3.49, 56, 57] following improvement in the accuracy of the experimental results on samples of increasing quality. The equation for one-dimensional propagation of either longitudinal or transverse elastic waves along [001] reads:

$$\frac{\partial}{\partial t}\left[\varrho(z)\,\frac{\partial u}{\partial t}\right]=\frac{\partial}{\partial z}\left[C(z)\,\frac{\partial u}{\partial z}\right], \tag{3.1}$$

where $\varrho(z)$, $C(z)$, $u(z)$ are the local values at z of the density, elastic constant (different for longitudinal and transverse modes), and atomic displacement. This equation is also valid for propagation along [111] provided one uses the appropriate effective Cs.

For an alternating structure of two materials A and B (3.1) reduces to:

$$\varrho_{A,B}\,\frac{\partial^2 u_{A,B}}{\partial t^2}=C_{A,B}\,\frac{\partial^2 u_{A,B}}{\partial z^2} \tag{3.2}$$

in each layer.

At a given frequency ω, the sound waves in each layer are a linear combination of two plane waves of wavevectors $\pm k_A(\omega)$ for layer A and $\pm k_B(\omega)$ for layer $B\,[k_{A,B}(\omega)=\omega/v_{A,B}]$. As is well known for electromagnetic waves, and in order to take into account the reflection at each interface, we must write the displacement field in each layer as a linear combination of a forward ($+k_{A,B}$) and a backward ($-k_{A,B}$) elastic wave of unknown amplitudes. The solution of the problem then reduces to the determination of the four amplitudes of the four independent plane waves appearing for a given angular frequency ω.

Integrating the wave equation over an infinitesimal interval crossing any interface lying at z_i leads to the following boundary condition:

$$C_A\,\frac{\partial u_A}{\partial z}\bigg|_{z_i}=C_B\,\frac{\partial u_B}{\partial z}\bigg|_{z_i} \tag{3.3}$$

which expresses the continuity of the stress at each interface and holds together with the continuity of the atomic displacements:

$$u_A(z_i)=u_B(z_i)\ . \tag{3.4}$$

Imposing these two boundary conditions at each interface, and using Bloch's theorem to obtain the displacement field in the two unit cells on either side of the one at the origin, leads to a 4×4 secular determinant which provides the dispersion relation between the frequency ω and the superlattice wavevector $q=k_z$ [3.50]:

$$\cos(qd)=\cos\left(\frac{\omega d_A}{v_A}\right)\cos\left(\frac{\omega d_B}{v_B}\right)$$
$$-\frac{1}{2}\left(\frac{\varrho_B v_B}{\varrho_A v_A}+\frac{\varrho_A v_A}{\varrho_B v_B}\right)\sin\left(\frac{\omega d_A}{v_A}\right)\sin\left(\frac{\omega d_B}{v_B}\right), \tag{3.5}$$

where $d_{A,B}$ are the thicknesses of the A and B layers and $d=d_A+d_B$ is the period of the structure.

This relation has the same form as the well known Kronig-Penney dispersion relation for electrons in a square-wave potential [3.47] which reads (see Eq. (10.21) of [3.48]):

$$\cos(qd)=\cos(k_A d_A)\cos(k_B d_B)$$
$$-\frac{1}{2}\left(\frac{k_A}{k_B}+\frac{k_B}{k_A}\right)\sin(k_A d_A)\sin(k_B k_B)\ . \tag{3.6}$$

In both relations the physical details of the problem are contained in the coefficient of the second term which describes the nature and the amplitude of the modulation. The rest of the equation reflects the geometry of the structure. To better analyze the effect of this modulation on the dispersion, we write (3.5) in the equivalent form:

$$\cos(qd)=\cos\left[\omega\left(\frac{d_A}{v_A}+\frac{d_B}{v_B}\right)\right]-\left(\frac{\varepsilon^2}{2}\right)\sin\left(\omega\frac{d_A}{v_A}\right)\sin\left(\omega\frac{d_B}{v_B}\right), \tag{3.7}$$

where the parameter ε is given by:

$$\varepsilon=\frac{\varrho_B v_B-\varrho_A v_A}{(\varrho_B v_B \varrho_A v_A)^{1/2}}\ . \tag{3.8}$$

This parameter describes the acoustic modulation through the relative difference between the acoustic impendances $\varrho_i v_i$ of both bulk constituents. For available superlattices made of IV, III–V, or II–VI compounds, the acoustic modulation is usually small and $\varepsilon^2/2\sim10^{-2}$. This suggests to neglect, to a first approximation, the second term in (3.7) which is proportional to $\varepsilon^2/2$. In doing so, we only consider the "geometrical" contribution of the modulation which creates a new periodicity without modulating the physical quantities involved. Relation (3.7) then reduces to:

$$\cos(qd)=\cos\left[\omega\left(\frac{d_A}{v_A}+\frac{d_B}{v_B}\right)\right] \quad \text{or:} \tag{3.9}$$

$$qd=\pm\omega\left(\frac{d_A}{v_A}+\frac{d_B}{v_B}\right)+2\nu\pi\,, \qquad \nu=0\,,\ \pm1\,,\ \pm2\,\ldots \tag{3.10}$$

which simply corresponds to the folding of an average elastic dispersion curve as shown in Fig. 3.7. The average sound velocity v follows from the averages of the inverse velocities weighted with the respective thickness d_A, d_B

$$v=\frac{v_A v_B}{(1-\alpha)v_B+\alpha v_A} \quad [\text{with } \alpha=d_B/(d_A+d_B)] \tag{3.11}$$

and reflects the inner structure of the supercell modulation. As will be emphasized later, this velocity is not the same as that of the average bulk compound. This velocity can be understood very simply in terms of transit time

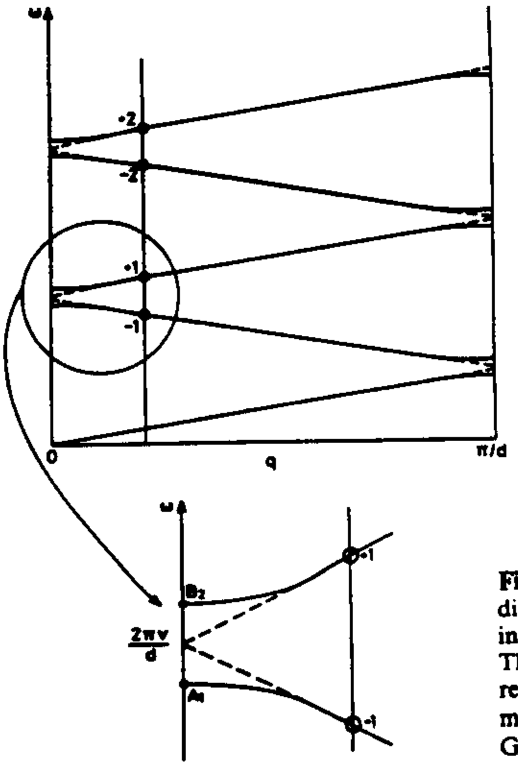

Fig. 3.7. Schematic diagram of a folded acoustic dispersion relation, neglecting (---) or taking into account (——) the acoustic modulation. The wavevector along the growth direction is represented by q. A_1 and B_2 indicate the symmetries found for these modes in gallium rich GaAs/AlAs superlattices

through the superlattice: in the absence of interface reflectivity ($\varepsilon = 0$), the transit time is the sum of the transit times through each layer, hence, inverse velocities weighted by path lengths must be added.

Within this approximation doubly degenerate modes appear at the zone center and zone edge of the SBZ (at $k = 0$ and π/d) with the energies:

$$\Omega_\nu = \frac{\nu\pi v}{d}, \tag{3.12}$$

where ν takes even (odd) integer values at the zone center (edge). This degeneracy will be lifted when the finite magnitude of the modulation through the second term in (3.7) is taken into account. As well known from the theory of nearly free electrons in a periodic potential, the splitting for weak modulation is proportional to the amplitude of the modulation.

The limiting frequencies of these gaps at the zone center and edge correspond to eigendisplacements with equal amplitudes of the backward and forward propagating components. Thus, these modes do not transport energy. As shown recently [3.57], an exact analytic expression for the corresponding splittings can be obtained.

The splittings induced by the modulation at the zone center and edge can be also obtained with excellent accuracy by expanding the exact frequency ω to second order in $\Delta\Omega = \omega - \Omega$. The dispersion relation then reads:

$$\eta - \cos\left[(\omega + \Delta\Omega)\frac{d}{v}\right] = \frac{\varepsilon^2}{2}\sin\left[(\omega + \Delta\Omega)\frac{d_A}{v_A}\right]\sin\left[(\omega + \Delta\Omega)\frac{d_B}{v_B}\right], \tag{3.13}$$

where η equals $+1$ (-1) at the zone center (edge).

Keeping only the second order terms in $\Delta\Omega$ in the left hand side of (3.13) and the zeroth order terms in the right hand side, one obtains the shift of zone center and zone edge frequencies given by the same expression:

$$\Delta\Omega_\nu \cong \pm\varepsilon\frac{v}{d}\sin\left[\frac{\nu\pi}{2}\,\frac{(1-\alpha)v_B - \alpha v_A}{(1-\alpha)v_B + \alpha v_A}\right]. \tag{3.14}$$

The band gap openings are therefore symmetrical relative to Ω and the average velocity of the two converging branches remains unchanged for this order of perturbation. The magnitude of the gap $2\Delta\Omega_\nu$, which is comparable for all ν, is proportional to the modulation parameter ε and inversely proportional to the period d. It displays an oscillatory behavior as a function of α as illustrated in Fig. 3.8. Note that all zone center gaps vanish for the same value of α:

$$\alpha = \frac{v_B}{v_A + v_B}. \tag{3.15}$$

The eigendisplacement fields are piecewise sinusoidal functions. In each layer A,

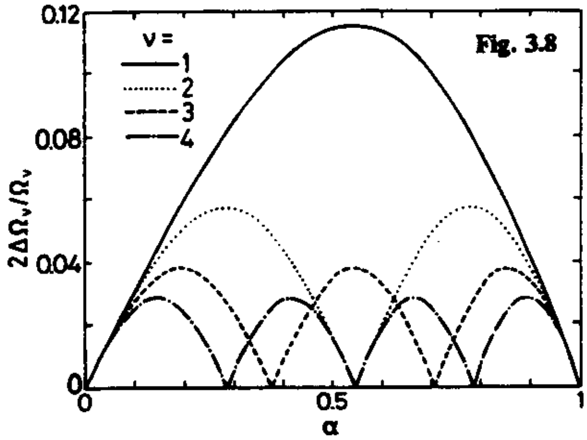

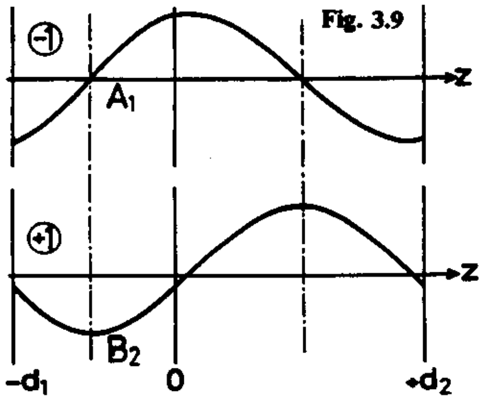

Fig. 3.8. Variation of the acoustic gaps at the lower zone center ($\nu = 2, 4$) and zone edge ($\nu = 1, 3$), normalized to the corresponding average frequency, as a function of the thickness ratio α in a GaAs/AlAs superlattice (the normalized gaps do not depend on the period) [3.60]

Fig. 3.9. Eigendisplacement for folded acoustic waves in a supercell with the two components of the lower zone center doublet (the symmetries are those found for Ga rich GaAs/AlAs) [3.22]

B, they are defined by the local wavevector $k_{A,B}$ which is slightly different in layer A and B. At the zone center, the two split modes correspond to very close local wavevectors but their displacement fields, represented in Fig. 3.9, display different symmetries: one is symmetric relative to each midlayer plane and the other antisymmetric. In Sect. 3.4.3 we shall give further details about the predictions of the elastic model and compare them with the results of various experiments. An outstanding feature is the extreme difficulty to obtain experimental evidence of the acoustic gaps. This is due to their small magnitude and to the fact that the backscattering wavevector usually lies beyond the range of significant coupling between folded zone center modes.

The same type of calculations has been recently performed [3.58] for superlattices with a period composed of three different layers. Very similar results were obtained, as should be the case for any piecewise constant profile. In such complex structures, a transfer matrix technique may, from the numerical point of view, be more convenient.

In the case of periodic structures with a smooth modulation, as for instance the erf function introduced in [3.59] to model the interdiffusion between neighboring layers of an abrupt structure, one cannot find an analytical solution of the elastic wave equation. Provided the modulation is not too strong, a perturbative approach can be applied and the wave equation approximately solved using a Fourier transform technique.

The Fourier method was first introduced by *Colvard* et al. [3.42] and applied to the square profile where a comparison with the exact solution is possible. Following [3.60] we present here a similar comparison but without the drastic approximations introduced in [3.42] to obtain analytical expressions. Such approximations give rise to less accurate predictions of the gap splittings. Let us first decompose the periodic quantities ϱ, C, and u_q in Fourier series:

$$u_q(z) = e^{iqz} \Sigma u_{n,q} e^{ingz}$$

$$C(z) = \Sigma C_n e^{ingz}$$

$$\varrho(z) = \Sigma \varrho_n e^{ingz} ,$$

where $g = 2\pi/d$ and u_q is the displacement field at frequency ω and wavevector q.

The wave equation then transforms into an infinite set of linear equations:

$$\sum_{n_1} [\omega^2 \varrho_{n-n_1} - (q+n_1 g)(q+ng) C_{n-n_1}] u_{n,q} = 0 \qquad (3.16)$$

whose secular determinant provides the dispersion relation. Usually, there is an infinite set of non-vanishing Fourier coefficients whose magnitude rapidly decreases with increasing Fourier order. Thus (3.16) can be truncated. Let us first neglect all the coefficients but the average ϱ_0 and C_0. The eigenfrequencies then reduce to:

$$\omega_\nu = (q + \nu g)\,(C_0/\varrho_0)^{1/2}$$

which just correspond to the folding of the dispersion relation of the average bulk compound (note that both ϱ and C must be averaged separately). This average dispersion curve does not coincide with the one obtained for zeroth order from the exact solution of the square profile where the inverse velocities were averaged (3.11). As a consequence, for such square profiles, accounting for the higher order Fourier component should not only induce a splitting between degenerate modes but also shift the whole set of eigenfrequencies. This feature cannot be obtained by only retaining the coupling between degenerate modes at the SBZ center and at the edge. The coupling between u_n and u_{-n} at the zone center or u_{n+1} and u_{-n-1} at the zone edge is of first order in the fluctuations of the material properties, as well known from the nearly-free-electron model. When one takes it into account, frequency gaps appear at the zone center proportional to $\sin(\nu\pi\alpha)$ [3.42] which differs from the oscillatory factor in (3.14). This difference, which is approximately proportional to squares of fluctuations in the material parameters (higher order perturbation theory), is due to non-degenerate couplings between branches of close Fourier order (n and $n \pm 1$) which may be comparable with degenerate couplings between branches of distant Fourier order (n and $-n$). As concerns the square wave profile considered in [3.42] and here, the degenerate approximation is fairly good as illustrated on Fig. 3.10. The variation of the first and third zone center gaps is shown as a function of α, both taking into account either only degenerate couplings or a large set of couplings. In Fig. 3.11 we show for a given square profile the variation of the dominant Fourier components of the vibrational

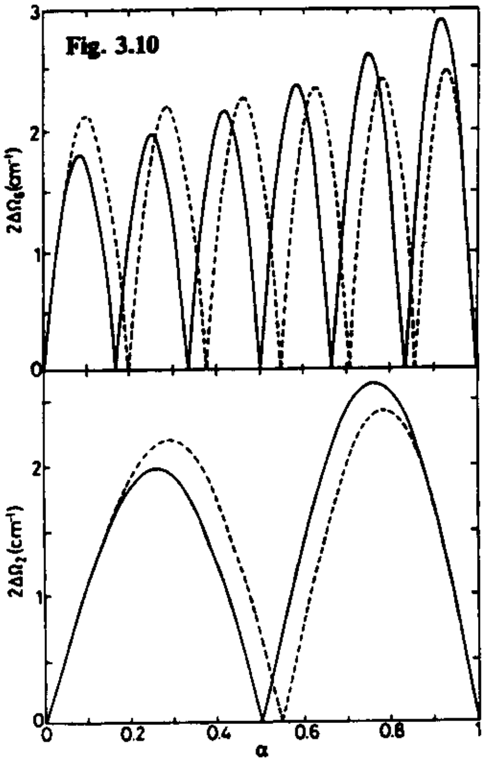

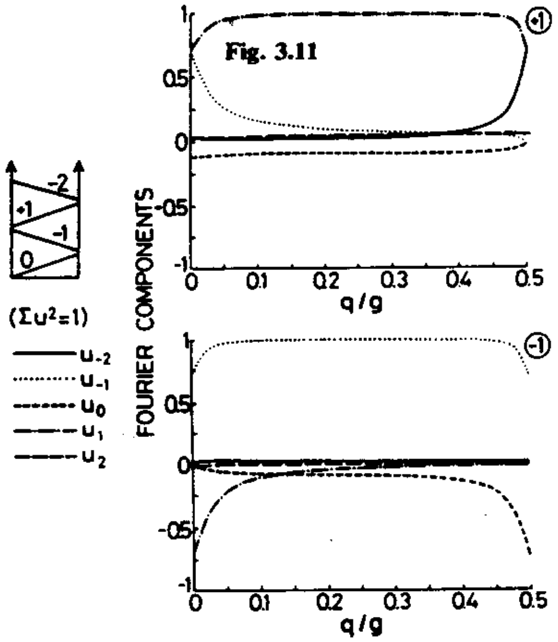

Fig. 3.10. Variation of the lower (*bottom*) and third (*top*) zone center gaps as a function of the thickness ratio in a GaAs/AlAs structure of period 40 Å, taking into account: (i) only the degenerate first order coupling (——) (ii) a large set of higher order couplings (- - -)

Fig. 3.11. Variation as a function of the wavevector q from mini-Brillouin zone edge ($q/g = 0.5$) of the dominant Fourier components of the eigendisplacements associated with the two lowest folded acoustic branches [3.60]

amplitudes of the lower branches as a function of the wavevector throughout the whole SBZ. Beside the single dominant component for intermediate q values, one clearly notices the effect of zone center and zone edge degenerate couplings. They induce pairs of Fourier components of equal or opposite magnitude, corresponding at the zone center to the symmetric and antisymmetric modes. One also notices the presence of additional components with a typical magnitude of 0.1 or less.

As outlined before, the Fourier transform analysis only becomes necessary for continuously varying (but well defined) profiles. Its application has been thus limited due to the lack of samples displaying such profiles. Moreover, the experimental observation of gap openings and other effects of the coupling between folded branches is extremely difficult due to their small magnitude and to limitations in the experimental conditions. However, as we will show later, the intensities of the folded acoustic Raman lines are much more sensitive to the details of the modulation and will allow us to obtain experimental confirmation of the main results of this section. The analysis of the intensities for interdiffused profiles [3.59] will in particular require the Fourier transform method.

3.2.3 The Alternating Linear Chain Model

We justified in Sect. 3.2.1 the description of the vibrational properties of superlattices along the [001] growth direction using linear chain models and discussed some more or less complex versions that one can find in the literature. The purpose of this subsection will not be to compare the validity of this description, which will be done in Sect. 3.4.2 for the GaAs – AlAs system, but to present the alternating linear chain model in its simplest version and to analyze the vibrational behavior predicted within its framework. They will not be qualitatively modified in more sophisticated models.

Let us consider the alternating linear chain *AB*/*AC* defined in Fig. 3.12 with its spring constants $K_{1,2}$ and the definition of the displacement $u_j^{(1,2)}$ and $v_j^{(1,2)}$ of atoms *A* or *B*/*C* in the *AB* or *AC* layers. Following the method used in the alternating elastic model, we will first look for the atoms which are not directly sensitive to the modulation. Due to the nearest neighbor range assumed for the interactions, the interface atoms *A* are the only ones perturbed: they are surrounded by *B* and *C* atoms. We can thus define the eigendisplacement at frequency ω of all atoms, except the *A* interface atoms, as a linear combination of corresponding eigendisplacements of the bulk:

$$u_j^{(1)} = \lambda_1 K_1 (1 - e^{-ik_1a_1}) e^{ijk_1a_1} + \mu_1 K_1 (1 + e^{ik_1a_1}) e^{-ijk_1a_1} \tag{3.17}$$
$$v_j^{(1)} = \lambda_1 (2K_1 - m_A\omega^2) e^{ijk_1a_1} + \mu_1 (2\mathrm{K}_1 - m_A\omega^2) e^{-ijk_1a_1}$$

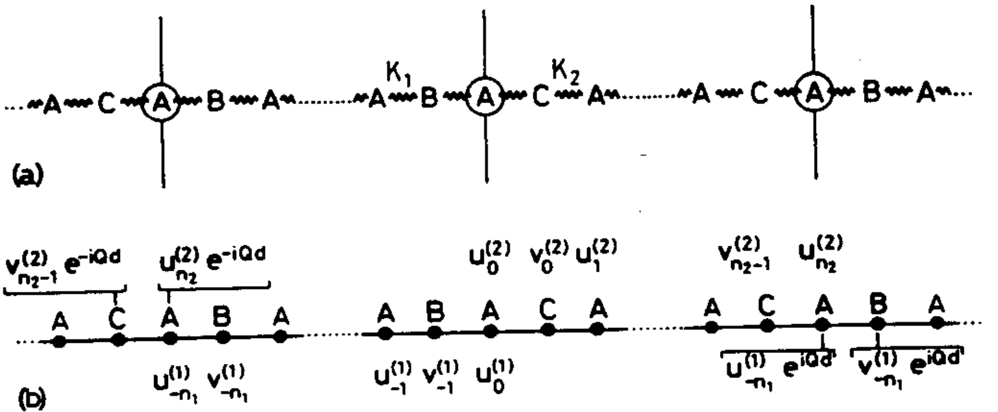

Fig. 3.12a, b. Description of the alternating linear chain model used in the text and definition of the eigendisplacements in the supercell. The *A* atoms are the boundaries between alternating chains

if the jth cell belongs to layer AB. Similar expressions are obtained for layer AC by replacing 1 by 2 in both expressions, a_1 and a_2 are the lattice spacings in AB and AC chains. Moreover, the interface atom displacement can be deduced from the dynamical equations of both of its neighbors and we obtain the first interface condition by identifying both expressions:

$$u_0^{(1)} = u_0^{(2)} = u_0 \tag{3.18}$$

which reflects the identity of the interface atom displacement "seen" from AB and from AC. This displacement must also satisfy the dynamical equation of the interface atom itself:

$$-m_A\omega^2 = K_2[v_0^{(2)} - u_0] + K_1[v_{-1}^{(1)} - u_0] \tag{3.19}$$

and this provides the second interface condition. Equation (3.19) can be simplified by drawing the analogy to the equation of motion of an A atom imbedded in AB (or in AC) to become:

$$K_2[v_0^{(2)} - u_0] = K_1[v_0^{(1)} - u_0]\ , \tag{3.20}$$

where the $v_0^{(1)}$ displacement is a fictitious one obtained by extrapolating compound AB beyond the interface. For equal spring constants, the set of boundary conditions reduces to:

$$\begin{aligned} &u_0^{(1)} = u_0^{(2)} \quad \text{and} \\ &v_0^{(1)} = v_0^{(2)} \end{aligned} \tag{3.21a}$$

at the first interface ($z = 0$) and

$$\begin{aligned} &u_{n_2}^{(2)} = u_{-n_1}^{(1)}\,\mathrm{e}^{iqd} \quad \text{and} \\ &v_{n_2}^{(2)} = v_{-n_1}^{(1)}\,\mathrm{e}^{iqd} \end{aligned} \tag{3.21b}$$

at the other one.

In a model involving longer range force constants, the same method can be applied to define each of the unknown displacements progressively from the AB and AC layers. For equal spring constants in both constituents, one again obtains (3.21a, b) which can actually be written for any atomic site in the chain.

The dispersion relation found by solving the 4 × 4 secular determinant can thus be written (k_1 and k_2 are the wavevectors for frequency ω in the two bulk materials):

$$\begin{aligned} \cos(qd) = {} & \cos(n_1 k_1 a_1)\cos(n_2 k_2 a_2) \\ & -\eta \sin(n_1 k_1 a_1)\sin(n_2 k_2 a_2)\ , \end{aligned} \tag{3.22}$$

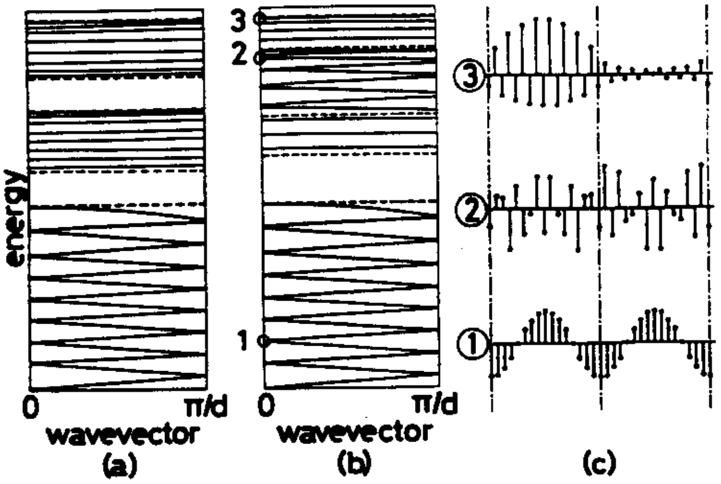

Fig. 3.13a–c. Dispersion relations for the LO phonons of a $(AB)_8/(AC)_8$ structure, with two different sets of parameters: $m_A=70$ amu, $m_B=50$ amu, $m_C=25$ amu (a), or 40 amu (b), calculated with (3.22). c Three eigendisplacement sets in the supercell corresponding to the three zone center modes labeled by the same numbers of dispersion curve (b) [3.22]

where only the factor η, in this case given by:

$$\eta=\frac{1-\cos(k_1a_1)\cos(k_2a_2)}{\sin(k_1a_1)\sin(k_2a_2)}\,,$$

depends on the choice of the lattice dynamical model. One can find for instance in [3.42] the dispersion relation for a chain with modulated nearest neighbor interactions. The dispersion curves obtained with (3.22) for an alternating linear chain with $n_1=n_2=8$ and two different choices of masses are shown in Fig. 3.13 together with some typical zone center eigendisplacements. For both cases, the common atom A is the heaviest one in both AB and AC. This choice allows a unified analysis of the acoustic and optic branches but prevents the emergence of such features as interface modes, confined acoustic modes, and mixed modes corresponding, respectively, to modes with evanescent character in both layers, with acoustic character in one and an evanescent in the other, and with acoustic character in one and optic in the other. These features have never been actually observed in AB/CD systems or Si/Ge superlattices where they have been predicted theoretically [3.40, 61]. We shall briefly describe their properties at the end of this subsection.

One easily notices the analogy of the dispersion relation (3.22) with (3.5). One indeed recovers (3.5) by taking the elastic limit for both AB and AC bulk compounds. The eigendisplacement labeled 1 in Fig. 3.13 corresponds to such a folded acoustic mode: the eigendisplacement of neighboring atoms is nearly the same. This analogy suggests to us to rewrite (3.22) in the following form:

$$\cos(qd)=\cos(\bar{k}d)-\frac{2\sin^2[(k_1a_1-k_2a_2)/2]}{\sin(k_1a_1)\sin(k_2a_2)}\sin(n_1k_1a_1)\sin(n_2k_2a_2) \qquad (3.23)$$

with the "average" $\bar{k}$ given by:

$$\bar{k}=\frac{n_1k_1a_1+n_2k_2a_2}{n_1a_1+n_2a_2} \tag{3.24}$$

and thus to separate the geometrical contribution from the physical ones. For acoustic frequencies, we could previously show the validity of this approach because $k_1 \cong k_2$. For optic frequencies, k_1 is usually very different from k_2. The energy splitting between the optic bands of two different III–V compounds is usually of the same order or even larger than the width of the bands. Thus, the perturbative approach is inadequate. At frequencies belonging to the optic band of *AB*, k_2 can even be complex when these frequencies fall out of the optic branch of *AC*. The corresponding displacements are then confined in the *AB* layers.

Two different behaviors actually appear corresponding to both sets of dispersion curves presented in Fig. 3.13. In the most frequent one, which is relevant to the GaAs/AlAs system, the two optic bands are well separated and all the superlattice modes constructed from these bands are confined either to the *AB* or to the *AC* layers (Fig. 3.13a). In the second case, which corresponds to the InAs/GaSb system and, with some approximation, to the GaAs/$Ga_{1-x}Al_xAs$ system, the two optic bands partially overlap and some optic modes display a confined character while some others propagate (Fig. 3.13b). Whereas the latter case must be treated exactly by solving (3.22), the former (strong confinement behavior) is suitable for an approximation "orthogonal" to the one used for elastic properties. One can treat the confined vibrations as *perfectly* confined, by making the imaginary part of the complex wavevector in the barrier (i.e. the layer where the mode is vanishing) infinitely large. One obtains, after some algebra [3.62]:

$$k_1=\frac{\pi}{(n_1+1)a_1}m \qquad 1 \leqq m \leqq n_1 . \tag{3.25}$$

The modes are then simply standing waves of the *XAB … ABX* finite chain where the *X*s are infinitely heavy atoms. This approximation appears to be extremely good when one compares the results with the numerical solution of (3.22). A similar comparison, illustrated in Fig. 3.14, has been performed in [3.63] using the results of Molinari's model [3.64]. Some small disagreement can be noticed for large values of m: the corresponding modes being less perfectly confined when calculated with (3.22). Even if for these m values the penetration depth becomes clearly larger than one interatomic distance, the perfect confinement approximation still provides an excellent estimate of the mode frequencies.

The idea of treating the optic phonons in GaAs/AlAs superlattices as perfectly confined is actually rather old and gave rise to numerous theoretical considerations in connection with the so-called slab modes. Already in [3.65] the confined frequencies were analyzed by analogy with the properties of a particle

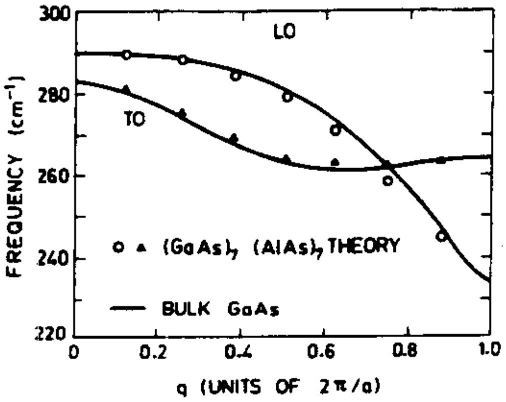

Fig. 3.14. Comparison between *calculated* GaAs-type TO and LO superlattice modes frequencies plotted as a function of $m\pi/a(n_1+1)$ and the corresponding reference bulk GaAs dispersion curves. From [3.63]

confined to a small box or a vibrating string with clamped ends, i.e., with the following relation:

$$k=\frac{\pi}{d_1}m\,,\quad m=1,2,3,\ldots \tag{3.26}$$

where d_1 is the thickness of the layer (size of the box or string). This relation has been used in several works [3.66a, b] and constitutes a reasonable approximation to the results of solving (3.22). However, it becomes questionable for small layer thicknesses where the difference between d and $(n_1+1)a$ [i.e. between (3.25) and (3.26)] is no longer small, as pointed out in [3.62]. In this case, the microscopic details of the thin vibrating layer and of the interface conditions have to be taken into account. The same conclusion was drawn for isolated thin GaAs layers by *Kanellis* et al. [3.53]. These authors treat in detail the lattice dynamics of isolated slabs using a rigid ion model with second neighbor short range forces and Coulomb long range forces evaluated by using a two-dimensional version of Ewald's summation method. They demonstrated that the optical modes of vanishing in-plane wavevector can almost be described as "small box modes". Some discrepancies, however, appear due to boundary conditions. In the isolated layer case, free displacement of the surface atoms has to be imposed instead of clamped neighboring atoms, as done for superlattices. This boundary condition also forces the transformation of some bulk modes into true microscopic surface modes, for which the displacement is maximum near the surface. These modes decay within a few lattice constants from the surface.

Let us now return to the alternating linear chain model in the case of overlapping optical bands. The corresponding dispersion curves are shown in Fig. 3.13b together with the displacement patterns of a confined and a propagating optic mode (Fig. 3.13c). The band ordering in this case is very similar to the one encountered in the study of electronic properties of superlattices, as already pointed out in [3.67]: in a finite energy range the modes are confined to potential wells and above the top of the potential barrier they become propagative. Thus, the notion of an "optic-phonon quantum well" is

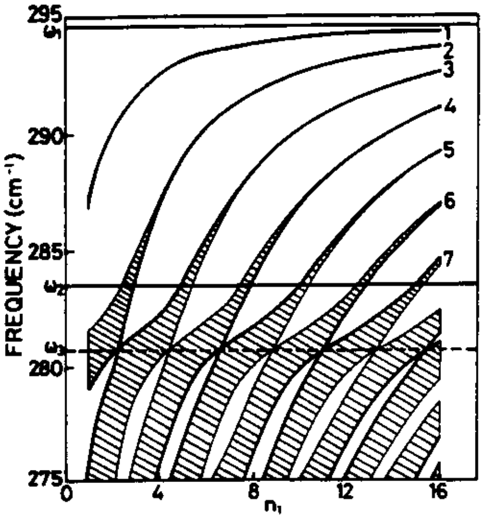

Fig. 3.15. Variation as a function of the well thickness n_1 of the highest allowed frequency bands calculated using an $(AB)_{n_1}/(AC)_5$ alternate linear chain. The bulk effective parameters are fitted to describe the GaAs-type optic modes in a GaAs/GaAlAs structure. From [3.67]

introduced. In Fig. 3.15 we show the upper optic mode frequencies of a typical alternating linear chain as a function of the well thickness n_1 for a fixed value of the barrier thickness n_2. The effect of confinement increases with decreasing n_1, a fact which is well known for electronic states, inducing a shift of the optical modes towards lower frequency. A single confined mode ($n=1$) persists, whatever the width and the depth of the well, whereas the others progressively couple together across the barriers as their frequencies approach the top of the barrier, and become propagative beyond. Their dispersion curves then display minigaps and minibands. At the frequency ω_3, pairs of upper and lower band extrema cross without interacting since they are of different symmetries (different parity). For instance, the zone center modes are alternately symmetric (m even) and antisymmetric (m odd) relative to each midlayer plane.

As mentioned earlier, interface modes never appear in the *AB*/*AC* linear chain. On the other hand, they have been predicted for the *AB*/*CD* sequence [3.40] in the special case of InAs/GaSb structures. This pair of compounds is favorable to the emergence of such modes since one can demonstrate that they easily appear when the two optic bands strongly overlap. If such conditions are verified, the interface vibration which corresponds to a "wrong bond", to be specific a GaAs bond in GaSb/InAs structures, is fairly similar to both the gallium local mode in InAs and an arsenic local mode in GaSb. It thus becomes a common local mode and can be strongly localized at the interface. Another type of localized mode, namely a surface mode appearing in semi-infinite structures, has been described within different simple theories and, in particular, within the alternating diatomic linear chain model [3.68]. Surface modes are predicted in the gaps of the dispersion relations of bulk constituents of the infinite superlattice. Whereas the surface optic modes are localized near the surface in a manner similar to that of the interface modes near interfaces, low frequency surface modes corresponding to acoustic minigaps lie very close to the band edges and are weakly bound to the surface. The propagation properties of such surface elastic waves in the layer plane have been extensively studied using continuous three-dimensional models [3.68] which give evidence of the layering effect on the various types of surface acoustic waves.

Except in the last paragraph, we have only considered vibrations propagating along the superlattice axis because they are the only ones involved in almost all of the published experimental results and also because they are by far the easiest to model. One-dimensional models are indeed unable to account for propagation perpendicular to the superlattice axis. Three-dimensional lattice dynamics is thus unavoidable if one wants to tackle the problem of in-plane superlattice vibrations. Three-dimensional microscopic calculation have been performed rather recently for small period superlattices of GaAs – AlAs [3.35]. The few experimental results involving in-plane vibrations have been analyzed using macroscopic treatments of the layering effect on the electromagnetic field associated with the polar optical vibrations. They will be the topic of the next subsection.

3.2.4 The Effect of Layering on the Macroscopic Field: Interface Modes

In polar crystals, the zone center longitudinal-transverse (LO – TO) splitting is well known to arise from the association of a macroscopic electric field with the zone center LO mode [3.69]. Whereas a correct treatment, taking into account the polaritonic effect, yields zone center properties consistent with symmetry considerations (see Fig. 2.10 of [3.10]), the retardation effect in the long range Coulomb forces for finite k is generally neglected, however, an approximation which leads to a good description of the optic dispersion curves down to very small finite values of k, ($k > 2\pi/\lambda$, where λ is the *reststrahlen* wavelength in the medium). This was illustrated for superlattices in the early work of *Tsu* and *Jha* [3.38] who calculated the polaritonic effect on vibrations along the growth axis of a GaAs/AlAs structure. Since the experimental results are mainly obtained by Raman backscattering, which involves phonons with a large wavevector as compared with those in the region of strong polaritonic interaction, further theoretical work in this field has systematically neglected the retardation effect. Calculations involving retardation have been recently presented in [3.70] for the case of free carrier plasmons which is susceptible to generalization to polar phonons [3.70a].

The first reference to the dielectric modulation in superlattices and its effects on Raman spectra was made by *Merlin* et al. [3.71] to explain the emergence near resonance of an additional peak between TO and LO modes. They assigned this peak to an optical mode of an "effective medium" propagating in the plane of the layers, activated in Raman backscattering by an unidentified relaxation of the selection rules. To describe the frequency of the mode, they derived the anisotropic superlattice dielectric constant from those of the bulk constituents by imposing interface continuity conditions for the electric field (continuity of

E_x, E_y) and displacement (continuity of εE_z). The axial and in-plane components of the dielectric constant of the "effective medium" then read:

$$\varepsilon_z = \frac{\varepsilon_1 \varepsilon_2 (d_1 + d_2)}{\varepsilon_2 d_1 + \varepsilon_1 d_2} = \langle \varepsilon^{-1} \rangle^{-1} , \qquad (3.27)$$

$$\varepsilon_{x,y} = \frac{\varepsilon_1 d_1 + \varepsilon_2 d_2}{d_1 + d_2} = \langle \varepsilon \rangle .$$

Within this model the zeros of ε_z and the poles of $\varepsilon_{x,y}$ correspond, respectively, to longitudinal and transverse modes propagating along the superlattice axis; these are basically the confined modes discussed in Sect. 3.2.3. Their frequencies coincide with the bulk values. This is a specific feature of the macroscopic approaches which neglect dispersion. Thus, their validity becomes questionable for small layer thicknesses. Additional propagating modes appear when:

$$\begin{aligned} d\langle \varepsilon \rangle &= d_1 \varepsilon_1 + d_2 \varepsilon_2 = 0 \\ d\langle \varepsilon^{-1} \rangle &= d_1/\varepsilon_1 + d_2/\varepsilon_2 = 0 . \end{aligned} \qquad (3.28)$$

These obviously correspond to LO and TO modes of an effective average medium, propagating in the layer plane.

The corresponding frequencies lie between the TO and LO bulk frequencies. For $d_1 = d_2$, these two solutions become degenerate and satisfy the following equation:

$$\varepsilon_1 = -\varepsilon_2 \qquad (3.29)$$

which is the standard equation for modes localized at the interface between semi-infinite materials in the absence of retardation [3.71].

Merlin et al. [3.71] assigned an additional peak observed in the Raman spectra of GaAs – GaAlAs superlattices to a solution of (3.28) and described the corresponding mode as the long wavelength limit of bulk optic modes propagating in the plane of the superlattice layers. They also noticed the connection with modes localized at and propagating along the interface between semi-infinite media. This point of view has been shown to be basically correct [3.55].

As mentioned before, the bulk optic modes in GaAs/AlAs superlattices are strongly confined in one type of layer and their frequencies can be described using a single layer model. In the macroscopic approach, where the dispersion is neglected, the small differences due to details at the interface [e.g., (3.25)] disappear. With this caveat, it is justified to use a single-slab electrostatic model [3.72] to analyze the bulk-confined optic modes whereas the more sophisticated models dealing with the complete layered dielectric medium [3.73] allow analysis of the interface modes. We follow the simple treatment given in [3.21] to describe the basic features of these models.

We proceed with the detailed mathematical treatment of the dielectric model which leads to interface and confined modes. In this model, the properties of the bulk materials 1 and 2 are solely represented by the frequency-dependent dielectric constant:

$$\varepsilon_{1,2}(\omega)=\varepsilon_{1,2}^{\infty}\frac{\omega^2-\omega_{\mathrm{L}1,2}^2}{\omega^2-\omega_{\mathrm{T}1,2}^2}\,, \tag{3.30}$$

where, in principle, ω_{L} and ω_{T} may be made to depend on the wave vector $\boldsymbol{k}$ so as to represent the dispersion of the longitudinal $[\varepsilon_{1,2}(\omega_{\mathrm{L}},\boldsymbol{k})=0]$ and transverse $[\varepsilon_{1,2}(\omega_{\mathrm{T}},\boldsymbol{k})=\infty]$ frequencies. We shall neglect this dependence unless otherwise specified.

In the absence of retardation, the electric field (displacement) in each medium can be represented as the sum of a curl-free and a solenoidal part [3.21], i.e., derived from a scalar ϕ and a vector potential $\boldsymbol{V}$:

$$\boldsymbol{E}=-\nabla\phi+\frac{1}{\varepsilon}\nabla\times\boldsymbol{V}\,. \tag{3.31}$$

This field must fulfill the equation:

$$\varepsilon\nabla\cdot\boldsymbol{E}=0 \tag{3.32}$$

which is automatically satisfied by the solenoidal part ($\nabla\times\boldsymbol{V}$). If the term in the scalar potential ϕ is not to vanish it must fulfill Poisson's equation:

$$\varepsilon\nabla^2\phi=0\,, \tag{3.33}$$

which is also automatically satisfied for $\varepsilon(\omega)=0$. According to (3.30) this condition leads to longitudinal modes which can only have non-vanishing fields in one of the two media since, in general, $\omega_{\mathrm{L}1}\neq\omega_{\mathrm{L}2}$. These modes are of longitudinal character, confined either to medium 1 or 2. Another possible solution of (3.32) is obtained for $\nabla^2\phi=0$. As we shall see, this leads to interface modes which propagate along the axis of the superlattice. Concerning the solenoidal term $\nabla\times\boldsymbol{V}$ the continuity of the x,y-components of $\boldsymbol{E}$ and the z-component of $\boldsymbol{D}$ requires that $\varepsilon_1=\infty$ if $\boldsymbol{E}$ is not to vanish in medium 1. This leads, according to (3.30), to transverse modes localized in medium 1. Both localized LO and TO modes so obtained can be made to depend on the $\boldsymbol{k}$ vector defined by (3.25, 26) simply by using $\boldsymbol{k}$-dependent ω_{L} and ω_{T} frequencies in (3.30).

Before treating the interface modes ($\nabla\phi_{1,2}=0$ plus appropriate boundary conditions), we want to discuss some particular properties of the LO modes found through the dielectric formalism. Fourier expansion of ϕ_1 leads to the two families of components:

$$\phi_1(x,z)=\phi_0\mathrm{e}^{\mathrm{i}kx}\cos(qz)\,, \tag{3.34a}$$

$$\phi_2(x,z)=\phi_0\mathrm{e}^{\mathrm{i}kx}\sin(qz)\,, \tag{3.34b}$$

where the dependence on y has been neglected, a rather inconsequential fact. In order to obtain localized modes we must assume that $E_2=0$ and impose the corresponding boundary conditions for E_x and D_z at the interface. For the $\phi_1(x,z)$ of (3.34a) this leads to (assuming that the origin of coordinates is at the center of layer 1):

$$\text{continuity of } E_x\text{: } \mathrm{i}k\phi_0 \mathrm{e}^{\mathrm{i}kx}\cos(qd_1/2)=0\ , \tag{3.35}$$

$$\text{continuity of } D_z\text{: } \varepsilon_1 q\phi_0 \mathrm{e}^{\mathrm{i}kx}\sin(qd_1/2)=0\ , \tag{3.36}$$

and similar equations for the case of (3.34b). Equation (3.36) leads to $\varepsilon_1=0$, i.e., to the frequencies of bulk longitudinal modes. While (3.35, 36), representing the boundary conditions for the electric field, are automatically fulfilled for $\varepsilon_1=0$ and $k=0$, one must also keep in mind that the superlattice is a mechanical system and thus the mechanical displacement of the atoms, $\boldsymbol{u}$, must also be continuous across the boundary. This mechanical displacement is proportional to the electric polarization it generates which, in turn, is proportional to the electric field associated with the vibration. Hence the continuity of u_x is equivalent to that of E_x which we have already imposed in (3.35); that of u_z leads to an equation similar to (3.36) but without the factor ε:

$$q\phi_0 \mathrm{e}^{\mathrm{i}kx}\sin(qd_1/2)=0\ . \tag{3.37}$$

Except for the cases $q=0$ or $k=0$ it is impossible to simultaneously fulfill (3.35) and (3.37). For $k=0$ we find from (3.35)

$$q=\frac{\pi}{d_1}m \qquad m=2,\ 4,\ 6,\ \dots \tag{3.38a}$$

an analogous reasoning for (3.34b) leads to, in the case of $k=0$:

$$q=\frac{\pi}{d_1}m \qquad m=1,\ 3,\ 5,\ \dots \tag{3.38b}$$

Equations (3.38a, b) are equivalent to (3.26) which was derived for one-dimensional models that imply $k=0$. Note that it is reasonable to obtain (3.26) and not (3.25) since the dielectric model is a continuum model in which the boundary conditions are imposed *exactly* at the interface.

The result of (3.38) can also be applied to the case $k\neq 0$ provided k is small compared with the qs of (3.38a, b). Such is the case which applies to phonons excited in optical experiments provided d_1 is not too large. In this case the boundary condition in (3.35) is more stringent than that in (3.37) and the latter can be neglected: the results obtained for $k=0$ remain approximately valid. Ultimately of course, an additional weak field pattern will have to be developed around the interface in order to strictly fulfill (3.37). For most purposes, however, this additional field can be disregarded. For a recent discussion of the somewhat confusing simultaneous role of mechanical and electrostatic boundary conditions see [3.73a].

After illustrating the origin of confined modes with the electrostatic continuum model we discuss the interface modes. They arise by replacing in (3.34a, b) the pure imaginary values of q, ie., by making for ϕ the ansatz:

$$\phi_{1,2}=\phi_0 e^{ikx} e^{\pm Qz} , \tag{3.39}$$

where the origin is chosen to be at an interface. The potential of (3.39) fulfills Laplace's equation (3.33) provided $k=Q$. For a simple interface between semi-infinite media 1 (left) and 2 (right) the sign in front of Q in (3.39) must be chosen so as to avoid unphysical divergences for $z\rightarrow -\infty$ (medium 1) and $z\rightarrow +\infty$ (medium 2). The boundary condition for D_z then leads to (3.29). In the case of a single interface between semi-infinite media it is easy to modify (3.29) so as to include retardation [3.74].

For a periodic array of interfaces, such as that found in a superlattice, linear combinations of both types of solutions in (3.39) are acceptable. We impose electrostatic boundary conditions at each interface and use Bloch's theorem in order to relate the potential ϕ_0 in slab 0 to that in an equivalent slab (n). For this purpose we reintroduce a wavevector component q along z and write:

$$\phi_0(x,z)=\phi_0(x,z)e^{iqnd} . \tag{3.40}$$

As shown in [3.73] this procedure leads to the secular equation:

$$\cos(qd)=\cosh(kd_1)\cosh(kd_2)+\frac{1}{2}\left[\frac{\varepsilon_1}{\varepsilon_2}+\frac{\varepsilon_2}{\varepsilon_1}\right]\sinh(kd_1)\sinh(kd_2) \tag{3.41}$$

[note that (2.20, 21) are equivalent to (3.41)] where q is the axial superlattice wavevector. [Note also the similarity with other equations derived so far, e.g. (3.6, 22)]. The numerical solutions of (3.41) have been studied in detail in [3.73] and compared with experimental results for GaAs/AlAs superlattices in [3.55]. The results are illustrated in Fig. 3.16. For each value of k and q, four different frequencies are obtained which form two different energy bands in the range of the optical modes of each constituent. Their frequencies lie between the TO and LO bulk frequencies.

Some limiting cases of (3.41) can be further treated analytically. Let us first consider the limit of vanishing superlattice wavevector q. The dispersion relation then reduces to the two bands

$$-\frac{\varepsilon_1(\omega)}{\varepsilon_2(\omega)}=\begin{cases}\tanh\left(\dfrac{kd_1}{2}\right)\coth\left(\dfrac{kd_2}{2}\right)\\[2ex] \tanh\left(\dfrac{kd_2}{2}\right)\coth\left(\dfrac{kd_1}{2}\right).\end{cases} \tag{3.42}$$

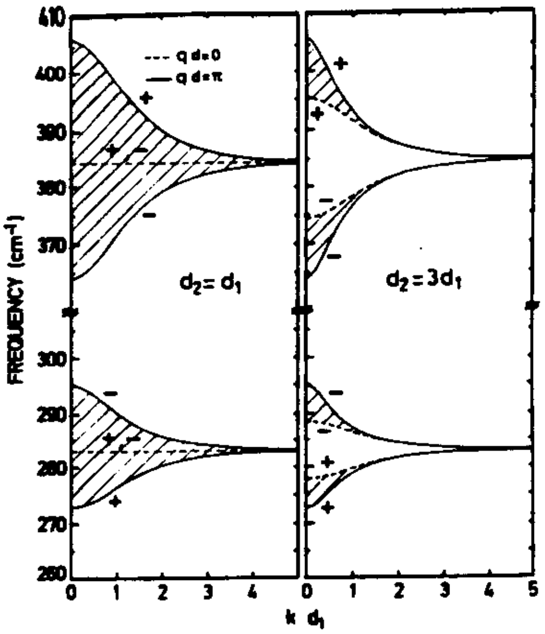

Fig. 3.16. Allowed frequency bands corresponding to the electrostatic interface modes in GaAs/AlAs structures with two different thickness ratios. The *plusses* and *minusses* indicate the parity of the corresponding electrostatic potential relative to the center of the GaAs layers. The *hatched bands* represent the axial dispersion (vs. q) for a given value of the in-plane wavevector k. From [3.55]

For interface bands corresponding both to compound 1 and compound 2, the two solutions of (3.42) lead to the limiting dashed lines of Fig. 3.16 which evidently coalesce for $d_1 = d_2$. In the latter case the interface frequencies are then obtained by solving:

$$\varepsilon_1(\omega) = -\varepsilon_2(\omega)$$

which is again equivalent to the secular equation for the interface between semi-infinite media (3.29).

In this limit ($q = 0, k \to 0$), the superlattice interface modes can be understood in terms of an interaction between equidistant single interface modes, which leads to the formation of collective modes symmetric and antisymmetric with respect to the bisector plane of an individual layer. When $d_1 = d_2$, both components appear to be degenerate, as is the case for zone-center folded acoustic modes for some values of α. Similarly, the symmetric mode belongs either to the upper or the lower branch depending of the relative magnitude of d_1 and d_2.

The limit for vanishing in-plane wavevector k of the $q = 0$ dispersion relation coincides with the early result of *Merlin* et al. [3.71]. In this limit, both solutions only coalesce if both thicknesses are equal. Otherwise, we obtain two frequencies corresponding to (3.28). These modes are then a limiting case of the interface solutions but display a special behavior: the decay length around the interface becomes infinite. These modes are thus not really localized at the interfaces even if their dependence on the dielectric properties of both bulk constituents is a consequence of their "interfacial character". Note also that for $k \to \infty$ (3.41) leads to $\varepsilon_1(\omega) = -\varepsilon_2(\omega)$ regardless of the values of d_1 and d_2, i.e., the condition for interface modes of a semi-infinite slab: for an infinite wavelength along the slab, and infinitesimal decay length, the vibrations of one interface are independent of those of the others. If the background dielectric constants of both constituents are similar and the corresponding bulk frequencies very different we obtain the approximate frequency at the zone edge ($q = \pi/d$):

$$\omega_{1,2}^2 = \frac{(\omega_{\mathrm{T}1,2})^2 + (\omega_{\mathrm{L}1,2})^2}{2} . \tag{3.43}$$

The electrostatic analysis just given has a broad range of applicability. It can be easily generalized to other longitudinal excitations such as plasmons which have been recently observed by Raman backscattering in infinite and finite layered structures [3.75]. To apply this theory to the optic phonons of real superlattices one must examine the validity of the approximations involved.

As concerns bulk modes, the electrostatic approximation predicts, for $k \ll \pi m/d_1$, modes near the LO frequency of the bulk which, accordingly to (3.35, 36), are mainly polarized with the field perpendicular to the layer plane ($E_z \gg E_x$). Likewise, one finds transverse-like modes for $\boldsymbol{E}$ parallel to either x or y. This fact explains the results of *Zucker* et al. [3.54].

For interface modes, the validity is more questionable: the calculated dispersion of interface modes overlaps with allowed bulk modes. This overlap does not take place in the non-dispersive macroscopic model where the optic band is assumed to be perfectly flat. Moreover, the mechanical boundary conditions have not been included [3.73a]. Thus, there is a need for a microscopic treatment of the superlattice vibrations of the type to be discussed in the next subsection [3.35]. Such calculations are only easy to perform for small period superlattices due to the large dimension of the secular equation for larger periods. Work performed for larger period superlattices with simplified lattice dynamical modes, even if not perfectly realistic from the quantitative point of view, should certainly bring new insight to the understanding of the vibrational properties of polar superlattices.

In the case of isolated slabs, microscopic calculations have been performed by several groups. We present here some details relevant to superlattices. The calculations by *Kanellis* et al. for GaAs slabs [3.53] are unfortunately restricted to axial modes. Thus, we must consider older publications devoted to thin slabs of NaCl structure such as those of *Tong* and *Maradudin* [3.51] or *Jones* and *Fuchs* [3.52]. The latter authors, in particular, analyze the in-plane dispersion curves in order to identify the two Fuchs-Kliever surface modes [3.72]. In Fig. 3.17 the predictions of Fuchs and Kliever for the in-plane dispersion together with the nondispersive bulk TO and LO modes are illustrated. Although axial dispersion is precluded by the model, the general trends of the surface modes are rather similar to those of interface modes in superlattices. Depending on the zone center curvature and the width of the real optic bands, these surface modes should or should not cross the whole set of bulk-like

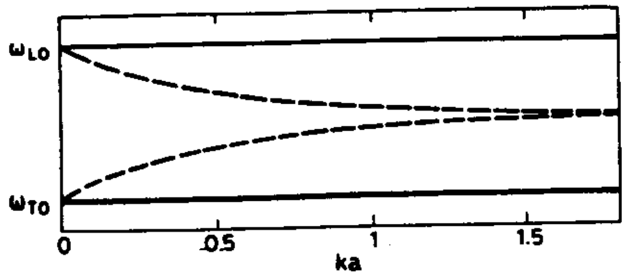

Fig. 3.17. Schematic representation of the in-plane dispersion of the bulk LO and TO modes and of both surface modes as predicted for an isolated slab in the electrostatic approximation. From [3.72]

confined modes before reaching a forbidden energy range. For instance, in the NaCl case, the LO band is very broad and decreases with k, so that no real upper surface mode appears. In the overlap range, couplings between surface and bulk modes of the same parity take place so that some bulk modes display partial surface-like character. Similar conclusions should hold for GaAs/AlAs superlattices where interface modes and bulk quantized ones lie in the same energy range. Due to the axial dispersion of the interface modes, their crossing with the quantized bulk modes will depend on k and the whole dispersion pattern should be very complex [3.76]. The interpretation of some experimental results [3.55] in terms of interface modes and wavevector relaxation will be discussed in Sect. 3.4.

Finally, the presence of a free surface for semi-infinite superlattices, already considered from the mechanical point of view, also imposes special boundary conditions on the electric fields, giving rise to surface electrostatic modes of the whole superlattice. These modes have been observed recently by Electron Energy Loss Spectroscopy (EELS) [3.77]. To analyze their frequencies, the authors of [3.77] introduce an original formulation of the dispersion relation of interface and surface modes which, in particular, allows the study of non-periodic stackings of layers.

3.2.5 Full Three-Dimensional Microscopic Calculations for Superlattices

a) Symmetry Considerations

We start this subsection with some considerations of the symmetry properties of zinc-blende-type superlattices (e.g. $(GaAs)_{n_1}-(AlAs)_{n_2}$) grown along [001]. We first note that the primitive cell of the superlattice is composed of n_1 (n_2) primitive cells of constituent 1 (2). Two space groups are possible for such superlattices depending on whether n_1+n_2 is even or odd. In the even case the translation lattice of the superlattice is primitive tetragonal, with space group $P\bar{4}m2$ (D_{2d}^5 in Schönfliess notation) while in the odd case it is body centered tetragonal, with space group $I\bar{4}m2$ (D_{2d}^9) [3.78]. The point group is in both cases $\bar{4}m2$ (D_{2d}). We give here for future reference, the character table of this group [3.79]:

	E	C_2	$2S_4$	$2C_2'$	$2\sigma_d$	
A_1	1	1	1	1	1	$x^2+y^2,\ z^2$
A_2	1	1	1	-1	-1	$(x^2-y^2)z$
B_1	1	1	-1	1	-1	x^2-y^2
B_2	1	1	-1	-1	1	$xy,\ z$
E	2	-2	0	0	0	$xz, yz;\ x, y$

(3.44)

where C_2 and C_2' represent two-fold rotations, the former about [001], the latter about either [100] or [010]. The symmetry elements $2\sigma_d$ are the two (100) and (010) reflection planes, while $2S_4$ are improper fourfold rotations about [001]. The last column in (3.44) gives the simplest combinations of the coordinates which belong to the corresponding representation: they are useful for figuring out optical (Raman, IR) selection rules: transverse phonons propagating along the superlattice axis have E-symmetry, their longitudinal counterparts either A_1 or B_2 symmetries (3.55, 56).

We show in Fig. 3.18 the Brillouin zone of the superlattice with $n_1=n_2=1$. It is isomorphic to that for other values of n_1, n_2 provided n_1+n_2 is even: one simply has to change the $\Gamma-Z$ length to ΓX divided by n_1+n_2. For n_1+n_2 odd we must use the Brillouin zone of the body centered tetragonal lattice, which can be found in standard textbooks [3.80].

b) Generation of the Dynamical Matrix from that of the Bulk Constituents

As we have seen, the primitive cell of the superlattice, SPC, is composed of $n_1+n_2=N_0$ primitive cells (PC) of the original bulk crystals. Its volume V_s is thus

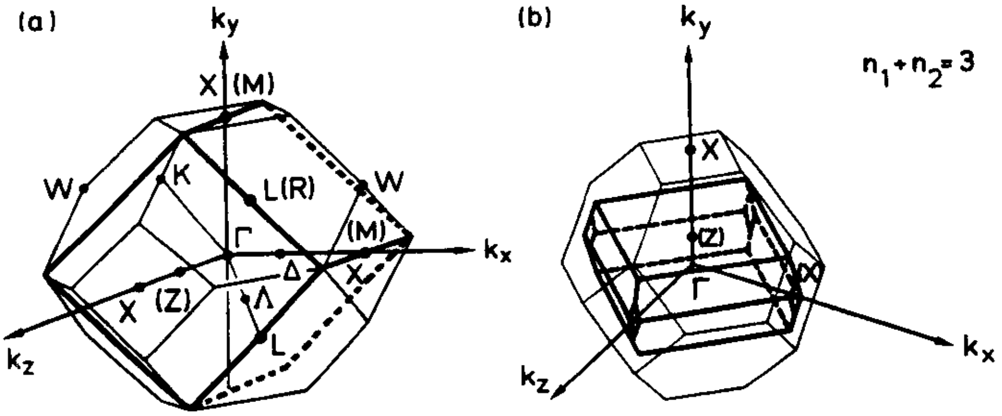

Fig. 3.18. (a) Brillouin zone (BZ) of a [001] $(GaAs)_1(AlAs)_1$ superlattice (*thick line*) inscribed in the BZ of the bulk crystal (*thin line*). The special symmetry points are given outside (*inside*) parentheses for the bulk (superlattice). (b) Same as Fig. 3.18a but for a superlattice with $n_1=n_2=3$ (BZ of body centered tetragonal lattice)

equal to $N_0 V_0$, where V_0 is the volume of the bulk PC. The folded Brillouin zone of the superlattice (SBZ) has a volume equal to $(2\pi)^3/N_0 V_0$, i.e., that of the bulk crystal divided by N_0. Hence, if we describe a bulk crystal using only the translational symmetry of the superlattice, each band of the original BZ gives rise to N_0 folded bands. They are obtained by solving the corresponding secular equation for the dynamical matrix of the bulk:

$$|\omega^2 \delta_{\alpha\beta} - D^0_{\alpha\beta}(\kappa\kappa'|\boldsymbol{b}_m + \boldsymbol{k})| = 0\ , \tag{3.45}$$

where α, β represent cartesian components, κ the two atoms of the bulk PC, $\boldsymbol{b}_m$ the N_0 reciprocal lattice vectors of the superlattice involved in folding the bulk BC, and $\boldsymbol{k}$ a vector of the SBZ. $\underset{\approx}{D}^0$ can be used to generate the dynamical matrix of the superlattice $\underset{\approx}{D}^{\mathrm{s}}$ in the following way. We first construct a block diagonal $\underset{\approx}{D}^{\mathrm{b}}$ of dimensionality N_0-times that of D^0 (i.e., $6(n_1+n_2)$) [3.33]:

$$D^{\mathrm{b}}_{\alpha\beta}(\kappa\kappa';\, mm'\boldsymbol{k}) = D^0_{\alpha\beta}(\kappa\kappa'/\boldsymbol{b}_m + \boldsymbol{k})\delta_{mm'}\ . \tag{3.46}$$

The matrix $\underset{\approx}{D}^{\mathrm{b}}$ must be related to that of the bulk material in the standard superlattice representation $\underset{\approx}{D}^{\mathrm{s}}$ (i.e., using instead of two atoms κ, all atoms of the SPC) through a unitary transformation since it gives the bands of the superlattice in the SBZ.

$$\underset{\approx}{D}^{\mathrm{s}} = \underset{\approx}{G} \cdot \underset{\approx}{D}^{\mathrm{b}} \cdot \underset{\approx}{G}^{-1}\ . \tag{3.47}$$

Kanellis [3.33] finds for the matrix elements of $\underset{\approx}{G}$:

$$G_{\alpha\beta}(\kappa\kappa' mm') = \sqrt{N_0}\exp[\mathrm{i}\boldsymbol{b}_m \cdot \boldsymbol{r}(\kappa, s)]\delta_{\alpha\beta}\delta_{\kappa\kappa'}\ , \tag{3.48}$$

where s labels the bulk PCs within the SPC.

Once the matrix $\underset{\approx}{D}^{\mathrm{s}}$ for the bulk in the superlattice representation is found with (3.47) it becomes easy to introduce the superlattice modulation, i.e., to change atomic masses and interatomic force constants. The former is the easiest to vary. This can be achieved following the prescription [3.33]

$$D^{\mathrm{s}}_{\alpha\beta}(\bar{\kappa}, \bar{\kappa}' \ldots) \rightarrow \left(\frac{M_\kappa M_{\kappa'}}{M_{\bar{\kappa}} M_{\bar{\kappa}'}}\right)^{1/2} D^{\mathrm{s}}_{\alpha\beta}(\kappa, \kappa'; \ldots)\ , \tag{3.49}$$

i.e. by by renormalizing the matrix elements of $\underset{\approx}{D}^{\mathrm{s}}$ with the square root of the new masses of atoms κ and κ' (which now become $\bar{\kappa}$ and $\bar{\kappa}'$).

Kanellis has applied this technique to $(\mathrm{GaAs})_1(\mathrm{AlAs})_1$ superlattices grown both along [001] and [111]. The calculations were performed with an 11-parameter Born-von Karman rigid ion model which included first and second nearest neighbors interaction and an effective ionic charge [3.81]. Unfortunately, in [3.33] only results for $\boldsymbol{k}$ along [001] and no information about "interface" modes (propagating perpendicular to [001]) is given. This information should be obtainable within this formalism.

A somewhat similar calculation has been performed for $n_1 = n_2 = 1$ and $n_1 = n_2 = 2$) in [3.82]. In this work a rigid ion model with *central forces* up to third neighbors was used (four force constants). Starting values for these force constants were taken from the bulk. They were then adjusted and modulated so as to fit observed values in these superlattices. Calculations were also only performed for $\boldsymbol{k} \cong 0$ along [001].

c) Off-Axis Propagation

The most complete three-dimensional calculations have been performed for $[\mathrm{GaAs}]_{n_1}[\mathrm{AlAs}]_{n_2}$ superlattices by *Richter* and *Strauch* [3.35, 35a]. They include calculations for $n_1 = n_2 = 1, 2, 3, 4, 5$ and also for $(n_1, n_2) = (10, 6), (6, 10), (5, 4), (1, 7), (2, 6)$, and $(3, 5)$. The thesis in [3.35] contains not only the dispersion relations for some of these superlattices for $\boldsymbol{k}$ along and perpendicular to [001] but also a large amount of information concerning eigenvectors, in particular comparison with interface modes (optical phonons) and with partly confined *acoustic* modes which also propagate perpendicular to [001] (related to the Lamb modes and Love modes of single slabs [3.83]). The authors of [3.35] chose as a lattice dynamical model the Valence-Overlap Shell Model (VOSM) [3.84] with 10 parameters fitted to neutron data for GaAs. The same model was used for the force constants involving Al instead of Ga (i.e., only the masses were changed).

Figure 3.19 shows the results obtained by Richter and Strauch for $n_1 = n_2 = 1, 2, 3, 4$ along various high symmetry directions of the SBZ (Fig. 3.18) parallel and perpendicular to the growth axis. A number of interesting trends can be recognized in these figures. For $\boldsymbol{k}$ along [001] ($\Gamma \to Z$ line) one sees the confined modes predicted by (3.25). Examples for a $n_1 = n_2 = 5$ superlattice can be seen in Fig. 3.20. Figure 3.20b shows clearly the correctness of (3.25) and the inaccuracy of (3.26): The Ga atoms immediately outside the interface stand still while the As atoms at the interface move.

In Fig. 3.21 we show some of the corresponding eigenvectors calculated in [3.35] for modes propagating along [100] (i.e. $k_z \neq 0$). In the optical region we find the characteristics of the interface modes discussed in Sect. 3.2.4 (both components of the displacement u_z and u_x are given). Note, however, that the origin of the exponential decay for the AlAs-like modes is shifted from the interface to the nearest Al atoms, no doubt an effect of the mechanical boundary conditions. Only the antisymmetric (B_2-like for $k_x \to 0$) interface modes are shown. Note also that the acoustic-like Love and Lamb modes are predominantely localized in the GaAs.

The interface optical modes can also be recognized in Fig. 3.19 for $\boldsymbol{k}$ vectors perpendicular to [001], e.g., along the ΓX and ΓM directions (see modes labeled "I"). The dispersion relations along these directions are indeed remindful of those calculated for the interface modes with the electrostatic model for $q = k_z = 0$ (Fig. 3.16) and $d_1 = d_2$. Contrary to the predictions of the electrostatic model, however, the odd and even I modes are slightly split for $k_{x,y} \to 0$. We also note that the dependence on the direction of $\boldsymbol{k}$ for $\boldsymbol{k} \to 0$, associated with the

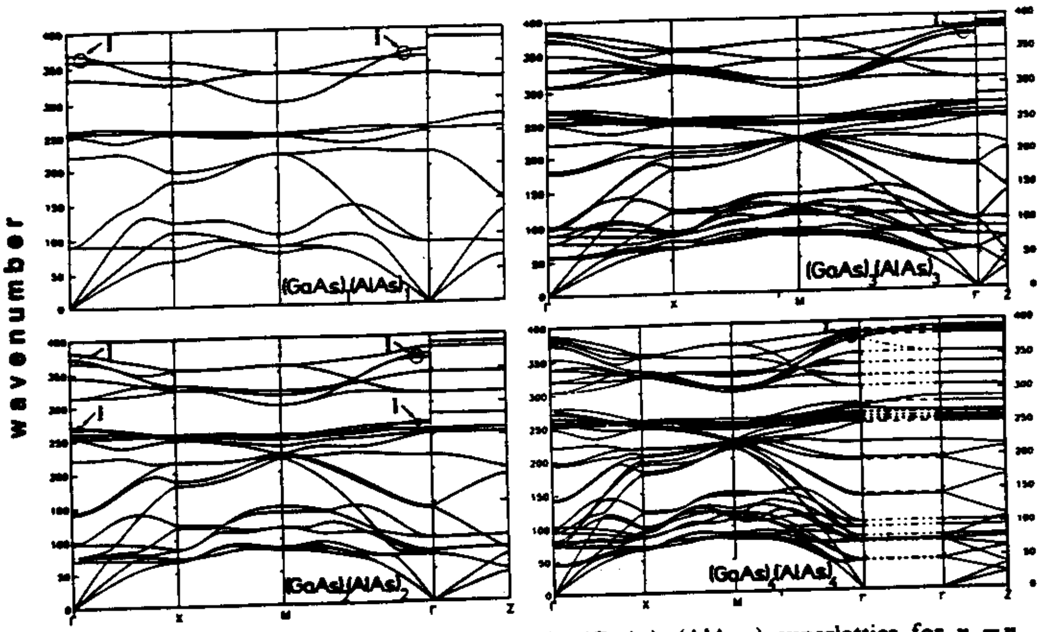

Fig. 3.19. Dispersion relations of phonons in (GaAs)$_{n_1}$(AlAs$_{n_2}$) superlattice for $n_1 = n_2 = 1, 2, 3, 4$ calculated by *Richter* and *Strauch* ([3.35] and private communication). "I" indicates interface modes propagating parallel to the layer planes. For $n_1 = n_2 = 4$ we show the angular dispersion ($\Gamma \dots \Gamma$) of interface modes for $k \simeq 0$

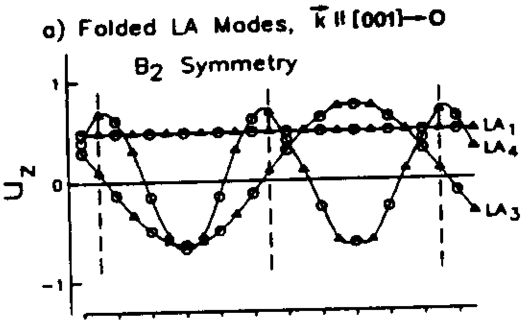

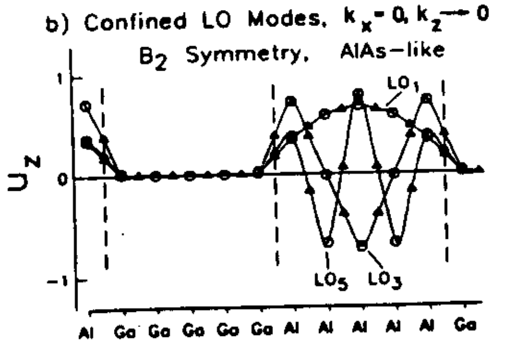

Fig. 3.20. Displacement pattern u_z of folded (acoustic) and confined (optical) modes of B_2 symmetry (3.44) for a (GaAs)$_5$(AlAs)$_5$ superlattice. The triangles represent u_z for the As atoms, with the sign reversed for the optical modes, while the circles represent u_z for Ga or Al. From [3.35]

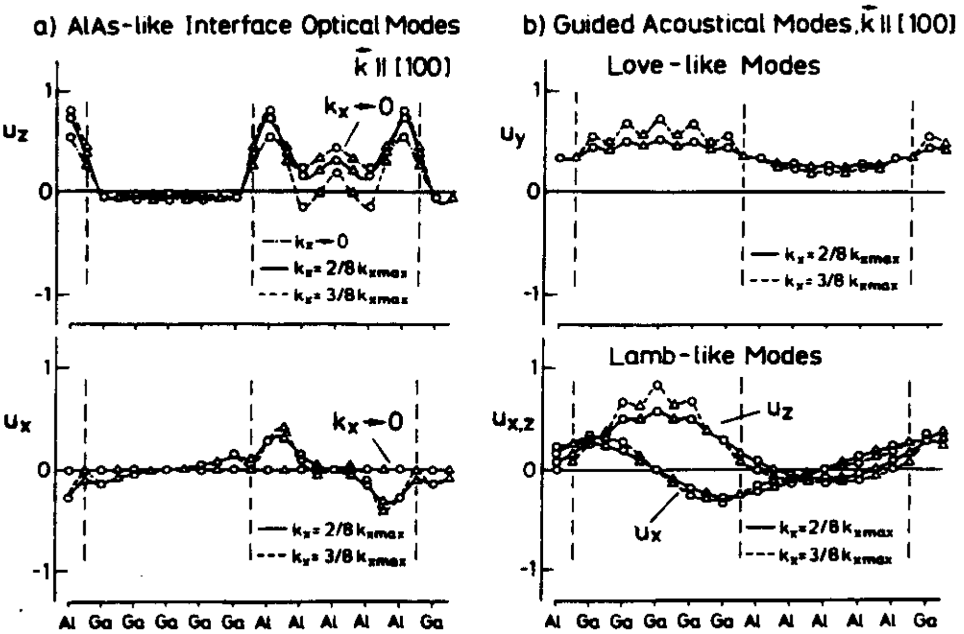

Fig. 3.21. Eigenvectors for modes propagating along [100] in a $(GaAs)_5(AlAs)_6$ superlattice grown along [001]. The optical modes are AlAs-like interface modes while the acoustical ones correspond to Love and Lamb modes of a slab. For the optical modes the signs of the displacements of cations and anions have been reversed. From [3.35]

appearance of interface modes, is clearly observable for the first confined LO and TO modes ($m = 1$ in (3.25)). For m even no such dependence occurs while for m odd > 1 the calculated dependence is small. This also agrees qualitatively with the electrostatic model: for $q = k_z \gtrsim \pi/d$ and k_x small the frequencies of the interface modes tend to the LO and TO frequencies found for $k = 0$ and $q = k_z \neq 0$.

Another interesting observation that can be made in Fig. 3.19 is the variation of the LO − TO splitting for $k \parallel [001] \to 0$ (ΓZ direction near $k = 0$) with $n_1 = n_2$.

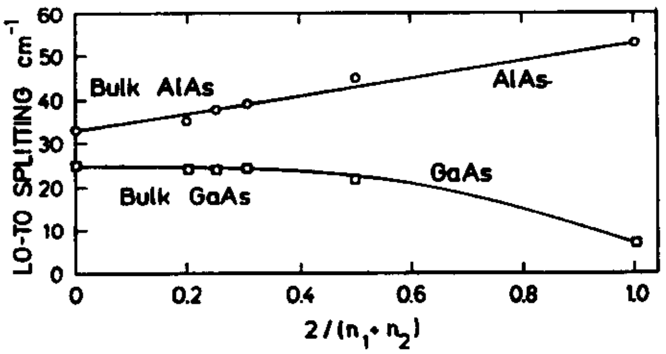

Fig. 3.22. LO-TO splitting of the GaAs- and AlAs-like modes of $(GaAs)_{n_1}$-$(AlAs)_{n_2}$ superlattice vs. $2/n_1+n_2$. From the calculations of [3.35]

As shown in Fig. 3.22 this splitting becomes smaller for GaAs and larger for AlAs as the period of the superlattice decreases. This striking effect seems to have been qualitatively confirmed by experiments [3.82]. It is related to the fact that the LO – TO splitting of bulk AlAs increases with increasing k while that of GaAs decreases (the LO and TO bands actually cross with increasing k_x, see Fig. 3.1), a difference which is simply due to the fact that the mass of Al is much smaller than that of Ga: At the X point for the LO modes only Ga moves while at Γ both Ga and As move. Thus, the effect of replacing Ga by Al is larger at X than at L.

3.2.6 Conclusions

In this section we have presented the different approaches which have been used to describe the lattice dynamics of superlattices: elastic, linear chain, electrostatic models, and full three-dimensional calculations. These approaches provide a rather good description of the axial vibrations in periodically layered polar structures. The primary result is the coexistence of propagating modes (mainly acoustic) and modes strongly confined in one type of layers (mainly optic). Although a complete three-dimensional description is only available for small period superlattices, an approximate macroscopic description of the large period case has been developed to explain the limited experimental information which exists about out-of-axis superlattice vibrations. The concepts of interface optical modes and Lamb and Love acoustical modes have been introduced.

3.3 The Light Scattering Activity of Superlattice Vibrations

3.3.1 Experimental Methods

The usual methods to study lattice vibrations involve one of three types of spectroscopies:

- far-infrared spectroscopy (reflectivity, transmission)
- inelastic neutron scattering
- light scattering (Brillouin or Raman spectroscopy)

Actually, almost all experimental results available for superlattices have been obtained by means of light scattering. Before describing the mechanisms involved in the case of superlattices, we shall briefly compare the different techniques mentioned above.

Far-infrared spectroscopy has been little used to study vibrations of III–V compounds since the development of high power visible lasers for Raman spectroscopy [3.84a]. Besides technical difficulties and only a moderate frequency resolution, another drawback of this technique is the limited possibility to vary the experimental conditions. For instance, the incident frequency is fixed for each vibration probed. In contrast, visible light scattering is a non-linear process involving one (or more) phonons and two photons. One can thus vary the incident photon frequency and probe the variation of the scattering efficiency. This gives information on electron-phonon interaction [3.10]. Nevertheless, because far-infrared spectroscopy and light scattering involve different selection rules, they can provide complementary information. However, for the non-centrosymmetric III–V compounds and their superlattices all vibrations at the BZ center are Raman active for some polarization configurations and far-infrared spectroscopy may seem superfluous. Due to limitations in the available polarization configurations and sample orientations, however, some Raman active modes cannot be observed. For instance, GaAs/AlAs samples have only been available till recently for [001] oriented substrates. Backscattering experiments on [001] faces are not sensitive to transverse vibrations. Therefore, studies in the far-infrared would be very useful [3.84a]. The infrared reflectance work of [3.85] was performed for GaAs/$Al_{0.35}Ga_{0.65}As$ superlattices of rather large period. It was interpreted on the basis of effective medium theory and yielded no microscopic information on superlattice vibrations.

As concerns neutron scattering, its main advantage lies in the neutron wavelength, which is on the order of a few Å instead of a few μm as for photons. As a consequence, with neutrons one can probe the whole Brillouin zone of crystals with lattice constants of a few Å, while, as discussed in Sect. 3.1, photons can only probe near the zone center. The application of inelastic neutron scattering is, however, limited by the very small magnitude of the scattering cross sections and neutron fluxes available. Large samples are therefore needed, a fact which hinders the application of neutron scattering to epitaxial layers and superlattices. Also, the frequency resolution of neutron scattering is never better than a few cm^{-1}, i.e., worse than for light scattering and clearly inadequate for the study of superlattice vibrations. Moreover, as we will show in Sect. 3.4, the superlattice mini-zone may be very small (comparable with a typical photon wavevector). For all these reasons, and also for its relative experimental simplicity, light scattering has been and remains the preferred technique to probe superlattice vibrations.

3.3.2 Some General Properties of Light Scattering

In the classical description of the light scattering process, the incident light at frequency ω and the lattice vibrations at frequency Ω cannot efficiently interact directly: their interaction takes place through the electronic susceptibility [3.10]. In the adiabatic or quasi-static approximation, the electronic susceptibility is modulated at the frequency Ω by the atomic displacements. The radiation, emitted by the electronic polarization induced by the incident light, is also modulated by the phonon and contains oscillating components at frequencies $\omega_i \pm \Omega$. In a light scattering experiment, the frequency shift between incident and scattered light provides the phonon frequencies, whereas their relative intensities are related to the scattering efficiency. This quantity reflects two multiplicative contributions: the average squared amplitude (actually the matrix element) of the atomic displacements and the squared magnitude of the derivative of the electronic susceptibility relative to the phonon displacement. In the case of thermal vibrations, the first contribution is proportional to $n(\omega)$ for anti-Stokes ($\omega_s = \omega_i + \Omega$) and to $n(\omega)+1$ for Stokes scattering ($\omega_s = \omega_i - \Omega$), where $n(\omega)$ is the Bose-Einstein population factor at energy ω and temperature T. The analysis of the second contribution, involving the so-called Raman susceptibility, will be the main topic of this section. We shall leave resonance effects, i.e., the strong enhancement in Raman susceptibility in the neighborhood of electronic interband energy gaps, for Sect. 3.5.

In crystalline solids, the analysis of the Raman activity is usually done in two steps. One first derives by symmetry considerations the non-vanishing independent components of the Raman tensor. No reference is made to the microscopic details of the mechanism involved. In the second step one calculates the Raman activity in the framework of a model for the modulated susceptibility. Before developing the case of superlattices of zincblende-type bulk compounds, we must recall the selection rule, mentioned in Sect. 3.1, which expresses the wavevector conservation during the scattering process:

$$\boldsymbol{k}_s = \boldsymbol{k}_i \pm \boldsymbol{q} \, , \tag{3.50}$$

where $\boldsymbol{k}_s$, $\boldsymbol{k}_i$, and $\boldsymbol{q}$ are wavevectors inside the sample of the scattered and incident light and the phonon involved, respectively and $-(+)$ applies to Stokes (anti-Stokes) scattering. The vectors of (3.50) are confined to the first (mini)-Brillouin zone (SBZ).

Due to the very large value of the photon frequency of visible light ($\sim$20.000 cm^{-1}) as compared to that of a typical phonon ($\sim$200 cm^{-1}), the difference between k_i and k_s is often neglected, and one obtains:

$$k_i = \frac{2\pi n_i}{\lambda_i} \cong k_s = \frac{2\pi n_s}{\lambda_s} \, , \tag{3.51}$$

where n_i (n_s) is the refractive index of the sample at the incident λ_i (or scattered λ_s) wavelength: $n_i \cong n_s \cong n$. Depending on the experimental configuration, the magnitude of the allowed phonon wavevector lies between $\sim$0 (forward scattering) and $4\pi n/\lambda_i$ (backscattering). Its maximum value is much smaller (by a factor of 100) than the typical Brillouin zone extension of a bulk III–V compound and one usually considers that light scattering experiments probe only zone center excitations. Raman selection rules are thus determined using the zone center (Γ) symmetry. Taking into account the finite value of $\boldsymbol{q}$ will relax some selection rules: forbidden lines become allowed and their intensity increases when $\boldsymbol{q}$ moves away from zone center. This feature is important for the acoustic modes: at the zone center they correspond to a rigid displacement of the whole crystal which evidently induces no Raman scattering (translational invariance). To treat this $\boldsymbol{q}$-dependent scattering process in the vicinity of $q=0$, one introduces a new term in the modulated susceptibility which describes the effect of the strain on the susceptibility ($\partial\chi/\partial e$). The resulting phenomenon is called Brillouin scattering. This term actually does not give rise to a q-dependent scattering intensity since the Bose population factor diverges for $\omega\rightarrow 0$ like q^{-1}. Taking also into account the proportionality of the phonon amplitude to $q^{-1/2}$ and that of the strain to q, we find a scattering efficiency independent of q.

Another case of q-dependent processes is encountered for the LO component of IR-active phonons near resonance: intra-band Fröhlich terms, which give a vanishing contribution at the zone center, become large (see Sect. 3.5 and [3.10]).

To determine the dipole (q-independent) allowed modes at the zone center, one must find the irreducible representation of the crystal point group to which they belong, as well as those of the components of the susceptibility tensor which is usually assumed to be symmetric (see, however, Sect. 3.5.3b). A mode will be allowed if its representation coincides with one of those of the susceptibility tensor [3.10]. For zincblende-type crystals (point group T_d) the representation which expresses the total symmetry of the atomic displacements Γ_M can be decomposed into irreducible components as:

$$\Gamma_M = 2T_2 , \tag{3.52}$$

where T_2 corresponds to the triply degenerate zone center acoustic and optic modes, respectively [3.10]. The corresponding representation of the *symmetric* susceptibility tensor reads:

$$\Gamma_s = A_1 + E + T_2 \tag{3.53}$$

and contains T_2. The zone center optic mode is thus allowed (note that A_1 corresponds to the trace of the tensor, E to the diagonal components less the trace and T_2 to the off-diagonal components). The related scattering efficiency is then proportional to:

$$|\boldsymbol{e}_s \cdot \boldsymbol{R}_{T_2} \cdot \boldsymbol{e}_i|^2 , \tag{3.54}$$

where $\boldsymbol{e}_s$ and $\boldsymbol{e}_i$ are the polarization vectors of the scattered and incident light. $\boldsymbol{R}_{T_2}$ is the Raman tensor associated with the vibration proportional to T_2 components (off-diagonal) of the susceptibility tensor. It is easy to show that for the backscattering configuration on a [001] face of a T_d crystal the longitudinal optical mode is allowed. This mode distinguishes itself from the transverse one because of the concomitant field which slightly alters the allowed Raman tensor. This alteration is determined by the Faust-Henry coefficient of zincblende materials [3.10, p. 58].

Let us now consider superlattices grown along the [001] axis. The superperiodicity induces (see Sect. 3.2.5a)

1) a lowering of the crystal symmetry from cubic (T_d) to tetragonal (D_{2d}).
2) an expansion of the primitive cell from 2 to $2(n_1 + n_2)$ atoms.

The lowering of the symmetry comes from two different features: the superperiodicity in the axial direction, which then becomes inequivalent to the two orthogonal ones, and the elastic deformation of the constituent compounds which appears in order to accommodate any lattice mismatch between them. The latter effect is often neglected (a good approximation for $(\mathrm{GaAs})_{n_1}-(\mathrm{AlAs})_{n_2}$). Some experimental results on strained systems will be presented in Sect. 3.4.4. While the point group of (001) oriented superlattices is always D_{2d} (tetragonal), their space group depends on the details of the structure (3.78). For instance, AB/AC structures are simple tetragonal or body centered tetragonal depending on the relative parity of n_1 and n_2. For AB/C superlattices where C is a group IV element (Ge, Si), the situation should be even more complex since n_2 can be half-integer, a fact which induces a doubling of the superlattice unit cell.

The representations of the mechanical vibrations at Γ are (see character table (3.44) and [Ref. 3.10, p. 50] for the method to derive these representations):

$$\Gamma_{\mathrm{M}}=2(B_2+E)+(n_1+n_2-1)(A_1+B_2+2E)\,, \tag{3.55}$$

including the $k=0$ acoustic phonons. Those of the susceptibility tensor (3.44):

$$\Gamma_{\mathrm{S}}=2A_1+B_1+B_2+E\,. \tag{3.56}$$

Thus all modes are again Raman active. In (3.55) we have divided the mechanical representations into two sets. The first one corresponds to cubic representations at Γ which are split by the tetragonal distortion. The second one contains modes which come from out-of-zone-center points in the cubic Brillouin zone folded to the zone center, due to the increase in the size of the primitive cell. The emergence of a Raman active A_1 representation is a specific consequence of this increase. The intensity of all modes activated by supercell formation vanishes with vanishing amplitude of the modulation. In the backscattering configuration along the (001) direction, the E modes (transverse) are forbidden whereas the A_1 and B_2 modes (longitudinal) are allowed in $z(x,x)\bar{z}$ and $z(x,y)\bar{z}$ configurations, respectively. The E and B_2 modes thus follow the same selection rules as the cubic modes from which they arise, while the A_1 modes appear in a cubic *Raman inactive* configuration (remember, however, that in this configuration LO modes become Raman active near resonance due to intraband Fröhlich interaction).

Before discussing the microscopic models used to describe the modulated susceptibility, we shall reconsider the symmetry of the superlattice eigenmodes as predicted from the one-dimensional models described in Sect. 3.2. In the AB/AC case, zone center eigenmodes correspond to symmetric or antisymmetric displacement amplitudes of the rigid layer planes (relative to each midlayer plane). The symmetric *amplitudes* correspond to the B_2 modes and the antisymmetric to the A_1 modes, a fact which seems surprising since the A_1 representation is totally symmetric. The displacement amplitudes, however, are lengths of vectors whose direction is antisymmetric.

3.3.3 The Bond Polarizability Model

One of the most popular models to calculate the polarizability and its derivatives with respect to the atomic displacement is the so-called bond-polarizability model, due originally to Wolkenstein [3.20], which describes the polarizability of the whole crystal as the sum of the independent contributions of each bond. One then obtains a local description of these quantities. Such models have been extensively used for group IV [3.86] and III–V bulk crystals [3.87], various layered crystals [3.88–90] and introduced for GaAs/AlAs superlattices by *Barker* et al. [3.39]. Its predictions were considered in more detail and compared with experiments in [3.91]. In a bond-related set of axes, the polarizability tensor simply reads:

$$\begin{pmatrix} \alpha_{\parallel} & 0 & 0 \\ 0 & \alpha_{\perp} & 0 \\ 0 & 0 & \alpha_{\perp} \end{pmatrix}, \tag{3.57}$$

where the bond direction has been taken to be the x axis. The rest of the calculation is simply a transformation of all tensors related to each bond in the unit cell to crystal-related axes. While differentiating the crystal polarizability tensor relative to the atomic displacements, one has to take into account (i) the variation of the individual bond polarizabilities and (ii) the variation of the bond orientation which makes itself felt through the coordinate transformation. One usually assumes that the bond polarizability (3.57) only depends on bond lengths. In zinc-blende-type superlattices the differential polarizability tensor only involves the following parameters of each of the constituent bonds:

$$\begin{aligned} \alpha_{xx} &= \frac{2}{\sqrt{3}} \left.\frac{d\alpha_0}{dl}\right|_{l_0} - \frac{4}{l_0\sqrt{3}}\,\alpha_2 \\ \alpha_{xy} &= \frac{2}{\sqrt{3}} \left.\frac{d\alpha_2}{dl}\right|_{l_0} - \frac{4}{l_0\sqrt{3}}\,\alpha_2 \\ \alpha_{zz} &= \frac{2}{\sqrt{3}} \left.\frac{d\alpha_0}{dl}\right|_{l_0} + \frac{8}{l_0\sqrt{3}}\,\alpha_2 \quad \text{where:} \end{aligned} \tag{3.58}$$

$$\begin{aligned} \alpha_0 &= \tfrac{1}{3}\,(\alpha_{\parallel} + 2\alpha_{\perp}) \\ \alpha_2 &= \tfrac{1}{3}\,(\alpha_{\parallel} - \alpha_{\perp}) \end{aligned} \tag{3.59}$$

and l_0 is the bond length.

For a bulk crystal and the zone center LO modes propagation along [001], one obtains [3.86]:

$$\Delta\chi \propto 2 \begin{pmatrix} 0 & \alpha_{xy} & 0 \\ \alpha_{xy} & 0 & 0 \\ 0 & 0 & 0 \end{pmatrix} \delta u_x \tag{3.60}$$

which, when replaced into (3.54) reproduces the well-known selection rules [3.10]. $\delta \boldsymbol{u}$ is the bond vector variation: its *magnitude* is the same for all bonds in the crystal in the case of this phonon.

For *AB*/*AC* superlattices, two different bonds appear and $\Delta\chi$ is obtained through a summation over all the bonds in the supercell:

$$\Delta\chi = \begin{pmatrix} A_{xx} & A_{xy} & 0 \\ A_{xy} & A_{xx} & 0 \\ 0 & 0 & A_{zz} \end{pmatrix} \quad \text{where:} \tag{3.61}$$

$$\begin{aligned} A_{xx,zz} &= \alpha^{(1)}_{xx,zz} \sum_{i=-n_1}^{-1} \left(u_i^{(1)} - u_{i+1}^{(1)}\right) + \alpha^{(2)}_{xx,zz} \sum_{i=0}^{n_2-1} \left(u_i^{(2)} - u_{i+1}^{(2)}\right) \\ A_{xy} &= \alpha^{(1)}_{xy} \sum_{i=-n_1}^{-1} \left(u_i^{(1)} + u_{i+1}^{(1)} - 2v_i^{(1)}\right) \\ &\quad + \alpha^{(2)}_{xy} \sum_{i=0}^{n_2-1} \left(u_i^{(2)} + u_{i+1}^{(2)} - 2v_i^{(2)}\right) . \end{aligned} \tag{3.62}$$

The indices 1, 2 specify whether the bond belongs to compound 1 or to 2. In this manner one recovers the previously derived selection rules as A_{xx} vanishes for symmetric modes (B_2) and A_{xy} for antisymmetric ones (A_1). The activity A_{xx} of the A_1 modes can be considerably simplified and reads:

$$A_{xx}(As) = 2u_1\left(\alpha^{(1)}_{xx} - \alpha^{(2)}_{xx}\right) , \tag{3.63}$$

where u_1 is the displacement of the interface atom. This result can be understood by noticing that the A_1 representation is not compatible with a zone center representation of phonons in the bulk materials. In a model where the cubic symmetry is locally preserved almost everywhere, contributions to the Raman activity of these modes can only come from the non-cubic regions, namely the interfaces, and is proportional to the local polarizability modulation.

In contrast, the $A_{xy}(S)$ terms are nonzero even for a non-modulated polarizability. As we pointed out previously, due to the large optic frequency modulation, the superlattice optic modes are not well described in terms of folding. As a consequence, the successive confined modes, and not only the first one, have significant intensities. They decrease with increasing order m, independently of the modulation of their interaction with radiation. For large layer thicknesses it is easy to show that their intensity decreases with mode order m (m odd) like m^{-2}. We illustrate these features in Fig. 3.23. The intensity variation of the upper optic modes confined to *AB* for the alternate linear chain also used in Fig. 3.15 is shown as a function of the *AB* layer thickness. The bond polarizability has been assumed to be unmodulated (the same in *AB* as in *AC*). These parameters are not well known for III–V bulk compounds, especially in the visible where resonances occur, and one can only expect to obtain a

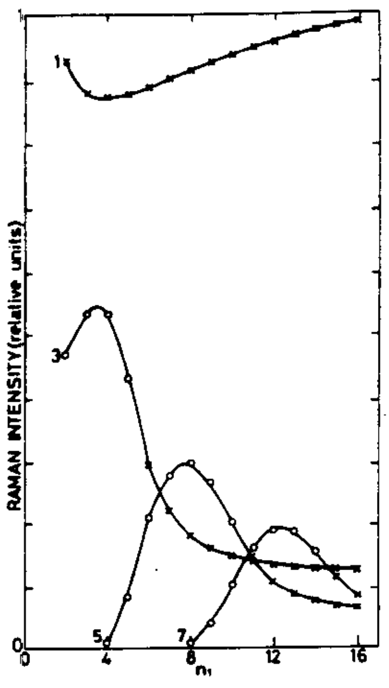

Fig. 3.23. Variation as a function of the well thickness n_1 (in monolayers) of the Raman intensity of the highest B_2 modes whose frequencies are shown in Fig. 3.15, calculated using the bond polarizability model. The results are shown by circles or crosses depending on whether the modes are propagative or confined [3.91]

qualitative description when using that assumption, as will be illustrated in Sect. 3.2.4. Moreover, this model completely fails in reproducing the light scattering intensities of the acoustic modes. It predicts very weak folded acoustic lines due to the weak deviation of the folded modes from those of the bulk, which also reduces the intensity of the acoustic Raman lines (the true Brillouin line excepted).

Actually a large modulation of the bond polarizability may allow to reproduce the typical folded acoustic intensity as suggested in [3.39]. We have already mentioned that a macroscopic description of the scattering efficiencies by folded acoustic modes becomes possible by using the derivatives of the susceptibility with respect to the strain, i.e., the so-called photoelastic constants. These photoelastic constants can, in principle, be related to the differential bond polarizabilities α_{xx}, α_{xy}, and α_{zz} [3.86, 92]. However, in semiconductors it is not possible to describe both the Raman tensor and the photoelastic constants with the same bond polarizabilities [3.86], the problem being the existence of electronic resonances in the visible region (note that such a description is possible for insulators such as diamond [3.93]). Hence, we decouple the photoelastic constants from the bond polarizabilities and give below the treatment of the scattering efficiencies for folded acoustic modes on the basis of photoelastic constants.

We should mention at this point a bond polarizability calculation that appeared recently [3.94] which includes the effect of disorder in the $Ga_{1-x}Al_x$ layers.

3.3.4 The Photoelastic Model

The polarizability modulation per SPC [3.42, 95] due to the photoelastic coupling associated with an acoustic mode reads:

$$\Delta\chi = \int_0^d \Pi(z) e_i^q(z) dz \tag{3.64}$$

where $e_i^q(z) = d(u_i^q(z))/dz$ is the strain related to the mode of wavevector q in branch i and $\Pi(z)$ is the relevant profile of the photoelastic coefficient along the superlattice axis z. For longitudinal modes propagating along [001], i in (3.64) represents the xz or yz cartesian components and thus $\Pi(z)$ is related to the p_{12} component of the photoelastic tensor $\boldsymbol{p}$ through:

$$4\pi\Pi(z) = -\frac{1}{\varepsilon^2} p_{12} , \tag{3.65}$$

where ε should be the dielectric constant of the laser or scattered frequency (assumed to be the same). The values of p_{12} and its spectral distribution have been determined for many diamond and zincblende-type semiconductors below the absorption edge [3.96]. In this region $\Pi(z)$ is real. Actually most measurements for superlattices are performed in the region where at least one of the bulk constituents absorbs and thus the corresponding ε and p_{12} become complex. In this region little information is available for p_{12} [3.97]. Hence, at the present time, the information about the photoelastic tensor $\boldsymbol{p}$ of the bulk constituents required to interpret the intensities of scattering by folded acoustic modes is not available. Even if this information were available the effects of the superlattice on the electronic properties would considerably modify it. For a discussion see Sect. 3.5.4 and [3.10].

In spite of this lack of precise information about the tensor $\boldsymbol{p}$ it is possible to obtain expressions for the efficiency for scattering through folded acoustic modes using the components of $\boldsymbol{p}$ in both media as parameters.

It is useful to discuss this problem with the Fourier formalism of Sect. 3.2.2 [3.42] which can be applied not only to the case of the sharp interfaces but also to diffuse ones of arbitrary one-dimensional profile. We expand the quantities $\Pi(z)$ and $u_i^q(z)$ in Fourier series:

$$\begin{aligned} \Pi(z) &= \sum_n P_n e^{ingz} \\ u_i^q(z) &= e^{iqz} \sum_n u_{i,n}^q e^{ingz} . \end{aligned} \tag{3.66}$$

One then obtains:

$$\Delta\chi = \sum_n P_{-n} u_{i,n}^q (ng+q) , \tag{3.67}$$

where we have omitted the common multiplicative factors of (3.65) in $\Pi(z)$.

The scattering efficiency for each mode is proportional to $|\Delta\chi|^2$. The eigendisplacements $u_j^q(z)$ have already been determined by solving the wave equation (see Sect. 3.2.2) and different approaches have been used to describe the photoelastic profile. The simplest one, performed by *Babiker* et al. [3.98] crudely assumes an unmodulated photoelastic coefficient P_0. These authors take into account the acoustic modulation obtained from a Green's function treatment of the wave equation. The resulting efficiencies are simply proportional to $|P_0|^2$ and can be compared without any knowledge of the photoelastic properties. As we pointed out before, the acoustic modulation in the GaAs/AlAs system is small, and correspondingly, these authors predict very small intensities which are strongly decreasing with increasing folding order. They arise, in this model, exclusively from the coupling of the folded modes with the Brillouin mode of the bulk. The predictions of this model for the intensity variation of the line ± 1 and ± 2 as a function of the relative thickness α of the two layers constituting the supercell are illustrated in Fig. 3.24. The model of [3.98] also includes the effect of optical absorption, which induces some uncertainty in the wavevector of the phonons involved and thus some broadening of the corresponding Raman lines. Due to this broadening, and to the very small magnitude of the folded lines as compared to the Brillouin line, strong coupling between the different components takes place, giving rise to complex line shapes. All these features have not yet been observed because on all the available systems, the contribution of the photoelastic modulation appears to be dominant.

This contribution was first introduced by *Klein* et al. [3.95] in a complementary model in which any effect of the acoustic modulation is neglected. The folded eigendisplacements are then plane waves propagating at the average velocity of the superlattice, a correct approximation far from zone center and edge. The calculated intensities only depend on the non-zero Fourier components of $\Pi(z)$. In the usual case of the periodic stacking of abrupt layers of two

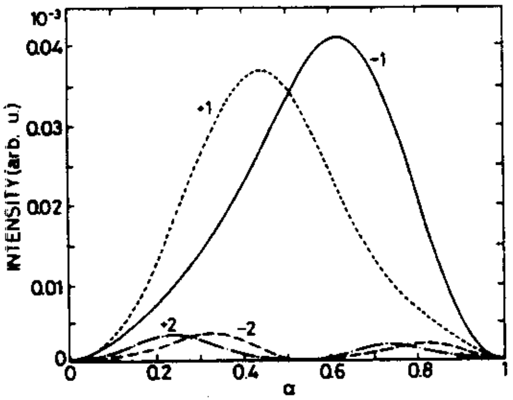

Fig. 3.24. Variation, as a function of the thickness ratio $\alpha = d_2/(d_1 + d_2)$ in a GaAs/AlAs structure, of the room temperature intensity of the four lowest folded branches at $q/g = 0.06$ (g is the length of the first reciprocal lattice vector of superlattice), calculated neglecting the photoelastic modulation, as done in [3.98], The line labelling was introduced in Fig. 3.7

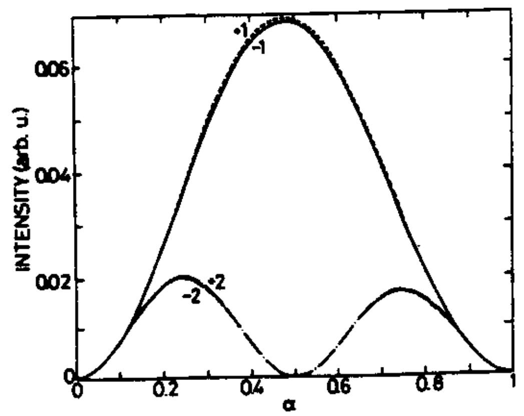

Fig. 3.25. Same as Fig. 3.24 but neglecting the acoustic modulation, and considering only the photoelastic one, as done in [3.95]

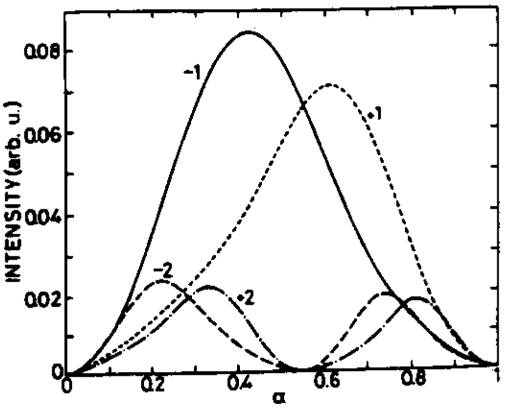

Fig. 3.26. Same as Fig. 3.24 but taking into account both acoustic and photoelastic modulations and assuming $P(\mathrm{AlAs})/P(\mathrm{GaAs})=0.1$. From [3.60]

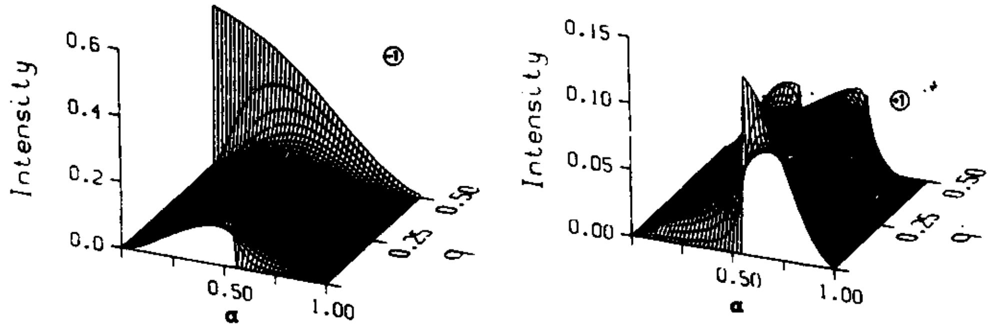

Fig. 3.27. Calculated variations of the intensity of the two lowest folded ($\nu=\pm1$) branches at room temperature as a function of the thickness ratio α and of the wavevector q normalized to g, calculated assuming $P(\mathrm{AlAs})/P(\mathrm{GaAs})=0.1$. From [3.60]

different bulk compounds, all these components are simply obtained from the Fourier components of the compositional profile, multiplied by the difference between the (complex) photoelastic constants of the bulk constituents. Again one can compare the *relative* intensities without any knowledge of the photoelastic parameters. The results of the model are illustrated in Fig. 3.25 for the same phonons as Fig. 3.24. In the present approximation, the intensities of lines $\pm n$ are equal and almost independent of wavevector. These two features are the main deficiencies of a model which otherwise provides a good qualitative description of the experimental results.

In [3.60] a numerical calculation of the intensity of the folded lines, taking into account both acoustic and photoelastic modulations was performed. With a reasonably large set of Fourier components, one can determine the scattered intensities to a good approximation. We show in Fig. 3.26 the results for the same phonons as Figs. 3.24, 25 obtained under this assumption for a wavevector

q typical of those involved in a backscattering experiment. As a matter of fact, the intensities of lines $+n$ and $-n$ are now different and this difference strongly depends on the scattering wavevector. This effect can be understood from the results shown in Fig. 3.27. For an intermediate wavevector, the intensities of lines $+n$ and $-n$ are similar and reflect the nth Fourier component of the profile. At the zone center, due to the strong mixing of the two modes, one is allowed and the other forbidden. For a typical backscattering wavevector, the intensity difference reflects the progressive softening of the zone center selection rules. Furthermore, due to the couplings between the "Brillouin" acoustic and the folded branches the calculation becomes sensitive to the relative magnitude of the photoelastic coefficients of the bulk constituents. The line intensities are then the result of the interference between the acoustic and the photoelastic modulations. Such models can be easily applied to any periodic profile with a piecewise constant modulation. In the case of a smooth modulation, however, a detailed knowledge of the photoelastic profile is needed: a linear approximation to the dependence of the photoelastic coefficient on the composition is often inadequate [3.99].

We mention that an attempt to incorporate in the intensity model superlattice effects on the optical properties, i.e., to take into account the modulation of the complex refractive index along the z axis, has been recently presented by *He* et al. [3.100].

3.3.5 Conclusions

We have presented in this section two types of models introduced to describe the light scattering activity of superlattice vibrations. The bond polarizability model refers to the local deformation of bonds induced by the (optic) vibrations while the photoelastic one involves the macroscopic strain associated with the folded acoustic modes. Although the two models may be quantitatively related to each other, this connection leads to an inaccurate description of Raman and Brillouin scattering in the corresponding bulk materials. In the first model, the amplitudes of the B_2 optic-like modes ensuing from the cell multiplication are strongly modulated and their scattering intensity is significant, even in the absence of modulation of their coupling with radiation. On the other hand, the acoustic modulation being extremely small, the observation of the folded lines requires the modulation of the photoelastic process.

We must emphasize that these models are only useful far from electronic resonances, which will be considered in Sect. 3.5.

3.4 Selected Light Scattering Results for Vibrations in Superlattices

3.4.1 Introduction and Historical Aspects

The trends in experimental work on phonons in superlattices have been influenced by the evolution of the type of available structures and their crystalline quality. Until recently, the dominant systems were based on GaAs and AlAs bulk compounds. In the late 1970s, following the ideas of *Esaki* and *Tsu* [3.25], structures including a very few molecular layers of pure GaAs or AlAs as superperiod were considered. Due to the immaturity of the Molecular Beam Epitaxy (MBE) technique, these samples did not clearly exhibit the expected properties, including those concerning phonons [3.101], and were often found to be very close to random $Ga_{1-x}Al_xAs$ alloys. Consequently, the emergence of the concept of multi-quantum-wells, and the exploding interest in the remarkable electronic properties of these structures [3.102], less demanding on growth quality, slowed down the interest on real superlattice effects and the experimental work on phonons. One must mention some resonant Raman scattering investigations from this period, mainly devoted to elucidation of confinement effects on electronic states [3.103] or some controversial reports on additional lines in the optical phonon range [3.71, 104]. One fundamental result was obtained by *Colvard* et al. [3.49]: the first observation by light scattering of folded acoustic phonons, a result that one can consider as a milestone of the experimental work we describe in this section.

Since 1983, increasing interest has been devoted to the vibrations of superlattices, leading to a rather detailed understanding of these properties, at least for propagation along the growth axis. Again, the main stages concern results on GaAs/GaAlAs structures but new systems appeared involving other III–V, II–VI compounds, Si and Ge, and more recently, amorphous semiconductors. Even if these systems display a new additional feature, i.e., they involve layers strained because of lattice constant mismatch, their vibrational properties are not qualitatively different from those of the GaAs/GaAlAs system. Light scattering studies of strain effects have thus found their main interest in sample characterization. Among these systems, that based on bulk Si and Ge and their alloys has attracted the most attention and some interesting results have been obtained in both the acoustic and optic phonon ranges. Related results have also been reported for the folded acoustic modes of systems based on the periodic stacking of amorphous semiconducting layers. In the following we will illustrate all these results in three subsections. As already emphasized, the folded acoustic and the optic vibrations display very different properties and will be considered separately in Sects. 3.4.2, 3. Section 3.4.4 will focus on the results related to material characterization, mainly including strain and interdiffusion effects.

3.4.2 Experimental Results for Folded Acoustic Phonons

As we mentioned in the introduction, the first clear evidence from light scattering of a superlattice effect on vibrations was reported in 1980 by *Colvard* et al. [3.49]. These authors observed (see Fig. 3.28) a doublet around 60 cm^{-1} for a superlattice consisting of alternating 13.6 Å GaAs and 11.4 Å AlAs layers and attributed it to the lower near-zone-center folded longitudinal acoustic doublet. Before them, *Narayanamurti* et al. [3.105] had reported the observation of a dip in the acoustic transmission spectrum through a superlattice and attributed it to the lowest zone edge gap opening due to the superperiodicity. Recently, acoustic transmission has again attracted some interest [3.106, 107] and provided some results complementary to light scattering.

Following this first observation, obtained under resonance conditions (laser line close to strong electronic absorption), many reports have been devoted to these lines in:

- GaAs/AlAs and GaAs/$\mathrm{Ga}_{1-x}\mathrm{Al}_x\mathrm{As}$ structures [3.41, 42, 56, 59, 60, 65, 78, 82, 95, 100, 108–119]
- other III–V compounds: GaSb/AlSb [3.120–123], InGaAs/InP [3.124], InAs/GaSb [3.124], InGaAs/GaAs [3.124, 125]
- II–VI compounds: CdTe/CdMnTe [3.126, 127]
- Si/Ge and Si/$\mathrm{Si}_x\mathrm{Ge}_{1-x}$ layers [3.128–131]
- amorphous semiconductors:
  a – Si: H/a.SiN_x:H [3.57, 132–133], a.Si:H/a.Ge:H [3.134].

Thus, these modes have been observed for a wide variety of systems, with periods ranging from 10 Å [3.111, 112] to 500 Å (for instance, in [3.100]). Several doublets are often recorded even out of resonance (17 doublets are identified in [3.130]). In Fig. 3.29, we present a few Raman spectra of folded acoustic phonons obtained for several typical superlattices. Recently, folded acoustic lines have been investigated in samples whose period is composed of more than two different layers [3.58, 60], large and complex supercells [3.135], built up according to Fibonacci sequences [3.136] and even on aperiodic

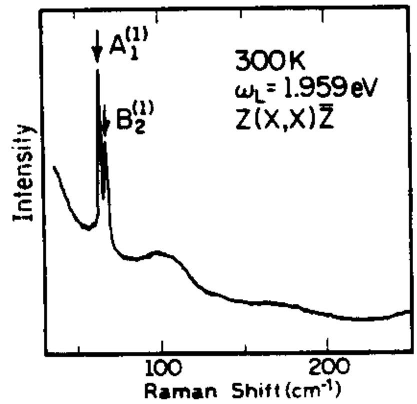

Fig. 3.28. First reported observation of a folded acoustic doublet in a GaAs/AlAs superlattice [3.49]

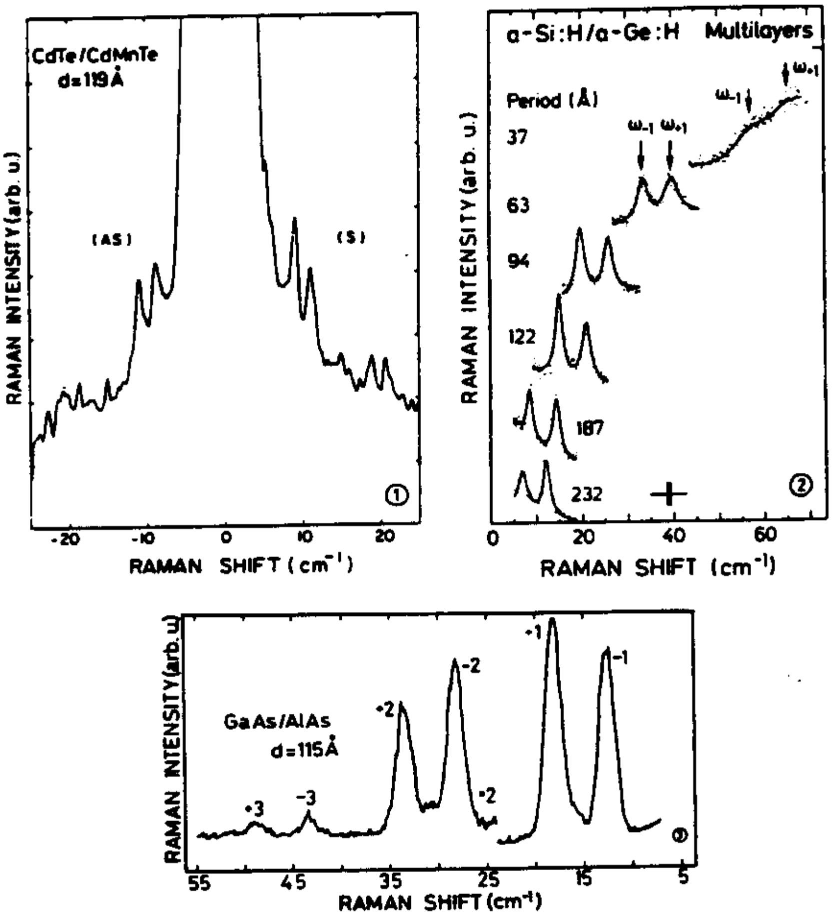

Fig. 3.29. Some typical Raman spectra exhibiting folded acoustic lines on: (*1*) a CdTe/CdMnTe superlattice [3.126]; (*2*) amorphous Si/Ge multilayers [3.134]; (*3*) a GaAs/AlAs superlattice [3.60]

structures [3.137, 138], a topic which will be considered in Chap. 5 of this book. One must also note that the folded acoustic modes are similar to those observed for SiC polytypes [3.17] and for graphite intercalated compounds [3.139] as a consequence of the periodic introduction of dopants in these crystals. Though less extensively studied experimentally, these systems exhibit essentially the same features as those described in this section.

Among these numerous reports, some only mention the observation of folded lines or roughly compare their frequencies with the period of the sample. Nevertheless, two particular topics have attracted increasing attention in the past few years:

- the quantitative understanding of the line frequencies, and in particular, the doublet splittings
- the stringent Raman selection rules and the quantitative description of the measured intensities.

These topics will be considered in the two following sections. The line profiles have attracted less attention [3.116], the main result being that they are extremely narrow, usually narrower than the resolution of classical Raman set-ups. A detailed investigation of these profiles has been undertaken recently using a Brillouin-Raman coupled apparatus [3.140].

a) The Raman Frequencies of Folded Phonon Branches

In [3.49] the folded LA line frequencies were already successfully analyzed by using the elastic model. The parameters one needs for this comparison are bulk properties such as densities and sound velocities, and the structural parameters of the superlattice. There are limitations to checking the validity of a model of the GaAs/AlAs structures. The first is the lack of knowledge of the sound velocities of AlAs [3.140a], the second the uncertainties in the determination of the superlattice parameters. As explained in Sect. 3.2, the acoustic dispersion curves are obtained first by folding an average dispersion curve and then by opening energy gaps at the zone center and boundaries. As long as the acoustic modulation is small, an assumption, which appears to be valid in all systems considered so far, the average frequency of a given near-zone-center doublet reads [see (3.11, 12)]:

$$\Omega_{\nu}=\nu\frac{\pi}{d}\left(\frac{\alpha}{v_{B}}+\frac{1-\alpha}{v_{A}}\right)^{-1}; \quad \alpha=\frac{d_{B}}{d}, \qquad \nu=0,1,2,\ldots \tag{3.68}$$

and does not depend on the wavevector.

Again due to the relatively small difference between v_A and v_B, this quantity essentially varies as $1/d$, nearly independently of α. Such variation has been checked by different groups [3.95, 141] by using values of the period estimated from the growth conditions or, even better, values determined by x-ray diffraction [3.142]. This method provides an excellent determination of d from the distance between superlattice satellites which accompany the bulk reflexes. Moreover, taking into account the actual value of α in the samples provides a moderately accurate determination of the sound velocity in bulk AlAs which is found to be $\sim 5.7\times10^{5}$ cm/s (for longitudinal waves). This value corresponds to almost the same elastic constants as in GaAs: therefore, the acoustic modulation must essentially come from the density modulation.

From the determination of the doublet splittings one expects complementary information and more insight on the physics of the problem. These quantities are indeed proportional to the relevant modulation. The approximate relation for the splitting $\Delta\Omega_{\nu}$ (3.14) was obtained in Sect. 3.2. It shows that the gaps depend strongly on the details of the supercell structure, i.e., in the simplest case, on the ratio α. The experimental results are in apparent disagreement with these features. The doublet splitting seems to be independent of sample details and doublet order. It amounts to about 5 cm^{-1} for the usual Raman backscattering experiments performed at 5145 Å, a much larger value than predicted from the elastic model at $k=0$ using the sample parameters deduced from the average frequency measurements. As mentioned in [3.49, 109] and studied in detail in [3.110], this result can be understood by taking into account the finite wavevector of the phonon involved in the light scattering process. This quantity is usually neglected in Raman studies of bulk materials because it is much smaller than the size of the Brillouin zone. Also, optic branches are often weakly dispersive around the zone center. Nevertheless, Brillouin scattering experiments are well known to be sensitive to this parameter since the frequency of the true acoustic branch is linear near $k=0$ [3.13].

A similar effect has to be taken into account for superlattices. Due to the weak modulation, the wavevector range of interaction between a pair of converging acoustic folded branches is very small, and these "optic" modes, with quadratic dispersion at the zone center, rapidly transform into "acoustic"-like modes in the sense that their dispersion becomes linear. From a comparison between both modulation and dispersion contributions to the doublet splittings, one concludes that the second one is dominant in usual backscattering conditions on GaAs/AlAs structures for periods larger than 20 Å, i.e., for almost all available samples. This unusual feature in Raman scattering has both negative and positive consequences on the amount of information to be deduced from the line frequencies. On the negative side, Raman backscattering is nearly unable to probe the physical nature of the modulation and is also only weakly sensitive to the inner structure of the supercell, though being an excellent probe of its periodicity. On the positive side, as emphasized in [3.110], Raman backscattering does provide dispersion curves as neutron scattering does for bulk compounds. By varying the incident wavelength, one can change the k_z since it is inversely proportional to λ when neglecting the refractive index variation. This will change the doublet splitting without changing its average frequency. Such dispersion measurements have been performed by several groups on the GaAs/AlAs [3.95, 100, 110], GaSb/AlSb [3.121–123], Si/Ge [3.129], and on amorphous structures [3.132]. They are able to provide large portions of the dispersion curves. Representative results are shown in Fig. 3.30.

Different ways of circumventing the difficulty involved in probing very close to the zone center by Raman backscattering and to obtain information on the gaps have been presented. The most natural one is to extrapolate to the zone center the frequencies obtained at various wavelengths. As already pointed out in [3.95] and apparent in Fig. 3.30, this extrapolation provides no evidence for a zone center gap in the GaAs/AlAs system. For a.Si:H/a.SiN$_x$:H, evidence of a zone center gap has been obtained [3.133] thanks to the lower refractive index of these compounds, which allows one to get closer to the zone center. The second way is based on the possibility of adjusting both the period and the incident wavelength in order to probe the region close to the SBZ edge. This method has been first successfully applied by *Brügger* et al. to Si/Ge [3.129]. In this system, thanks to the large average sound velocity, the lowest zone edge doublet is accessible to a Raman set-up (at $\sim 5\ \mathrm{cm}^{-1}$), which is not the case for the GaAs/AlAs system ($\sim 2.5\ \mathrm{cm}^{-1}$). The agreement between measured and calculated splittings near the zone edge is good, as illustrated in Fig. 3.31. More

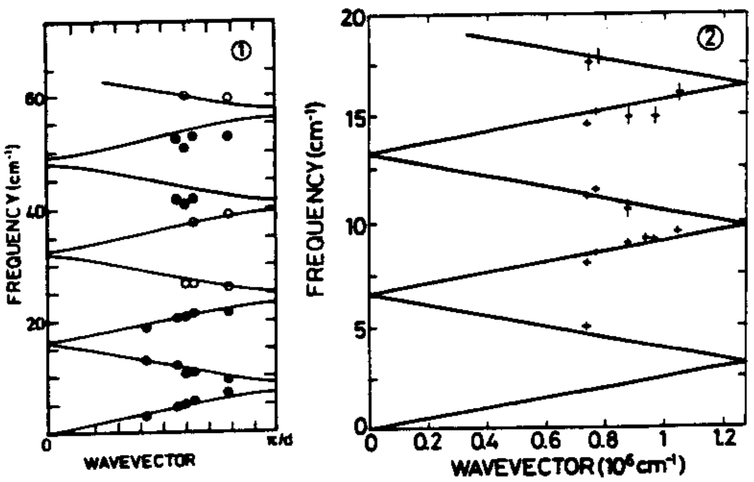

Fig. 3.30. Folded acoustic dispersion curves, calculated using the alternating elastic model, compared with the Raman frequencies measured at different incident wavelengths for: (*1*) a Si/SiGe superlattice ($d = 163$ Å) [3.129]; (*2*) a GaAs/GaAlAs superlattice ($d = 257$ Å) [3.110]

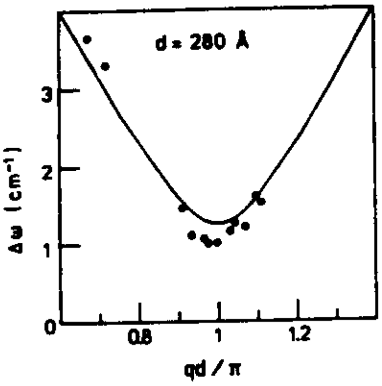

Fig. 3.31. Frequency splitting of the lowest folded acoustic doublet recorded on a Si/SiGe structure at different incident wavelengths, compared with calculation around the zone boundary [3.129]

recently, similar ideas have been applied to GaAs/AlAs large period superlattice [3.100] using a Brillouin-Raman apparatus which allows recording of Raman spectra down to 1 cm^{-1} [3.140] and also to amorphous structures [3.132] using a Brillouin (Fabry-Pérot) spectrometer.

The first reported attempt to obtain information on the folded acoustic mode coupling actually involved a forward scattering configuration [3.56]. This configuration allows one to probe the dispersion curves very close to the zone center and is thus perfectly adapted to this problem. Serious technical difficulties, related to the opacity of the involved compounds to usual ion laser frequencies have, however, restricted its application. In order to collect the scattered light on the other side of the sample, one must first remove the opaque substrate from a small area of the sample by using selective etching. Moreover, the parameters of the superlattices must be chosen so that they become sufficiently transparent. Figure 3.32 shows both forward and backward Raman spectra obtained in this way for one of the two different samples considered in

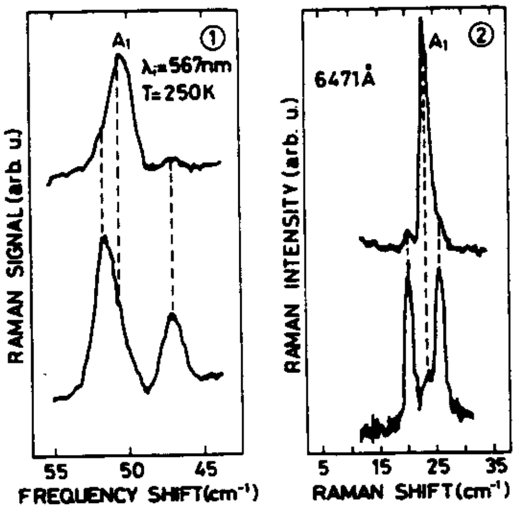

Fig. 3.32. Comparison between the Raman spectra obtained in backscattering (*bottom*) and in forward scattering (*top*) configurations around the lowest folded acoustic doublet for two different systems: (*1*) GaAs/AlAs [3.56]; (*2*) amorphous Si/SiN$_x$ [3.57]

[3.56]. In forward scattering, a single line lying between the two components of the backscattering doublet is observed. This line is attributed to the A_1 component of this doublet, the B_2 component being Raman forbidden by parity. Due to this selection rule,this method appears to be unable to give a pure experimental evidence of a zone center gap. Nevertheless, from the splitting between the forward scattering line and the center of the backscattering doublet, the authors obtained an estimate of the gap in both samples, again in correct agreement with the predictions of the elastic model. Considerable attention is paid in [3.56] to the dependence of the acoustic gaps on structural parameters. The strong oscillatory behavior of these quantities as a function of the ratio α is supported by the few available experimental results. Moreover, new insight is obtained on the selection rules, a topic to be treated in the next subsection. Very recently, similar experiments were reported [3.57] for amorphous structures. They are easier in this case because the substrate is transparent; the results illustrated in Fig. 3.32 are also in good agreement with the elastic model.

To summarize, a departure from the alternating elastic model has not been evidenced in most studies devoted to LA folded line frequencies.Only recently [3.123] some evidence for departure from the elastic continuum model (and better agreement with the alternating linear chain model) has been obtained for GaSb/AlSb superlattices. This effect should be easier to observe for TA modes. The bulk TA dispersion curves are known to be flat over a large region of the Brillouin zone (Fig. 3.1). Whereas these modes are forbidden in a backscattering experiment on a [001] surface, they have been observed as weak structures [3.95, 118] thanks either to departures from the ideal backscattering configuration or to defect-induced scattering. Similarly, some observation of zone edge disorder activated folded LA and TA modes has been reported and compared with the case of bulk disordered systems [3.143]. Recently, *He* et al. [3.100] extracted part of the folded TA dispersion curves from these structures, but without reaching sufficiently high energies to obtain evidence of sublinearities.

On the other hand, from the small amount of experiments on structures with other surface orientations [3.144], no reliable information on folded TA modes has been extracted to our knowledge.

It is interesting to note that, for vanishing in-plane wavevectors, folded TA and LA modes are decoupled since they have different symmetries. Thus, their respective dispersion curves cross. In contrast, new "internal" acoustic gaps appear for finite in-plane wavevectors which are out of the scope of light scattering experiments but have been observed by phonon spectroscopy using superconducting diodes [3.106, 107].

As concerns the opening of zone center and edges gaps, no real departure from the alternating elastic model has been observed till now. Due to the small amplitude of the acoustic modulation between the constituents of presently available systems, the folded frequencies are essentially sensitive to the periodicity, and unfortunately, not so much to the physical details of the problem. The few studies of this point have demonstrated the existence of acoustic gaps in rough agreement with the elastic model, but have been unable to provide accurate quantitative information on their magnitudes. Structures with larger acoustic modulation would be of interest to further investigate this problem.

b) The Intensities and Selection Rules of Folded Acoustic Modes

In contrast to their frequencies, whose main features have been understood from the beginning, the selection rules of lines which correspond to folded acoustic modes have generated some controversy. There is indeed a clear disagreement between the predicted selection rules for *zone center* Raman modes and the *backscattering* results. Both components of the folded doublets are systematically observed in parallel $z(x,x)\bar{z}$ configuration and not in the perpendicular $z(x,y)\bar{z}$ one, whereas the zone center selection rules predict the observation of one line (A_1) in parallel and the other (B_2) in perpendicular configuration. One thus has to explain why both lines are observed in the parallel (polarized) configuration but not in the perpendicular (depolarized) one. It has been suggested in [3.49] that the vanishing intensity in the latter case could be attributed to the macroscopic nature of the photoelastic process involved which introduces additional (cylindrical) symmetry: a strain along the z-axis produces a change in χ_{xx} and χ_{yy} but not in χ_{xy}.

The observation of the *alleged* B_2 modes in parallel configuration was attributed to resonance conditions in the early publications [3.49]. Its relation to the finite value of the scattering wavevector involved was recognized later. Conclusive proof of this fact was obtained in [3.56], the forward scattering spectra displaying a single component corresponding to the A_1 mode (see Fig. 3.32) and in [3.60], where the increasing relaxation of the zone center selection rules with increasing superlattice period was demonstrated.

Beyond the determination of the nature of the light scattering process, the quantitative description of the intensities has attracted a great deal of attention.

The modulation which underlies the observation of the folded acoustic modes can either appear in the elastic or in the photoelastic properties. In other words, it can be an intrinsic property of the object one looks at or a property of the method one uses to look at it. As we briefly analyzed in Sect. 3.2, this appears explicitly in the Fourier-transformed expression of the scattered intensities:

$$I_{i,q} \propto \left|\sum_n P_{-n} u^q_{i,n}(ng+q)\right|^2 \qquad (3.69)$$

first introduced in [3.95].

The *u*-terms in (3.69) reflect the mechanical modulation and the *P*'s the photoelastic one. *Babiker* et al. [3.98] studied the predictions of such a model as a function of various sample parameters but neglected the photoelastic modulation. They considered, in particular, the case of the GaAs/GaAlAs structure but did not attempt to compare their calculations with experimental results. *Colvard* et al. [3.65] on the other hand, in view of the small amplitude of this acoustic modulation in the GaAs/AlAs systems as deduced from the folded line frequencies, made the complementary approximation of neglecting the mechanical modulation and investigated the effects issuing from the photoelastic modulation. They pointed out two features well suited to experimental proof: (i) the relative intensity of the folded lines and the true acoustic line and (ii) the vanishing intensity of the *even index* lines, for equal thickness of both constituting layers. Whereas feature (i) has not been considered till recently, feature (ii) was successfully checked by those authors. As illustrated in Fig. 3.33 the second doublet disappears in a sample consisting of the periodic stacking of 85 Å of GaAs and 88 Å of GaAlAs as long as the experiment is performed sufficiently far from electronic resonances. However, as can be seen in Fig. 3.24, such a vanishing intensity is predicted in the mechanical model even when neglecting the photoelastic modulation, as in [3.98]. The corresponding

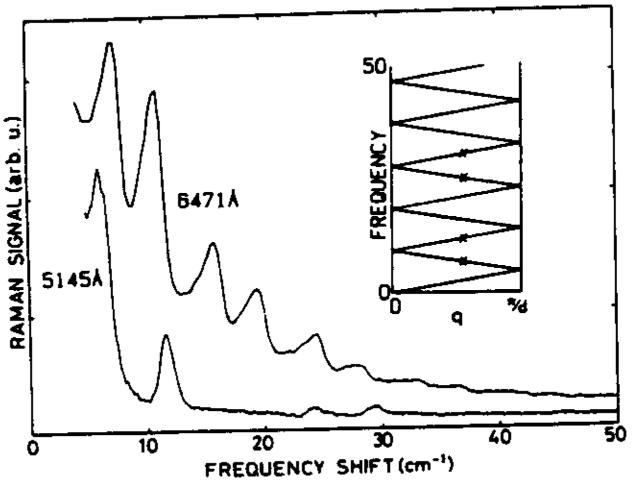

Fig. 3.33. Low frequency Raman spectra of a GaAs/GaAlAs superlattice with nearly equal layer thicknesses (85/88 Å) obtained out of resonance (*lower trace*) and close to resonance (*upper trace*) [3.95]

thickness ratio α does not equal 0.5 in this case but the value at which the acoustic gaps vanish [see (3.14)]:

$$\alpha = \frac{v_B}{v_A + v_B} \tag{3.70}$$

Since α amounts to 0.55 for GaAs/AlAs structures, the observation of a vanishing intensity around 0.5 is not a conclusive proof of the photoelastic mechanism. Nevertheless, we feel that the photoelastic modulation must dominate the physics of the problem: the small acoustic modulation could not induce the strong (compared to the optic modes) scattering observed for folded modes.

In order to obtain more conclusive evidence, a quantitative comparison of the predicted and measured line intensities is of interest. Besides the comparison between different folded orders, another feature was shown to be sensitive to the details of the process [3.60], namely the asymmetry of the lower doublet. As seen in Figs. 3.24–26, the asymmetry in the relative intensity of both components of the first doublet vanishes when neglecting the acoustic (mechanical) modulation. If the mechanical modulation is included, the asymmetry reverses upon switching on of a strong photoelastic modulation. The absence of asymmetry when neglecting the acoustic modulation is easy to understand as both components are related to the same Fourier coefficient of the photoelastic profile. Colvard et al. emphasized that their model was valid away from zone boundaries. They claimed that this assumption was correctly fulfilled in the usual backscattering conditions, where the mode frequencies are indeed insensitive to the opening of gaps. As demonstrated in detail in [3.60], asymmetries are actually often observed by backscattering on GaAs/AlAs structures. they depend strongly on the sample parameters and can be quantitatively explained by taking into account both modulations. The predictions one obtains in this framework were illustrated in Fig. 3.27 through the intensity of both lower folded branches ($\nu = -1$ and $+1$ modes) as a function of α and the wavevector $\boldsymbol{q}$. At the SBZ center one recovers the parity selection rules, a single line (A_1) being active, while as $\boldsymbol{q}$ moves aways from the SBZ center, a continuous softening of the selection rules takes place. Figure 3.34 compares two series of experimental results and the predictions of the photoelastic model for different amplitudes of the photoelastic modulation. One finds the following qualitative results:

- the sign of the asymmetry supports the dominant role played by the photoelastic modulation
- the decrease in the amplitude of the variation of the asymmetry with α when increasing the sample period d reflects the softening of the zone center selection rules as the corresponding wavevector, normalized to the size of the Brillouin zone, moves away from zone center.

These asymmetries are not very sensitive to the exact value of the photoelastic modulation: a quantitative estimate is made in [3.60] (for $P_{\mathrm{AlAs}}/P_{\mathrm{GaAs}} \sim 0.1$). As concerns the relative intensity of the different doublets, some comparisons have

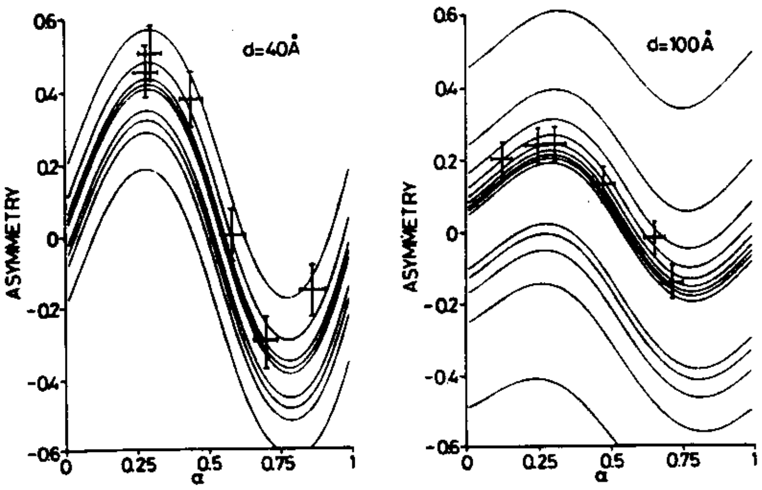

Fig. 3.34. Variation as a function of the thickness ratio α of the asymmetry of the lowest folded acoustic doublet measured on two series of GaAs/AlAs superlattices with two different fixed periods. The experimental results are compared with the predictions of the photoelastic model for different values of the photoelastic ratio (AlAs to GaAs) from −1 to 2 (see [3.60]). The experimental data correspond to ratio ≈ −0.2

been made for GaAs/AlAs or Si/Ge$_x$Si$_{1-x}$ systems [3.131] which further support the dominance of the photoelastic mechanism for both types of structures. The relative intensities are not very sensitive to the exact value of the photoelastic ratio. They are, however, sensitive to the detail of the compositional profile [3.59].

A rather good method to obtain information about these properties is to compare the folded line intensities to the true acoustic one (Brillouin), as suggested in [3.65]. The very low frequency of the latter has, however, hindered such measurements. Even if on the Si/Ge system measurements with Raman spectrometers have detected these lines [3.128, 131], no attention has yet been focussed on this particular point. On the other hand, *He* et al. [3.100] have recently carefully analyzed the scattering intensities, including the Brillouin scattering, for GaAs/AlAs structures, with their Brillouin-Raman coupled set-up. They used a theoretical model which included the acoustic and photoelastic modulations and also the modulation of the optical properties of the samples. They thereby calculated the ratio $P_{\mathrm{AlAs}}/P_{\mathrm{GaAs}}$ which depends on the incident wavelength. The value they found in the blue, 0.43, is in some disagreement with the one obtained in [3.60].

To summarize, a reasonable description has been obtained of the intensities of the acoustic lines on the basis of the coupled acoustic and photoelastic (and possible optical) modulation model. One must emphasize that the observation of the acoustic modes on superlattices is mainly due, like for the Brillouin effect of bulk crystals, to photoelastic modulation, and displays a close analogy to the observation of satellites in the x-ray diffraction patterns of superlattices. In the latter case, a competition takes place between a "sample modulation", namely the one of the lattice parameter along the growth axis, and a "coupling modulation", the one of the atomic scattering factors. On the nearly-lattice-matched superlattices (GaAs/AlAs) the latter is dominant and the intensity patterns and their variation with sample parameters are similar to the ones obtained in Raman scattering [3.145]. On the other hand, for strained-layers superlattices, the lattice parameter modulation becomes dominant and the diffraction patterns may look very different [3.146]. Such a situation has, unfortunately, never been encountered for phonons.

The limits of validity of the photoelastic model have been clearly indicated by *Klein* [3.99]. They lie in the dispersive character of the (complex) photoelastic tensor of the bulk constituents. Even if a good knowledge of these bulk properties exists, which is not often the case, is it justifiable to extrapolate them to structures displaying very different electronic properties and to large unfolded q's? Such a question emphasizes how careful one has to be when trying to interpret the intensities of folded acoustic modes as a function of incident wavelength.

3.4.3 Experimental Results on Optic Phonons

a) Introduction and Historical Aspects

In the analysis of the superlattice effects on the sample symmetry, we pointed out the two main consequences of the superperiodicity: (1) the modification of the zone center cubic modes and (2) the folding of cubic out-of-zone-center modes to the zone center. In our analysis of the experimental result in the acoustic range, we mainly focussed on the second aspect. When discussing the results in the frequency range of the bulk optic modes, one has to consider both features. The zone center optic modes are indeed easy to observe in cubic crystals, contrary to the acoustic ones, and they remain qualitatively unchanged in superlattices. Therefore, the observation of such modes in multilayer systems has often been possible, sometimes with a small shift in their frequencies, without giving any evidence of a superlattice effect. In the following we shall mainly discuss experimental work which carefully demonstrates, by means of the dependence on layer thicknesses, phonon *confinement* effects. Such results have been obtained mainly for GaAs/AlAs structures, where (i) the competing effects of strain are negligible and (ii) the bulk frequencies are resonably well known. The oldest light scattering study to be found in the literature on superlattices [3.101] already discussed the dependence of the LO frequencies of GaAs and AlAs on the layer thicknesses in samples containing a few monolayers per period. Such studies have been repeated and extended by several groups [3.66b, 82, 112, 147–148].

Particularly convincing evidence of the confinement of optic phonons is obtained when new additional modes are observed in the optic phonon frequency range, due to the primitive cell multiplication. Such additional lines have also been observed mainly for the GaAs/AlAs system. While new lines were recorded in resonant conditions [3.71, 104] and attributed either to confinement or anisotropy effects, the first off-resonance observation [3.41] and quantitative demonstration [3.67] of this effect, was performed in 1983 on GaAs/$Ga_{1-x}Al_xAs$ samples. Somewhat similar structures have actually been previously observed at resonance [3.108] but without detailed assignment. Several subsequent studies have been devoted to these features mainly for pure GaAs/AlAs superlattices [3.42, 62–66a, 111, 149]. Recently, observations of confined modes have been reported for two different II–VI superlattices containing, respectively, CdTe and ZnTe [3.150] and CdTe and CdMnTe [3.127], and also for GaSb/AlSb systems [3.122, 123]. The observation of these *additional* optic modes is difficult, as compared to the folded acoustic ones, because of the low dispersion of the optic phonon branches. They must be resolved from the close, more intense main optic line. Since the properties of GaAs/$Ga_{1-x}Al_xAs$ and GaAs/AlAs structures present some important differences due to the overlapping or non-overlapping character of the optic phonon branches involved, we shall describe them separately in the two following subsections. In both cases, a good description of the frequencies is obtained by using the alternating linear chain model, and the zone center Raman selection rules are fulfilled.

A third subsection will be devoted to experimental results which stand out of the common framework of the work described so far, namely, scattering involving a non-vanishing in-plane wavevector. This condition was first intentionally obtained by *Zucker* et al. [3.54] using right angle scattering on a specially designed structure. Interesting selection rules were thereby observed.

A definitive understanding of the additional lines observed at resonances [3.71] and a detailed study of their line shape and dependence on sample parameters was obtained by *Sood* et al. [3.55]. These lines attributed to interface modes can be observed near resonance, according to these authors, due to some unspecified relaxation of the wavevector conservation. Similar results have been reported for GaAs/$Ga_{1-x}Al_xAs$ [3.151–153], CdTe/CdMnTe [3.127] and CdTe/ZnTe [3.150] structures. Related results for GaAs/$Ga_{1-x}Al_xAs$ structures have been obtained as well by *Lambin* et al. using high resolution electron energy loss spectroscopy [3.77]. An important feature in optic vibrations propagating off-axis is the role played by long range Coulomb forces.

b) The Optic Vibrations in GaAs/$Ga_{1-x}Al_xAs$ Superlattices

Figure 3.35 shows Raman spectra obtained in the frequency range of the GaAs LO mode for various GaAs/GaAlAs superlattices [3.67, 154]. The spectra are shown as two series. The first one corresponds to samples with all parameters fixed except the thickness of the GaAs layer. In the second one, the only varying parameter is the Al concentration in the $Ga_{1-x}Al_xAs$ layer. These spectra display four lines in the frequency range of the LO phonon of bulk GaAs, more precisely, at frequencies smaller or nearly equal to it. The upper line, whose shift from the bulk LO frequency is only noticeable for GaAs layer thicknesses smaller than 30 Å, always dominates the spectra. When the GaAs layer thickness is

105

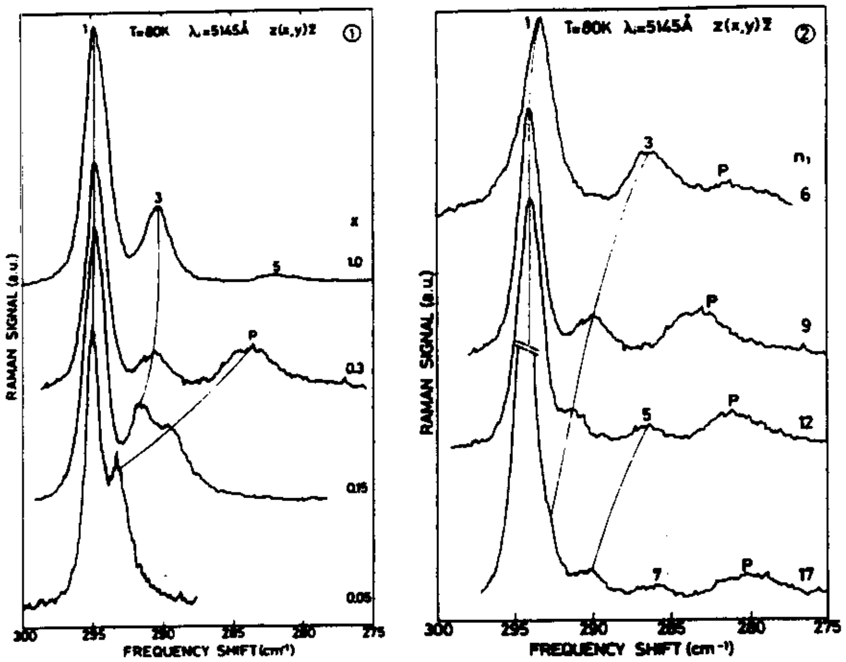

Fig. 3.35. Raman spectra in the GaAs optic modes frequency range obtained for two series of GaAs/$Ga_{1-x}Al_xAs$ superlattice with a single varying structural parameter: (*1*) the Al concentration x, [3.154]; (*2*) the number of GaAs monolayer in each period n_1 [3.67]

reduced, the lines labeled 1, 3, 5 shift towards lower frequency, whereas the line labeled P is almost unchanged. When the Al concentration is reduced, line P strongly shifts towards higher frequency whereas the other lines are pushed only slightly in the same direction. This behavior is rather similar to that of quantum levels in an electronic quantum well. The confined frequencies depend strongly on the well thickness and only slightly on its depth, at least as long as they are sufficiently below the top of the well. As pointed out in Sect. 3.2, such phonon quantum wells appear for partly non-overlapping optic phonon branches of the two bulk constituents, a feature approximately displayed by the pure GaAs band and the GaAs-type band of $Ga_{1-x}Al_xAs$. However, contrary to the case of acoustic phonons, whose frequencies in the alloy can be well described by using the virtual crystal approximation, the optic phonons in these alloys display a qualitatively different behavior from that of pure compounds. $Ga_{1-x}Al_xAs$ is a prototype of two-mode-behavior [3.155]: over the whole concentration range, two different optic bands coexist. Their frequencies vary only slightly with x, each of them lying in the vicinity of the optic band of one of the constituting pure compounds. Moreover, their relative intensity qualitatively reflects the concentration of the corresponding compound. They have thus been identified as GaAs-type and AlAs-type optic bands of $Ga_{1-x}Al_xAs$. This identification has been further supported by CPA calculations of the alloy lattice dynamics [3.156] which demonstrated that the local density of states at frequencies inside, say, the

GaAs-type band is large on the Ga – As bonds of the alloy. Moreover, these calculations provide "thick" (broadened) dispersion curves [3.157], an extension of the usual notion of sharp eigenstates in perfectly ordered crystals to moderately disordered systems. Since $Ga_{1-x}Al_xAs$ is indeed a weakly disordered system [3.158], these "thick" dispersion curves display only small broadenings, in good agreement with the results of light scattering. In [3.67] the following approximate description of the Raman spectra in the GaAs-type energy range of $GaAs/Ga_{1-x}Al_xAs$ superlattices (with $x \cong 0.3$) is thus introduced. In order to apply the simple alternating linear chain model described in Sect. 3.2.3, the authors fit both the pure GaAs and the GaAs-type LO dispersion curves in $Ga_{1-x}Al_xAs$ with linear chain models. In both cases, "effective masses" must be introduced and the free parameters are chosen so that the effective masses of As as well as the spring constants are the same in both compounds. This description greatly simplifies the dynamical properties of the alloy: the AlAs-type band is neglected as well as disorder in the GaAs-type band of the alloy. Better descriptions, which use, for instance, the CPA technique for superlattices, are beyond the present computational capabilities of most workers. On the other hand, replacing in the calculation the alloy layer by an ordered chain of the same average composition, as suggested by *Worlock* [3.159], is not very useful. Even if the zone center frequencies of, for example, the $Ga_{0.5}Al_{0.5}As$ alloy and $GaAlAs_2$ compound are nearly the same, their dispersion curves should be rather different. Using this rough model provides, however, a reasonable description of the experimental results. A comprehensive comparison is not easy because the frequencies depend on three different sample parameters: both layer thicknesses and the aluminium concentration x. As concerns the confined modes, their frequency strongly depends on the GaAs well thickness, slightly on its depth which is related to x, and very weakly on the barrier thickness. Among the bulk parameters introduced in the fit, three of them have a significant effect on the confined frequencies: both zone center LO modes, which are well known, and the curvature of the GaAs LO dispersion curve, which is extracted from the bulk neutron scattering data [3.160]. As we shall emphasize in the case of pure GaAs/AlAs superlattices, this feature is not known very well (recent and more accurate measurements for GaAs are shown in Fig. 3.1): it has been suggested that Raman scattering on superlattices may provide a rather good method to determine the bulk dispersion curves.

As concerns the selection rules and line intensities off-resonance, a good description is obtained using zone center Raman selection rules and the bond polarizability model. Contrary to the folded acoustic case, the finite value of the superlattice wavevector involved is insignificant. Confined optic modes are indeed not sensitive to the periodicity of the system but rather to the thickness of the individual layer in which they are confined. Since their penetration depth in the barriers is generally less than one monolayer, this statement is valid even for very small thicknesses. As for electronic *multiquantum wells*, the corresponding spectra are a superposition of the contribution of each quantum well and reflect the periodicity of the sample only through the superposition of these contributions. In terms of frequency, the dispersion curves for $\boldsymbol{k} \parallel z$ are very flat and thus the results are independent of scattering wavevector.

The Raman selection rules predict the observation of the B_2 modes in $z(x, y)z$ and the A_1 modes in $z(x, x)z$ configuration. One should observe in $z(x, y)z$ configuration only odd parity modes, i.e., those belonging to the B_2 representation. The origin of the non-observation of the A_1 modes off-resonance has already been suggested in Sect. 3.2.3 within the framework of the bond polarizability model: the A_1 modes are forbidden for the exact cubic symmetry. Their activation, in a local description, comes only from the non-cubic sites in the structure, i.e., from the interface atoms. In usual superlattices, such atoms are not so frequent and their displacement is very small for confined modes. On the other hand, their activity is proportional to the polarizability modulation, contrary to that of the B_2 modes. The Raman activity of the latter can be described semi-quantitatively on the basis of the bond polarizability model. It is large when the contributions of the different bonds interfere constructively. This is the case in particular when a local wavevector is small, i.e., when the frequency of the modes is close to the zone center bulk frequency in a given layer. This explains why mode 1 is always intense due to the contribution of the well layers, and the other modes when they are close to the top of the barrier due to the contribution of the barrier layers (see Fig. 3.23), a fact which agrees with experimental observations. From an analysis of these intensities, one could estimate the relative magnitude of α_{xy} in both constituents. However, the description of an alloy as a pure effective compound is more questionable for eigendisplacements than for eigenenergies. These relative intensities have been experimentally shown to be strongly dependent on the incident wavelength, especially near resonance with electronic transitions, a fact that reveals the rough nature of the model.

c) The Optic Vibrations of GaAs/AlAs Structures

The optic phonons of these structures are similar in many ways to those of the GaAs/$\mathrm{Ga_{1-x}Al_xAs}$ structures. From the lattice-dynamical point of view, they are simpler but also poorer in unusual features since the optic phonons are all confined, either to the GaAs or to the AlAs layers. Due to the large difference between the Ga and Al atomic masses there is no overlap between the optic phonon bands of the two compounds. On the other hand, this system is very interesting as it involves two pure compounds and thus, can be described without the drastic approximations introduced for the $\mathrm{Ga_{1-x}Al_xAs}$ alloy.

Due to the large energy separation between the optical bands of GaAs and AlAs, the properties of the modes confined in, let us say, the GaAs layers, are almost independent of the details of the AlAs layers, including the dynamical properties of bulk AlAs. This has stimulated several groups to perform quantitative comparisons between calculated and measured frequencies [3.39, 42, 59, 62–66b, 101, 111–113, 147–149]. The common aim was to check the validity of the model for the GaAs modes, the bulk properties of this compound

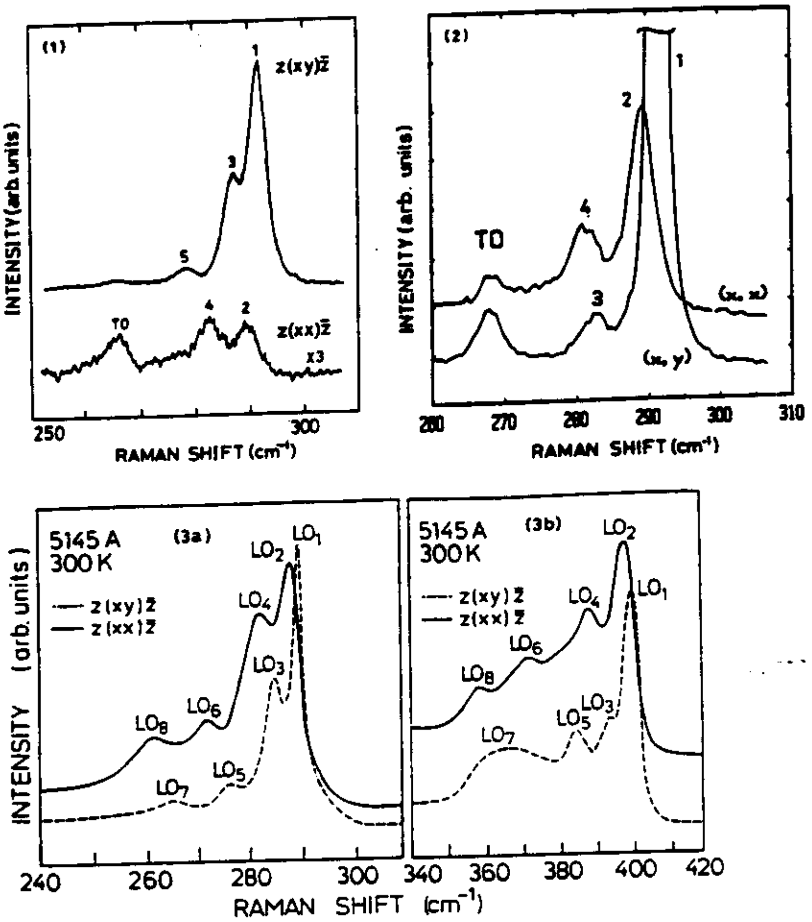

Fig. 3.36. Typical Raman spectra of confined optic modes in GaAs/AlAs superlattices obtained: (*1*) out of resonance, in the GaAs optical phonon range [3.111], (*2*) in resonant conditions in the same frequency range [3.108], (*3*) out of resonance for both the GaAs (*a*) and the AlAs (*b*) optical phonon ranges [3.149]

being assumed to be well known. In a second step, one could determine the bulk LO dispersion curve for AlAs which has not been determined so far. Figure 3.36 shows typical Raman spectra obtained on GaAs/AlAs structures by various groups, including both GaAs-type and AlAs-type modes of both A_1 and B_2 character. Contrary to the GaAs/Ga$_{1-x}$Al$_x$As structure, the A_1 modes have indeed been observed on GaAs/AlAs superlattices, first out of resonance as very weak structures [3.22, 111], then very clearly under resonance conditions [3.66a]. From these observations and the concomitant polarization selection rules, it was proved that the confined modes display alternating symmetries: the odd (even) indices corresponding to the B_2 (A_1) representation [3.66a]. Very recently, new Raman results have been obtained [3.149] giving evidence of well-resolved A_1 and B_2 modes, even out of resonance. Moreover, contrary to the previous works devoted to GaAs-type modes, these authors report the observation of all possible confined modes both in the GaAs and AlAs energy range. For instance, they report the observation in a $(GaAs)_8/(AlAs)_8$ structure, of eight GaAs and eight AlAs optic modes. These observations are rather impressive and they differ qualitatively from all previous reports. In the AlAs energy range, the spectra are usually weak, and higher order confined modes are thus difficult to resolve.

Let us now return to the analysis of the confined frequencies. Whereas some authors [3.39, 66b, 101, 111, 112, 147, 148] compared the measured frequencies with those calculated by using the alternating chain formalism as a function of the corresponding layer thickness, following the same approach as used for GaAs/GaAlAs structures, some others [3.42, 62–66a, 149, 150] took advantage of the strong confinement to introduce a direct comparison between the measured frequencies and the dispersion relation of the corresponding bulk compound. This method has the advantage of providing a comprehensive comparison between results depending on two parameters (the line index and the layer thickness) with a single curve (the bulk dispersion curve). The idea underlying this method was suggested in [3.65]: one can assign to each confined mode in a layer of given thickness an effective bulk wavevector depending on these two parameters. By analogy with a vibrating string, the effective wavevector was first taken to be that of (3.26) where $m=1, 2, 3,$ ~~is~~ the line index and d the layer thickness. *Sood* et al. [3.66a] plotted their experimental results obtained for three different samples and involving several confined modes together with the bulk neutron scattering results and emphasized some discrepancies. *Molinary* et al. [3.64], in a comment to [3.66a], demonstrated that calculated confined frequencies displayed a somewhat similar discrepancy with the bulk reference dispersion curve and attributed this discrepancy to superlattice effects. Finally, *Jusserand* et al. in another comment to the same paper [3.62], demonstrated that this discrepancy was more likely a boundary conditions effect than a superlattice effect. They derived from the alternating linear chain dispersion relation an approximate relation valid for strong confinement. It reduces to the definition of the effective bulk wavevector given in (3.25) which differs from (3.26). This difference originates from the microscopic nature of the problem and becomes important only for small layer thicknesses. It can be easily understood by considering that interfacial As atoms (separated by the period d) are not fixed but, instead, the first Al atoms in the barrier (distance between Al atoms both sides of the GaAs layer $d+a$). Using this more accurate expression reduces the discrepancy pointed out in [3.66], whereas more recent results [3.149] plotted vs q using (3.25) do not give any evidence of a discrepancy with bulk dispersion relations, as illustrated in Fig. 3.37.

The basic question which remains open is whether Raman scattering on thin layer superlattices can be used reliably to determine the dispersion relations of the phonons of the bulk constituents. Raman scattering does indeed provide a better frequency accuracy, but the validity of (3.25) for the determination of the equivalent wavevector is not always evident. The sensitivity of q to the interface quality may also be a serious problem. On the other hand, this method remains

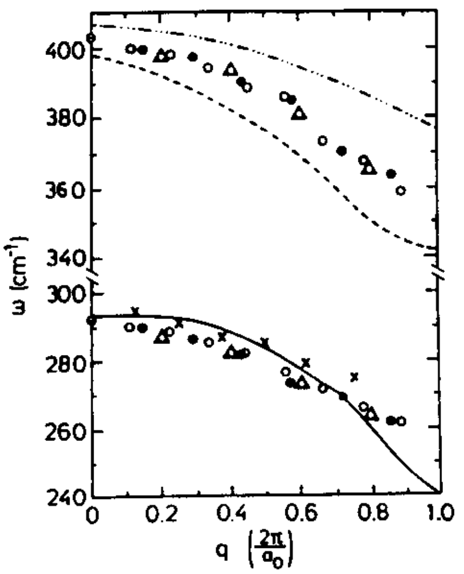

Fig. 3.37. Confined GaAs-type and AlAs-type LO frequencies measured for different GaAs/AlAs superlattices (*symbols*) plotted vs. q with the use of (3.25) compared to the GaAs bulk dispersion curve measured by neutron scattering (——) and two different calculations of the dispersion relations of AlAs (- - -, –·····–) [3.149]

unique for compounds which are not available in large volume. For instance, the recent results on AlAs (see Fig. 3.37) should generate some new interest in the lattice dynamics of this frequently used and poorly known compound.

Very recent work [3.35a] shows that calculated and measured frequencies of GaAs/AlAs superlattices oriented along [100] and [012] can also be mapped on the corresponding bulk dispersion relations with (3.25). In these superlattices, however, longitudinal and transverse modes are mixed, a fact which leads to interesting effects (m odd-even mixing) in the eigenvectors.

d) Experimental Results Involving Out-of-Axis Vibrations

The single reported experiment which involves light propagation out of the superlattice axis [3.54] is illustrated in Fig. 3.38. The difficulty in obtaining these scattering conditions is due to the small thickness of the epitaxial layers (~1 μm), and the large refractive index which makes oblique incidence outside the sample nearly normal to that inside. The authors of [3.54] thus performed a right-angle scattering experiment, the incident light focussed as usual on the (001) surface of the sample and the scattered light being collected through the side (edge). This collection is possible with good efficiency thanks to two circumstances: (i) the incident wavelength is just at the band edge so that the structure is transparent to the *scattered* light and (ii) two cladding layers of $Al_xGa_{1-x}As$ enclose the superlattice, which forms a waveguide for the scattered light. Near-resonant conditions are thus also involved in this experiment.

The spectra obtained in different polarization configurations are shown in Fig. 3.38 for a GaAs/GaAlAs sample with $d_1 \cong d_2 \cong 100$ Å. For such thicknesses, confinement effects on the optic phonon frequencies are not expected. They mainly emphasize the observation of puzzling selection rules given the local cubic symmetry: an LO (TO) line is observed in a configuration where a TO (LO)

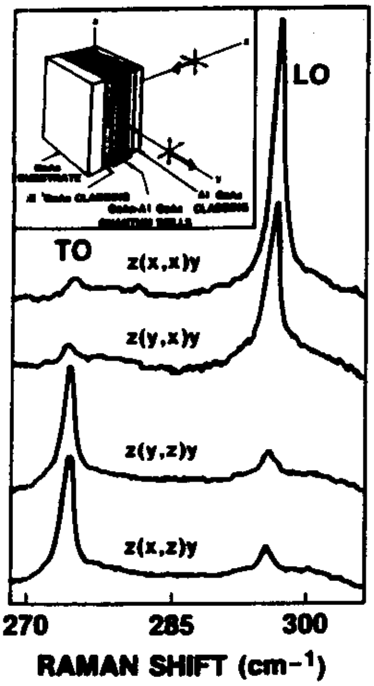

Fig. 3.38. Raman spectra of a GaAs/GaAlAs superlattice in the frequency range of optical phonons of GaAs obtained for different polarizations in the right angle scattering configuration illustrated in the inset together with the structure of the sample [3.54]. The superlattice is clad with GaAlAs so as to act as a waveguide for the scattered radiation

mode is Raman allowed. In these experiments, the wavevector of the phonon emitted in the scattering process is indeed oriented along y (the dispersion along z, and thus the corresponding wavevector component can be neglected). In the $z(y,x)z$ configuration,which allows the observation of a mode of eigendisplacement along u_z, it thus seems that a TO line should be observed, while in the $z(x,z)y$ configuration, which allows the observation of a mode of eigendisplacement along u_y, one might expect an LO line. The experimental results are just the opposite. This can be understood as due to the confinement of the vibrations. One must therefore take into account the *axial* local wavevector associated with the confined modes (3.25). As long as the in-plane wavevector component is smaller than the effective axial one (3.25) fixed by the layer thickness, the latter dominates and fixes the longitudinal or transverse character of the modes and an apparent, but understandable, breaking of the selection rules takes place.

The second series of experimental results concerning out-of-axis vibrations is of a different nature since the in-plane wavevector is not created purposely in a controlled manner, but appears due to some relaxation of the selection rules. Such relaxation is often observed near resonance and its origin is generally assigned to impurity assisted scattering processes (see Sect. 3.5). Such an effect has been first invoked by *Merlin* et al. [3.7] to explain the emergence near resonance of a new line between the TO and LO components of both the GaAs-type and the AlAs-type modes in a 14 Å AlAs superlattice (see Fig. 3.39). To explain this feature, they introduced the electrostatic anisotropic effective medium model (Sect. 3.2) and attributed these new modes to additional roots and poles in the effective dielectric constants (3.28). *Merlin* et al. [3.71] described,

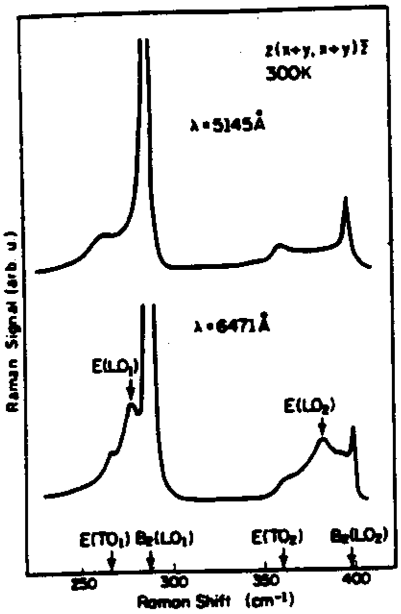

Fig. 3.39. Raman spectra of a GaAs/AlAs superlattice obtained out of resonance (*upper trace*) and at resonance (*lower trace*) [3.71]. The lines $E(LO_1)$ and $E(LO_2)$ which appear at resonance are believed to be due to interface modes. [3.55]

the corresponding vibrations as "bulk" confined modes propagating in the layer plane. Similar structures have indeed been later observed and re-interpreted in [3.55]. Their interpretation was based on the following observations:

- the AlAs and GaAs modes both display a resonant behavior near electronic transitions strongly confined to the GaAs layers,
- they appear as broad bands spread out between the TO and LO modes and display asymmetric lineshapes depending on the relative thickness of both GaAs and AlAs constituting layers.

A common feature of these observations and of the expression of the additional solutions introduced by *Merlin* et al. [3.71] is that the parameters of both layers are involved. These additional structures should thus be assigned to interface modes and not to bulk confined ones.

On the basis of the electrostatic model for layered structures we described in Sect. 3.2, *Sood* et al. [3.55] explained the lineshapes of the bands and their dependence on the layer thickness ratio. This is more clearly seen in the AlAs region, where the confined modes are less intense, as illustrated in Fig. 3.40. The asymmetric line shape is attributed to the different symmetry of the two interface modes existing in this frequency range (see Fig. 3.16). The antisymmetric component, which appears at lower or higher frequency depending on the relative thicknesses, is indeed not active via intra-band Fröhlich interaction (Sect. 3.5.1) which dominates the scattering process near resonance. The same analysis in the GaAs-type frequency range is not as clear, the spectra being dominated by the confined modes.

One must point out two main hypotheses of this description:

- the axial and in-plane selection rules must both be strongly relaxed for these modes, and not for bulk confined ones

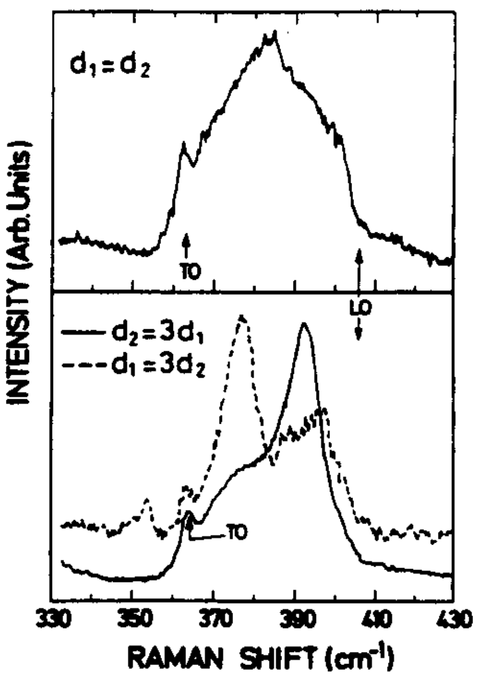

Fig. 3.40. Raman spectra in the frequency range of the optical phonons of bulk AlAs obtained at resonance in the $z(x,x)\bar{z}$ configuration for three GaAs/AlAs structures with different layer thickness ratios [3.55]

- there is no effect of coupling between the two families of modes although they are degenerate and some share the same symmetry (see Fig. 3.19).

Thus, some questions remain open in this novel field. Interface modes have been recently observed on other superlattice such as CdTe/ZnTe [3.160], diluted magnetic structures [3.127] and GaAs/Ga$_{1-x}$Al$_x$As [3.153]. Moreover, a magnetic field enhancement of the resonant Raman spectra on confined LO modes and an even stronger one on interface modes has been recently reported [3.151]. Also, an enhancement with decreasing laser power density has been observed [3.152]. These results seem to support the role played by the in-plane wavevector relaxation in these observations. Nevertheless, the need for a microscopic description of these features remains, even if a qualitative description is obtained using the electrostatic approximation [3.73a].

3.4.4 Light Scattering in Superlattices: Application to Sample Characterization

a) Introduction

In the former subsections we discussed the information that one can extract from light scattering experiments concerning the lattice dynamics of superlattices. As the main features are now reasonably established for the well characterized GaAs–AlAs system, it is interesting to look at the information that one can obtain from light scattering spectra on the structural parameters of superlattices:

- the dispersion curves of the constituting bulk compounds

- the thickness of the constituting layers or, more generally, the size and structure of the supercell
- the modifications of these properties due to strain when the two constituents are not lattice matched.

We have already considered the first point when extracting the AlAs sound velocity from the average frequency of folded acoustic doublets and when comparing the bulk optic dispersion curves with the frequencies of the modes confined to GaAs and AlAs. These methods are very useful for finding information about compounds which are difficult to produce as large samples. We already emphasized the sensitivity of these determinations to the accuracy in the structural parameters and to imperfections in the compositional profile. Here we shall consider the structural information one can extract from the Raman scattering spectra of superlattices and compare it with that obtained by the more usual x-ray diffraction method.

So far we have neglected the difference in lattice parameters between the two constituent cubic bulk compounds and also between them and the substrate. This approximation was justified for GaAs/AlAs structures grown on a GaAs substrate since the relative difference of the lattice parameters of GaAs and AlAs is less than 1‰. We will analyze, in a second subsection, the effect of strain on the vibrations of the superlattice.

b) Structural Characterization Using the Vibrations of a Superlattice

The usual method to determine the structural parameters of superlattices is x-ray diffraction [3.145]. From the distance between the satellites which appear around the diffraction peaks of the average compound, an easy accurate and direct determination of the period of the sample is obtained. In perfectly lattice-matched structures, no more structural information can be deduced from these positions and the observation of these satellites originates only from the modulation of the atomic structure factor. Using an inverse Fourier transform, one can then deduce the structure profile from the satellite intensities with an accuracy depending on the number of observed satellites. Real superlattices are actually divided into nearly lattice-matched (mismatch $< 1\%$) ones and strained ones. In the former case, the previous analysis remains valid [3.161]. Moreover, the diffraction peak of the substrate is now slightly separated from the one for the average compound, a fact which enables us to determine its composition. Thanks to this additional feature, the thicknesses d_1 and d_2 of a simple GaAs/AlAs structure can be deduced by considering only the satellite positions. For strained layer superlattices, two modulations are involved and the x-ray diffraction patterns look very different [3.146]. A numerical fit of the positions and intensities is needed in this case.

The superlattice vibrations provide two probes of different nature, which potentially make light scattering an interesting tool to characterize the structural properties. The folded acoustic modes which propagate along the axis are mainly sensitive to the long range order. They thus provide information on the periodicity of the system and on the inner structure of the supercell, in a way rather similar to the x-ray satellites. Assuming perfect acoustic matching, the period of the sample can be easily deduced from the average doublet frequency. Taking into account the small acoustic mismatch displayed by presently existing superlattices makes this measurement less direct. In the experimentally derived quantity vd, the average sound velocity v (3.11) actually depends slightly on the details of the structure. Nevertheless, a good estimate of the period is obtained from this rapid and easy measurement. *Brugger* et al. used this method for Si/Ge structures [3.128] with an additional refinement. From the doublet splitting and the knowledge of the phonon wavevector, one can derive the superlattice velocity v and thus determine the period d with a better accuracy. Moreover, from the value of v, a rough estimate of the thickness ratio in a simple structure can be obtained. On the other hand, the determination of this ratio from the gap openings, which strongly depend on its value, is not accurate due to their small magnitude.

Thanks to the large modulation of the photoelastic coefficient, the line intensities are strongly sensitive to the thickness ratio, as we showed previously, and more generally to the inner structure of the supercell. This feature has been investigated in two different contexts: (i) the analysis of samples containing more than two layers by period and (ii) the characterization of interdiffusion profiles.

As concerns the first point, such complex samples have been first considered by *Nakayama* et al. [3.58]. They pointed out that for several GaAs/$Ga_{0.5}Al_{0.5}As$/AlAs structures the folded mode frequencies were strongly dependent on the period but not on the relative thicknesses of the three layers, whereas the relative intensities were strongly affected by the thickness ratio (see Fig. 3.41). This feature has been analyzed quantitatively in [3.60]. As illustrated in Fig. 3.42 for a $(GaAs)_{d_1}(AlAs)_{d_2}(GaAs)_{d_1}(AlAs)_{d_3}$ period, the calculated spectra only reproduce the line intensities when the details of the supercell are taken into account. A similar problem has recently attracted interest in connection with the Fibonacci superlattice [3.135–138], (see Chap. 5 of this volume). Raman intensities have indeed been demonstrated to be very sensitive to the long range quasiperiodic order in these systems.

Raman scattering studies of superlattices with smeared out interfaces were first reported in [3.65]. A decrease of the intensity of the lower acoustic doublet was observed when the superlattice was annealed at 850 K for an increasing length of time; the frequencies of the lines remained unchanged. This result was assigned to the diffusion of the interfaces which induces a decrease in the non-zero Fourier components of the profile. A similar effect was observed later [3.59] on analogous samples grown by MBE at different substrate temperatures. A simple quantitative analysis of the intensities was performed. By using an erf-function profile involving a free interface broadening parameter, one can describe the variation of the average intensity of both the first and second folded doublets by using the same broadening parameter. Some insight on the quality of the samples was thereby obtained for the first time using Raman scattering and

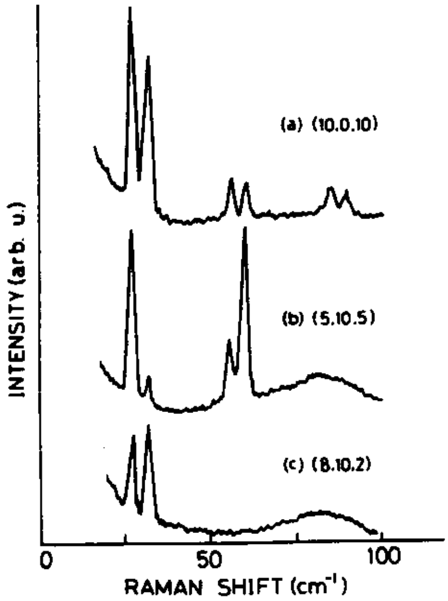

Fig. 3.41. Low frequency Raman spectra obtained for GaAs/GaAlAs/AlAs samples with equal periods and different individual layers thicknesses ($n1, n2, n3$ in monolayers) [3.58]

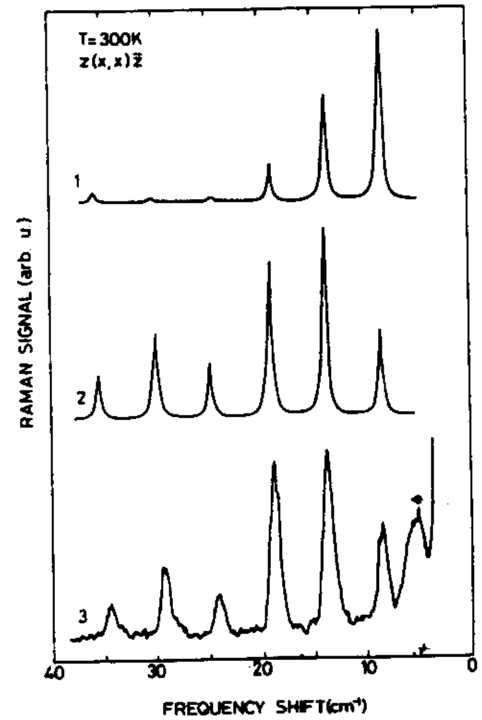

Fig. 3.42. Low frequency Raman spectra (*3*) obtained for a $(\mathrm{GaAs})_{d_1}/(\mathrm{AlAs})_{d_2}/(\mathrm{GaAs})_{d_1}/(\mathrm{AlAs})_{d_3}$ sample [3.60] compared with calculated spectra which either take into account the detail of the structure (*1*) or consider a $(\mathrm{GaAs})_{2d_1}/(\mathrm{AlAs})_{d_2+d_3}$ simplified cell (*2*)

the study was later extended to superlattices grown by organometallic vapor phase epitaxy (OMVPE) [3.114]. This analysis has been recently applied to annealed structures and correlated with the predictions of the diffusion theory and with x-ray measurements for the same samples [3.119]. However, as pointed out by *Klein* [3.99], the photoelastic model is easy to apply when the photoelastic coefficient varies linearly with x. In continuously varying GaAs/Ga$_{1-x}$Al$_x$As structures, this description is questionable as the usual incident energies lie between the frequency gaps of GaAs and AlAs and resonant features in the photoelastic profiles are expected.

To summarize, Raman scattering spectra of folded acoustic lines provide information similar to x-ray diffractometry. However, as the measured quantities are less directly connected to the structure parameters, lower accuracy can be expected. No real systematic comparison has been reported so far, and Raman scattering is certainly very useful when x-ray diffraction is not available or difficult to set up (for instance in the case of in situ characterization in high vacuum chambers).

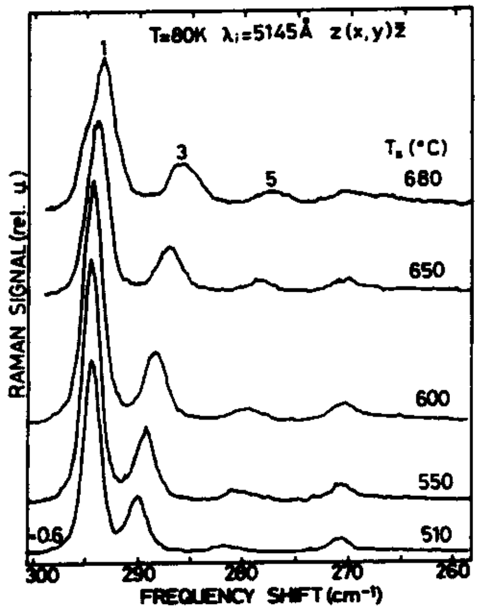

Fig. 3.43. Raman spectra in the GaAs optical phonon range for a series of GaAs/AlAs superlattices with the same structural parameters but grown at different substrate temperature T_s [3.59]

Raman scattering also provides a second type of probe of the sample parameters through the confined optic vibrations. Contrary to the folded acoustic modes, they are sensitive to the local properties of the structure and give information on the potential well in which they are confined. This can be applied to determine individual layer thicknesses in superlattices and thus complete or check the data extracted from the folded acoustic lines. This has also been shown to be powerful for probing the shape of the interfaces [3.59]. Figure 3.43 shows the Raman spectra of phonons confined to the 25 Å thick GaAs layers of the same series of MBE sample used for folded acoustic intensity measurements. In all samples, three LO confined modes are observed whose intensity and width change only slightly from sample to sample. Their peaks shift towards lower frequencies, a fact which is assigned to the effective shrinkage of the layer thickness due to interface broadening. Because of the non-abrupt profile, the thickness seen by a confined mode depends on its frequency. As a consequence, the Raman spectra cannot be reproduced using the alternating linear chain model except for samples grown at low substrate temperature. A crude quantitative model has been introduced on the basis of an alternating linear chain with continuously varying effective parameters [3.59].

Using the erf-function profile allows the authors to fit the three confined mode positions with the same interface broadening parameter; the values obtained for this parameter are close to those deduced from the folded acoustic line intensities. While this method requires the knowledge of the corresponding bulk dispersion curve, the authors introduce a semi-quantitative test of the interface profile which only makes reference to the nearly parabolic shape of the dispersion curves involved. Under this assumption, the relative frequency separation between the confined modes directly reflects the shape of the well. For a rectangular (or parabolic) profile, the successive confined frequencies follow a quadratic (linear) progression. From the comparison of the line separation, an estimate of the profile abruptness is obtained. A similar analysis was not possible in the AlAs-type frequency range as only one confined mode was observed. From the recent Raman determination of the bulk dispersion curve [3.149], an analysis of the AlAs layer shape could be undertaken on the basis of the shift of this single confined frequency. As in the case of folded acoustic line intensities, a similar analysis has been applied to superlattices grown by OMVPE under different conditions [3.114] and recently, to annealed superlattices [3.119, 162].

c) Strained Layer Superlattices

Thus far, we have neglected the difference between the lattice parameters of the superlattice bulk constituents and that of the substrate. When "pseudomorphic growth" is achieved, the substrate, which is very thick compared to the epitaxial layer, imposes its lattice parameter in the directions perpendicular to the growth axis. The epitaxial layers then suffer a tetragonal elastic deformation. When the substrate is identical to one of the superlattice constituents (e.g. GaAs in GaAs/AlAs structures), the strain is localized in the other constituent (this can be changed by using a buffer layer between substrate and superlattice). These deformations accumulate elastic energy in the sample. Above a critical thickness, whose magnitude is not well understood, misfit dislocations appear which relax the strain in the layers. In superlattices two different critical thicknesses must be considered: the first one is related to the relaxation of the individual layers, one relative to the other, and the second one is related to the relaxation of the superlattice considered as a whole, relative to the substrate.

The strain due to lattice mismatch is invariant under the point group of the superlattice (D_{2d} for a [001]-grown superlattice). Hence, some shift of the LO and TO modes is expected without any additional splitting. Some change in the acoustic velocities is also predicted. This, together with the small lattice mismatch in the usual systems, explains why so little work has been devoted to this problem, only in the following structures:

- GaSb/AlSb [3.120–123], GaAs/InGaAs [3.154, 163]
- $Si/Si_{1-x}Ge_x$ [3.164, 165]
- some II–VI compounds: ZnTe/ZnSe [3.166], ZnTe/ZnS [3.167], CdTe/ZnTe [3.150], $ZnSe/ZnS_xSe_{1-x}$ [3.19]
- ZnSe on GaAs [3.168], ZnTe on GaAs [3.19].

In all these studies of superlattices except [3.150], the effect of strain is investigated on the LO line confined in layers whose thickness is too large or whose crystalline quality is too poor to induce a significant confinement effect. Raman scattering can then be used as a probe of the local strain exactly as for the global strain in a thick layer [3.169]. This interesting feature appears thanks to the local character of the Raman probe. Depending on the substrate, Raman

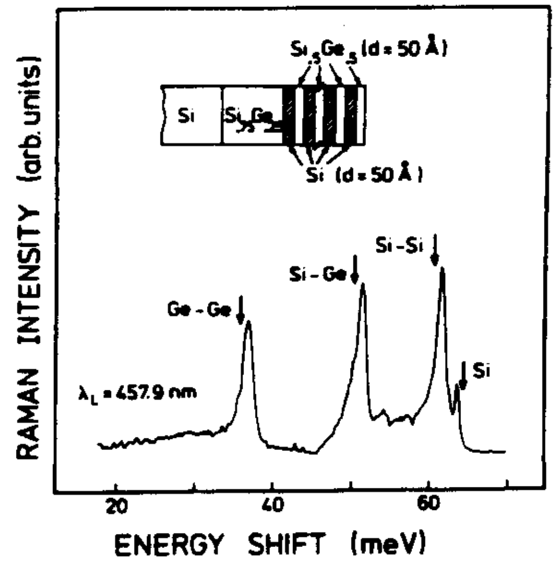

Fig. 3.44. Raman spectrum of the Si/SiGe structure described in the inset. *Arrows* indicate the corresponding frequencies in absence of strain [3.164]

shifts can be observed either for both compounds in opposite directions or restricted to the single strained one. The former case is illustrated in Fig. 3.44 in Si/$Si_{0.5}Ge_{0.5}$ structures grown on a $Si_{0.75}Ge_{0.25}$ buffer layer. The optic mode of the Si layers is shifted towards lower frequency whereas the three different modes of the alloy are shifted in the opposite direction. In the case of GaSb/AlSb structure grown on AlSb buffer layers, a Raman shift is only observed on the

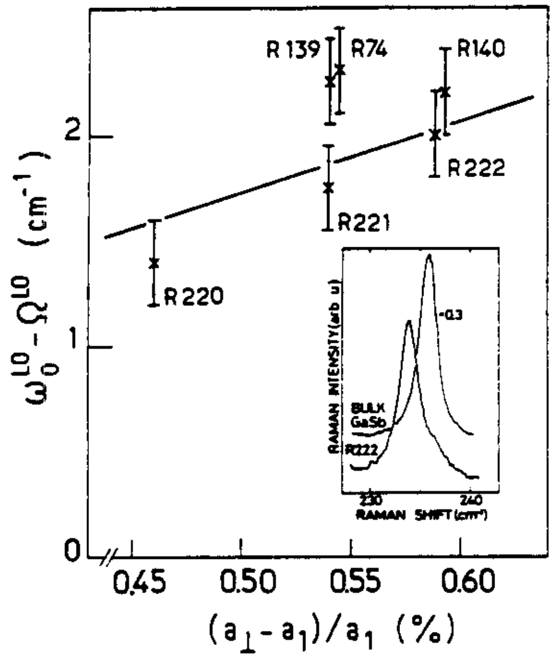

Fig. 3.45. Theoretical (——) and experimental values of the strain-induced shift of the GaSb-type LO frequency in GaSb/AlSb superlattices shown as a function the strain-induced change in lattice parameter of the GaSb layers along the superlattice axis. From [3.120]

12c

GaSb LO line and can be quantitatively assigned to the elastic deformation (see Fig. 3.45). The strain has striking consequences in GaAs/$In_{1-x}Ga_xAs$ structures. As reported in [3.163], a single GaAs-like LO line is observed in this system, contrary to the prediction, based on unstrained data, of a GaAs-like band ordering very similar to that of GaAs/$Ga_{1-x}Al_xAs$. However, due to the strain, which almost exactly compensates the alloying effect, there is no modulation of the GaAs-like optic phonon frequency in this system [3.154].

Recently, *Menéndez* et al. [3.150] reported the observation at resonance of several confined modes in the highly strained CdTe – ZnTe system. They extract information on strain from a quantitative analysis of the confined frequencies with the alternating linear chain model and look for the corresponding shift of bulk optical branches. It would be interesting to investigate by these methods the strain-induced change in the shape of the optic dispersion curves or in the value of the sound velocity obtained from the zone folded frequencies in strained layer superlattices. We should also mention that *Olego* et al. [3.19] have been recently able to determine strain profiles. vs. depth in superlattices and in single epitaxial layers by measuring Raman spectra for different laser wavelengths (i.e., penetration depths). The strain has been shown to decrease from the interface to the substrate to the outermost free surface.

In order to quantify the effects of strain on the optical phonons of a zincblende-type bulk material, a dimensionless fourth rank tensor $\tilde{K}_{ij}$ (in contracted index notation) is defined [3.170]. The relative frequency shifts are obtained by contracting this tensor once with the strain and twice with the direction of the vibration under consideration. This tensor has, for the T_d point group, three independent components $\tilde{K}_{11}$, $\tilde{K}_{12}$, and $\tilde{K}_{44}$ which are sometimes replaced by three parameters p, q, r with the dimensions of a frequency squared [3.171]:

$$p=\tilde{K}_{11}\omega^2\,, \qquad q=\tilde{K}_{12}\omega^2\,, \qquad r=\tilde{K}_{44}\omega^2\,. \tag{3.71}$$

These parameters are usually determined by means of Raman and IR measurements on samples subjected to uniaxial [3.170] or hydrostatic stress [3.169]. Results for zincblende-type materials are listed in Table 3.1. It is thus customary to split the strain into hydrostatic and uniaxial components. The effect of the hydrostatic component is described by the Grüneisen parameter γ related to $\tilde{K}_{ij}$ through

$$\gamma=-\frac{\tilde{K}_{11}+2\tilde{K}_{12}}{6}\,. \tag{3.72}$$

The other two independent components of $\tilde{K}_{ij}$, $\tilde{K}_{11}-\tilde{K}_{12}$ and $\tilde{K}_{44}$, described the effects of a pure shear (traceless strain tensor) along [100] and [111], respectively. For lattice matched adjacent layers A, B perpendicular to [001] with different bulk lattice constants one find [3.165] for the "singlet" vibration along [001]:

$$\frac{\Delta\omega_s}{\omega}=\frac{\tilde{K}_{11}}{2}\,\varepsilon_{zz}+\frac{\tilde{K}_{12}}{2}\,(\varepsilon_{xx}+\varepsilon_{yy})\,, \tag{3.73}$$

Table 3.1. Coefficients which determine the hydrostatic shift ($\tilde{K}_{11}+2\tilde{K}_{12}$) and the shear splittings ($\tilde{K}_{11}-\tilde{K}_{12}, \tilde{K}_{44}$) of diamond- and zincblende-type bulk semiconductors. In the cases where the coefficients for LO and TO phonons are given as equal, no sufficient experimental information is available to determine the separate values.

	$\tilde{K}_{11}+2\tilde{K}_{12}$		$\tilde{K}_{11}-\tilde{K}_{12}$		$\tilde{K}_{44}$	
	LO	TO	LO	TO	LO	TO
Si[a,b]	−5.5	−5.5	0.48	0.48	−0.61	−0.61
Ge[a,b]	−6.7	−6.7	0.46	0.46	−0.87	−0.87
AlSb[c]	−6.0	−5.2	0.97	0.55	−0.34	−0.71
GaP[a,d]	−6.5	−5.7	1.03	0.60	−0.50	−0.58
GaAs[a,e]	−7.4	−8.3	0.70	0.30	−0.53	−0.88
GaSb[f,g]	−7.3	−8.0	0.22	0.22	−1.08	−1.08
InP[a,h]	−7.4	−8.6	1.20	0.69	−0.18	−0.47
InAs[f,g]	−6.4	−7.3	0.57	0.57	−0.76	−0.76
InSb[f]	−7.0	−8.5	–	–	–	–
ZnS[a]	−6.0	−6.6	–	–	–	–
ZnSe[a,g]	−5.4	−8.4	1.24	1.24	−0.43	−0.43
ZnTe[a]	−7.2	−10.2	–	–	–	–

[a] [3.169]. [b] M. Chandrasekhar, J.B. Renucci, M. Cardona: Phys. Rev. **B17**, 1623 (1978).
[c] [3.173]. [d] I. Balslev: Phys. Stat. Sol. **B61**, 207 (1974).
[e] [3.170]. [f] K. Aoki, E. Anastassakis, M. Cardona: Phys. Rev. **B30**, 681 (1984).
[g] F. Cerdeira, C.J. Buchenauer, F.H. Pollak, M. Cardona: Phys. Rev. **B5**, 580 (1972).
[h] [3.172].

where ε_{zz} and $\varepsilon_{xx}=\varepsilon_{yy}$ are the components of the strain tensor related, for medium A, to the lattice mismatch $\varepsilon=(a_A-a_B)/\langle a\rangle$ through

$$\varepsilon_{xx}=\varepsilon_{yy}=-\varepsilon;\ \varepsilon_{zz}=-[2S_{12}/(S_{11}+S_{12})]\varepsilon\ , \tag{3.74}$$

where S_{11} (>0) and S_{12} (<0) are the elastic compliance constants of A. We have assumed medium B to be unstrained, i.e., to be much thicker than A or to equal the substrate and match its lattice constant. Generalizations to other situations, e.g. A and B disconnected from the substrate, are straightforward (see Appendix 3.A).

The "doublet" vibration (perpendicular to [001]) shifts by an amount:

$$\frac{\Delta\omega_d}{\omega}=\frac{\tilde{K}_{11}}{2}\,\varepsilon_{xx}+\frac{\tilde{K}_{12}}{2}\,(\varepsilon_{yy}+\varepsilon_{zz})\ . \tag{3.75}$$

We should note that, in principle, the parameters $\tilde{K}_{ij}$ are somewhat different for the LO and TO components of the optical phonons. Accurate determination of both sets of independent parameters, however, have only been recently performed for GaAs [3.170], InP [3.172], and AlSb [3.173]. This problem does not arise in the group IV materials (Ge, Si) since they have no LO−TO splittings.

We should report, in closing this section, that strained layer heterojunctions (InGaAs−GaAs−AlGaAs) have been successfully used to fabricate lasers which operate CW at room temperature (8250 Å) [3.174]. Effects of strain due to lattice mismatch on optical phonons have also been observed for single epitaxial layers, the most conspicuous case being that of silicon on sapphire (SOS) [3.175]. ZnSe on GaAs [3.168] and gray tin on InSb [3.176] have also been investigated.

3.5 Resonant Scattering

The electronic states of superlattices fall into two categories: Those with energies within the potential wells have wavefunctions confined to those wells with exponential decay into the barriers [3.177–180]. For sufficiently large barriers there is no interaction between wells and these states do not show any dispersion (band formation) along k_z. In this case, one speaks of multiple quantum wells (MQW). This concept is valid for states which correspond to those near the lowest band edges of the bulk material of the well (note that the well of the conduction band may be in material A while that of the valence band is in material B in the so-called type II superlattices). States of the well which lie above the barrier top are propagating states since they always find other states in the barrier to which to couple. Nevertheless, this coupling can be small, and resonant (nearly confined) states can result. For small period superlattices ($n_1 = n_2 \leqq 8$) all states disperse appreciably along k_z. For large well thicknesses the lowest (highest) conduction (valence) states do not appreciably disperse and one has a MQW. The energies and wavefunctions of these states are the same as for a single quantum well [3.181] except for the enhanced degeneracy.

The light scattering mechanism discussed in Sect. 3.3.3 ignores the dependence of the Raman tensor on laser frequency ω_i, although it could be easily assumed that the $\alpha_{\parallel,\perp}$ of (3.57) and its derivatives depend on ω_i. Even than, the resonance phenomena in which either $\hbar\omega_i$ or $\hbar\omega_s$ are equal to the energy $\hbar\omega_g$ of strong electronic inter-band transition (e.g., between valence and conduction states confined to the same material) would not be appropriately described: resonance phenomena appear both for $\omega_i = \omega_g$ and for $\omega_s = \omega_g$ (incoming and outgoing resonances, respectively). The theory of Sect. 3.3.3 implies that $\omega_i \simeq \omega_s$ and thus leads to only one resonance frequency for each ω_g. The assumptions of this "quasi-static" or "adiabatic" theory are justified whenever the phonon frequency ω_0 satisfies:

$$\omega_0 \ll |\omega_g - \omega_i + \mathrm{i}\Gamma_g| \,, \tag{3.76}$$

where Γ_g is the Lorentzian broadening of ω_g. Condition (3.76) usually holds at room temperature. At lower temperatures, however, it does not hold for optical phonons at the lowest ω_gs since Γ_g becomes very small.

Resonance Raman scattering is rather rich in phenomenology even for bulk materials [3.10]. The theoretical interpretation is performed usually within the framework of the uncorrelated electron-hole approximation. Experimental results, however, sometimes reflect Coulomb interaction between these particles, i.e., the so-called excitonic effects [3.182].

3.5.1 Resonance Effects in the Bulk Constituents of Silicon and Zincblende-Type Superlattices

a) Resonant Electronic Transitions

The details of the electronic transitions which produce resonance in the Raman scattering by phonons in Si and GaAs-type materials is discussed in Sect. 2.2.4 ff. of [3.10]. Here we shall recall some general features and recent developments useful to the discussion of superlattices. The bulk resonances which have been mainly investigated occur at the so-called E_0, $E_0+\Delta_0$, E_1, and $E_1+\Delta_1$ gaps (see Fig. 2.37 of [3.10]). These gaps, transition energies, or critical points all have counterparts in superlattices. The E_0 gap, the lowest direct gap at the Γ ($k=0$) point of the bulk BZ, takes place between *p*-like valence states (mainly anionic) and *s*-like conduction states (mainly cationic). The *p*-states are spin-orbit split by an amount Δ_0, a fact which gives rise to the $E_0+\Delta_0$ gap. The strong E_1 and $E_1+\Delta_1$ transitions are also spin-orbit partners. They take place along the four equivalent $\langle 111\rangle$ directions between the split top valence bands and the lowest conduction band [Ref. 3.10; Fig. 2.37]. The standard Feynman diagram of resonant scattering by one phonon is shown in Fig. 3.46. One usually distinguishes between two-band and three-band terms in the scattering amplitude. In the former the phonon connects electronic states belonging to the same band ($c=c'$ or $v=v'$ in Fig. 3.46) while in the latter the phonon couples states belonging to different bands. Two-band terms are usually more strongly resonant than the three-band ones since the former have two energy denominators resonating at nearly the same frequency, while the latter only have one.

Expressions for the scattering efficiencies near the E_0, $E_0+\Delta_0$, E_1 and $E_1+\Delta_1$ gaps (also called critical points) are given in [3.10]. They contain two- and three-band terms and are based on the quasi-static approximation. They can be presented either in terms of analytic expressions for the combined densities of states at critical points [(2.194) of [3.10]] or, equivalently, of the dielectric function and its derivatives with respect to ω [(2.195, 201) of [3.10]]. These expressions can be easily transformed into others which do not require fulfillment of (3.76) [Ref. 3.1; Sect. 2.3.2]; see also [3.183, 184]). This is accomplished by replacing in the two-band terms the derivatives of $\chi(\omega_i)$ by the

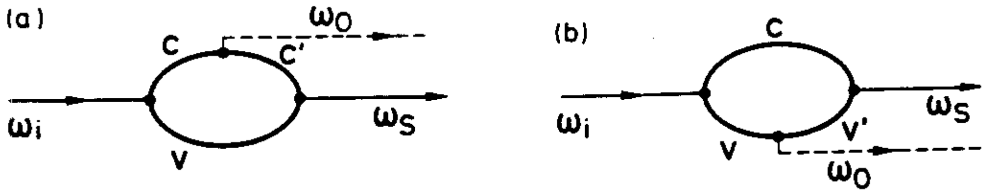

Fig. 3.46a, b. Feyman diagrams of resonant Raman scattering by one phonon (---) in semiconductors. The thin lines represent photons, the thick ones electrons and holes. The phonon is shown to couple to either the conduction (**a**) or the valence states (holes) (**b**)

finite difference ratios $[\chi(\omega_i)-\chi(\omega_s)]/\omega_0$ and the three-band terms $\chi(\omega_i)$ by the average of $\chi(\omega_i)$ and $\chi(\omega_s)$.

The expressions (2.194, 195) of [3.10] are based on the three-dimensional parabolic expansion of the E_0 and $E_0+\Delta_0$ critical points. That for the E_1 and $E_1+\Delta_1$ critical points [(2.201 of [3.10]), is based on a two-dimensional expansion of the energy differences between conduction and valence bands vs. $\boldsymbol{k}$: this difference is constant *along* the [111] direction over a large region of the BZ. Hence, the longitudinal mass can be assumed to be infinite, and a cylindrically symmetric (i.e., two-dimensional) situation results. The equations so obtained for the E_1 and $E_1+\Delta_1$ critical points can be easily transformed for application to the case of MQW [3.103].

We close this subsection by pointing out that the expressions mentioned apply to phonons at $\boldsymbol{k}\simeq 0$ i.e., they lead to scattering efficiencies independent of $\boldsymbol{k}$. This is the so-called (dipole) allowed scattering. In the case of LO phonons, "forbidden" scattering of amplitude proportional to k, is induced by the electrostatic field which accompanies such phonons (Fröhlich mechanism, see Sect. 3.5.1c).

b) Deformation Potential Electron-Phonon Interaction

The matrix element of the electron-phonon Hamiltonian between electronic states is usually written in terms of coupling constants called deformation potentials (in eV, representing matrix elements per unit dimensionless phonon deformation; see for instance [Ref. 3.10; Eqs. (2.187, 199)]).

Resonant scattering at the E_0 and $E_0+\Delta_0$ gaps is determined by a single deformation potential called d_0 ($\simeq +30$ eV for most materials treated here [3.185]). It is easy to see by using standard character tables for the T_d group of

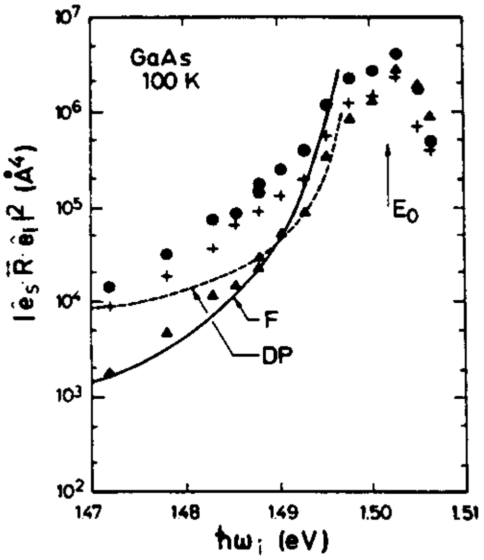

Fig. 3.47. Resonance measured for deformation potential (DP) scattering by phonons in GaAs in the allowed $\boldsymbol{e}_i \parallel [100]$, $\boldsymbol{e}_s \parallel [010]$ configuration, and forbidden scattering (*F*) obtained for $\boldsymbol{e}_i \parallel \boldsymbol{e}_s \parallel [100]$. From [3.183]. The solid and dashed curves are fits obtained with the theory of [3.186]

zincblende [3.80] that the Raman phonon of Γ_{15} (T_2) symmetry couples neither with the Γ_6 conduction band nor with the split-off valence band Γ_7. Thus, the $E_0+\Delta_0$ gap only exhibits weakly resonant three-band terms related to the coupling of the Γ_7 valence band with its split-off mate Γ_8 (see structure at $\sim$1.8 eV for GaAs in [Ref. 3.10; Fig, 2.8]). Two-band terms occur at the E_0 gap since the corresponding valence band (Γ_{15}) couples with itself via the Γ_{15} phonon. Thus, very strong resonances result, as shown in Fig. 3.47. The resonance at $E_0+\Delta_0$, determined by three-band terms, has a strength proportional to $(d_0/\Delta_0)^2$. It should be much stronger for InP ($\Delta_0 \simeq 0.1$ eV) [3.187] than for GaSb ($\Delta_0 \simeq 0.8$ eV) [3.188].

The orbital wavefunctions of Γ_{15} states have p-like symmetry and thus vary under the operations of the T_d point group like the coordinates x, y, z. We represent them by X, Y, Z. The wavefunctions of the spin-split Γ_8 and Γ_7 states can be labeled in angular momentum notation:

$$\Gamma_8\left\{\begin{array}{ll} \left(\frac{3}{2},\frac{3}{2}\right)=\frac{1}{\sqrt{2}}(X+\mathrm{i}Y)\uparrow\,; & \left(\frac{3}{2},-\frac{3}{2}\right)=\frac{1}{\sqrt{2}}(X-\mathrm{i}Y)\downarrow \\ \left(\frac{3}{2},\frac{1}{2}\right)=\frac{1}{\sqrt{6}}(X+\mathrm{i}Y)\downarrow+\sqrt{\frac{2}{3}}\,Z\uparrow\,; & \left(\frac{3}{2},-\frac{1}{2}\right)=\frac{1}{\sqrt{6}}(X-\mathrm{i}Y)\uparrow-\sqrt{\frac{3}{2}}\,Z\downarrow \end{array}\right.$$

$$\Gamma_7\ \left(\frac{1}{2},\frac{1}{2}\right)=\frac{1}{\sqrt{3}}(X+\mathrm{i}Y)\downarrow-\frac{1}{\sqrt{3}}Z\uparrow\,;\quad \left(\frac{1}{2},-\frac{1}{2}\right)=\frac{1}{\sqrt{3}}(X-\mathrm{i}Y)\uparrow+\frac{1}{\sqrt{3}}Z\downarrow \tag{3.77}$$

The matrix elements of the electron-phonon Hamiltonian H_{ep} for Stokes scattering can be easily obtained by using the relationship (in atomic units [Ref. 3.10; Eq. (2.187)]):

$$\langle X|H^Z_{\mathrm{ep}}|Y\rangle=\frac{d_0}{2a_0}\left(\frac{3}{2\omega_0\mu N}\right)^{1/2}(n_B+1)^{1/2}\,, \tag{3.78}$$

where H^Z_{ep} represents the Hamiltonian for a phonon polarized along z, μ the reduced mass of the primitive cell (PC), a_0 the lattice constant N the member of PCs, and n_{B} the Bose-Einstein factor. Other non-vanishing matrix elements of H_{ep} can be obtained from (3.78) through circular permutation.

The E_1 and $E_1+\Delta_1$ resonances are determined by two deformation potentials, $d^5_{3,0}$ and $d^5_{1,0}$ [3.183, 184]. The former determines the three-band terms which couple the spin-orbit split valence states while the latter determine the two-band terms; the three-band terms usually dominate even at resonance [3.183, 184]. The E_1, $E_1+\Delta_1$ resonances should be important in superlattices containing Ge, InSb, InAs, and GaSb since they occur in the region of standard ion lasers (2–3 eV). (For energies of these gaps see [3.96]). However, we shall not discuss these resonances any further since only one detailed report concerning them has appeared [3.189].

c) Fröhlich Interaction

The deformation potential is assumed to be independent of the $\boldsymbol{k}$ of the phonon and thus can be considered to be *local* in real space. In polar materials longitudinal phonons are accompanied by electric fields which contribute a long range ($\boldsymbol{k}$-dependent) term $H_{\mathrm{ep}}^{\mathrm{F}}$, to the so-called Fröhlich Hamiltonian [Ref. 3.10; Eq. (2.212)], proportional to $|\boldsymbol{k}|^{-1}$. The three-band terms arising from $H_{\mathrm{ep}}^{\mathrm{F}}$ result in a small renormalization of the allowed Raman tensor [Ref. 3.10; Sect. 2.1.12] of [3.10]). The two-band terms, however, lead to a forbidden contribution [Ref. 3.10; Sect. 2.2.8] whose Raman tensor is usually diagonal and its scattering efficiency proportional to $|\boldsymbol{k}|^2$. Expressions for this tensor as a function of band parameters are given in [3.10] for the adiabatic case. This restriction has been lifted in [3.190] and [3.191] for three- and two-dimensional critical points, respectively. The latter results can be adapted to an in-plane propagation in MQWs. The results are the same as those of [3.103].

The forbidden scattering discussed above is usually small because of its proportionality to $|\boldsymbol{k}|^2$, which is basically zero for forward scattering and rather small for backscattering $|\boldsymbol{k}| = 4\pi n/\lambda_i$. It can, nevertheless, become dominant at resonance. An enhancement mechanism, based on an additional interaction with charged impurities which increases the effective $|\boldsymbol{k}|$, has been suggested [3.192]. This mechanism generates incoherent phonons with varying (but small) $\boldsymbol{k}$s. The generation of incoherent phonons has been experimentally demonstrated [3.193]. A particularly reliable signature of the impurity-induced process is the fact that the *outgoing* resonance becomes dominant, while in the $\boldsymbol{k}$-induced process structures of the same strength are seen both at the incoming and outgoing resonances [3.194].

d) Interference Between Fröhlich and Deformation Potential Scattering

The Raman tensors for Fröhlich, $\boldsymbol{R}_{\mathrm{F}}$, and deformation potential scattering, $\boldsymbol{R}_{\mathrm{D}}$, have the forms:

$$\boldsymbol{R}_{\mathrm{F}} = a_{\mathrm{F}} \begin{pmatrix} 1 & & \\ & 1 & \\ & & 1 \end{pmatrix}, \quad \boldsymbol{R}_{\mathrm{D}} = a_{\mathrm{D}} \begin{pmatrix} 0 & 1 & 0 \\ 1 & 0 & 0 \\ 0 & 0 & 0 \end{pmatrix} \tag{3.79}$$

for LO phonons propagating along z. It is easy to see that (3.79) leads to scattering for $\boldsymbol{e}_{\mathrm{i}} \| \boldsymbol{e}_{\mathrm{s}} \|$ [110] which is different to that for $\boldsymbol{e}_{\mathrm{i}} \| \boldsymbol{e}_{\mathrm{s}} \|$ [1$\bar{1}$0] as a result of the interference of the complex quantities a_{F} and a_{D} near resonance. The scattering efficiencies are proportional to $|a_{\mathrm{D}} + a_{\mathrm{F}}|^2$ and $|a_{\mathrm{D}} - a_{\mathrm{F}}|^2$ in the former and latter case, respectively. Such *interference* effects have been observed at $E_0 + \Delta_0$ [3.187, 188, 193] and at E_1, $E_1 + \Delta_1$ [3.194]. Similar effects have been reported at E_1, $E_1 + \Delta_1$ for MQWs [3.189].

3.5.2 Resonance Scattering by Phonons in Superlattices

The E_0 absorption of bulk zincblende materials transforms into a series of discrete lines when the material forms a quantum well (or MQW). The electronic states become localized to the wells and in the lowest conduction band at Γ a ladder with indices $l = 1, 2, 3 \ldots$, whose envelope wavefunctions are similar to the envelopes of the phonons of (3.34, 38), results. The top valence band develops into two such series: that of the heavy holes (HH) and that of the light holes (LH). In an "allowed" optical absorption process between such valence and conduction levels, l must be conserved: two such series develop, corresponding to the heavy and light hole ladders for $\Delta l = 0$. The absorption spectrum for uncorrelated electrons should thus be two such series of step functions. Excitonic effects actually sharpen up the leading edge of the step functions into series of peaks. Figure 3.48 shows the peaks of the heavy hole ladder of $GaAs/Al_{0.2}Ga_{0.8}As$ quantum wells. The light hole ladder is not seen, except possibly a shoulder on the high energy side of the $n = 1$ peak for $L_z = 140$ Å. Both ladders can be clearly observed in [3.196] for $Ga_{0.47}In_{0.53}As/Al_{0.48}In_{0.52}As$ MQWs. Each one of these absorption peaks is expected to lead to resonances in the Raman scattering cross section.

Such resonances were first observed in [3.103] for the heavy hole ladders associated with the E_0 edge of $GaAs/Ga_{1-x}Al_xAs$ superlattices and MQWs with $x = 0.1$ and 0.25. We show these observation in Fig. 3.49 for two MQWs (a, b) and two superlattices with subband widths δ_1. The solid curves in these figures represent fits using a theory which assumes uncorrelated electrons, the dashed curves the corresponding absorption spectra. No attempt was made in this work to determine the polarization selection rules. The fit (solid line) to the resonance profile $S(\omega_i)$ was obtained with the approximate expression:

$$S(\omega_i) \propto |\chi(\omega_i) - \chi(\omega_s)|^2 \, , \tag{3.80}$$

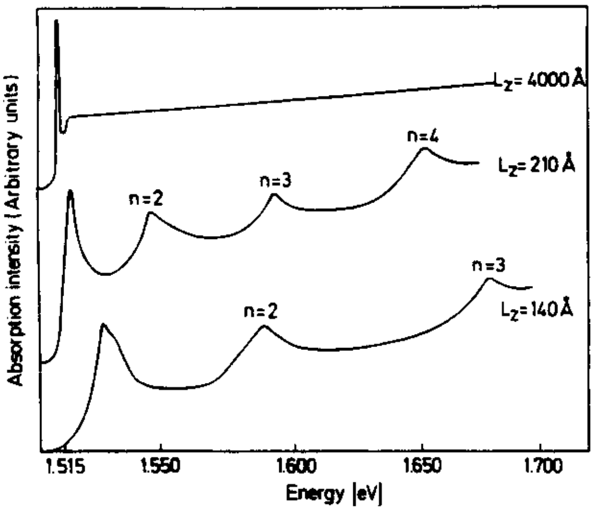

Fig. 3.48. Absorption spectra of $GaAs/Al_{0.2}Ga_{0.8}As$ quantum wells of three different widths d_1. From [3.195]

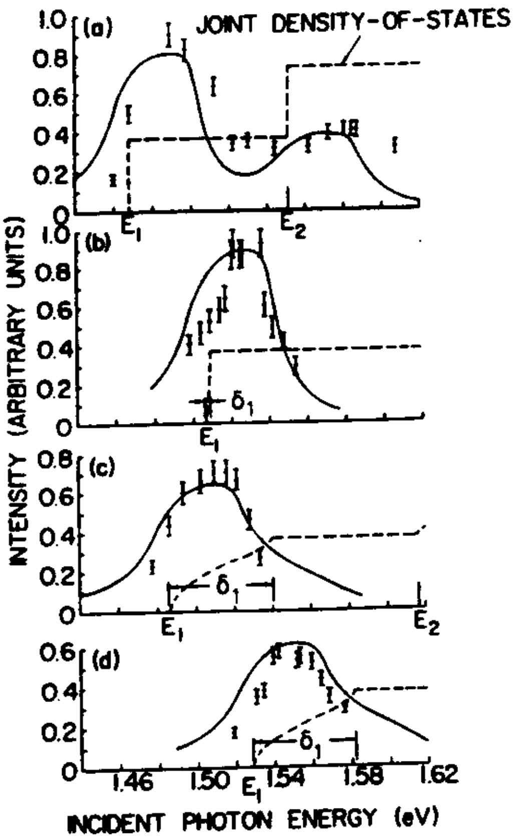

Fig. 3.49. Resonant Raman scattering by LO phonons for two MQWs (**a**, **b**) and two superlattices (**c**, **d**) of GaAs/Al$_x$Ga$_{1-x}$As. $x=0.25$ for (**a**, **b**, **d**), $x=0.1$ for (**c**). The well widths d_1 are 100 (**a**), 52 (**b**), 39 (**c**), and 35 Å (**d**). The lines are theoretical fits (see text) [3.103]

which is justified, according to [3.103], very close to resonance, with $\chi(\omega)$ obtained from the two-dimensional expressions for uncorrelated electrons ((2.178) of [3.10]) in the case of the MQWs (a, b) and with a generalized three-dimensional expression for the true superlattices (c, d). The theory represents the data rather well. Similar measurements involving the $E_0+\Delta_0$ localized levels associated with the $E_0+\Delta_0$ gap are presented in [3.104] together with evidence for $l_v=2 \rightarrow l_c=2$ and $l_v=3 \rightarrow l_c=3$ transitions at the E_0 gap. These measurements were performed at room temperature.

Similar measurements, but performed at $T \simeq 2$ K, were reported in [3.197]. These temperatures allow the resolution of the incoming and outgoing components of the resonance (Fig. 3.50) associated with the $l=l_c=l_v=1, 2, 3$ levels of the E_0 gap of GaAs in GaAs/Al$_{0.27}$Ga$_{0.73}$As MQWs. For $l=1$ only the incoming resonance associated to the heavy hole (HH) ladder is seen: the outgoing one is swamped by the luminescence of the $l=1$ light hole transition. For $n=2$, both incoming and outgoing HH resonances are seen. In the region of ω_i between 1.75 and 1.85 eV, both $l=2$ LH and $l=3$ HH incoming and outgoing resonances are observed. In [3.198] a slightly different MQW allows the observation of the $l=1$ incoming and outgoing HH resonances and the LH outgoing one. Interesting in all these measurements is the fact that the incoming

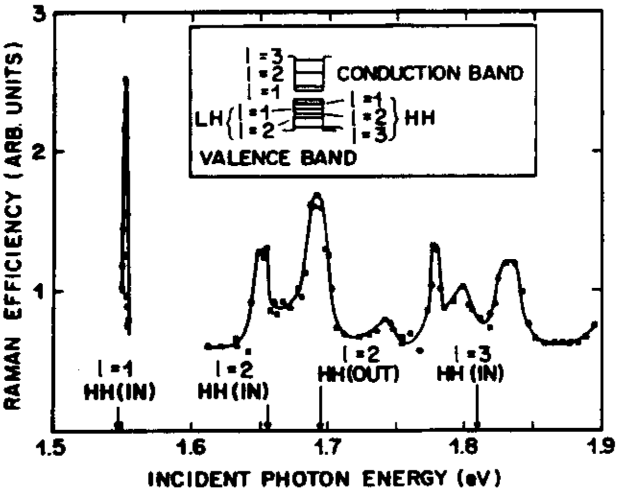

Fig. 3.50. Resonant profile for Raman scattering by GaAs-like LO phonons in an $(\mathrm{GaAs})_{36}(\mathrm{Al}_{0.27}\mathrm{Ga}_{0.73}\mathrm{As})_{73}$ MQW. The arrows indicate the exciton energies calculated for the corresponding single quantum wells [3.197]

resonances are somewhat weaker (~ one-half) than the outgoing ones. In [3.197] this is attributed to a three-band scattering mechanism, with the phonon coupling two different l-subbands ($l=2$ and 3 for the $l=2$ resonances of Fig. 3.50): the non-resonant denominator of the three-band process is smaller in this case for the outgoing than for the incoming resonance. This explanation is supported by the fact that sometimes a stronger incoming resonance is found [3.199] a fact that follows from the above model if the non-resonant state lies *below* the resonant one. In [3.199] resonances related to the lowest gap of the barrier (unconfined) are seen: not only for the LO phonons of the GaAs well but for the Ga-like and Al-like phonons of the alloy barrier.

An alternative explanation of the usually encountered dominance of outgoing resonances is given in [3.198]. It follows naturally and in a general way from the impurity enhanced Fröhlich mechanism [3.192]: for the outgoing resonance the other two energy denominators lie in the continuum of electronic excitations, a fact which introduces divergences in the k-space integrations. This does not happen for the incoming resonances. A fit with this model to the $l=2$ HH resonances is shown in Fig. 3.51. This mechanism has the advantage of its generality while that based on three-band models depends strongly on the details of the electronic structure. Three-band terms may become dominant under certain circumstances, especially when the separation between the two gaps involved equals the phonon frequency. In this case both the energy denominator may vanish (or nearly vanish) and double resonances occur [3.200, 200a] (Sect. 3.5.3b).

Resonances have also been observed for CdTe/CdMnTe MQWs [3.201]: incoming and outgoing (stronger) resonances appear for the $l=1$, HH transition while for $l=1$, LH transition the ratio of incoming/outgoing strengths may be reversed. In this case the MQWs strain enhances the HH − LH separation.

The scattering intensity at the peak of the $l=1$ and $l=2$ resonance has been measured vs. temperature in [3.202]. These measurements yield information on

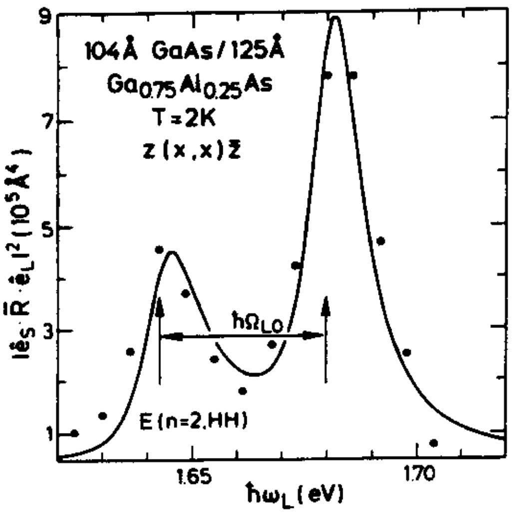

Fig. 3.51. Raman scattering resonance with $l=2$ for a GaAs-$Al_{0.25}Ga_{0.75}As$ MQW displaying the asymmetry between the incoming (smaller) and outgoing components. The points are experimental data, the line a theoretical fit based on the impurity enhanced Fröhlich mechanism [3.198]

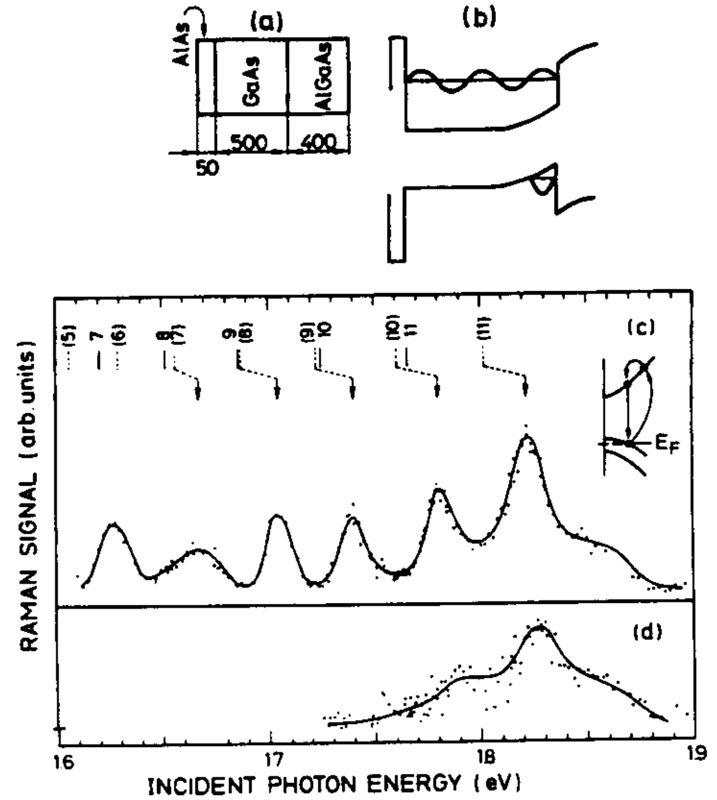

Fig. 3.52. (a) Period of the MQW of [3.203]. (b) Electronic structure of the well in real space. (c) Resonance scattering profile for the LO phonons of a GaAs well. (d) As in (c), for the GaAs-like LO phonons of the barrier to the right. The solid vertical bars indicate calculated positions of the $l_c \neq l_v = 1$ transitions and the accompanying number the corresponding l_c. The dashed lines show the position of the related outgoing resonances with l_c in brackets

the temperature dependence of the *homogeneous* linewidth of the corresponding excitons and its origin.

A particularly astute resonance experiment has been reported in [3.203]. The authors use a MQW consisting of asymmetric quantum wells composed of an AlAs barrier on the left, a 500 Å GaAs well, and a Be-doped $Al_{0.33}Ga_{0.67}As$ barrier (modulation doping) on the right (Fig. 3.52). The 500 Å GaAs localizes the heterojunction on the right, because the Be-doping produces a triangular well which localizes the electrons very close to the interface. This configuration lifts the $\Delta l = 0$ selection rule since the valence and conduction wavefunctions are not localized in the same region and the envelope functions of different l_c and l_v are not orthogonal. In this manner one sees *outgoing* resonances from $l_v = 1$ to l_c between 5 and 11 (see Fig. 3.52). These experiments can be used to map out details of the envelope functions of the confined states.

Most of the Raman work discussed so far was performed for MQWs with nearly k_z-independent electronic states (exception: Fig. 3.49c, d). A simple test of this condition can be made by measuring the ratio of the scattering intensities of the barrier modes to those of the well modes. Such a test has been applied to $(GaAs)_n/(AlAs)_n$ superlattices in [3.204]: this ratio increases from about 0.1 for $n \geqq 10$ to 0.9 for $n = 2$. For $n = 1$, 2 both the GaAs- and AlAs-like phonons resonate at the E_0-like gap of the superlattices at ~ 2.15 eV [3.205], Fig. 3.53. A weaker resonance related either to a folded or an indirect gap appears at 1.92 eV for $n = 1$. Unfortunately, these resonances have only been measured at room temperature: strong luminescence makes low temperature observation hard. Similar results have been reported in [3.206] for a $(GaAs)_2/(AlAs)_1$ superlattice.

The only report of resonances at the E_1 and $E_1 + \Delta_1$ gaps of superlattices has appeared in [3.189] for GaSb/AlSb samples. An increase in the E_1 gaps of bulk

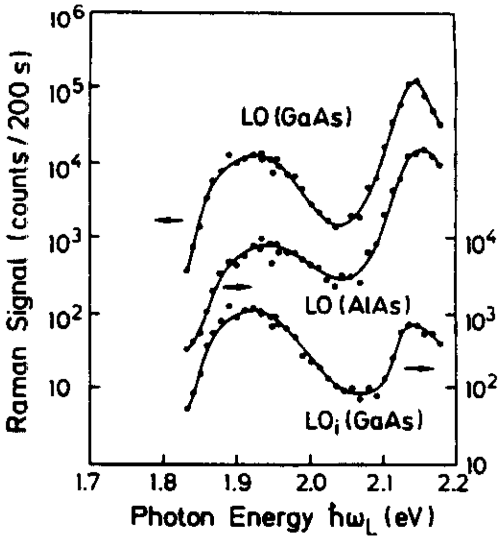

Fig. 3.53. Resonance of the Raman scattering of GaAs- and AlAs-like LO phonons in $(GaAs)_1(AlAs)_1$ superlattices. LO_i represents an additional peak above the main LO (GaAs) which becomes strong at the low frequency resonance (its strength has been divided by 10 in the plot). The origin of this peak is not clear. It may be a phonon away from $k = 0$

GaSb is observed, possibly related to partial confinement of the electronic states. Calculations of this confinement effect, however, indicate that it is much smaller than the observed one.

3.5.3 Scattering Mechanisms for the E_0-gap Related Transitions of Superlattices

a) LO-Phonons: Deformation Potential vs Fröhlich Interaction

In bulk zincblende-type material the Raman phonons have Γ_{15} symmetry. Consequently, the dipole-*allowed* Raman tensors have only off-diagonal components referred to the cubic axes. For backscattering at a [001] face the LO-phonons (Γ_{15}^z) have the Raman tensor of (3.60). These phonons generate in the D_{2d} group of the [001]-grown superlattice phonons of symmetries A_1 and B_2 (Sect. 3.3.2). Those of symmetry A_1 correspond to (3.34a, 38a) while those of B_2 symmetry are represented by (3.34b, 38b). The latter have a Raman tensor of the same form as the bulk (3.60), while the former have an *allowed* diagonal Raman tensor [diagonal components of (3.61)]. The diagonal tensor is forbidden in the bulk, thus it is expected to be small off-resonance. A dipole-*forbidden* diagonal tensor also appears in the bulk at resonance [3.10]: it is induced by the electrostatic Fröhlich interaction. The allowed tensor of the bulk is usually described by the deformation potential interaction. New deformation potentials, forbidden in the bulk, must thus be induced by the superlattice potentials: they are, however, expected to be small except for very small period superlattices. This fact has already been illustrated in Sect. 3.3.3 in connection with the bond polarizability model.

The confined B_2 modes are related to bulk modes through (3.38b) or, more accurately, (3.25) with m odd, the A_1-modes likewise through (3.25) for m even. The B_2 modes should scatter via a deformation potential but it is easy to see that they cannot lead to two-band terms: the matrix element for the coupling of an electronic state with itself must vanish since the product of the electronic state with itself has A_1 symmetry. A_1 phonons thus lead to two-band terms which should be strong (even dominant!) near resonances. They should appear in parallel scattering configurations while the B_2 phonons appear either in crossed polarizations parallel to the x and y axes or in parallel polarizations parallel to [110] (or [$1\bar{1}0$], see Sect. 3.5.1).

If n_1 and n_2 are not too small one can break up the matrix element of the *short-range* electron-phonon interaction (bulk deformation potential) into matrix elements of H_{ep} over the bulk PCs and a matrix element of the envelope functions (two electron states, one phonon). This is appropriate to B_2 phonons. At the E_0 gaps the phonons must then connect the $(\frac{3}{2}, \pm\frac{3}{2})$ valence bands with their $(\frac{3}{2}, \pm\frac{1}{2})$ counterparts (see (3.77), the quantization axis is z). In this manner three-band terms involving the HH or $(\frac{3}{2}, \pm\frac{3}{2})$, LH $(\frac{3}{2}, \pm\frac{1}{2})$, and conduction bands result. If the HH and LH splitting equals the phonon frequency, strong double resonance obtains [3.200].

A_1 symmetry forbidden scattering results in the bulk from the k-dependent Fröhlich interaction. In a superlattice of intermediate period (n_1, n_2 between 5 and 50) the periodicity fixes the value of k_z. Thus, for not too large values of $k_{x,y}$, the matrix element of the electron-phonon interaction becomes k-independent and can also be represented by a deformation potential. The resulting Raman resonances, for m even, are supposed to be very strong (two-band terms). In fact, although they should only appear for parallel incident and scattered polarizations, they can even mask the B_2 peaks (m odd) which should be observed in crossed (x,y) polarizations [3.65, 200a]. Because of the separation of B_2 and A_1 modes, the interference effects discussed in Sect. 3.51d do not take place. As n_1 increases, however, A_1 and B_2 modes begin to overlap within their linewidths and interferences should again reappear [3.206a].

We have, so far, discussed the k-conserving Fröhlich-like A_1 scattering. It implies, for backscattering, coupling to phonons with $k_{x,y}=0$. As in the case of the bulk (Sect. 3.5.1c), impurity scattering may enhance these processes and allow coupling to phonons with $k_{x,y}\neq 0$ [3.200a]. This can be inferred from the fact that the outgoing resonance becomes stronger than the incoming one (see Fig. 3.54). Another Fröhlich-related mechanism, which appears even at $k_{x,y}=0$, should exist in superlattices. In this case, in the bulk the contributions of electron and hole diagrams (Fig. 3.46a, b) cancel because of the opposite charges of electrons and holes. In MQWs the phonons may be strongly confined while the electrons (holes) may penetrate different amounts into the barrier, depending on

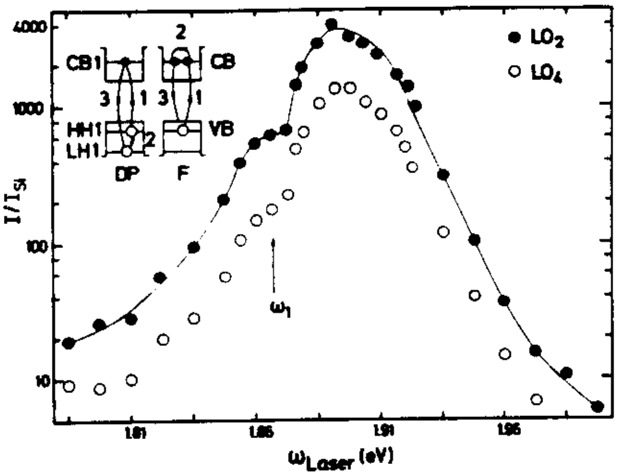

Fig. 3.54. Observed scattered intensity, measured with respect to that of the Raman phonon of Si, versus incident laser frequency for the $m=2$ and $m=4$ phonons of a $(GaAs)_7(AlAs)_7$ superlattice. The inset shows scattering diagrams for deformation potential (DP) and Fröhlich (F) electron-phonon interaction. The three steps indicated correspond to deformation potential (three-band) and Fröhlich (two-band) terms. For the F-case, a similar diagram with step 2 in the HH1 miniband, has to be subtracted. The resonant gap is ω_1: the outgoing resonance dominates [3.66a]

the masses and barrier heights. Thus, the matrix elements of $H_{\mathrm{ep}}^{\mathrm{F}}$ do not cancel exactly, leading to "allowed" non-impurity-induced scattering for $k_{x,y}=0$.

For superlattices of intermediate period, the confined modes resonate only with transitions between overlapping confined electronic states. The interface modes, however, extend to both sides of the interfaces and thus resonate with electronic transitions confined to either side [3.55].

b) Double Resonances

Several examples of double resonances in the scattering by LO phonons in quantum wells have been reported by the *Bell* group [3.200, 207, 208]. Similar effects have been observed in bulk GaAs samples under unaxial stress [3.209, 210]: the stress-induced splitting of the Γ_8 valence bands equals, in these cases, the scattering phonon frequency.

The work of [3.208] was performed for a $(\mathrm{GaAs})_{10}$ *single* quantum well with $\mathrm{Ga}_{0.3}\mathrm{Al}_{0.7}\mathrm{As}$ as a barrier, for which the $l=1$ HH $-l=1$ LH splitting $E_{1\mathrm{H}}-E_{1\mathrm{L}}$ equals the LO phonon energy $\hbar\omega_0$. As mentioned above, those two states are then coupled by the LO phonon via the deformation potential [see (3.77, 78)]:

$$\left\langle \frac{3}{2}, \frac{3}{2} \middle| H_{\mathrm{ep}}^{Z} \middle| \frac{3}{2}, -\frac{1}{2} \right\rangle = \frac{d_0}{a_0} \left(\frac{1}{2\omega_0 \mu N} \right)^{1/2} (n_{\mathrm{B}}+1)^{1/2} \tag{3.81}$$

and likewise for the coupling between $(\frac{3}{2}, -\frac{3}{2})$ and $(\frac{3}{2}, \frac{1}{2})$. The $(\frac{3}{2}, -\frac{1}{2})$ LH electron states can be excited to the conduction band by using a circularly polarized photon of (+)-polarization ($J_z=+1$), while the excited conduction state can return to the $(\frac{3}{2}, \frac{3}{2})$ hole by emitting a (−)-polarized ($J_z=-1$) photon (these polarizations are given with respect to fixed axes and not to the direction of propagation). Hence, the double resonant process should only occur for (+)-polarized incident and (−)-polarized scattered photons. A polarization ratio P:

$$P=\frac{I(+,-)-I(+,+)}{I(+,-)+I(+,+)} \tag{3.82}$$

equal to 0.79 is found, instead of the expected $P=1$. The discrepancy is explained in [3.208] as due to loss of polarization in the virtual intermediate exciton state. In this work detailed scattered intensity measurements were performed in six different linear and circular polarization configurations. From the results, the authors derive information about exciton population and dephasing lifetimes.

In [3.200, 207] double resonances induced by the Fröhlich interaction are reported. They arise from coupling by the LO phonon between an $l=1$ HH and an $l=3$ HH state. The optical transitions involve the $l_{\mathrm{c}}=1$ state and thus the incoming one violates the $\Delta l=0$ selection rule. This violation is interpreted by the authors as due to the mixing of $l_{\mathrm{v}}=3$ with $l_{\mathrm{v}}=1$ by the excitonic interaction. The polarization selection rules for this process are opposite to those for deformation potential coupling, as corresponds to the A_1 nature of the phonons involved: the

$(+,+)$ process is dominant. One finds for the corresponding polarization ratio:

$$P=\frac{I(+,+)-I(+,-)}{I(+,+)+I(+,+)} \tag{3.83}$$

$P=0.885$, thus confirming the hypothesis of a Fröhlich interaction mechanism. The difference between this value of P and the expected $P=1$ is attributed to lifetime processes in the intermediate excitonic excitation (dephasing time τ_2 and scattering time between the two excitonic states τ_1).

We should mention, in closing, an interesting recent observation [3.211] of doubly resonant Raman scattering in QWs in which one of the resonant states is the $l_v=1$ continuum strongly modified by electron-phonon interaction. A very large number of peaks (at least 27) in the scattered intensity vs. ω_i are observed and assigned to various combinations of GaAs-like, AlAs-like and interface phonons. A requirement for these observations, which have not yet been completely theoretically analyzed, is the use of a very perfect quantum well: $n_1=9$ and also $n_1=8$ were used.

c) Photoelastic Mechanism

It has been well documented that the photoelastic mechanism is responsible for the Brillouin scattering in the bulk materials of interest here [Ref. 3.10; Sect. 2.3.4], [3.212]. In this case the phonon frequency ω_0 is very small and (3.76) is usually well satisfied even for $\omega_g=\omega_i$. For very sharp excitonic transitions at low T, however, polariton scattering may become important (Chap. 7 of *Light Scattering in Solids III*). By performing experiments for various scattering configurations it is actually possible to extract the three independent photoelastic constants p_{11}, p_{12}, and p_{44}, (Sect. 3.3.4) at least in the region of transparency [3.212, 213]. Most of the available experimental data [3.96] for p_{ij} apply to this region; some of them have been measured by Brillouin techniques and some by optical methods with the sample under static stress. Unfortunately, the latter measurements are usually confined to $p_{11}-p_{12}$ and p_{44} and do not give information on p_{11} and p_{12} separately: backscattering measurements for LA phonons (and their folded partners) in superlattices require the knowledge of p_{12} (Sect. 3.3.4).

We show in Fig. 3.55 the values of $p_{11}-p_{12}$ obtained with Brillouin and static piezo-birefringence techniques below the E_0 gap of ZnSe. The agreement between different methods is excellent. The theoretical fitting lines emphasize the strong resonant dispersion of these coefficients (and, correspondingly, the scattering efficiencies) at E_0. The separate values of p_{11}, p_{12}, and p_{44} obtained from Brillouin data are shown in Fig. 3.56. Note that p_{44} crosses zero before the resonance at E_0, while p_{11} and p_{12} do not (but $p_{11}-p_{12}$ does, Fig. 3.55), a fact common to most large gap materials of the family [3.215].

The data of Figs. 3.55 and 3.56 apply to the region below E_0. Photoelastic data above E_0 are rare. Not too precise results can be obtained by the piezo-

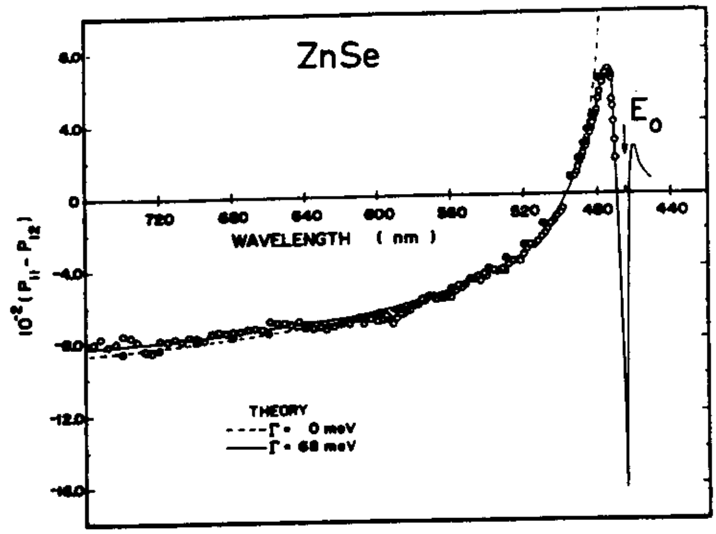

Fig. 3.55. Dispersion of the photoelastic coefficients $p_{11}-p_{12}$ of ZnSe at room temperature as measured by Brillouin scattering (○○○) and by piezo-birefringence techniques (●●●). The lines represent theoretical fits with expressions similar to those in [3.10]. Note the strong resonance at the E_0 edge which is preceded by an anti-resonance (zero) [3.212]

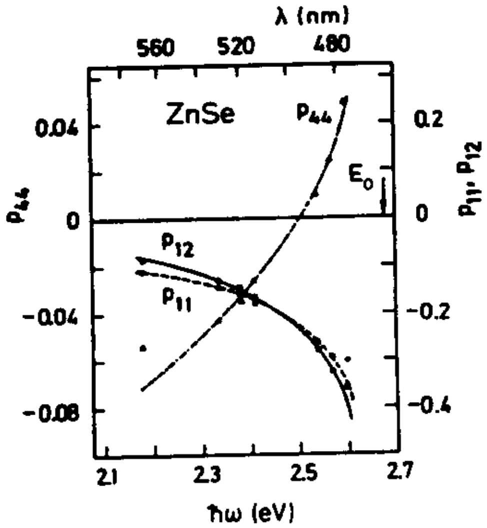

Fig. 3.56. Photoelastic coefficients p_{11}, p_{12}, and p_{44} of ZnSe at 295 K as measured by Brillouin scattering. The lines through the points are theoretical fits [3.214]

reflectance technique [3.216]. Kramers-Kronig analysis of piezo-reflectance data, or fits with theoretical expressions, can be used to obtain the related imaginary parts of p_{ij}. Data for GaAs, with details of the E_0, $E_0+\Delta_0$, E_1, and $E_1+\Delta_1$ resonances, are shown in Fig. 4 of [3.217] for the imaginary parts of p_{ij}: the real parts should be obtainable through Kramers-Kronig transformation. Accurate data for p_{12} below E_0 can be calculated from the $p_{11}-p_{12}$ results of [3.96] and those for $p_{11}+2p_{12}$ given in Fig. 13 of [3.215]. These data, however, have not been used for the interpretation of light scattering in superlattices (the corresponding data for AlAs are not available)!

The data just discussed are usually fitted with expressions similar to those in Sect. 2.2.12 of [3.10]. Near E_0 and $E_0+\Delta_0$ three deformation potentials (a, b, d) determine the resonant behavior [Ref. 3.10; Eqs. (2.255–257)] while four deformation potentials are needed to determine the behavior at E_1 and $E_1+\Delta_1$. The photoelastic constants can be used near resonance for folded acoustic phonons provided their frequency fulfills (3.76), i.e., in the whole resonant range provided $\omega_0 \ll \Gamma_g$. Otherwise (2.255–259) of [3.10] must be converted into those for finite ω_0 (with incoming and outgoing resonances) by using the prescription given in Sect. 3.5.1. These split resonances have yet to be observed for folded acoustic modes. On the whole, little quantitative work on resonant scattering by folded acoustic modes has been performed (see [3.123] for qualitative work on GaSb/AlSb superlattices).

d) Effects of Electric Fields on the Resonant Raman Scattering

The dielectric response and other optical properties of superlattices and MQWs are known to be affected by strong electric fields [3.218, 219]. These effects also appear in Raman scattering. Longitudinal fields distort the sinusoidal confined electronic wavefunctions as they lift the two-fold rotation axes in the superlattice planes: violation of the $\Delta l=0$ selection rule results. In particular, $\Delta l = \pm 1$ transitions are enhanced while those for $\Delta l=0$ decrease in strength. Theoretical and experimental investigations of these effects in resonant Raman scattering can be found in [3.220, 221].

3.5.4 Resonant Scattering by Two Phonons

Resonant scattering by two and more phonons has been intensively studied for the bulk constituents of semiconductor superlattices [3.10]. One usually observes overtones of the LO phonons near Γ. They are induced by the Fröhlich mechanism, since the k of *each* phonon involved does not have to vanish (only the total sum does) these processes are dipole allowed. One also observes density of two phonon states and related effects, usually induced by deformation potential interaction. They are represented by Raman tensors of all possible symmetries: Γ_{15}, Γ_{12}, and Γ_1 (or, equivalently, T_2, E, A_1) in the zincblende structure.

Scattering by two phonons is also encountered in superlattices and QWs, especially near resonant conditions. Work for GaAs/Ga$_{1-x}$Al$_x$As systems has been published in [3.222–224]. Strong resonances appear in $e_i \| e_s$ scattering configurations and thus can be safely attributed to Fröhlich processes.

We show in Fig. 3.57 Raman spectra obtained for a (GaAs)$_7$/(AlAs)$_{21}$ MQW including two confined LO (GaAs-like) and mixed GaAs- and AlAs-like interface phonons. The resonant profile has a weak incoming (at the $l=1$ gap, labeled ω_1) and a dominant outgoing peak: such behavior is standard in two-phonon scattering [3.187]. More complicated combinations of interface modes,

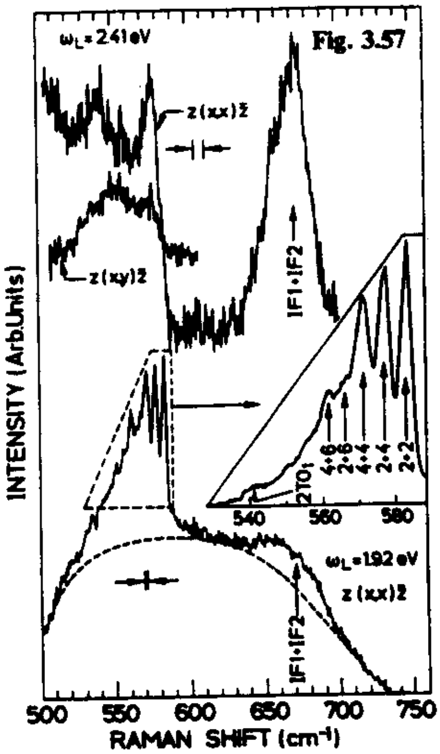

Fig. 3.57. Second order Raman spectra of a $(GaAs)_7(AlAs)_{21}$ MQW at 10 K. The peaks in the triangular insets are assigned to two GaAs-like confined phonons labeled by their *m*s. Combinations of GaAs- and AlAs-like interface phonons are also observed

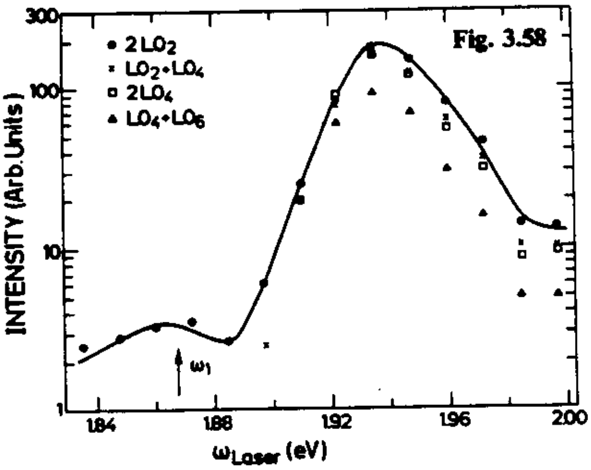

Fig. 3.58. Profile of the resonances by two confined phonons of Fig. 3.57. The resonating electronic transition is indicated by ω_1. The main peak corresponds to the outgoing resonance, as is usual in the case of higher order Raman scattering

involving up to four phonons, were observed in [3.223] for a $(GaAs)_7/(AlAs)_7$ sample. Resonance profiles of the two-phonon peaks are shown in Fig. 3.58. Recently, triply resonant scattering by two phonons has been reported [3.200a].

3.5.5 Conclusions

We have discussed the resonant scattering mechanisms of the bulk constituents of semiconductor superlattices and shown how they can be carried over to the latter. Fröhlich interaction is dominant for LO-phonons at resonance, a fact which usually leads to a dominance in the outgoing peak of the resonance profile. Confined phonons of odd *m* resonate through a deformation potential while those of even *m* do it through a Fröhlich interaction. Interface phonons extend to both sites of the heterojunction and thus resonate at the gaps of both constituents. In some cases double resonances are observed.

While the photoelastic mechanism seems to be mainly responsible for scattering by acoustic phonons, it must be modified to take into account resonance phenomena: real and imaginary parts of the photoelastic constants (and also the finite phonon frequency) must be included. Scattering by two or more phonons, usually induced by the Fröhlich mechanism, can also be observed near resonance. It leads to dominant *outgoing* peaks in the resonance profiles and, under the proper conditions, to triple resonances [3.200a].

3.A Appendix

Strains in a pseudomorphic superlattice with a total thickness D_1 of material 1 and D_2 of material 2.

If the superlattice is attached pseudomorphically to a substrate of "infinite" thickness of material 1, we must take $D_1=\infty$. We consider the general case of cubic materials with different elastic stiffness constants $c_{ij,1}$ and $c_{ij,2}$ and growth along either [100] or [111] for which the strains in the superlattice *plane* $\varepsilon_{\perp,1}$ and $\varepsilon_{\perp,2}$ are isotropic. Generalization to non-isotropic $\varepsilon_\perp$ (such as for [110] growth) is straightforward. By imposing the condition of pseudomorphism:

$$\Delta=\frac{a_2-a_1}{\langle a\rangle}=\varepsilon_{\perp 1}-\varepsilon_{\perp 2} \tag{3.A.1}$$

and the condition of equal and opposite planar forces in materials 1 and 2 we obtain:

$$\varepsilon_{\perp,1}=\frac{Q_2D_2}{Q_1D_1+Q_2D_2}\,\Delta \tag{3.A.2}$$

$$\varepsilon_{\perp,2}=\frac{-Q_1D_1}{Q_1D_1+Q_2D_2}\,\Delta \tag{3.A.3}$$

where $Q_{1,2}$ are functions of the elastic compliance constants of each material. For the [100] superlattice case we have:

$$Q=c_{11}+c_{12}-\frac{2(c_{12})^2}{c_{11}} \tag{3.A.4}$$

The in-plane strain in each layer is given by

$$\varepsilon_{\parallel}=-\frac{2c_{12}}{c_{11}}\,\varepsilon_\perp\,. \tag{3.A.5}$$

For the [111] case we obtain

$$\begin{aligned}Q&=\frac{2}{3}\left[c_{11}+2c_{12}+c_{44}-\frac{(c_{11}+2c_{12}-2c_{44})^2}{c_{11}+2c_{12}+4c_{44}}\right]\\ \varepsilon_{\parallel}&=-\frac{2(c_{11}+2c_{12}-2c_{44})}{c_{11}+2c_{12}+4c_{44}}\,\varepsilon_\perp\,.\end{aligned} \tag{3.A.6}$$

Acknowledgements. It is a pleasure to acknowledge J. Menéndez, R. Merlin, D. Olego, D. Paquet, and A. Pinczuk for careful reading of the manuscript and numerous illuminating discussions.

References

3.1 M. Cardona (ed.): *Light Scattering in Solids I*, Topics Appl. Phys., Vol. 8 (Springer, Berlin, Heidelberg 1983) p. 31

3.2 M. Cardona, G. Güntherodt (eds.): *Light Scattering in Solids II*, Topics Appl. Phys., Vol. 50 (Springer, Berlin, Heidelberg 1983) p. 39

3.3 H. Vogt: In [3.2], p. 208

3.4 See, for instance, W. Marshall, S.W. Lovesey: *Theory of Thermal Neutron Scattering* (Clarendon, Oxford 1971)

3.5 H. Bilz, W. Kress: *Phonon Dispersion Relations in Insulators* (Springer, Berlin, Heidelberg 1979)

3.6 See, for instance, P.M. Fauchet: IEEE Circuits and Devices Mag. **2**, 37 (1986)

3.7 R.K. Chang, M.B. Long: In [3.2], p. 179

3.8 I. Tsang: Chapter 6 of this volume

3.9 D. von der Linde, J. Kuhl, H. Klingenberg: Phys. Rev. Lett. **44**, 1505 (1980)

3.10 M. Cardona: In [3.2], p. 19

3.11 M. Cardona: *Proc. SPIE Conf. #822* (San Diego, California, USA 1987) in press

3.12 M. Cardona: In *Proc. 1984 Seoul Int. Symp. Physics of Semiconductors and its Applications* (Korean Physical Society, Seoul 1985)

3.13 J.R. Sandercock: In *Light Scattering in Solids III*, ed. by M. Cardona, G. Güntherodt, Topics Appl. Phys., Vol. 51 (Springer, Berlin, Heidelberg 1982) p. 173;
A.S. Pine: In [3.2], p. 253

3.14 M.H. Brodsky: In [3.1], p. 205

3.15 M. Cardona: *Phonon Physics* (World, Singapore 1982) p. 2, and references therein

3.16 N. Saint-Circq, R. Carles, J.B. Renucci, A. Zwick, M.A. Renucci: Solid State Commun. **39**, 1137 (1981)

3.17 D.W. Feldman, J. Parker, W. Choyke, L. Patrick: Phys. Rev. **173**, 787 (1978)

3.18 S. Mizushima, T. Shimanouchi: J. Am. Chem. Soc. **71**, 1320 (1949);
W.L. Peticolas, G.W. Hibler, J.L. Lippert, A. Peterlin, H.G. Olf: Appl. Phys. Lett. **18**, 87 (1971)

3.19 D.J. Olego, K. Shahzad, J. Petruzello, D. Cammack: Phys. Rev. B**36**, 7674 (1987);
D.J. Olego, K. Shahzad, D. Cammack, H. Cornelissen: Phys. Rev. B**38**, 5554 (1988)

3.20 M. Wolkenstein: Compt. Rend. Acad. Sci. URSS 32, 185 (1941)

3.21 M.V. Klein: IEEE J. QE-**22**, 1760 (1986)

3.22 B. Jusserand, D. Paquet: In *Semiconductor Heterojunctions and Superlattices*, ed. by G. Allan, G. Bastard, N. Boccara, M. Lannoo, M. Voos (Springer, Berlin, Heidelberg 1986) p. 108

3.23 M. Cardona: In *Lectures on Surface Science*, ed. by G.R. Castro, M. Cardona (Springer, Berlin, Heidelberg 1987) p. 2

3.24 F. Nizzoli, K.H. Rieder (eds.): *Dynamical Phenomena at Surfaces, Interfaces, and Superlattices*, Springer Ser. Surf. Sci. Vol. 3 (Springer, Berlin, Heidelberg 1984)

3.25 L. Esaki, R. Tsu: IBM J. Res. Dev. **14**, 61 (1970)

3.26 L.L. Chang, K. Ploog (eds.): *Molecular Beam Epitaxy and Heterojunctions* (M. Nijhoff, Dordrecht 1985)

3.27 K. Ploog, N.T. Linh (eds.): *Semiconductor Quantum Well Structures and Superlattices* (Editions de Physique, Les Ulis 1985)

3.28 E.H.C. Parker (ed.): *The Technology and Physics of Molecular Beam Epitaxy* (Plenum, New York 1985)

3.29 A.C. Gossard: *Treatise on Materials Science and Technology* (Academic, New York 1982) p. 13
3.30 K. Ploog: J. Cryst. Growth **79**, 887 (1986)
3.31a M.J. Ludowise: J. Appl. Phys. **58**, R31 (1985)
3.31b R.D. Dupuis: Science **226**, 623 (1984)
3.32 K. Kunc, R. Martin: Phys. Rev. Lett. **48**, 406 (1982);
C. Falter: Physics Rep. **164**, 1 (1988)
3.33 G. Kanellis: Solid State Commun. **58**, 93 (1986); Phys. Rev. **B35**, 746 (1987)
3.34 K. Yip, Y.C. Chang: Phys. Rev. **B30**, 7037 (1984)
3.35 E. Richter, D. Strauch: Solid State Commun. **64**, 867 (1987)
see also: E. Richter: Diplomarbeit Universität Regensburg, (1986) and unpublished work by these authors;
see also: F. Ren, H. Chu, Y.C. Chang: Phys. Rev. Lett. **59**, 1841 (1987)
3.35a For calculations of (110) and (012) GaAs/AlAs superlattices and corresponding experiments see Z.V. Popović, M. Cardona, L. Tapfer, K. Ploog, E. Richter, D. Strauch: Appl. Phys. Lett. and Phys. Rev., to be published
3.36 M.T. Yin, M.L. Cohen: Phys. Rev. **B25**, 4317 (1982)
3.37 E. Molinari, A. Fasolino, K. Kunc: Superlattices and Microstructures **2**, 397 (1986)
3.38 R. Tsu, S.S. Jha: Appl. Phys. Lett. **20**, 16 (1972)
3.39 A.S. Barker, Jr., J.L. Merz, A.C. Gossard: Phys. Rev. **B17**, 3181 (1978)
3.40 A. Fasolino, E. Molinari, J.C. Maan: Phys. Rev. **B33**, 8889 (1986)
3.41 B. Jusserand, D. Paquet, J. Kervarec, A. Regreny: J. Phys. (Paris) **45–C5**, 145 (1984)
3.42 C. Colvard, T.A. Gant, M.V. Klein, R. Merlin, R. Fischer, H. Morkoc, A.C. Gossard: Phys. Rev. **B31**, 2080 (1985)
3.43 B. Jusserand: Unpublished
3.44 E.L. Albuquerque, M. Babiker, P. Fulco, S.R.P. Smith, D.R. Tilley: Unpublished
3.45 B. Djafari-Rouhani, J. Sapriel, F. Bonnouvrier: Superlattices and Microstructures **1**, 29 (1985)
3.46 L.M. Brekhovskikh: *Waves in Layered Media* (Academic, New York 1960)
3.47 R.L. Kronig, W.G. Penney: Proc. Roy. Soc. London **A130**, 499 (1930)
3.48 See for instance A.J. Dekker: *Solid State Physics* (Prentice Hall, Englewood Cliffs, N.J. 1957) p. 244
3.49 C. Colvard, R. Merlin, M.V. Klein, A.C. Gossard: Phys. Rev. Lett. **43**, 298 (1980)
3.50 S.M. Rytov, Akust. Zh. **2**, 71 (1956) [Sov. Phys. Acoust. **2**, 68 (1956)]
3.51 S.Y. Tong, A.A. Maradudin: Phys. Rev. **181**, 1318 (1969)
3.52 W.E. Jones, R. Fuchs: Phys. Rev. **B4**, 3581 (1971)
3.53 G. Kanellis, J.F. Morhange, M. Balkanski: Phys. Rev. **B28**, 3390, 3398, and 3406 (1983)
3.54 J.E. Zucker, A. Pinczuk, D.S. Chemla, A. Gossard, W. Wiegmann: Phys. Rev. Lett. **53**, 1280 (1984)
3.55 A.K. Sood, J. Menéndez, M. Cardona, K. Ploog: Phys. Rev. Lett. **54**, 2115 (1985)
3.56 B. Jusserand, F. Alexandre, J. Dubard, D. Paquet: Phys. Rev. **B33**, 2897 (1986)
3.57 P. Santos, L. Ley, J. Mebert, O. Koblinger: Phys. Rev. **B36**, 4858 (1987)
3.58 M. Nakayama, K. Kubota, S. Chika, H. Kato, N. Sano: Solid State Commun. **58**, 475 (1986)
3.59 B. Jusserand, F. Alexandre, D. Paquet, G. Le Roux: Appl. Phys. Lett. **47**, 301 (1986)
3.60 B. Jusserand, D. Paquet, F. Mollot, F. Alexandre, G. Le Roux: Phys. Rev. **B35**, 2808 (1987)
3.61 A. Fasolino, E. Molinari: J. Phys. (Paris), **48–C5**, 569 (1987)
3.62 B. Jusserand, D. Paquet: Phys. Rev. Lett. **56**, 1751 (1986)
3.63 A.K. Sood, J. Menéndez, M. Cardona, K. Ploog: Phys. Rev. Lett. **56**, 1753 (1986)
3.64 E. Molinari, A. Fasolino, K. Kunc: Phys. Lett. **56**, 1751 (1986)
3.65 C. Colvard, R. Fischer, T.A. Gant, M.V. Klein, R. Merlin, H. Morkoc, A.C. Gossard: Superlattices and Microstructures **1**, 81 (1985)
3.66a A.K. Sood, J. Menéndez, M. Cardona, K. Ploog: Phys. Rev. Lett. **54**, 2111 (1985)

3.66b A. Ishibashi, M. Itabashi, Y. Mori, K. Kaneko, S. Kawado, N. Watanabe: Phys. Rev. **B33**, 2887 (1986)
3.67 B. Jusserand, D. Paquet, A. Regreny: Phys. Rev. **B30**, 6245 (1984)
3.68 A. Nagaoui, B. Djafari-Rouhani: Surface Sci. **185**, 125 (1987) and references therein
3.69 M. Born, K. Huang: *Dynamical Theory of Crystal Lattices* (Clarendon, Oxford 1954)
3.70 W.L. Mochan, M. del Castillo-Mussot, R.G. Barrera: Phys. Rev. **B35**, 1088 (1987); R.F. Wallis, R. Szenics, J.J. Quinn, G.F. Giuliani: Phys. Rev. **B36**, 1218 (1987)
3.70a For a recent observation of phonon polaritons in a GaAs/AlAs heterostructure see M. Nakayama, M. Ishida, N. Sano: Phys. Rev. **B38**, 6348 (1988)
3.71 R. Merlin, C. Colvard, M.V. Klein, H. Morkoc, A.Y. Cho, A.C. Gossard: Appl. Phys. Lett. **36**, 43 (1980)
3.72 R. Fuchs, K.L. Kliever: Phys. Rev. **140A**, 2076 (1965)
3.73 R.E. Camley, D.L. Mills: Phys. Rev. **B29**, 1695 (1984)
3.73a See Chap. 2, p. 25
3.74 M. Cardona: Am. J. Phys. **39**, 1277 (1971)
3.75 G. Fasol, N. Mestres, H.P. Hughes, A. Fisher, K. Ploog: Phys. Rev. Lett. **56**, 2517 (1986)
3.76 A very simple lattice dynamical model which includes both interface and confined modes and their interaction has been given by K. Huang, B.F. Zhu: Phys. Rev. **B38**, 2183 (1988); **B38**, 13377 (1988). Also, T. Tsuchiya, H. Akera, T. Ando: Phys. Rev. B, in press
3.77 Ph. Lambin, J.P. Vigneron, A.A. Lucas, P.A. Thiry, M. Liehr, J.J. Pireaux, R. Caudano, T.J. Kuech: Phys. Rev. Lett. **56**, 1842 (1986)
3.78 See the appendix of J. Sapriel, J.C. Michel, J.C. Toledano, R. Vacher, J. Kervarec, A. Regreny: Phys. Rev. **B28**, 2007 (1983)
3.79 M. Tinkham: *Group Theory and Quantum Mechanics* (McGraw-Hill, New York 1964) p. 328
3.80 G. Koster: *Solid State Physics, Vol. 5* (Academic, New York 1957); D.L. Rousseau, R.P. Bauman, S.P.S. Porto: J. Raman Spectr. **10**, 253 (1981)
3.81 K. Kunc: Ann. Physiq. (Paris) **8**, 319 (1973–1974)
3.82 T. Toriyama, N. Kobayashi, Y. Horikoshi: Jap. J. Appl. Phys. **25**, 1895 (1986)
3.83 A.A. Maradudin: *Festkörperprobleme/Advances in Solid State Physics XXI*, ed. by J. Treusch (Vieweg, Dortmund 1981) p. 25
3.84 K. Kunc, H. Bilz: Solid State Commun. **19**, 1027 (1976)
3.84a For recent work see B. Lou, R. Sudharsanan, S. Perkowitz: Phys. Rev. **B38**, 2212 (1988)
3.85 K.A. Maslin, T.J. Parker, N. Raj, D.R. Tilley, P.J. Dobson, D. Hilton, C.T.B. Foxon: Solid State Commun. **60**, 461 (1986)
3.86 S. Go, H. Bilz, M. Cardona: Phys. Rev. Lett. **34**, 580 (1975)
3.87 S. Go, H. Bilz, M. Cardona: *Light Scattering in Solids*, ed. by M. Balkanski, R.C.C. Leite, S.P.S. Porto (Flammarion, Paris 1976) p. 377
3.88 S. Nakashima, M. Balkanski: Phys. Rev. **B34**, 5801 (1986) and references therein
3.89 E. López-Cruz, M. Cardona, E. Martínez: Phys. Rev. **B29**, 5774 (1984)
3.90 E. López-Cruz, M. Cardona: Solid State Commun. **45**, 787 (1983)
3.91 B. Jusserand, D. Paquet, A. Regreny: Superlattices and Microstructures **1**, 61 (1985)
3.92 A.A. Maradudin, E. Burstein: Phys. Rev. **164**, 1081 (1967)
3.93 D. Bermejo, S. Montero, M. Cardona, A. Muramatsu: Solid State Commun. **42**, 153 (1982)
3.94 B. Zhu, K.A. Chao: Phys. Rev. **B36**, 4906 (1987)
3.95 M.V. Klein, C. Colvard, R. Fischer, H. Morkoc: J. Phys. (Paris) **45-C5**, 131 (1984)
3.96 O. Madelung, M. Schulz, H. Weiss (eds.): *Landoldt-Börnstein Tables, Vol. 17a*, (Springer, Berlin, Heidelberg 1982) and references therein
3.97 For information on Si see: M.H. Grimsditch, E. Kisela, M. Cardona: Phys. Stat. Sol. **B60**, 135 (1980)
3.98 M. Babiker, D.R. Tilley, E.R. Albuquerque: J. Phys. **C18**, 1285 (1985)
3.99 M.V. Klein: In *Proc. 10th Int. Conf. on Raman Spectroscopy*, ed. by W.L. Peticolas, B. Hudson (University of Oregon, Eugene, Oregon 1986) p. 9–1

3.100 J. He, J. Sapriel, J. Chavignon, R. Azoulay, L. Dugrand, F. Mollot, B. Djafari-Rouhani, R. Vacher: J. Phys. (Paris), **48-C5**, 573 (1987)
3.101 J.L. Merz, A.S. Barker, Jr., A.C. Gossard: Appl. Phys. Lett. **31**, 117 (1977)
3.102 G. Abstreiter, A. Pinczuk, M. Cardona (eds.): *Light Scattering in Solids IV*, Topics Appl. Phys., Vol. 54 (Springer, Berlin, Heidelberg 1984) p. 5
3.103 P. Manuel, G.A. Sai-Halasz, L.L. Chang, Chin-an Chang, L. Esaki: Phys. Rev. Lett. **37**, 1701 (1976)
3.104 G.A. Sai-Halasz, A. Pinczuk, P.Y. Yu, E. Esaki: Solid State Commun. **25**, 381 (1978)
3.105 V. Narayanamurti, H.L. Stormer, M.A. Chin, A.C. Gossard, W. Wiegmann: Phys. Rev. Lett. **43**, 2012 (1979)
3.106 D.C. Hurley, S. Tamura, J.P. Wolfe, H. Morkoc: Phys. Rev. Lett. **58**, 2446 (1987); S. Tamura, J.P. Wolfe: Phys. Rev. B**35**, 2528 (1987)
3.107 P.V. Santos, J. Mebert, O. Koblinger, L. Ley: Phys. Rev. B**36**, 1306 (1987)
3.108 C. Colvard, R. Merlin, M.V. Klein, A.C. Gossard: J. Phys. (Paris) **42-C6**, 631 (1981)
3.109 J. Sapriel, J.C. Michel, J.C. Toledano, R. Vacher: J. Phys. (Paris) **45-C5**, 139 (1984)
3.110 B. Jusserand, D. Paquet, A. Regreny, J. Kervarec: Solid State Commun. **48**, 499 (1983)
3.111 M. Nakayama, K. Kubota, T. Kanata, H. Kato, S. Chika, N. Sano: Jap. J. Appl. Phys. **24**, 1331 (1985)
3.112 M. Nakayama, K. Kubota, H. Kato, S. Chika, N. Sano: Solid State Commun. **53**, 493 (1985)
3.113 B. Jusserand, D. Paquet, F. Alexandre, A. Regreny: Surface Sci. **174**, 94 (1986)
3.114 R. Azoulay, B. Jusserand, G. Le Roux, P. Ossard, L. Dugrand: J. Cryst. Growth **77**, 546 (1986)
3.115 B. Jusserand, D. Paquet, F. Mollot, F. Alexandre, G. Le Roux: Superlattices and Microstructures **2**, 465 (1986)
3.116 J. Sapriel, J. He, J. Chavignon, G. Le Roux, J. Burgeat, F. Alexandre, R. Azoulay, R. Vacher: In *Proc. 18th Int. Conf. on the Physics of Semiconductors*, ed. by O. Engström (World Scientific, Singapore 1987) p. 723
3.117 T.A. Gant, M.V. Klein, T. Henderson, H. Morkoc: In *Proc. 10th Int. Conf. Raman Spectroscopy*, ed. by W.L. Peticolas, B. Hudson (University of Oregon, Eugene, Oregon 1986) p. 9–2
3.118 J. Sapriel, J. Chavignon, F. Alexandre, R. Azoulay: Phys. Rev. B**34**, 7118 (1986)
3.119 D. Levi, S.L. Zhang, M.V. Klein, J. Kem, H. Morkoc: Phys. Rev. B**36**, 8032 (1987)
3.120 B. Jusserand, P. Voisin, M. Voos, L.L. Chang, E.E. Mendez, L. Esaki: Appl. Phys. Lett. **46**, 678 (1985)
3.121 G.P. Schwartz, G.J. Gualtieri, W.A. Sunder, L.A. Farrow, D.E. Aspnes, A.A. Studna: J. Vac. Sci. Technol. A**5**, 1500 (1986)
3.122 G.P. Schwartz, G.J. Gualtieri, W.A. Sunder, L.A. Farrow: Phys. Rev. B**36**, 4868 (1987)
3.123 P.V. Santos, A.K. Sood, M. Cardona, K. Ploog, Y. Ohmori, M. Okamoto: Phys. Rev. B**37**, 6381 (1988)
3.124 B. Jusserand: Unpublished
3.125 D.J. Lockwood, M.W.C. Dharma-wardana, W.T. Moore, R.L.S. Devine: Appl. Phys. Lett. **51**, 361 (1987)
3.126 S. Venugopalan, L.A. Kolodziejski, R.L. Gunshor, A.K. Ramdas: Appl. Phys. Lett. **45**, 974 (1984)
3.127 E.K. Suh, D.U. Bartholomew, A.K. Ramdas, S. Rodriguez, S. Venugopalan, L.A. Kolodziejski, R.L. Gunshor: Phys. Rev. B**36**, 4316 (1987)
3.128 H. Brugger, G. Abstreiter, H. Jorke, H.J. Herzog, E. Kasper: Phys. Rev. B**33**, 5928 (1986)
3.129 H. Brugger, H. Reiner, G. Abstreiter, H. Jorke, H.J. Herzog, E. Kasper: Superlattices and Microstructures **2**, 451 (1986)
3.130 M.W.C. Dharma-wardana, D.J. Lockwood, J.M. Baribeau, D.C. Houghton: Phys. Rev. B**34**, 3034 (1986)
3.131 D.J. Lockwood, M.W.C. Dharma-wardana, J.M. Baribeau, D.C. Houghton: Phys. Rev. B**35**, 2243 (1987)

3.132 P.V. Santos, M. Hundhausen, L. Ley: J. Non-Cryst. Solids **77–78**, 1069 (1985)

3.133 P.V. Santos, M. Hundhausen, L. Ley: Phys. Rev. B**33**, 1516 (1985)

3.134 P.V. Santos, L. Ley: Phys. Rev. B**36**, 3325 (1987)

3.135 B. Jusserand, F. Mollot, M.C. Joncour, B. Etienne: J. Phys. (Paris), **48–C5**, 577 (1987)

3.136 R. Merlin, K. Bajema, R. Clarke, F.Y. Juang, P.K. Bhattacharya: Phys. Rev. Lett. **55**, 1768 (1985)

3.137 M.W.C. Dharma-wardana, A.H. MacDonald, D.J. Lockwood, J.M. Baribeau, D.C. Houghton: Phys. Rev. Lett. **58**, 1761 (1987)

3.138 R. Merlin, K. Bajema, J. Nagle, K. Ploog: J. Phys. (Paris), **48–C5**, 503 (1987)

3.139 A. Magerl, H. Zabel: Phys. Rev. Lett. **46**, 444 (1981);
see also: M.S. Dresselhaus, G. Dresselhaus: In *Light Scattering in Solids III*, ed. by M. Cardona, G. Güntherodt, Topics Appl. Phys., Vol. 51 (Springer, Berlin, Heidelberg 1982) p. 3

3.140 J. Sapriel, J.C. Michel, J. Chavignon, R. Vacher, A. Langford, F. Alexandre: In *Proc. Second Int. Conf. Phonon Physics*, ed. by J. Kollar, N. Kroo, N. Menyhard, T. Siklos (World Scientific, Singapore 1985) p. 526

3.140a For recent values of elastic constants and sound velocities of AlAb see Landolt-Börnstein Tables, Volume 22, ed. by O. Madelung and H. Schulz (Springer, Heidelberg 1987) p. 65

3.141 B. Jusserand: Ph. D. Thesis, Université Paris VI (1987)

3.142 A. Segmuller, A.E. Blakeslee: J. Appl. Cryst. **6**, 19 (1973)

3.143 See for instance: B. Jusserand, J. Sapriel: Phys. Rev. B**24**, 7194 (1981)

3.144 H. Brugger, G. Abstreiter: J. Phys. (Paris), **48–C5**, 661 (1988)

3.145 J. Kervarec, M. Baudet, J. Caulet, P. Auvray, J.Y. Emery, A. Regreny: J. Appl. Cryst. **17**, 196 (1984)

3.146 M. Quillec, L. Goldstein, G. Le Roux, J. Burgeat, J. Primot: Appl. Phys. Lett. **55**, 2904 (1984)

3.147 K. Kubota, M. Nakayama, H. Katoh, N. Sano: Solid State Commun. **49**, 157 (1984)

3.148 A. Ishibashi, Y. Mori, M. Itabashi, N. Watanabe: J. Appl. Phys. **58**, 2691 (1985)

3.149 Z.P. Wang, D.S. Jiang, K. Ploog: Solid State Commun. **65**, 661 (1988)

3.150 J. Menéndez, A. Pinczuk, J.P. Valladares, R.D. Feldman, R.F. Austin: Appl. Phys. Lett. **50**, 1101 (1987)

3.151 D. Gammon, R. Merlin, H. Morkoc: Phys. Rev. B**35**, 2552 (1987)

3.152 G. Ambrazevicius, M. Cardona, R. Merlin, K. Ploog: Solid State Commun. **65**, 1035 (1988)

3.153 A.K. Arora, A.K. Ramdas, M.R. Melloch, N. Otsuka: Phys. Rev. B**36**, 1021 (1987);
A.K. Aora, E.-K. Suh, A.K. Ramdas, F.A. Chambers, A.L. Moretti: Phys. Rev. B**36**, 6142 (1987)

3.154 B. Jusserand, D. Paquet, F. Alexandre, M.W. Charane, A. Regreny: In *Proc. Second Int. Conf. Phonon Physics*, ed. by J. Kollar, N. Kroo, N. Menyhard, T. Siklos (World Scientific, Singapore 1985) p. 521

3.155 See for instance: I.F. Chang, S.S. Mitra: Adv. Phys. **20**, 359 (1971);
L. Genzel, T.P. Martin, C.H. Perry: Phys. Stat. Solid. B**62**, 83 (1974)

3.156 R. Bonneville: Phys. Rev. B**24**, 1987 (1981) and references therein

3.157 P. Soven: Phys. Rev. **178**, 1136 (1969)

3.158 B. Jusserand, D. Paquet, K. Kunc: In *Proc. 17th Int. Conf. Physics of Semiconductors*, ed. by J.D. Chadi, W.A. Harrison (Springer, Berlin, Heidelberg, New York 1985) p. 1165

3.159 J.W. Worlock: In *Proc. Second Int. Conf. on Phonon Physics*, ed. by J. Kollar, N. Kroo, N. Menyhard, T. Siklos (World Scientific, Singapore 1985) p. 506

3.160 J.L.T. Waugh, G. Dolling: Phys. Rev. **132**, 2410 (1963)

3.161 R.M. Fleming, D.B. McWhan, A.C. Gossard, W. Wiegmann, R.A. Logan: J. Appl. Phys. **51**, 357 (1980)

3.162 Shu-Lin Zhang, D.H. Levi, T.A. Gant, M.V. Klein, J. Klem, H. Morkoc: In *Proc. 10th Int. Conf. Raman Spectroscopy*, ed. by W.L. Peticolas, B. Hudson (University of Oregon, Eugene, Oregon 1986) p. 9–4

3.163 M. Nakayama, K. Kubota, H. Kato, N. Sano: Solid State Commun. **51**, 343 (1984)
3.164 G. Abstreiter, H. Brugger, T. Wolf, H. Jorke, H.J. Herzog: Phys. Rev. Lett. **54**, 2441 (1985)
3.165 F. Cerdeira, A. Pinczuk, J.C. Bean, B. Batlogg, B.A. Wilson: Appl. Phys. Lett. **45**, 1138 (1984)
3.166 S. Nakashima, Y. Nakakura, H. Fujiyasu, K. Mochizuki: Appl. Phys. Lett. **48**, 236 (1986)
3.167 Le Hong Shon, K. Inoue, K. Murase, H. Fujiyasu, Y. Yamazaki: Solid State Commun. **62**, 621 (1987)
3.168 D.J. Olego: Appl. Phys. Lett. **51**, 1422 (1987); J. Vac. Sci. Technol. B**6**, 1193 (1988)
3.169 B.A. Weinstein, R. Zallen: In *Light Scattering in Solids IV*, ed. by M. Cardona, G. Güntherodt, Topics Appl. Phys., Vol. 54 (Springer, Berlin, Heidelberg 1984) p. 463
3.170 P. Wickboldt, E. Anastassakis, R. Sauer, M. Cardona: Phys. Rev. B**35**, 1362 (1987)
3.171 E. Anastassakis, A. Pinczuk, E. Burstein, M. Cardona, F.H. Pollak: Solid State Commun. **8**, 133 (1970)
3.172 E. Anastassakis, Y.S. Raptis, M. Hünermann, W. Richter, M. Cardona: Phys. Rev. B**38**, 7702 (1988)
3.173 E. Anastassakis, M. Cardona: Solid State Commun. **63**, 897 (1987)
3.174 Y.J. Yang, K.Y. Hsieh, R.M. Kolbas: Appl. Phys. Lett. **51**, 215 (1987)
3.175 S.P.J. Brueck, B.Y. Tsaur, J.C.C. Fan, D.V. Murphy, T.F. Deutsch, D.J. Silversmith: Appl. Phys. Lett. **40**, 895 (1982)
3.176 J. Menéndez, M. Cardona: Phys. Rev. B**29**, 2051 (1984)
3.177 H. Kamimura, T. Nakayama: *Comments on Condensed Matter Physics* (in press)
3.178 L. Brey, C. Tejedor: Phys. Rev. Lett. **59**, 1022 (1987)
3.179 C. Mailhiot, D.L. Smith: Phys. Rev. B**35**, 1242 (1987)
3.180 N. Hamada, S. Ohnishi: Superlattices and Microstructures **3**, 301 (1987)
3.181 T. Ando, A.B. Fowler, F. Stern: Rev. Mod. Phys. **54**, 437 (1982)
3.182 see, for instance: A.K. Sood, W. Kauschke, J. Menéndez, M. Cardona: Phys. Rev. B**35**, 2886 (1987);
C. Trallero-Giner, A. Alexandrou, M. Cardona: Phys. Rev. B**38**, 10744 (1988)
3.183 A.K. Sood, G. Contreras, M. Cardona: Phys. Rev. B**31**, 3760 (1985)
3.184 M.I. Alonso, M. Cardona: Phys. Rev. B**37**, 10107 (1988)
3.185 L. Brey, N.E. Christensen, M. Cardona: Phys. Rev. B**36**, 2638 (1987)
3.186 R.M. Martin: Phys. Rev. B**3**, 676 (1971)
3.187 W. Kauschke, M. Cardona: Phys. Rev. B**33**, 5473 (1986)
3.188 W. Kauschke, M. Cardona: Phys. Rev. B**35**, 9619 (1987)
3.189 C. Tejedor, J.M. Calleja, F. Meseguer, E.E. Méndez, C.A. Chang, L. Esaki: Phys. Rev. B**32**, 5303 (1985)
3.190 R. Zeyher, C.S. Ting, J.L. Birman: Phys. Rev. B**10**, 1725 (1974)
3.191 W. Richter, R. Zeyher, M. Cardona: Phys. Rev. B**18**, 4312 (1978)
3.192 A.A. Gogolin, E.I. Rashba: Solid State Commun. **19**, 1177 (1976)
3.193 J. Menéndez, M. Cardona: Phys. Rev. Lett. **51**, 1297 (1983); Phys. Rev. B**31**, 3693 (1985)
3.194 W. Kauschke, N. Mestres, M. Cardona: Phys. Rev. B**36**, 7469 (1987)
3.195 R. Dingle, W. Wiegmann, C.H. Henry: Phys. Rev. Lett. **33**, 827 (1974)
3.196 W. Stolz, J.C. Mann, M. Altarelli, L. Tapfer, K. Ploog: Phys. Rev. B**36**, 4301 (1987)
3.197 J.E. Zucker, A. Pinczuk, D.S. Chemla, A. Gossard, W. Wiegmann: Phys. Rev. Lett. **51**, 1293 (1983);
J.E. Zucker, A. Pinczuk, D.S. Chemla: Phys. Rev. B**38**, 4287 (1988)
3.198 W. Kauschke, A.K. Sood, M. Cardona, K. Ploog: Phys. Rev. B**36**, 1612 (1987)
3.199 J.E. Zucker, A. Pinczuk, D.S. Chemla, A. Gossard, W. Wiegmann: Phys. Rev. B**29**, 7065 (1984)
3.200 D.A. Kleinman, R.C. Miller, A.C. Gossard: Phys. Rev. B**35**, 664 (1987)
3.200a A. Alexandrou, M. Cardona, K. Ploog: Phys. Rev. B**38**, 2196 (1988)
3.201 S.K. Chang, H. Nakata, A.V. Nurmikko, R.L. Gunshar, L.A. Kolodziejski: Appl. Phys. Lett. **51**, 667 (1987)

3.202 J.E. Zucker, A. Pinczuk, D.S. Chemla, A.C. Gossard: Phys. Rev. **B35**, 2892 (1987)

3.203 T. Suemoto, G. Fasol, K. Ploog: Phys. Rev. **B34**, 6034 (1986)

3.204 A. Ishibashi, M. Itabashi, Y. Mori, N. Watanabe: Opto-Electron. Devices and Technologies **1**, 51 (1986)

3.205 M. Cardona, T. Suemoto, N.E. Christensen, T. Isu, K. Ploog: Phys. Rev. **B36**, 5906 (1987)

3.206 N. Kobayashi, T. Toriyama, Y. Horikoshi: Appl. Phys. Lett. **50**, 1811 (1987)

3.206a T.A. Gant, M. Delaney, H.V. Klein, R. Houdré, H. Morkoç: Phys. Rev., in press

3.207 R.C. Miller, D.A. Kleinman, A.C. Gossard: Solid State Commun. **60**, 213 (1986)

3.208 R.C. Miller, D.A. Kleinman, S.K. Sputz: Phys. Rev. **B34**, 7444 (1986)

3.209 F. Cerdeira, E. Anastassakis, W. Kauschke, M. Cardona: Phys. Rev. Lett. **57**, 3209 (1986)

3.210 A. Alexandrou, M. Cardona: Solid State Commun. **64**, 1029 (1987)

3.211 A. Madhukar, P.D. Lao, W.C. Tang, M. Adam, F. Voillot: Phys. Rev. Lett. **59**, 1313 (1987)

3.212 S. Adachi, C. Hamaguchi: Phys. Rev. **B19**, 938 (1979)

3.213 E. Käräjämäki, R. Laiko, T. Levola, B.H. Bairamov, A.V. Gol'tsev, T. Toporov: Phys. Rev. **B29**, 4508 (1984)

3.214 B.H. Bairamov, A.V. Golt'sev, V.V. Toporov, R. Laiho, T. Lavola: Phys. Rev. **B33**, 5875 (1986)

3.215 M. Cardona: In *Atomic Structure and Properties of Solids*, ed. by E. Burstein (Academic, New York 1972) p. 514

3.216 see, for instance, M. Cardona: *Modulation Spectroscopy* (Academic, New York 1969)

3.217 J.E. Wells, P. Handler: Phys. Rev. **B3**, 1319 (1971). The data of Fig. 4 in this reference are piezo-optical constants. They can be transformed into photoelastic ones by multiplying by elastic shiftness constants

3.218 R.T. Collins, K. v. Klitzing, K. Ploog: Phys. Rev. **B33**, 4378 (1986)

3.219 L. Viña, R.T. Collins, E.E. Méndez, W.I. Wang: Phys. Rev. **B33**, 5939 (1986)

3.220 C. Tejedor, A. Hernandez-Cabrera: Phys. Rev. **B33**, 7389 (1986)

3.221 C. Tejedor, J.M. Calleja, L. Brey, L. Viña, E.E. Méndez, W.I. Wang, M. Staines, M. Cardona: Phys. Rev. **B36**, 6054 (1987)

3.222 A.K. Sood, J. Menéndez, M. Cardona, K. Ploog: Phys. Rev. **B32**, 1412 (1985)

3.223 M.H. Meynadier, E. Finkman, M.D. Sturge, J.M. Worlock, M.C. Tamargo: Phys. Rev. **B35**, 2517 (1987)

3.224 V.V. Gridin, R. Besserman, K.P. Jain, M.V. Klein, H. Morkoc: Superlattices and Microstructures **3**, 107 (1987)